Magnesiothermic synthesis of thermoelectric intermetallics : mechanisms, multi-scale characterizations and properties

Sylvain Le Tonquesse

UNIVERSITE MATIERE BRETAGNE MOLECULES LOIRE ET MATERIAUX

UNIVERSITÉ DE RENNES 1

THESE DE DOCTORAT DE

L'UNIVERSITE DE RENNES 1
COMUE UNIVERSITE BRETAGNE LOIRE

ECOLE DOCTORALE N° 596
Matière, Molécules, Matériaux
Spécialité : « *Chimie des Matériaux* »

Par

Sylvain LE TONQUESSE

Magnesiothermic synthesis of thermoelectric intermetallics: mechanisms, multi-scale characterizations and properties.

Thèse présentée et soutenue à Rennes, le 20 septembre 2019
Unité de recherche : Institut des Sciences Chimiques de Rennes (UMR CNRS 6226)

Rapporteurs avant soutenance :

Céline DARIE	Professeure, Université Grenoble Alpes
Franck GASCOIN	Maître de conférences, Université de Caen

Composition du Jury :

Examinateurs :

Nathalie AUDEBRAND	Professeure, Université de Rennes 1
Stéphane JOBIC	Directeur de Recherche, CNRS, Institut des Matériaux de Nantes
Mathieu PASTUREL	Chargé de Recherche, CNRS, Institut des Sciences Chimiques de Rennes
Valérie PAUL-BONCOUR	Directrice de Recherche, CNRS, Institut Chimie Matériaux Paris-Est

Invités

Valérie DEMANGE	Chargée de Recherche, CNRS, Institut des Sciences Chimiques de Rennes
Carmelo PRESTIPINO	Chargé de Recherche, CNRS, Institut des Sciences Chimiques de Rennes

Remerciements

Mes travaux de recherche présentés dans ce manuscrit ont été accompli au sein de l'Institut des Sciences Chimiques de Rennes dirigé par Monsieur Marc Fourmigué, dans l'équipe « Chimie du Solide et des Matériaux » dirigée par Monsieur Stéphane Cordier.

Je remercie vivement Madame Céline Darie, professeure à l'Université Grenoble Alpes, et Monsieur Franck Gascoin, maître de conférence à l'université de Caen, d'avoir accepté d'évaluer ce manuscrit. Madame Valérie Paul-Boncour, directrice de recherche à l'institut de chimie des matériaux de Paris-Est, et Monsieur Stéphane Jobic, directeur de recherche à l'institut des matériaux Jean Rouxel de m'avoir honoré de leur présence dans ce jury de thèse. Enfin, Madame Nathalie Audebrand, professeure à l'université de Rennes 1, d'avoir présidé ce jury. J'exprime toute ma reconnaissance aux membres de ce jury pour l'enthousiasme dont ils ont fait preuve envers mes travaux de thèse.

Je tiens à remercier toutes les personnes qui ont contribué à ce travail et tout particulièrement les personnes qui suivent :

Mon directeur de thèse, Mathieu Pasturel, qui a été très disponible, bienveillant et qui m'a accordé une totale confiance tout au long de mon doctorat. Merci beaucoup de m'avoir permis d'autant voyager et de rencontrer autant de personnes. Je retiendrai, bien sûr, tous les nombreux bons moments passés en dehors du laboratoire que ce soit à un barbecue, au bar ou à la pêche. Si je devrais refaire ma thèse, je te rechoisirais avec certitude comme directeur !

Mes co-encadrants Valérie Demange et Carmelo Prestipino qui ont tous les deux été très présents et qui m'ont apporté d'inestimables connaissances dans leurs domaines respectifs. Vous avez été géniaux !

Je remercie grandement David Berthebaud et Fabien Grasset du laboratoire LINK ainsi que Takao Mori du NIMS pour m'avoir accueilli au sein de leurs laboratoires à Tsukuba pendant un mois.

Stéphanie Fryars avec qui j'ai partagé de bons moments au laboratoire et Valérie Le Cam qui m'a énormément aidé avec mes montages réactionnels et les pannes d'appareils.

Le personnel du SCEBA, Loic Joanny et Francis Gouttefangeas, ainsi que du THEMIS, Vincent Dorcet et Ludivine Rault, pour leur professionnalisme et leur bonne humeur.

Je tiens aussi à remercier Eric Alleno pour notre collaboration et pour m'avoir accueilli quelques jours à ICMPE à Thiais. Nos échanges m'ont grandement aidé tout au long de ma thèse.

Tous les doctorants, permanents, stagiaires, secrétaires et barmans que j'ai pu côtoyer durant mes trois années de thèse, avec une mention spéciale pour : Laura, Maxence, Samuel, Barthelemie, Pierric, Zelia, Kevin, Clément, Nathalie, Touikou, Sophie et Clément du BB, Gilou du Sham'...

Et enfin à ma famille, à tous mes amis, à Moustapha Diallo et à Roger Federer.

Résumé en français

Les matériaux thermoélectriques (TE) permettent la conversion de chaleur en électricité et vice-versa, respectivement grâce aux effets Seebeck et Peltier.[1] Les générateurs thermoélectriques et modules Peltier consistent en des blocs de matériaux semiconducteurs de type N et P connectés électriquement en série et thermiquement en parallèle, et placés entre deux plaques de céramique (fig. 1a). L'avantage principal de ces dispositifs "tout-solides" est qu'ils sont très fiables, miniaturisables, silencieux et qu'ils ne nécessitent pas d'effort de maintenance particulier. Cette technologie, si elle était optimisée, pourrait être généralisée et grandement améliorer l'efficacité énergétique globale de nos sociétés modernes en permettant notamment la récupération partielle des grandes quantités de chaleur perdues par les moteurs thermiques, les lignes de production industrielles, les panneaux solaires ou encore par le corps humain. De plus, les modules Peltier sont une alternative aux dispositifs de réfrigération classiques fonctionnant grâce à des fluides caloporteurs à fort pouvoir d'effet de serre. Le développement à grande échelle est cependant freiné par les faibles rendements ($< 10\%$)[2] et par le coût élevé des matières premières et des procédés de fabrication des matériaux.[3] Pour ces raisons, les dispositifs thermoélectriques ne sont actuellement utilisés que dans des niches technologiques telles que l'exploration spatiale, le refroidissement localisé de systèmes électroniques ou dans des dispositifs de réfrigération mobiles.[4]

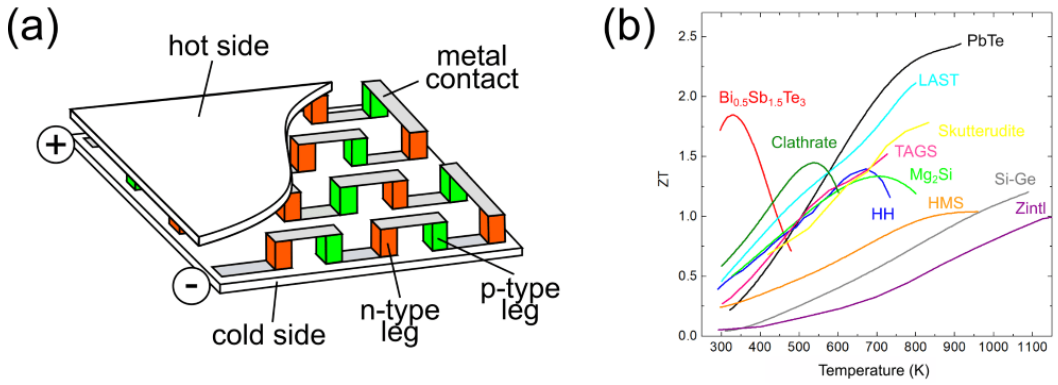

Figure 1: (a) Schéma d'un module thermoélectrique. (b) Dépendance en température du facteur de mérite ZT de quelques-uns des meilleurs matériaux actuels. Les données sont issues d'articles de la littérature.[5–15]

Le développement de matériaux plus performants est donc une priorité dans l'espoir de pouvoir agrandir le champ des applications possibles. Les performances des matériaux

thermoélectriques sont dictées par le facteur de mérite adimensionnel ZT défini comme :

$$ZT = \frac{\alpha^2}{\rho\,(\kappa_L + \kappa_e)}\,T \tag{1}$$

où α est le coefficient Seebeck, ρ la résistivité électrique, κ_L et κ_e les contributions du réseau et des porteurs de charge à la conductivité thermique κ=κ_L+κ_e totale du matériau et T la température absolue. Les matériaux présentant les meilleures propriétés thermoélectriques sont les semiconducteurs. Cependant, il est difficile de fortement améliorer le facteur de mérite ZT car les propriétés α, ρ et κ_e sont intercorrélées du fait qu'elles dépendent toutes de la concentration en porteurs de charge dans le matériau.[16] Pour cette raison, les meilleurs matériaux actuels n'ont que très rarement des valeurs de ZT dépassant 1,5 (fig. 1b).

La conductivité thermique de réseau κ_L reste donc le seul paramètre pouvant être optimisé indépendamment. Une des stratégies les plus utilisées pour réduire κ_L sans affecter les propriétés électroniques est de développer des matériaux polycristallins nano- (taille de cristallites inférieure à 100 nm) ou mesostructurés (taille de cristallites entre 100 nm et 1 μm).[17–19] En effet, de cette manière, il va être possible de diffuser sélectivement les phonons qui ont en général des libres parcours moyens bien plus importants que les porteurs de charge. Récemment, les propriétés thermoélectriques de matériaux nanostructurés ont pu être améliorées jusqu'à 30 % comparées à celles de leurs homologues massifs.[20–22] Cependant, la synthèse de ces matériaux par des méthodes métallurgiques classiques (fusion/solidification/recuit) suivies d'un broyage peut être délicate en plus d'être très consommatrice en temps et en énergie. Le coût de la synthèse des matériaux vient donc se rajouter au prix déjà élevé des éléments le constituant.

L'objectif de ma thèse est d'élaborer une méthode de synthèse de matériaux thermoélectriques par magnésioréduction. Les synthèses par magnésioréduction d'alliages ou d'intermétalliques consiste en la co-réduction d'oxydes métalliques par le magnésium selon la réaction :

$$\mathrm{MO}_x + \mathrm{M'O}_y + (\mathrm{x{+}y})\,\mathrm{Mg} \longrightarrow \mathrm{MM'} + (\mathrm{x{+}y})\,\mathrm{MgO} \tag{2}$$

Ce type de réaction est, par exemple, utilisé à l'échelle industrielle pour l'extraction du titane (Kroll process)[23], de l'uranium[24] ou des terres rares (procédé AMES).[25]

Cette méthode est en revanche assez peu utilisée pour la synthèse d'intermétalliques bien qu'elle présente de nombreux avantages en comparaison des méthodes de fusion/solidification conventionnelles telles que :

1. l'utilisation de précurseurs oxydes stables à l'air et généralement bien moins coûteux que les métaux correspondants ;
2. des températures plus faibles et temps réactionnels plus courts grâce au fort pouvoir réducteur de Mg (E° = - 2.372 V/ESH) ;
3. de bonnes perspectives de mise à l'échelle industrielle ;
4. l'obtention de produits directement sous forme de poudres submicroniques et bien cristallisées qui peuvent convenir pour la fabrication de matériaux nanostructurés.

Lors de ma thèse, j'ai développé une procédure de synthèse par magnésioréduction de skuttérudites dérivant de $CoSb_3$ et de siliciures de métaux de transition β-$FeSi_2$ et MnSiγ ($\gamma \approx 1.74$). Ces matériaux ont été choisis car leurs synthèses par des méthodes conventionnelles sont relativement difficiles à cause de leurs lentes formations peritectiques ou peritectoïdes à "basses" températures et qui nécessitent donc de long recuits.[26] De plus, ils sont constitués d'éléments présentant de fortes tensions de vapeur à hautes températures (Sb and Mn) ou des coefficients de diffusion à l'état solide très faibles (Si). Enfin, l'amélioration du ZT de ces matériaux passe obligatoirement par la réduction de leurs conductivités thermiques qui peuvent atteindre 10 et 16 W m^{-1} K^{-1} à température ambiante pour $CoSb_3$[27] et β-$FeSi_2$.[28] Des publications de la littérature ont rapporté d'importantes réductions de κ_L de ces matériaux grâce à la nanostructuration.[29,30] Pour chaque matériau sélectionné, mon travail a consisté à :

1. développer un montage réactionnel facilitant la réalisation d'un nombre important de synthèses à moindre coût ;
2. sélectionner/synthétiser les précurseurs ainsi qu'optimiser les conditions réactionnelles et de frittage afin obtenir des matériaux massifs purs avec un bon contrôle de la composition chimique et des tailles de grains les plus petites possibles ;
3. caractériser la (micro)structure (diffraction des rayons X et des électrons, microscopies électroniques...) des matériaux pulvérulents et massifs ;
4. mesurer et expliquer les propriétés thermoélectriques à haute température de mes échantillons par rapport à des échantillons de référence préparés par fusion solidification en terme de relation structure-microstructure-propriétés.

Les résultats obtenus lors de cette thèse ont fait l'objet de 4 articles publiés ou soumis à des journaux à comité de lecture et qui constituent les 4 chapitres principaux de ce manuscrit. Les deux premiers concernent la synthèse de skutterutites tandis que les deux suivants exposent les résultats obtenus pour la synthèse de siliciures de métaux de transition.

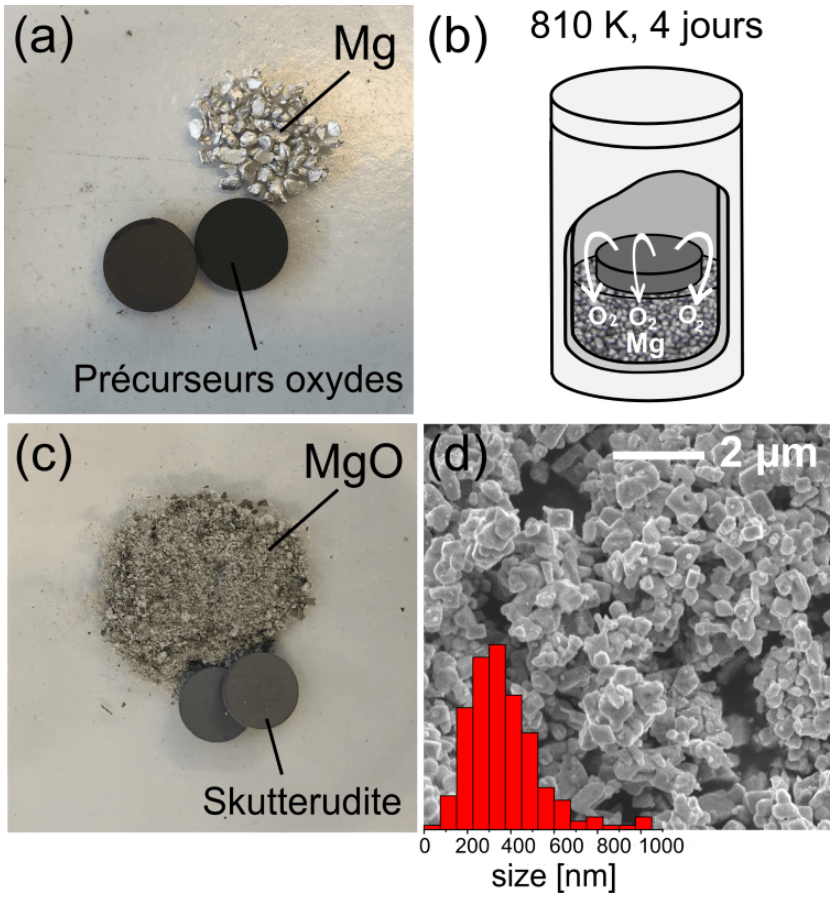

Figure 2: (a) Réactifs de la synthèse par magnésioréduction de skutterudites. (b) Schéma du creuset réactionnel en Mo dans lequel le traitement thermique est réalisé pendant 4 jours à 810 K. (c) Produits de la réaction. (d) Image en électrons secondaires réalisée par microscopie électronique à balayage (MEB) de la poudre de skutterudite et histogramme de la distribution de tailles de grains.

L'intérêt principal des skutterudites est la possibilité d'insérer des atomes lourds ("rattlers") dans les cages surdimensionnées de la structure cristalline et dont les modes de vibration vont permettre de diffuser très efficacement les phonons responsables de la conduction de chaleur.[31,32] La synthèse de $CoSb_3$ par magnésioréduction a pu être réalisée à partir de Co_3O_4 et Sb_2O_4. Cette réaction est réalisée à une température aussi basse que 810 K pendant 4 jours. J'ai montré que les morceaux de Mg sont progressivement oxydés en surface par la faible pression partielle d'O_2 dans le creuset réactionnel. Cette consommation d'O_2 engendre la réduction simultanée des oxydes. Les composi-

tions $Ni_{0.06}Co_{0.94}Sb_3$ et $In_xCo_4Sb_{12}$ (x = 0.13, 0.22) ont aussi pu être synthétisées en partant du précurseur Co_3O_4 correctement dopé au nickel ou à l'indium. À la fin de la réaction, des poudres de skutterudite très pures et avec des tailles moyennes de grains d'environ 300 - 500 nm sont obtenues. La synthèse de poudres fines de skutterudite est grandement améliorée en comparaison des méthodes classiques qui consistent, après la fusion des éléments, à recuire le lingot pendant un minimum de 4 jours avec des broyages intermédiaires puis à le broyer à haute énergie pendant quelques heures afin d'obtenir des poudres submicroniques.[26] D'un point de vue mécanisme réactionnel, j'ai montré que les oxydes précurseurs sont réduits par Mg en Sb_2O_3 et CoO qui forment par la suite des intermédiaires tels que $CoSb_2O_6$ et $CoSb_2O_4$. Ces intermédiaires sont ensuite progressivement réduits en $CoSb_3$.

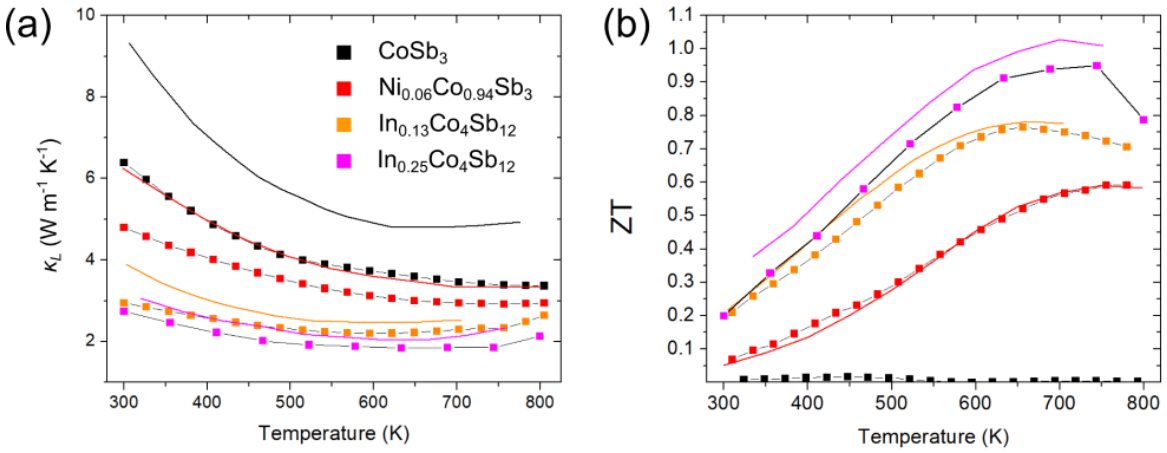

Figure 3: Dépendances thermiques (a) de la conductivité thermique de réseau κ_L et (b) du facteur de mérite ZT des échantillons de skutterudites synthétisés par magnésioréduction (carrés) et comparées à des valeurs de la littérature (lignes) pour des compositions similaires et synthétisées par des méthodes conventionnelles de fusion/recuit : $CoSb_3$ [27], $Ni_{0.06}Co_{0.94}Sb_3$ [33], $In_xCo_4Sb_{12}$ [27].

Les poudres ont ensuite été densifiées par la méthode "spark plasma sintering" (SPS) afin d'obtenir des échantillons massifs très denses (> 97 %) et présentant des tailles de grains d'environ 600 nm pour $CoSb_3$, $Ni_{0.06}Co_{0.94}Sb_3$ et $In_{0.13}Co_4Sb_{12}$ et 1.8 μm pour $In_{0.22}Co_4Sb_{12}$. De cette manière, la conductivité thermique de tous les échantillons présentant des tailles de grains submicroniques a pu être réduite jusqu'à 20 % à température ambiante (fig. 3a). Cette réduction est attribuée à une plus forte diffusion des phonons aux très nombreux joints de grains ainsi qu'aux défauts structuraux généralement associés. Cependant, les propriétés électroniques ont aussi été dégradées par la microstructure. Les facteurs de mérite ZT des skutterudites synthétisées par magnésioréduction sont donc similaires à ceux des échantillons de référence (fig. 3b).

D'un point de vue industriel, β-$FeSi_2$ et $MnSi_\gamma$ sont des matériaux thermoélectriques très intéressants car ils sont constitués d'éléments très abondants et donc peu chers mais aussi parce qu'ils ont de très bonnes propriétés mécaniques et de résistance à l'oxydation. Cependant ils présentent des ZT généralement inférieurs à 0,5, ce qui est bien inférieur à la plupart des skutterudites. La préparation des précurseurs a été réalisée par broyage planétaire d'un mélange de Si et Fe_2O_3 ou MnO afin d'avoir une poudre très fine et d'augmenter la vitesse de diffusion de Si lors de la synthèse. Les composés dopés β-$Co_{0.07}Fe_{0.93}Si_2$ et $V_{0.04}Mn_{0.96}Si_{1.74}$ ont aussi pu être synthétisés par cette méthode. Des poudres très pures avec des tailles de grains comprises entre 30 et 400 nm ont pu être obtenues par magnésioréduction à 1173 K en seulement 19 h. Contrairement aux skutterudites synthétisées à plus basses températures, les précurseurs sont ici réduits par la forte pression de vapeur de Mg. Cela a pour conséquence la présence de sous-produit MgO dans les poudres de siliciure qui doit être éliminé par un lavage à l'acide chlorhydrique dilué. Des pastilles frittées avec de bonnes densités (> 94 %) ont pu être réalisées à partir des poudres lavées. β-$FeSi_2$ n'a pas pu être fritté en dessous de sa température de décomposition et un recuit de 24 heures à 1100 K a dû être mis en œuvre pour reformer la forme cristalline basse température. Les tailles de grains après frittage sont en moyenne de 600 nm pour $MnSi_\gamma$ (fig. 4) et légèrement inférieures à 1 μm pour β-$FeSi_2$.

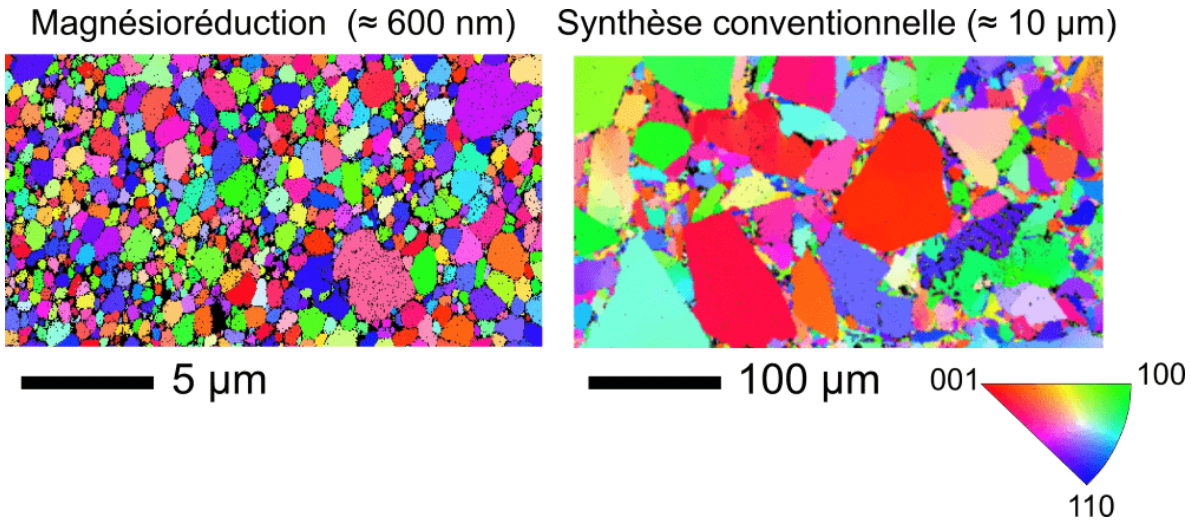

Figure 4: Cartographies en diffraction des électrons rétrodiffusés (EBSD) montrant la microstructure typique d'échantillons $MnSi_\gamma$ frittés par SPS à partir de poudres obtenues par magnésioréduction (gauche) et par fusion au four à arc (droite).

Les analyses de diffraction de rayons X (DRX) et de microscopie en transmission (MET) ont montré que ces composés présentent des structures et microstructures très complexes. Dans le cas de β-$FeSi_2$, une forte densité de fautes d'empilement a pu être

observée par MET et quantifiée par affinement Rietveld des diffractogrammes RX à l'aide du logiciel FAULTS. De plus, les pastilles présentaient des porosités ouvertes allant de quelques dizaines de nanomètres à 500 nm qui peuvent aussi participer à la réduction de κ_L. Dans le cas des siliciures de manganèse, la structure composite n'a pu être correctement décrite qu'en utilisant une approche de groupe de superespace 3D+1 lors de l'affinement Rietveld du diffractogramme. Des analyses MET détaillées ont montré que les composés présentaient une microstructure complexe avec une grande densité de défauts cristallins. Les faibles tailles de grains, les nombreux défauts structuraux ainsi que les porosités nanométriques résiduelles permettent de diminuer la conductivité thermique de réseau d'environ 15 % à température ambiante par rapport à des échantillons de référence mesurés dans les mêmes conditions (fig. 5a). Dans le cas des siliciures de manganèse et comme pour les skutterudites, la réduction de κ est exactement compensée par une diminution du facteur de puissance, $PF = \alpha/\rho$, ce qui conduit à des valeurs de ZT similaires aux échantillons de référence sur toute la plage de température étudiée (fig. 5b). En revanche, le facteur de mérite maximum de β-$Co_{0.07}Fe_{0.93}Si_2$ est amélioré à 0,18 à 800 K ce qui correspond à une augmentation d'environ 10 % par rapport à l'échantillon de référence (fig. 5b).

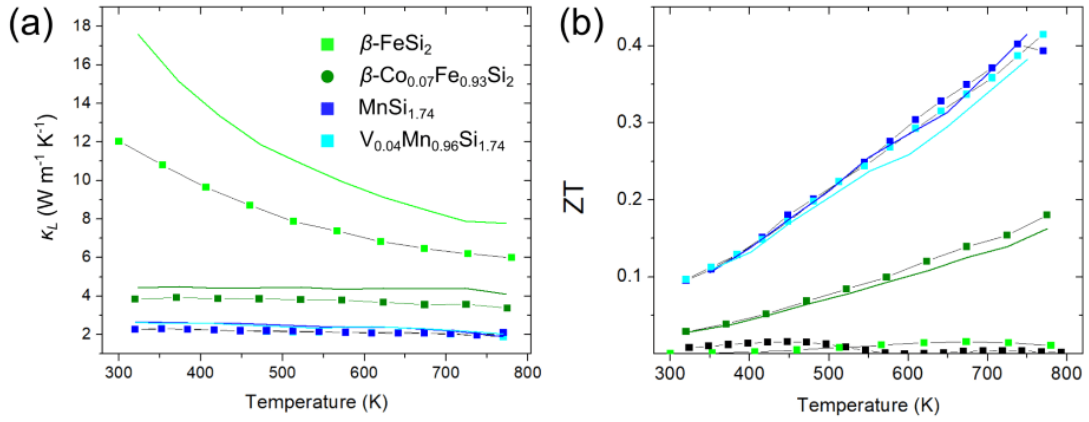

Figure 5: Dépendances thermiques (a) de la conductivité thermique κ_L de réseau et (b) du facteur de mérite ZT des échantillons de siliciures synthétisés par magnésioréduction (carrés) comparées aux échantillons de référence mesurés dans les mêmes conditions (lignes).

En résumé, lors de mes travaux de thèse, j'ai réalisé pour la première fois la synthèse de poudres de skutterudites et de siliciures de métaux de transition de grandes puretés et avec de très bons rendements par magnésioréduction. Cela n'a pu être réalisé que grâce à un travail important de synthèse et au développement d'un montage réactionnel facilitant la réalisation d'un nombre important de synthèses. Des poudres avec des tailles de grains submicroniques ont été directement obtenues par cette méthode

à des températures plus basses et avec des temps réactionnels plus courts que pour les méthodes conventionnelles de fusion/recuit/broyage. Des matériaux massifs mésostructurés ont ensuite été obtenus par frittage SPS. Les propriétés thermoélectriques de ces échantillons ont pu être mesurées grâce à des collaborations avec le Dr. Éric Alleno (ICMPE, Thiais, France) pour les skutterudites et le Dr. David Berthedaud (UMI LINK, Tsukuba, Japon) et le Pr. Takao Mori (NIMS, Tsukuba, Japon) pour les siliciures. La microstructure des échantillons obtenus par magnésioreduction a permis la réduction de κ_L de la majorité des échantillons. Cependant, la résistivité électrique est simultanément dégradée ce qui conduit à des facteurs de mérite similaires à ceux rapportés dans la littérature pour des matériaux synthétisés par des méthodes conventionnelles de fusion/solidification/recuit. Cette voie de synthèse pourrait cependant être appliquée avantageusement à une grande variété d'autres matériaux.

Références

[1] G. J. Snyder, E. S. Toberer, *Nat. Mater.* **2008**, *7*, 105–114.

[2] M. Karri, E. Thacher, B. Helenbrook, *Energy Convers. Manag.* **2011**, *52*, 1596–1611.

[3] S. LeBlanc, S. K. Yee, M. L. Scullin, C. Dames, K. E. Goodson, *Renew. Sust. Energ. Rev.* **2014**, *84*, 313–327.

[4] D. Champier, *Energy Conversion and Management* **2017**, *140*, 167–181.

[5] S. I. Kim, K. H. Lee, H. A. Mun, H. S. Kim, S. W. Hwang, J. W. Roh, D. J. Yang, W. H. Shin, X. S. Li, Y. H. Lee, G. J. Snyder, S. W. Kim, *Science* **2015**, *348*, 109.

[6] G. Tan, F. Shi, S. Hao, L.-D. Zhao, H. Chi, X. Zhang, C. Uher, C. Wolverton, V. P. Dravid, M. G. Kanatzidis, *Nat. Commun.* **2016**, *7*, 1.

[7] K. F. Hsu, S. Loo, F. Guo, W. Chen, J. S. Dyck, C. Uher, T. Hogan, E. K. Polychroniadis, M. G. Kanatzidis, *Science* **2014**, *303*, 818.

[8] S. R. Brown, S. M. Kauzlarich, F. Gascoin, G. J. Snyder, *Chem. Mater.* **2006**, *187*, 1873–1877.

[9] N. Shutoh, S. Sakurada, *J. Alloys Compd* **2005**, *389*, 204–208.

[10] A. Yamamoto, S. Ghodke, H. Miyazaki, M. Inukai, Y. Nishino, M. Matsunami, T. Takeuchi, *Jpn. J. Appl. Phys.* **2016**, *55*, 020301.

[11] G. Rogl, A. Grytsiv, P. Rogl, N. Peranio, E. Bauer, M. Zehetbauer, O. Eibl, *Acta Mater.* **2014**, *63*, 30–43.

[12] E. M. Levin, S. L. Bud'ko, K. Schmidt-Rohr, *Adv. Funct. Mater.* **2012**, *22*, 2766–2774.

[13] J.-A. Dolyniuk, B. Owens-Baird, J. Wang, J. V. Zaikina, K. Kovnir, *Mater. Sci. Eng., R* **2016**, *108*, 1–46.

[14] C. B. Vining, W. Laskow, J. O. Hanson, R. R. Van der Beck, P. D. Gorsuch, *J. Appl. Phys.* **1991**, *69*, 4333.

[15] H. Ning, G. D. Mastrorillo, S. Grasso, B. Du, T. Mori, C. Hu, Y. Xu, K. Simpson, G. Maizza, M. J. Reece, *Mater. Chem. A* **2015**, *3*, 17426.

[16] T. Mori, *Small* **2017**, *13*, 1702013.

[17] K. Koumoto, T. Mori, *Springer, Series in Materials Science* **2013**, *182*.

[18] W. Liu, J. Hu, S. Zhang, M. Deng, C.-G. Han, Y. Liu, *Mater. Today Phys.* **2017**, *1*, 50–60.

[19] L. Yang, Z.-G. Chen, M. S. Dargusch, J. Zou, *Adv. Energy Mater.* **2017**, *84*, 1701797.

[20] H. Mun, S.-M. Choi, K. Lee, S. Kim, *Chem. Sus. Chem* **2015**, *8*, 2312–2326.

[21] G. Rogl, A. Grytsiv, K. Yubuta, S. Puchegger, E. Bauer, C. Raju, R. Mallik, P. Rogl, *Acta Matter.* **2015**, *95*, 201–211.

[22] M. Zebarjadi, K. Esfarjani, M. S. Dresselhaus, Z. F. Ren, G. Chen, *Energy Environ. Sci.* **2012**, *5*, 5147.

[23] W. Kroll, *Z. Anorg. Allg. Chem.* **1940**, *234*, 42–50.

[24] F. H. Spedding, H. A. Wilhelm, W. H. Keller, *Patent US no. 2,830,894* **1947**.

[25] N. Krishnamurthy, C. K. Gupta, *Extractive Metallurgy Of Rare Earth* **2016**.

[26] E. Alleno, L. Chen, Chubilleau, B. Lenoir, O. Rouleau, M. Trichet, B. Villeroy, *J. Electron. Mater.* **2010**, *39*, 1966–1970.

[27] J. Leszczynski, V. D. Ros, B. Lenoir, A. Dauscher, C. Candolfi, P. Masschelein, J. Hejtmanek, K. Kutorasinski, J. Tobola, R. I. Smith, C. Stiewe, E. Müller, *J. Phys. D : Appl. Phys.* **2013**, *46*, 495106.

[28] S. Kim, M. Cho, Y. Mishima, D. Choi, *Intermetallics* **2003**, *11*, 399–405.

[29] M. Benyahia, V. Ohorodniichuk, E. Leroy, A. Dauscher, B. Lenoir, E. Alleno, *J. Alloys Compd.* **2018**, *735*, 1096–1104.

[30] S. Muthiah, R. C. Singh, B. D. Pathak, P. K. Avasthi, R. Kumar, A. Kumar, A. K. Srivastava, A. Dhar, *Nanoscale* **2018**, *10*, 1970–1977.

[31] B. C. Sales, D. Mandrus, R. K. Williams, *Science* **1996**, *272*, 1325–1328.

[32] G. S. Nolas, D. T. Morelli, T. M. Tritt, *Annu. Rev. Mater. Sci.* **1999**, *29*, 89–116.

[33] E. Alleno, E. Zehani, M. Gaborit, V. Orodniichuk, B. Lenoir, M. Benyahia, *J. Alloys Compd.* **2017**, *692*, 676–686.

Contents

Introduction

Modern societies are currently facing important environmental issues. In a context of an urgent necessity of greenhouse gases reduction, the ever increasing needs for transport and electricity production remain largely reliant on fossil fuel combustion. As an example, transports account for about 20 % of all carbon dioxide released into the atmosphere.[1] The depletion of the natural resources and the air pollution forces humanity to find alternative and sustainable technologies. Ubiquitous heat-losses represent a massive energy source that remains largely unexploited. For example, in modern car fuel engines almost 70 % of the energy provided by the gasoline combustion is directly lost as unused heat through the cooling system or exhaust gases.[2] Harvesting this wasted heat might represent a very interesting opportunity to improve the energy efficient of fuel engines and significantly reduce the global carbon footprint of transportation. A solution would be to directly convert the heat-losses into reusable electricity by thermoelectric generators (TEG). Compared to other waste heat recovery technologies such as Stirling or Rankine engines, TEGs have many desirable attributes such as small size, silent and long life time. In addition, they are highly reliable solid-state devices with the absence of fluids or moving parts. TEG can thus play a major role in the development of more efficient hybrid cars with limited greenhouse gases emission. For these reasons, many companies have demonstrated their interest in the thermoelectric technology in the past decade.[3–6]

However, TEGs have not found their way into mass production due to their limited energy efficiency reaching about 5 - 10 % in the best cases.[7] For example, the energy gains obtained by the integration of TEGs in cars currently do not justify the additional cost and weight load. For these reasons, TEGs are currently limited to niche applications such as space exploration, localized cooling of electronic systems or technological gadgets such as watches or electronic coolers. The best way to improve the TEGs performances is to develop more efficient thermoelectric (TE) materials. This must be realized in a sustainable manner considering the numerous environmental (element toxicity), economic (price and availability of the constituting chemical elements, process efficiency) and technological (soldering, mechanical and thermal stability) requirements.

This thesis has been devoted to the magnesiothermic synthesis of TE materials. This synthesis route which consists in the reduction of oxidized metal compounds (oxides, chlorides, fluorides) by magnesium is largely used in the industry for the extraction of metals (Ti, Zr, U, rare earths) form ores. In addition, the temperature and the

reaction time can be reduced thanks to the high reducing power of magnesium. The product can be obtained as submicronic powders which can be used for the sintering of nano- or mesostructured materials with lower thermal conductivities and therefore improved TE properties. Despite these advantages, magnesioreduction reactions remains largely unexplored for the syntheses of intermetallic thermoelectrics.

Magnesiothermic reactions have been applied to the synthesis of two classes of TE materials: skutterudites and transition metals silicides. Skutterudites are well known materials which can achieve high performances thanks to the insertion of 'rattlers' inside the structural voids resulting ni strongly reduced thermal conductivities. $MnSi_\gamma$ ($\gamma = 1.74$), also known as Higher Manganese Silicides (HMS), and β-$FeSi_2$ are promising candidates for large scale industrial applications because of their inexpensive constituting chemical elements as well as their high thermal and chemical stability. However, their performances remains relatively low due to high thermal conductivities.

In the first part, some generalities and the state of the art on thermoelectricity and magnesioreduction syntheses are exposed followed with the context and objectives of my thesis. Then, in the second part, the experimental techniques used during my work are shortly described. My results on skutterudites and transition metals silicides are given in the shape of 4 articles published or submitted to peer-review journals. These results will be discussed in the last part and general conclusions and perspectives will be drawn.

References

[1] International Energy Agency, *World Energy Outlook* **2012**.

[2] B. Orra, A. Akbarzadeha, M. Mochizukib, R. Singh, *Appl. Therm. Eng.* **2016**, *101*, 490–495.

[3] M. Mori, T. Yamagami, M. Sorazawa, T. Miyabe, S. Takahashi, T. Haraguchi, *SAE Int. J. Mater. Manuf.* **2011**, *4*, 1268–1276.

[4] N. Espinosa, M. Lazard, L. Aixala, H. Scherrer, *J. Electron. Mater* **2010**, *39*, 1446–1455.

[5] Q. Hussain, D. Brigham, C. Maranville, *SAE Int. J. Engines* **2009**, *2*, 1132–1142.

[6] J. LaGrandeur, D. Crane, S. Hung, B. Mazar, A. Eder, *International Conference on Thermoelectrics* **2006**, 343–348.

[7] M. Karri, E. Thacher, B. Helenbrook, *Energy Convers. Manag.* **2011**, *52*, 1596–1611.

Part I

State of the art, context and objectives

1 Generalities about thermoelectricity

This section is a short introduction to the field of thermoelectricity (TE). First of all, the three thermoelectric phenomena will be introduced. From the expression of their macroscopic manifestations, the maximum efficiency of thermoelectric devices is determined and, most importantly, the figure-of-merit ZT for materials is defined. The individual physical properties entering the expression of ZT are shortly discussed and criteria for TE materials selection are established. Finally, the last part reviews the state of the art of the materials for mid-temperature applications with special emphasis on skutterudites and transition metal silicides which are the materials of interest in my thesis work.

1.1 Thermoelectric phenomena

The thermoelectric effects are phenomena involving the reversible conversion of heat and electricity in materials. Three separate phenomena are identified: the Seebeck, the Peltier and the Thomson effects.

1.1.1 The Seebeck effect

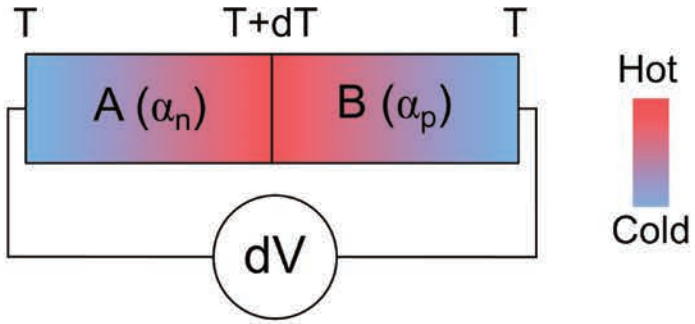

Figure 1: Schematic representation of the macroscopic manifestation of the Seebeck effect.

The Seebeck effect is named after Thomas Johann Seebeck who discovered in 1821 that a compass needle is deflected by applying a thermal gradient between the two junctions of a closed loop formed by two dissimilar metals *i.e.* by a thermocouple.[1] Later, Hans Christian Ørsted attributed this observation to the magnetic field induced by the formation of an electrical current through the junction and coined the term 'thermoelectricity'. The most basic thermocouple design is shown in fig. 1. It consists in two dissimilar metals rods A and B connected at a junction whose temperature is different than the two ends. For a small temperature difference dT [K], the open-circuit voltage dV [V] is produced according to:

$$dV = -\alpha_{AB}\, dT \tag{1}$$

where α_{AB} [V K^{-1}] is the Seebeck coefficient of the thermocouple defined from the Seebeck coefficients α_A and α_B of the respective constituting materials A and B according to:

$$\alpha_{AB} = \alpha_B - \alpha_A \tag{2}$$

In the case of semiconductors, the sign of α is directly related to the electrical conduction type. n-type (electrons) and p-type (holes) carriers result in negative and positive Seebeck coefficients, respectively. Thermocouples are thus commonly composed of n-type and p-type materials in order to maximize α_{AB} and consequently produce higher voltage.

The Seebeck coefficient of a given material varies with temperature. The Seebeck effect is the phenomena producing electricity from temperature gradient in thermoelectric generators.

1.1.2 The Peltier effect

Discovered in 1834 by Jean-Charles Peltier,[1] the Peltier effect corresponds to the absorption or emission of heat at the isothermal junction of an A/B thermocouple crossed by an electrical current (fig. 2). It is thus considered as the reciprocal of the Seebeck effect. The heat quantity Q [W] exchanged at the junction per unit of time is dictated by the relation:

$$Q = \pi_{AB} I \tag{3}$$

where π_{AB} [V] is the Peltier coefficient of the thermocouple which can be derived from the respective π_A and π_B of the constituting materials in a similar way as in (2) and I [A] the current intensity. The Seebeck and Peltier coefficients are linked by the first Kelvin relation:

$$\pi_{AB} = \alpha_{AB} T \tag{4}$$

The Peltier effect is the thermoelectric effect used to pump heat in thermoelectric cooling modules. The Peltier coefficient, as the Seebeck coefficient, is dependent on the temperature.

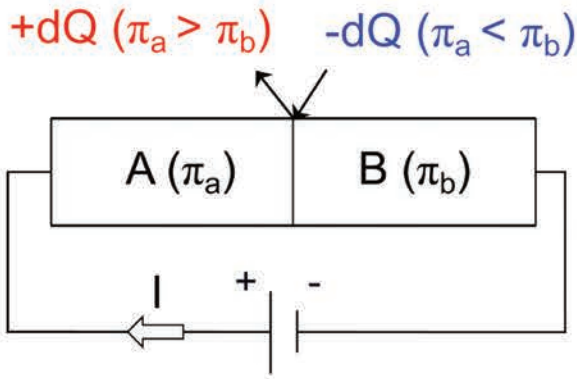

Figure 2: Schematic representation of the macroscopic manifestation of the Peltier effect.

1.1.3 The Thomson effect

The third and last thermoelectric phenomenon was evidenced by Lord Kelvin (W. Thomson) in 1851.[1] The Thomson effect corresponds to the emission or absorption of heat in current-carrying materials placed under a temperature gradient (fig. 3). It arises from the continuous change of the local Peltier coefficient from the cold to the hot side of a material due to the temperature dependence of π. The Thomson effect can thus be seen as a continuous version of the Peltier effect. For a longitudinal material placed in a small temperature gradient dT, the quantity of heat exchanged with the environment Q per unit of time is:

$$\frac{dQ(x)}{dx} = \tau\, I\, \frac{dT(x)}{dx} \tag{5}$$

where τ [V K^{-1}] is the Thomson coefficient of the materials and x is the spatial coordinate.

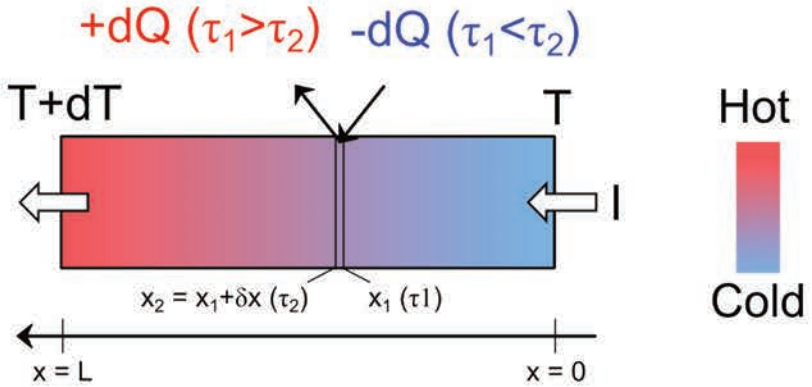

Figure 3: Schematic representation of the macroscopic manifestation of the Thomson effect.

The Thomson coefficient is linked to the Seebeck coefficient by the 2^{nd} Kelvin relation:

$$\alpha(T) = \int_0^T \frac{\tau(T)}{T}\, dT \tag{6}$$

As a consequence, the three thermoelectric phenomena are interdependent. This relation has also an experimental importance in the determination of the absolute Seebeck coefficient which can not be directly measured on the contrary to τ. It also means that the three thermoelectric phenomena can manifest simultaneously in materials.

1.2 Energy conversion by thermoelectric devices

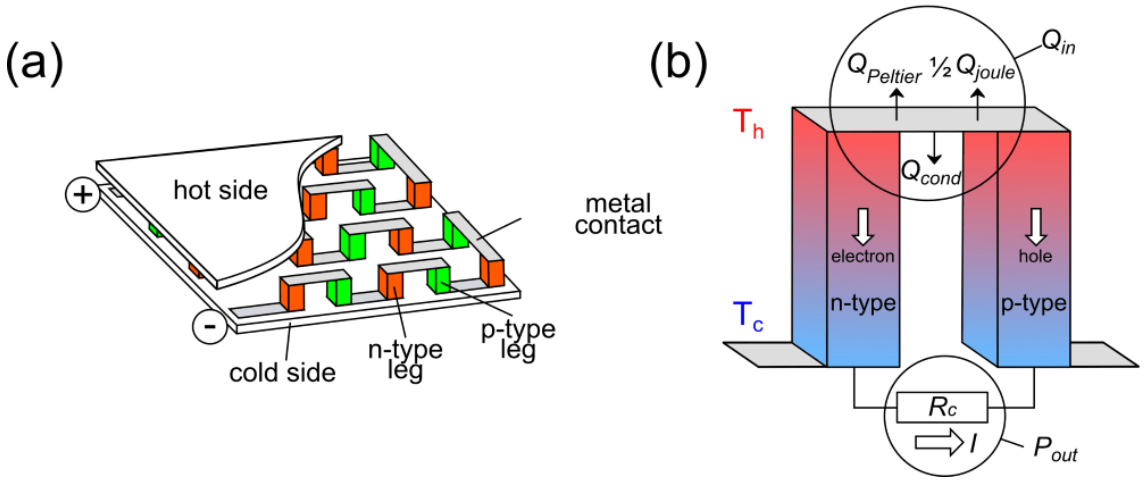

Figure 4: (a) Scheme of a thermoelectric module. (b) Scheme of a single thermocouple with the basic contributions to the heat exchange at the hot side.

Conventional thermoelectric devices are assemblies of thermocouples linked electrically in series and thermally in parallel, sandwiched between two ceramic plates (fig. 4a). Such arrangement enables one to achieve adequate heat pumping and optimal electrical power output, or inversely. Thermoelectric generators function as heat engines thus their efficiency relates to the quantity of useful output electrical power P_{out} produced for a given amount of heat Q_{in} being input. Let's consider a single thermocouple composed of one n- and one p-type leg with equal lengths and linked together by a metallic contact as shown in fig. 4b. For the sake of simplicity, the following hypotheses are assumed:

- Thermal and electrical resistances due to the metallic contacts are neglected;
- The Seebeck coefficient α, the electrical resistivity ρ [Ω m] and the thermal conductivity κ [W m^{-1} K^{-1}] are independent of the temperature (the Thomson effect is neglected);

- Only uniaxial thermal conduction from the heat source to the sink is considered, *e.g.* the loses by conduction *via* the ambient, the convection, and the radiation are neglected;
- The system has reached equilibrium.

The heat flow going from the heat source to the sink is considered as positive. The different contributions to the heat exchanged at the hot side are:

- The conduction heat flow Q_{cond} is given by the unidimensional Fourier's law:

$$Q_{cond} = -K\,\Delta T \tag{7}$$

  where ΔT is the temperature difference between the hot and the cold ends and K is the total thermal conductance of the thermocouple given by:

$$K = \frac{\kappa_A\,X_A}{L} + \frac{\kappa_B\,X_B}{L} \tag{8}$$

  where X is the cross-sectional surface area and L is the length of the legs.

- The Peltier heat $Q_{Peltier}$ released or absorbed per unit of time by the legs at the hot contact is given by equation (9) which can be obtained by combining relations (2), (3) and (4):

$$Q_{peltier} = (\alpha_B - \alpha_A)\,T_h\,I \tag{9}$$

  where I is the intensity of the electrical current flowing through the thermocouple an T_h the temperature of the hot side. The Peltier heat produced by the metallic contact at the isothermal junction perfectly compensates when considering the two legs simultaneously.

- The heat generated by the Joule effect Q_{Joule} is given by:

$$Q_{Joule} = R\,I^2 \tag{10}$$

  where R [Ω] is the total electrical resistance of the thermocouple calculated using:

$$R = \frac{\rho_A\,L}{X_A} + \frac{\rho_B\,L}{X_B} \tag{11}$$

As Q_{Joule} is considered as isotrope, one half of the heat flow is released at the hot end and the other half at the cold end.

The total heat pump Q_{in} at the hot side is obtained by summing the relations (7), (9) and (10):

$$Q_{in} \;=\; (\alpha_B - \alpha_A)\, T_h\, I \;+\; K\, \Delta T \;-\; \frac{1}{2}\, R\, I^2 \tag{12}$$

The intensity I of the electrical current generated by the thermocouple is given by:

$$I \;=\; \frac{(\alpha_B - \alpha_A)\, \Delta T}{(R + R_c)} \tag{13}$$

where R_c [Ω] is the load resistance. The electric power output P_{out} delivered by the thermocouple to the load resistance R_c is thus:

$$P_{out} \;=\; R_c\, I^2 \;=\; \frac{(\alpha_n - \alpha_p)^2\, \Delta T^2\, R_c}{(R + R_c)^2} \tag{14}$$

According to the maximum power transfer theorem (Jacobi's law),[2] maximum P_{out} is achieved if the condition:

$$R_c = R \tag{15}$$

is fulfilled. The efficiency of the thermocouple can be further maximized by optimizing the geometry of the legs according to:

$$\frac{L\, X_B}{L\, X_A} \;=\; \left(\frac{\rho_B\, \kappa_A}{\rho_A\, \kappa_B}\right)^{\frac{1}{2}} \tag{16}$$

If the conditions (15) and (16) are fulfilled, the maximum efficiency η_{max} of the TE generator is given by:

$$\eta_{max} \;=\; \frac{P_{out}}{Q_{in}} \;=\; \left(\frac{\Delta T}{T_h}\right) \frac{(1 + Z_{AB}\, \bar{T})^{\frac{1}{2}} - 1}{(1 + Z_{AB}\, \bar{T})^{\frac{1}{2}} + \dfrac{T_c}{T_h}} \tag{17}$$

with $\bar{T}$ the average temperature between T_c and T_h and Z_{AB} the figure-of-merit of the thermocouple defined by:

$$Z_{AB} \;=\; \frac{(\alpha_A - \alpha_B)^2}{[(\rho_A\,\kappa_A)^{\frac{1}{2}} + (\rho_B\,\kappa_B)^{\frac{1}{2}}]^2} \tag{18}$$

The expression of η_{max} (17) is the product of two terms. The first term $\frac{\Delta T}{T_h}$ corresponds to the Carnot efficiency. The second term corresponds to a coefficient depending on T_h and T_c but also on Z_{ab} which uniquely depends on the materials intrinsic properties ρ, α and κ.

Q_{in}, V and R are proportional to the number of thermocouples connected together into the device whereas ΔT, I and η do not change with the size of the device. In practice, the X/L ratios of the legs are chosen to place the optimal currents in a desirable range, and the number of thermocouples is matched to the projected thermal load. In selecting thermocouple materials, one aims to maximize Z_{ab}. In general, the legs are selected by choosing the best p-type and n-type materials according to their individual adimensional figure-of-merit ZT defined by:

$$ZT \;=\; \frac{\alpha^2}{\rho\,\kappa}\,T \tag{19}$$

Extremely high ZT would be theoretically achievable by selecting the best individual properties in distinct materials. In the practice, however, average ZT of the best materials are often limited to about 1 - 2 due to high interrelation between the individual components of ZT (fig. 5a). According to figure 5b, the maximum efficiency that could be reached with the current best materials is around 20 % considering ΔT lower than 400 K. In reality, the efficiency of thermoelectric generator are rarely above 10 % due to non-negligible electrical and thermal resistances of the metallic contacts.

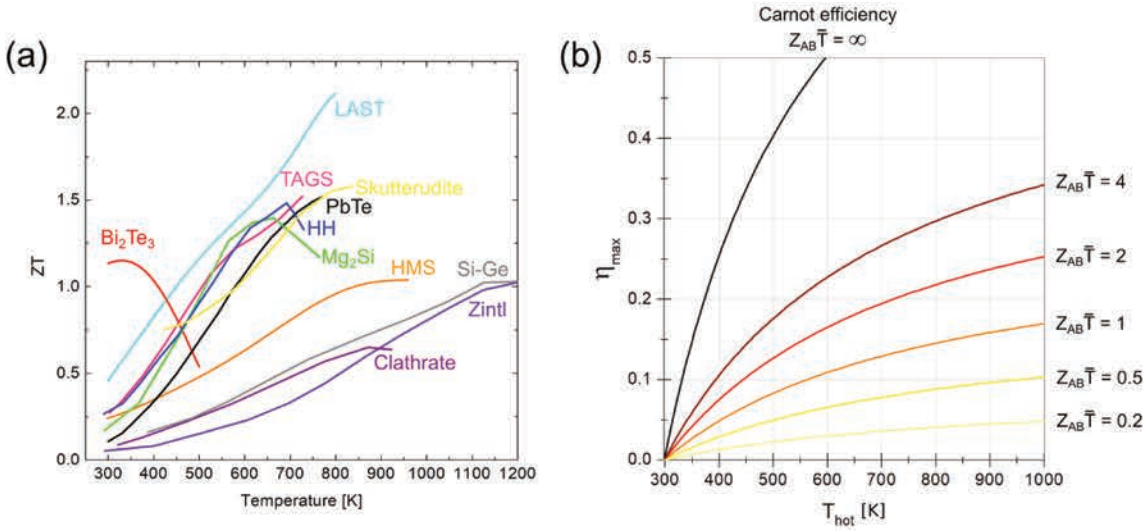

Figure 5: (a) Temperature dependence of ZT for some selected thermoelectric materials taken from ref.[3–13]. (b) ΔT dependence of η_{max} for different $Z_{AB}\bar{T}$ according to equation (17) and with $T_c = 298$ K

Although progresses are needed to achieve better device design and metallic contacts, the best way to improve the efficiency of TEGs remains to develop materials with better performances *i.e.* with higher ZT.

1.3 Criterion for TE materials selection

In the previous section, we have seen that the properties of the materials constituting the thermocouple play a fundamental role in the final energy conversion efficiency. In selecting the materials, the best possible combination of α, ρ and κ must be achieved in order to reach the highest possible figure-of-merit ZT in the temperature range of interest. In this section, the different components of ZT will be described from a solid state physics point of view in the aim to provide a guideline for the selection of TE materials.

1.3.1 Electrical resistivity ρ

The electrical resistivity describes the ability of a material to conduct electrical current. Electronic properties are greatly related by the position of the Fermi energy level in the band structure diagram. In the electron gas model, the electrical resistivity is inversely proportional to the density n [cm^{-3}] and mobility μ [$cm^2\ V^{-1}\ s^{-1}$] of the charge carriers *via* the relation:

$$\rho = \frac{1}{n\, e\, \mu} \tag{20}$$

with e the fundamental charge of the electron. In metals, the conduction band is partially occupied leading to high charge carriers concentrations ($> 10^{21}$ cm^{-3}) and

consequently low resistivities ($<$ $\mu\Omega$ m). Raising the metals temperature usually results in increased resistivities. This is attributed to enhanced carrier scattering at the more pronounced lattice vibrations thus affecting the carriers mobility. Intrinsic semiconductors have lower n than metals ($\approx 10^9$ - 10^{13} cm^{-3}) because the Fermi level is inside a forbidden gap with width between 0 and 4 eV resulting in higher resistivity ($\approx \Omega$ m). Charge carriers can be located at the top of the valence band (holes) and at the bottom to the conduction band (electrons). Unlike metals, raising the temperature will increase the probability for electrons to cross the gap thus increasing n and decreasing ρ. The electronic properties of semiconductors strongly depends on the presence of impurities (dopants). Degenerated (*e.g.* highly-doped) semiconductors are characterized by electronic properties between intrinsic semiconductors and metals. Finally, insulators have band gap larger than 4 eV and are not considered for TE applications because of their exceedingly high resistivity ($>$ 1 MΩ m).

1.3.2 Seebeck coefficient α

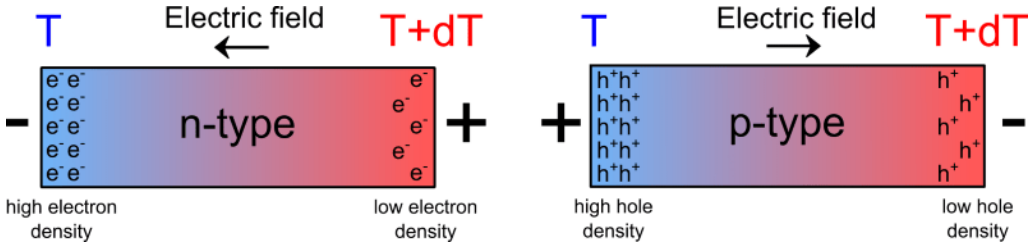

Figure 6: Schematic representation of the microscopic manifestation of the Seebeck effect.

The Seebeck effect is attributed to the uneven diffusion of charge carriers inside a material placed in a thermal gradient. In the case of a n-type material composed of a free electron gas, the electrons have in average a higher kinetic energy at the hot end than at the cold end. As a consequence, they will tend to migrate from the hot to the cold end thus creating an electric potential *i.e.* a Seebeck voltage. The absolute value of α describes the ability of a material to create a voltage in a temperature gradient of 1 K. As for the resistivity, the Seebeck coefficient is mainly dictated by the band structure of the materials at the Fermi level. As shown by the relation (21) which applies for metals or degenerate semiconductors in the parabolic band and energy-independent scattering approximations, α is inversely proportional to n:

$$\alpha \propto \frac{m^*}{n^{2/3}} T \tag{21}$$

where m^* [kg] is the charge carriers effective mass which is strongly related to the density of states at the Fermi level. Typical Seebeck coefficients are going from few μV K^{-1} for metals to several mV K^{-1} for intrinsic semiconductors such as Si and intermediate values of few hundreds of μV K^{-1} in highly degenerated semiconductors. The Seebeck coefficient is expected to increase with the temperature as long as one type of charge carriers is in large majority. The bipolar temperature corresponds to the thermal energy required to induce simultaneous n-type and p-type conductions in semiconductors. In this condition, carriers of opposite charge are diffusing to the cold end thus canceling out the Seebeck voltage. The energy of the band gap, which predominantly determines the bipolar transition temperature, needs to match with the application temperature targeted. For example, Bi_2Te_3-based materials operating around room-temperature have band gaps of ≈ 0.2 eV[14] while high-temperature materials (> 1000 K) such as $Si_{1-x}Ge_x$ alloys have larger band-gaps of ≈ 0.9 eV.[15]

1.3.3 Thermal conductivity κ

The thermal conductivity κ [W m^{-1} K^{-1}] describes the ability of a material to conduct heat. Heat can be transported by different mechanisms in materials. In metals, heat is predominantly carried by charge carriers. The Wiedemann-Franz law (22) links the electronic thermal conductivity κ_e to the electrical resistivity ρ:

$$\kappa_e = \frac{L}{\rho} T \tag{22}$$

where the Lorenz number L is equal to $2.45.10^{-8}$ W Ω K^{-2} for free electrons gas.

In insulators, heat is predominantly carried by phonons which are collective atomic vibration of the lattice. The lattice thermal conductivity κ_L is given in first approximation (phonons gas) by the Debye relation:

$$\kappa_L = \frac{1}{3} \sum_{\lambda_{ph}} C_p \, l \, v \tag{23}$$

where C_p [J K^{-1}] is the specific heat, l [m] is the phonons mean free path which describes the average traveling distance between two consecutive phonon scattering events and v [m s^{-1}] is the average group velocity for phonons with different wavelength λ_{ph}. The different values l of all the phonons participating to the heat conduction form a distribution with values going from few Å to several μm depending on the materials (fig. 7).

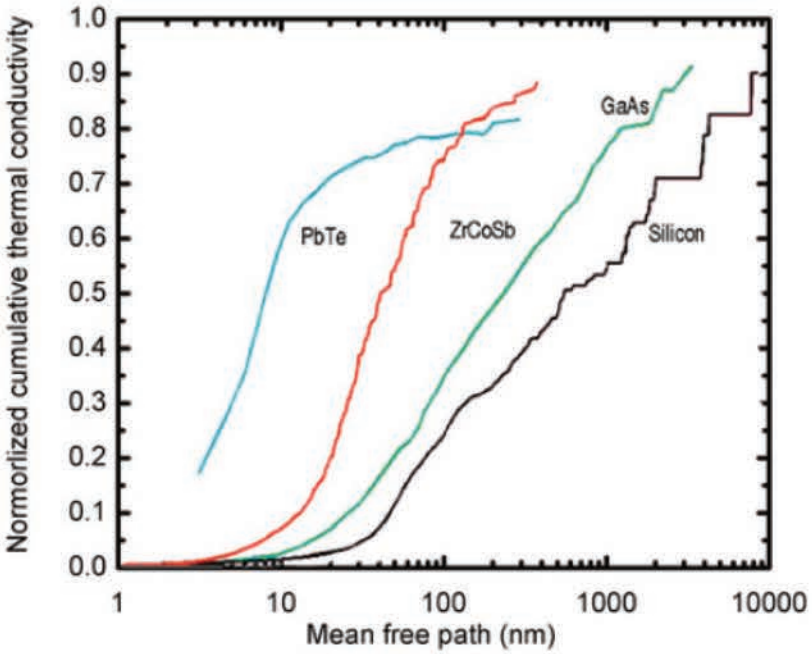

Figure 7: Normalized cumulative thermal conductivity versus phonons mean free path for various thermoelectric materials taken from ref.[16]

In semiconductors, heat can be carried by both mechanisms so the total thermal conductivity is considered as the sum of the two components:

$$\kappa = \kappa_L + \kappa_e \tag{24}$$

Interestingly, κ_L is the only component of ZT that does not rely on n. On the other hand, κ_L strongly depends on other parameters which are listed in the following along with some examples taken in the Si-Ge system:

- The complexity or crystallinity of the crystal structure: the thermal conductivity for amorphous silica is ≈ 1 W m^{-1} K^{-1} while for highly symmetric undoped Si single crystals it is as high 100 W m^{-1} K^{-1} at room temperature.[17]

- The microstructure or presence of defects: the thermal conductivity of bulk nanocrystalline Si materials with average crystallites size of 20 nm shows reduced thermal conductivity of 55 W m^{-1} K^{-1} which corresponds to a 45 % reduction compared to Si single crystal.[18]

- The weight of the constituting elements: compounds composed of heavy atoms usually feature lower thermal conductivity as can be seen for Ge (Z = 32) single crystal which has a thermal conductivity of 55 W m^{-1} K^{-1} which is almost twice smaller than for diamond Si (Z = 14) single crystal.[17]

- Mass fluctuation phenomena induced by isotropic or atomic disorder: $Si_{0.8}Ge_{0.2}$ alloys has a much lower thermal conductivity of 15 W m^{-1} K^{-1} than both pristine Si and Ge.[19]

With rising temperature and as long as only one major type of charge carriers is present, κ_L usually decreases due to phonon-phonon interactions leading to the diminution of l. However at high temperature, the bipolar thermodiffusion effect κ_{bi} which results from the presence of both electrons and holes in the material, becomes a substantial contributor to κ which increases exponentially.

1.3.4 Figure-of-merit *ZT*

As seen in §1.2, the performances of thermoelectric materials is determined by the figure-of-merit ZT which is defined in eq. (19) and which can be developed as :

$$ZT = \frac{\alpha^2}{\rho\,(\kappa_e + \kappa_L)}\,T \tag{25}$$

The typical trends of the thermoelectrics properties *versus* the charge carrier concentration n is shown in fig. 8 for the three types of material: insulators, semiconductors and metals.

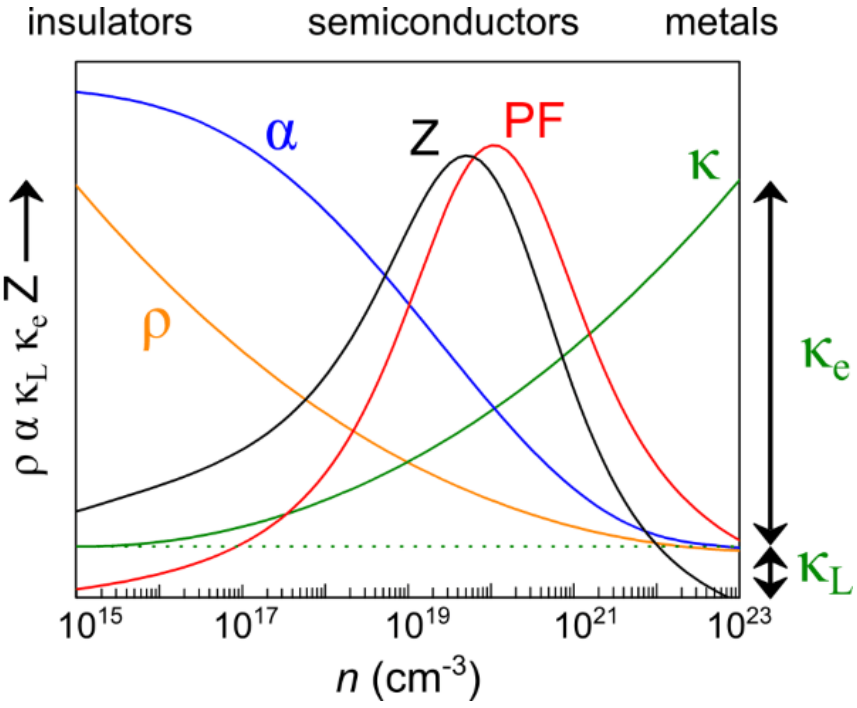

Figure 8: Schematic representation of the charge carrier concentration dependence of the Seebeck coefficient α, electrical resistivity ρ, thermal conductivity κ with the electronic κ_e and lattice contribution κ_L, power factor PF and figure-of-merit Z.

According to this figure, neither the metals nor the insulators can achieve large Z. Metals have excellent electrical resistivities but very small Seebeck coefficients and large thermal conductivities largely dominated by the charge carriers contribution. Insulators have high Seebeck coefficients which are counterbalanced by the exceedingly large electrical resistivities. The thermal conductivity of insulators is predominantly dominated by the lattice contribution which greatly varies according to structure and elementary composition of the compound as already discussed in §1.3.3. In the case of semiconductors, the intermediate n enables higher power factors PF defined as:

$$PF = \frac{\alpha^2}{\rho} \tag{26}$$

In addition, the charge carriers concentration of semiconductors can be controlled by doping enabling relatively easy optimization of PF. The highest PF are usually obtained for highly-doped semiconductors with charge carrier concentrations between 10^{19} and 10^{21} cm^{-3}. In this range, both charge carriers and phonons contribute to the heat transport. While κ_e is generally fixed by n achieving the highest PF, κ_L represents the only component of ZT that is not related to n and which can be optimized independently.

The conventional strategies imagined to improved ZT are thus based on two concepts: (i) increasing the power factor and (ii) decreasing the lattice thermal conductivity.[20–23] The fig. 9 shows the PF and κ of some of the current best materials.

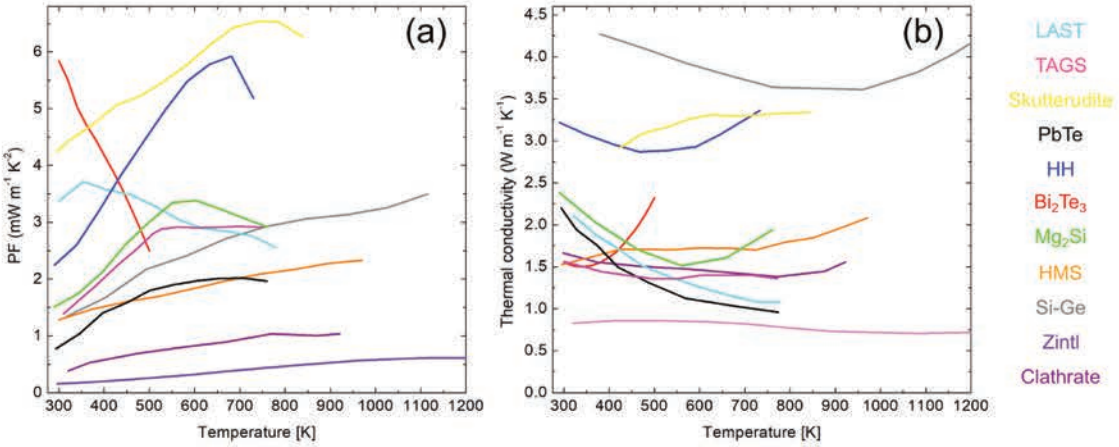

Figure 9: Temperature dependence of (a) PF and (b) κ of some selected thermoelectric materials taken from ref.[3–13].

1.3.5 Strategies to improve *ZT*

Maximizing *PF* is a very important requirement for achieving high *ZT*. This is however difficult because α and ρ are intrinsically in conflicts. Conventional approaches consist in the optimization of charge carriers concentration by doping (strategy 1), band structure engineering by doping (strategy 2) or nanostructuration (strategy 3). The lattice thermal conductivity is the only component of *ZT* not relying on n. Low lattice thermal conductivity is essential to achieve high *ZT*. This can be made possible by synthesizing complex materials composed of heavy constituting elements (strategy 4), introducing large mass fluctuation on the lattice (strategy 5) and by selectively scattering phonons at interphases or defects (strategy 6).

Strategy 1: Optimization of n by doping

As shown in section §1.3.4, *PF* is highly dependent on the charge carriers concentration. The intentional insertion of impurities in small amount is an efficient strategy to introduce localized energy states within the band gap and thus manipulate the electronic properties of semiconductors. Dopants can create donor levels near the conduction band or acceptors levels nears the valence band. In both cases, the energy difference between the bands and the localized states is small enough (about several meV) to thermally ionize the majority of the impurities thus injecting additional charge carriers in the respective bands. Donor levels inject electrons which favor n-type conduction while acceptor levels inject holes which favor p-type conduction. In most cases, it is possible to manipulate n by controlling the amount of impurities in the materials. The adequacy and the solubility of the dopant strongly depend on the materials.

Strategy 2: Increase of α by resonant doping

The insertion of some specific dopants introduce energy levels that are resonant with the host band structure.[24] This leads to a modification of the density of states near the Fermi level thus increasing the charges carriers effective mass m^* without significantly modifying n. According to eq. (21), it results in improved α without significantly degrading ρ. This could for example, be achieved in Tl-doped PbTe with a largely increased α reaching 350 μV K^{-1} and high *ZT* of 1.5 at 800 K.[4]

Strategy 3: Increase of α in nanomaterials

This strategy was proposed by Hick and Dresselhaus in the early 90's and is based on theoretical calculations predicting that α could be strongly improved in nanomaterials.[25,26] They correspond to materials with at least one dimension below 100 nm which can be thin films (2D), wires or tubes (1D) and nanoparticles (0D). Lowering the dimensionality of materials strongly modifies the band structure and the density of states near the Fermi level. Similarly to strategy 2, higher m^* and thus α could possibly be achieved.

Strategy 4: Heavy constituting elements and complex crystal structure

Initially proposed by A.F. Ioffe in the later 50's,[27] the presence of heavy atoms in materials may introduce weak chemical bondings and low-frequency vibrations which are beneficial to achieve low thermal conductivity. It is verified experimentally that crystals with complex structure have usually low lattice thermal conductivity. This inspired the 'Phonons Glass and Electron Crystal' (PGEC) concept first introduced by G.A. Slack in 1997.[28] The idea is to fabricate materials characterized by large and complex unit cells where the phonons propagation is strongly disturbed similarly to glasses, while keeping the good electronic properties of crystals. This can be realized, for example, in cage compounds such as skutterudites (§1.4.3),[29] clathrates (§1.4.5)[30] or Chevrel phases[31] where the large structural voids can be partially filled with loosely bound atoms often referred as 'rattlers'. While the atomic framework insures the good electronic properties of the materials, the additional low energy phonons and structural disorder introduced by the filling atoms enable significant thermal conductivity reduction.

Strategy 5: Large mass fluctuation induced by point defects

Point defects could be attributed to mixed atomic site (*e.g.* alloys, doped compounds), presence of vacancies or atoms clustering. The mass fluctuation introduced on the crystal lattice can disturb the collective vibration behavior and hence impede the heat transfer. Point defects can scatter efficiently the high energy spectrum of phonons. Doping, which is necessary for the optimization of n (strategy 1), is also an efficient way to introduce mass fluctuation at the atomic scale and consequently often results in strongly enhanced ZT.

Strategy 6: High density of interfaces in nano-/mesostructured materials

Grain boundaries in polycrystalline materials can disturb the propagation of phonons because the interfaces break the translation symmetry of the regular crystal lattice. Reducing the crystallites size and thus increasing the density of interfaces in polycrystalline materials often results in large reduction of the thermal conductivity.

This can be quantified for polycrystalline materials composed of spherical crystallites with diameter d in the effective medium approximation by the modified Nan and Birringer relation:[32,33]

$$\frac{1}{\kappa_L} = \frac{1}{\kappa_0} + \frac{R_k}{d} \tag{27}$$

where κ_0 and κ_L are the lattice thermal conductivity of the bulk and nanostructured material, respectively, and R_K is the interfacial thermal resistance (Kapitza resistance). However, reducing too much the crystallites size can also be detrimental to the electrical conductivity thus lowering the TE performances. Therefore, the key is to focus on the different characteristic mean free paths of electrical charge carriers and phonons. In pristine Si, for example, first principle calculation has shown that about half of the phonons responsible for the heat transport have mean free paths larger than 1 μm while electrons have mean free path in the order of about 20 nm.[16,34] Fabrication of nanostructured (crystallites size $<$ 100 nm) or mesostructured (crystallites size $<$ 1 μm) materials made of crystallites with comparable or slightly smaller sizes than the characteristic phonons mean free path can lead to strong selective scattering of phonons while being less detrimental to electrical conductivity. Microstructure can thus efficiently scatter the low energy phonons part of the spectrum. Another important fact is that there is no magic number for the characteristic phonons mean free path, and the distribution can vary much depending on the materials.[16]

Other strategies where shown to efficiently increase PF of materials such as the insertion of magnetic dopant[21] or the filtering of low energy electrons by crystallites interphases.[22,35] Several of the strategies descried here can be used simultaneously in materials to achieve higher ZT. For example, creation of point defects (strategy 4) and nano-/mesostructuration (strategy 6) can be used simultaneously to achieve efficient scattering of both the high and low part of the phonon energy spectrum and thus strongly reduce κ_L. Introducing phonon scattering centers at different length scales in materials is often referred as 'all-scale hierarchical thermoelectrics'.[23,36]

1.4 Thermoelectric materials for mid-temperature applications

In this paragraph, only the important families of materials exhibiting their ZT peak in the mid-temperature range (500 - 800 K) will be described.

1.4.1 Tellurides

Tellurium-based compounds such as PbTe, $AgSbTe_2$, GeTe and their related alloys have been studied since the 50's and they remain among the highest ZT materials ever reported. At high temperature, these alloys crystallize in the rock-salt structure-type (space group $Fm\bar{3}m$). Maximum ZT as high as 1.5, 2.2 and 2.5 around 800 K were reported for $(GeTe)_{0.85}(AgSbTe_2)_{0.15}$ (TAGS)[10,37], $(PbTe)_{0.94}$-$(AgSbTe_2)_{0.06}$ (LAST)[5] and PbTe[38,39], respectively. Such high performances are mainly attributed to the extremely low lattice thermal conductivity (0.5 W m^{-1} K^{-1}) approaching the glass limit. In addition of being exclusively composed of heavy constituting elements, the low thermal conductivity is attributed to the high microstructural complexity of the alloys both at the micro- and nanometric scale.[40,41] Indeed, LAST and TAGS are not true alloys and nanometric phase segregations form upon thermal treatment acting as efficient phonons scattering centers. The reproducibility of such performances is however difficult for this reason. In addition, they are constituted of rare/expensive (Ag,Ge) and toxic (Pb, Te) elements which is a strong drawback for large scale production.

1.4.2 Half-Heusler alloys

Half-Heusler (HH) compounds have general composition XYZ where X and Y are transition metals or rare earth elements and Z is generally a metalloid.[42] They crystallize in a cubic structure (s.g. $F\bar{4}3m$) where X in $4a$ (0, 0, 0) and Y in $4b$ (1/2, 1/2, 1/2) Wyckoff positions are forming a rock-salt type stacking while Z in $4c$ (1/4, 1/4, 1/4) site occupies alternatively one half of the cubic interstitial sites. The compositional space of Half-Heusler alloys covers almost 80 % of the periodic table creating enormous possibilities of alloying. Both n- and p-type semiconducting HH alloys can be synthesized with relatively good thermoelectric properties. Although very high PF reaching 7 mW m^{-1} K^{-2} can be achieved[43], ZT is often limited below unity because of high thermal conductivity caused by the simple crystal structure. However, materials with ZT of about 1.5 at 600 K were obtained for highly substituted TiNiSn with heavy elements such as Hf, Zr and Sb.[7,44]

1.4.3 Skutterudites

Skutterudites are intermetallic compounds with the general formula MX_3 where M is a transition metal and X is a pnictogen. Thermoelectric skutterudites are predominantly based on $CoSb_3$ which is a diamagnetic semiconductor with a band gap of $\approx$ 0.2 eV.[29] As shown in fig. 10, the crystal structure of $CoSb_3$ (s.g. $Im\bar{3}m$) is composed of slightly deformed antimony octahedra ($24g$ site) connected by the vertices and centered by a Co-atom ($8g$ site). The $[CoSb_6]$ tilted octahedra network generates (i) almost square $[Sb_4]$ rings with strong bonds and (ii) large icosahedral

voids centered on the $2a$ position. The Co-Sb bonding has a covalent character due to the small electronegativity differences (1.88 for Co and 2.05 for Sb).[45] The voids can be partially occupied by electronegative elements called 'fillers' or 'rattlers' whose radius is much smaller than the cage dimensions. The chemical formulas of filled skutterudites are more commonly expressed on the form $F_xM_4X_{12}$ where F is the filling atom. In this way, the filling fraction is directly explicitised. Figure 11 gives the different elements usually constituting skutterudites.

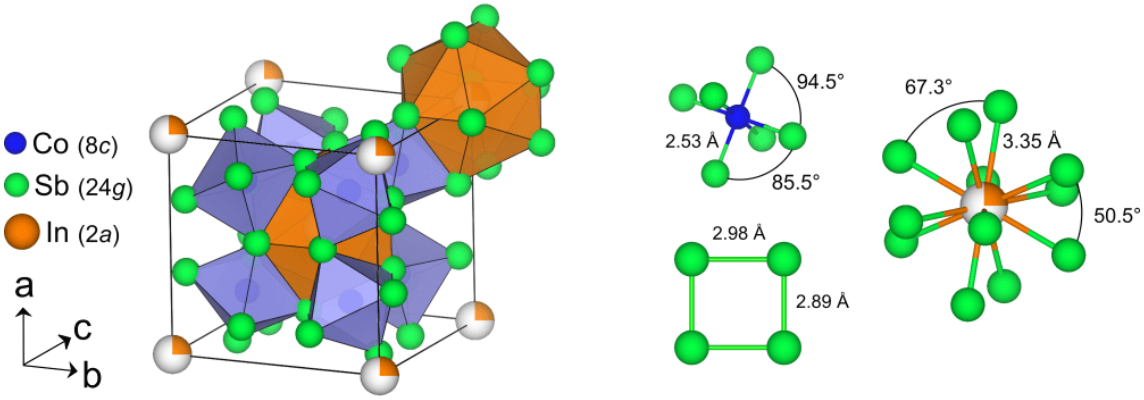

Figure 10: (left) Crystal structure of $In_{0.25}Co_4Sb_{12}$ (s.g. $Im\bar{3}$, $a = 9.050$ Å) with $[CoSb_6]$ octahedra network (blue) and filled $[In_{0.25}Sb_{12}]$ icosahedral cages (orange). (right) Detailed view of the atomic environment in the $[CoSb_6]$ octahedra, $[In_{0.25}Sb_{12}]$ icosahedra and $[Sb_4]$ squares.

Unfilled $CoSb_3$ has interesting electronic properties including high holes mobility and large Seebeck coefficient thanks to favorable electronic band structure.[46] Moreover, the large possibility of chemical substitution on the M or X sites offers many possibilities for charge carriers optimization and band structure engineering. Absolute Seebeck coefficient as high as 220 μV K^{-1} and resistivity as low as 10 $\mu\Omega$ m can be obtained simultaneously for fully optimized compositions.[47] Therefore skutterudites are among the materials showing the highest PF with values of about 4 - 5 mW m^{-1} K^{-1}. In addition, both n- and p-type conductions can be achieved making thus possible the manufacturing of TEG fully based on skutterudites.[47,48] Skutterudites are widely considered as one of the best candidates for large scale TEG production because of good mechanical properties, chemical stability and the relatively large abundance of the constituting elements.

The thermal conductivity, and especially the lattice contribution, remains however large ($\approx$ 10 W m^{-1} K^{-1} at 298 K) in pristine $CoSb_3$ mostly due of the strong Co-Sb covalent bonding. As pointed out by G.A. Slack with the PGEC concept, the insertion of filler elements in the structure is a very efficient strategy to lower the thermal conductivity of $CoSb_3$. The vibrational dynamics of the filler atoms weakly bonded

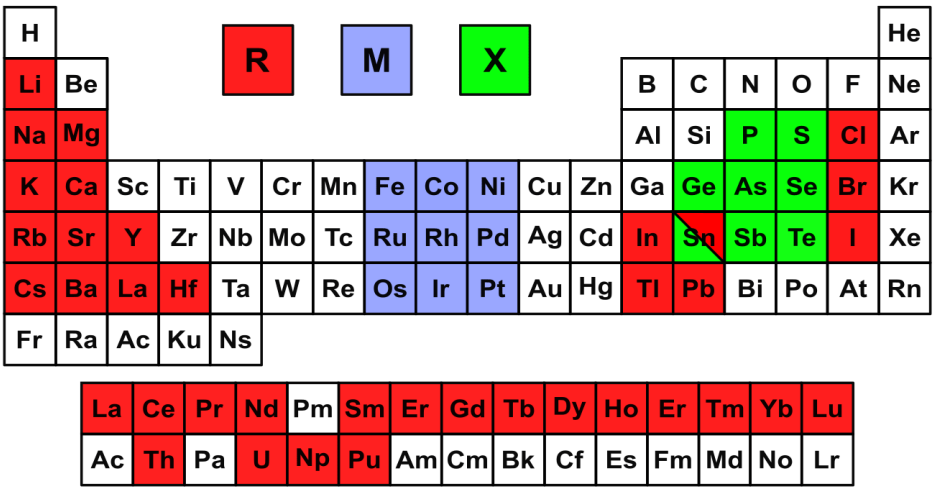

Figure 11: Elements forming a skutterudite structure $F_xM_4X_{12}$ with M in blue, X in red and F in orange.[29]

to the oversized cages efficiently scatter the heat carrying acoustic phonons without significantly damaging the electronic transport properties mostly attributed to the Co_4Sb_{12} framework. Electropositive filler atoms often act as donors (partially oxidized state) and participate to the optimization of the charge carriers concentration. Most of the research realized on thermoelectric skutterudites are aiming at further reducing the thermal conductivity of filled skutterudites by combining the strategies exposed in §1.3.5. Very low κ_L and high ZT were obtained by approaches such as multi-filling, complex chemical substitution, nano-/mesostructuration, nanocomposite... ZT and lattice thermal conductivities of state-of-the-art skutterudites are represented in fig. 12.

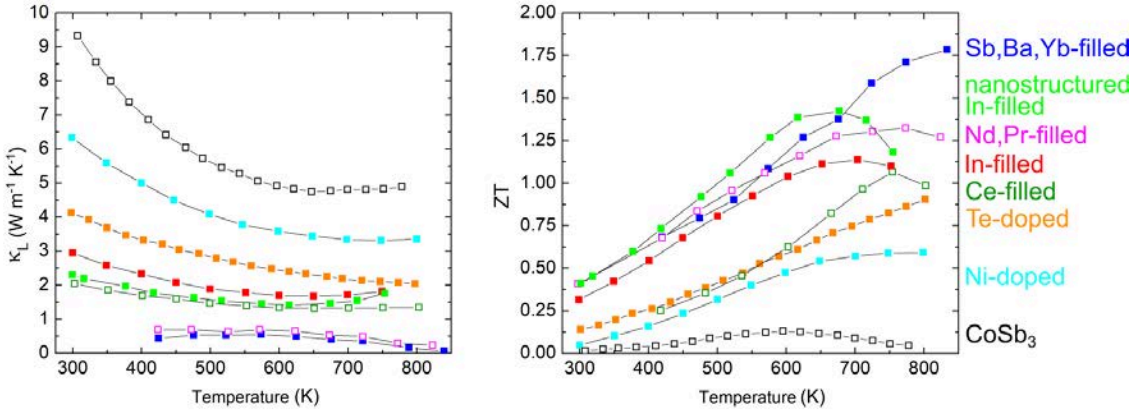

Figure 12: Temperature dependence of the lattice thermal conductivity (left) and ZT (right) of various p-type (empty symbols) and n-type (filled symbols) skutterudites taken from ref.[9,49–54]

Finally, the synthesis represents an important obstacle to the large scale production of $CoSb_3$-based materials. As shown in the Co-Sb phase diagram (fig. 13), $CoSb_3$

forms *via* two consecutive peritectic reactions:

$$CoSb + Sb \xrightarrow{1193\,K} CoSb_2 \tag{28}$$

$$CoSb_2 + Sb \xrightarrow{1135\,K} CoSb_3 \tag{29}$$

Therefore, $CoSb_3$ cannot be directly obtained after the classical melting/solidification step and the ingots must be further proceeded *via* an additional annealing step. Typical annealing treatments are 4 - 6 days long and require intermediate grindings because of the slow diffusion rate of Sb in $CoSb_2$ below 1135 K. This represents a substantial cost of time and money which should be taken into account in the production price of the materials. In addition, excess Sb is often required to compensate the high vapor pressure of this element at high temperature. These difficulties trigger the development of alternative synthesis methods. Ball-milling[55,56] or melt-spinning[57,58] the elementary metals followed by reactive sintering under the decomposition temperature enable the synthesis of material with good purity in short reaction time. Nanocrystalline powder of pristine and filled $CoSb_3$ could have been produced by hydrothermal or solution processes.[59? ,60] The yield are however usually low and the densification of the powders can be difficult due to absorbed species at the grain surface. More exotic techniques such as combustion synthesis,[61] high-pressure synthesis,[62,63] severe plastic deformation[64] or flash-spark plasma sintering[65] were also developed but remain so far more adapted to laboratory scale production.

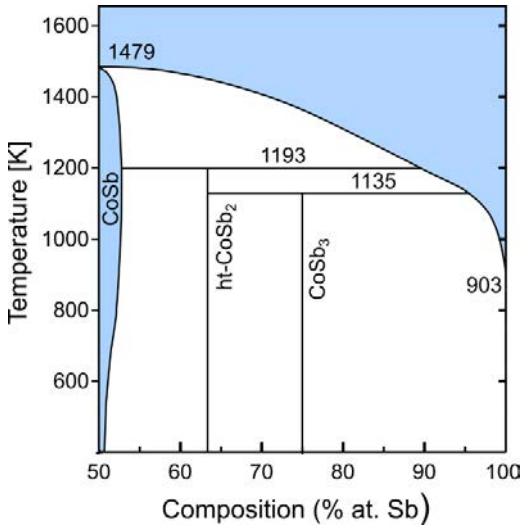

Figure 13: The Co-Sb phase diagram, from ref.[66]

1.4.4 Transition metals silicides

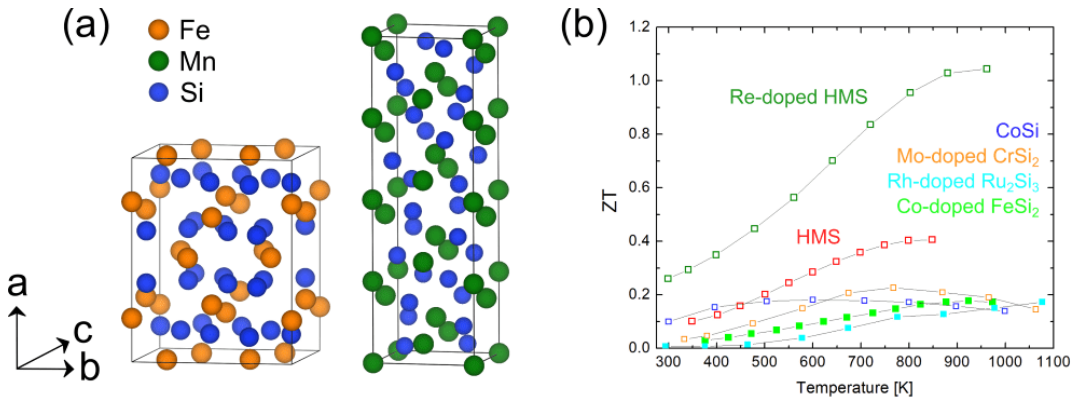

Figure 14: (a) Crystal structures of β-$FeSi_2$ (left) and $MnSi_{1.75}$ (right). (b) Temperature dependence of ZT for various p-type (empty symbols) and n-type (filled symbols) thermoelectric silicides taken from ref.[8,67–70]

Transition metals silicides have been studied as potential thermoelectric candidates as early as late 50's. The best performances are found in $FeSi_2$, HMS, $CrSi_2$, CoSi and Ru_2Si_3.[71] HMS stand for 'Higher Manganese Silicides' and correspond to compounds with composition close to $MnSi_{1.74}$ (see below for detailed description). They are all characterized by elevated melting point, high mechanical and chemical resistance which make them interesting for industrial applications. Among them, $FeSi_2$ and HMS have attracted much attention as they are n- and p-type, respectively, and constituted of extremely abundant and non-toxic elements.

The ideal crystal structures of $FeSi_2$ (s.g. $Cmce$) and $MnSi_{1.75}$ ($P\bar{4}c2$) are shown in fig. 14a. In reality, these compounds are characterized by a high structural complexity. HMS were originally described as a large family of stoichiometric compositions: Mn_4Si_7, $Mn_{11}Si_{19}$, $Mn_{15}Si_{26}$, $Mn_{27}Si_{47}$...[72] The structure is however more correctly described by considering only a single $MnSi\gamma$ phase with $1.72 < \gamma < 1.75$. As a direct consequence, the structure must thus be described by an incommensurate crystallographic approach.[73] The structural complexity also induces the formation of high density of microstructural defects. In β-$FeSi_2$, large density of stacking faults can be evidenced by transmission electron microscopy (TEM) and strongly affect the diffraction peak symmetry, broadening and positions.[74,75]

The ZT temperature dependence of state of some art silicides are shown in fig. 14b. While relatively high PF can be achieved in these materials, the figure-of-merit ZT remains small (< 0.5) because of the large thermal conductivities. This can be attributed, despite the complex crystal structures, to the constituting light elements compared to the other TE materials described until now. This is especially true for β-$FeSi_2$ which has a thermal conductivity as high as 16 W m^{-1} K^{-1} at 298 K.

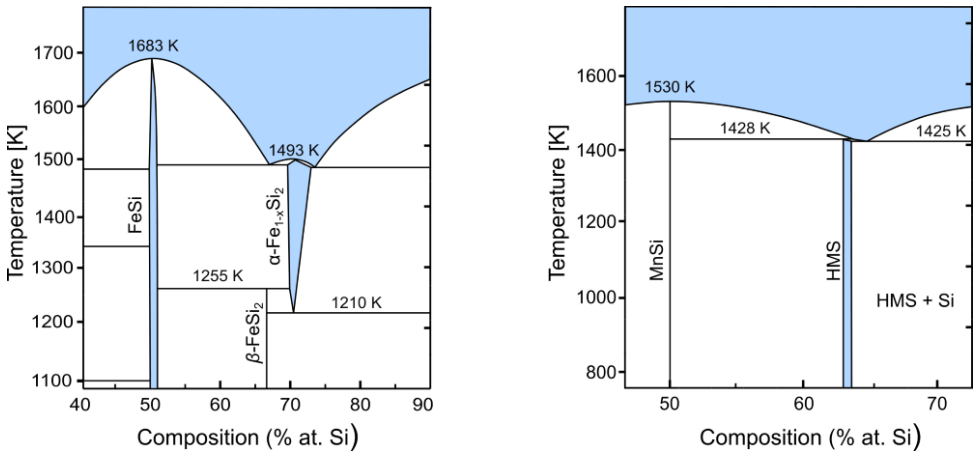

Figure 15: (a) Fe-Si and (b) Mn-Si phase diagrams taken from ref.[76,77]

The synthesis of $FeSi_2$ and $MnSi_{1.74}$ by conventional melting/solidification is quite problematic. As shown in their respective phase diagram in fig. 15a and 15b, β-$FeSi_2$ forms *via* a peritectoid reaction and $MnSi_{1.74}$ via a peritectic reaction. Subsequent annealings at about 800 K are thus required to obtain pure phase products. In the case of HMS, metallic MnSi striations are often observed inside the crystallites even after annealing that strongly deteriorates the thermoelectric and mechanical properties.[78]

Mg_2Si is another well-known material with high ZT of ≈ 1.4 at 600 K when doped with Sn.[13] It is often used as the n-type counterpart of p-type HMS for the fabrication of inexpensive TEGs.[79,80] Its application is severely limited by its reactivity with water and low mechanical properties.

1.4.5 Inorganic clathrates

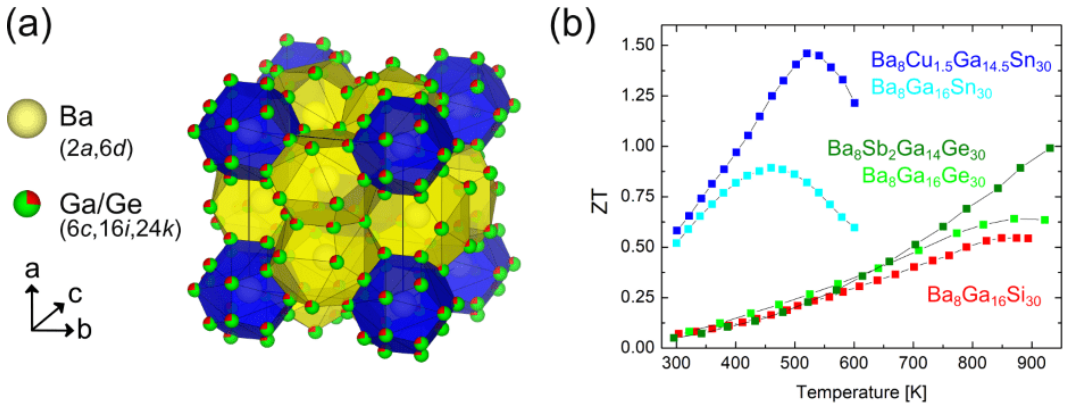

Figure 16: (a) Crystal structure of $Ba_8Ga_{16}Ge_{30}$ (s.g. $Pm\bar{3}n$, $a = 10.76$ Å) composed of two types of polyhedral cages with 20 (blue) and 24 (yellow) vertices. (b) Figure-of-merit ZT of state of the art polycrystalline clathrates taken from ref.[11,81–84]

Clathrates represent a large family of materials characterized by a three dimensional framework forming large polyhedral cages and encapsulating guest ions which include hydrates, silicates and intermetallics.[85] The best thermoelectric compositions crystallize in the cubic clathrates-II structure-type (fig. 16a) with general chemical formula $F_8Y_{16}X_{30}$ with F the filling atom being an alkaline earth or a rare earth metal, Y = Al, Ga, Au and X = Si, Ge, Sn. The bondings in the framework are essentially (polar) covalent while the weak interaction between the guest ions and the framework is essentially ionic. As for skutterudites, the rattling motion of the encapsulated atoms leads to low lattice thermal conductivities. For example, κ_L as low as 0.6 W m^{-1} K^{-1} is reported for $Ba_8Ga_{16}Sn_{30}$.[30] Good thermoelectric properties are reported in the 500 - 900 K range (fig. 16b). These materials are however extremely expensive (Ge, Ga and Au) in addition of being difficult to synthesize (Ba easily oxidizes).

2 Generalities on metallothermic reduction reactions

Metallothermic reduction reactions (MRR) consist in the reduction of MA_x metal salts where A is an anion by a reactive M' metal according to the reaction:

$$MA_x + y\,M' \longrightarrow M + y\,M'A_{x/y} \tag{30}$$

The metal salts are generally oxides ($A = O^{2-}$), chlorides ($A = Cl^-$) or fluorides ($A = F^-$) because they represent the majority of the minerals constituting the earth crust.[86,87] A great variety of reducing metal M' can be used but are generally alkaline metals, alkaline earth metals or aluminum. The first part of this section will give a short overview of the historical aspect of MRR as well as some thermodynamics background. Then, in the second section, industrial MRR processes currently used or envisaged for large scale production of metals from ores will be discussed. Finally, the third section will give a detailed account of the on-going academic researches on metallothermic reduction syntheses.

2.1 Historic of MRR & some thermodynamic considerations

One of the very first MRR was realized by Hans Cristian Ørsted and Friedrich Wöhler in 1826 who managed the reduction of $AlCl_3$ in metallic Al powder using a potassium amalgam.[88] Soon later, Wöhler isolated elemental Be and Y for the first time by reduction of the respective chlorides with K according to reactions:[89]

$$BeCl_2 + 2\,K \longrightarrow Be + 2\,KCl \tag{31}$$

$$YCl_3 + 3\,K \longrightarrow Y + 3\,KCl \tag{32}$$

Henri Deville improved the reactions of Ørsted and Wöhler by using sodium as reducing agent thus improving the process compatibility with large scale production of aluminum according to reaction:[90]

$$Al_2O_3 + 3\,Na \longrightarrow 2\,Al + 3\,NaO \tag{33}$$

In 1854, he opened the first aluminum production factory in the world producing about 500 kg per year. At that time, it was the only suitable process to produce aluminum from the reduction of the highly stable Al_2O_3.

In the middle of the 19^{th} century, Nikolay Beketov discovered that Al can be used to restore metals from their oxides under high temperatures *i.e.* aluminothermic reactions. His work was continued by Hans Goldschmidt who had, in 1895, the idea of using the large amount of heat released by aluminothermic reactions for welding.[91] Thermic welding, also known as the Goldschmidt's process, was widely used throughout the 20^{th} century for welding railways *via* reaction (34) or making electrical contacts *via* reaction (35):

$$2\,\mathrm{Al} + \mathrm{Fe_2O_3} \longrightarrow 2\,\mathrm{Fe} + \mathrm{Al_2O_3} \tag{34}$$

$$2\,\mathrm{Al} + 3\,\mathrm{CuO} \longrightarrow 3\,\mathrm{Cu} + \mathrm{Al_2O_3} \tag{35}$$

At the beginning of the 20^{th} century, there was a huge demand of novel cost-effective and industrial-scale compatible extraction methods for metals which are either easily carbonated or whose salts are too stable for being reduced by conventional carbothermic reaction. Guillaume Kroll patented in 1932 a magnesioreduction process for the production of Ti from $\mathrm{TiCl_4}$ according to:[92]

$$\mathrm{TiCl_4} + 2\,\mathrm{Mg} \longrightarrow \mathrm{Ti} + \mathrm{MgCl_2} \tag{36}$$

Later, he adapted the method to the production of Zr.[92] Magnesioreduction reaction was also successfully used for the production of uranium from $\mathrm{UF_4}$ in the framework of the Manhattan project (AMES process).[93] In the same period, all rare earth metals (except radioactive promethium) have been isolated as pure phases for the first time from trichlorides by potassium vapors.[94] Later, the AMES process has been applied to the large production of rare earth metals. All these extraction techniques based on MRR remain largely used nowadays and they will thus be discussed in more details in §2.2.

In 1944, Harold Ellingham first constructed the Ellingham diagrams which are a precious tool for the quick determination of the thermodynamic feasibility of MRR.[95] The thermal dependence of the standard free energies of formation ($\Delta \mathrm{G}_f^\circ$) of metal oxides from the native metals are represented considering one mole of $\mathrm{O_2}$. For the construction of the diagrams, the standard enthalpy ($\Delta \mathrm{H}_f^\circ$) and entropy ($\Delta \mathrm{S}_f^\circ$) of formation are set as constant in temperature ranges without any phase transition. Considering the Ellingham's approximation and according to the second law of thermodynamics (37), the thermal dependence of $\Delta \mathrm{G}_f^\circ$ can be expressed as a

linear function of the temperature:

$$\Delta G_f^\circ = \Delta H_f^\circ - T\ \Delta S_f^\circ \tag{37}$$

The Ellingham diagrams for some metals are shown is fig. 17. The lower a metal oxide is in the diagram, the more difficult it is reduced, *i.e.* the corresponding metal is a good reducing agent. Any redox reaction (30) is thermodynamically spontaneous if the condition:

$$y\ \Delta G_f^\circ[M'A_{x/y}] - \Delta G_f^\circ[MA_x] < 0 \tag{38}$$

is satisfied. In other words, metal oxides can be reduced at a given temperature if the line corresponding to the reducing agent is lower. It is not surprising to see the strongly reducing alkali and alkaline earth metals at the bottom of the diagrams. In addition, Al/Al_2O_3 is below Fe_2O_3 and CuO while being above Na thus predicting well the reactivity of the Goldschmidt and Deville experiments, respectively. The enthalpy of MRR is in the order of magnitude of hundreds of kJ mol^{-1} which explains the large amount of heat released during the reaction. It should be noticed that Ellingham diagrams are only constructed on a thermodynamic basis (standard conditions, pure reactants and products). As a consequence, they cannot predict the kinetics of reaction which are usually extremely slow for solid-state reactions at low temperature. Under non standard conditions, which correspond in the vast majority of the cases, the chemical activity a of each constituents is not necessarily equal to 1. The free energy of formation under non standard condition (ΔG_f) can be found from relations:

$$\Delta G_f\ =\ \Delta G_f^\circ + R\,T\,\mathrm{Ln}Q \tag{39}$$

where:

$$Q\ =\ \frac{a(M)\ a(M'A_{x/y})^y}{a(MA_x)\ a(M')} \tag{40}$$

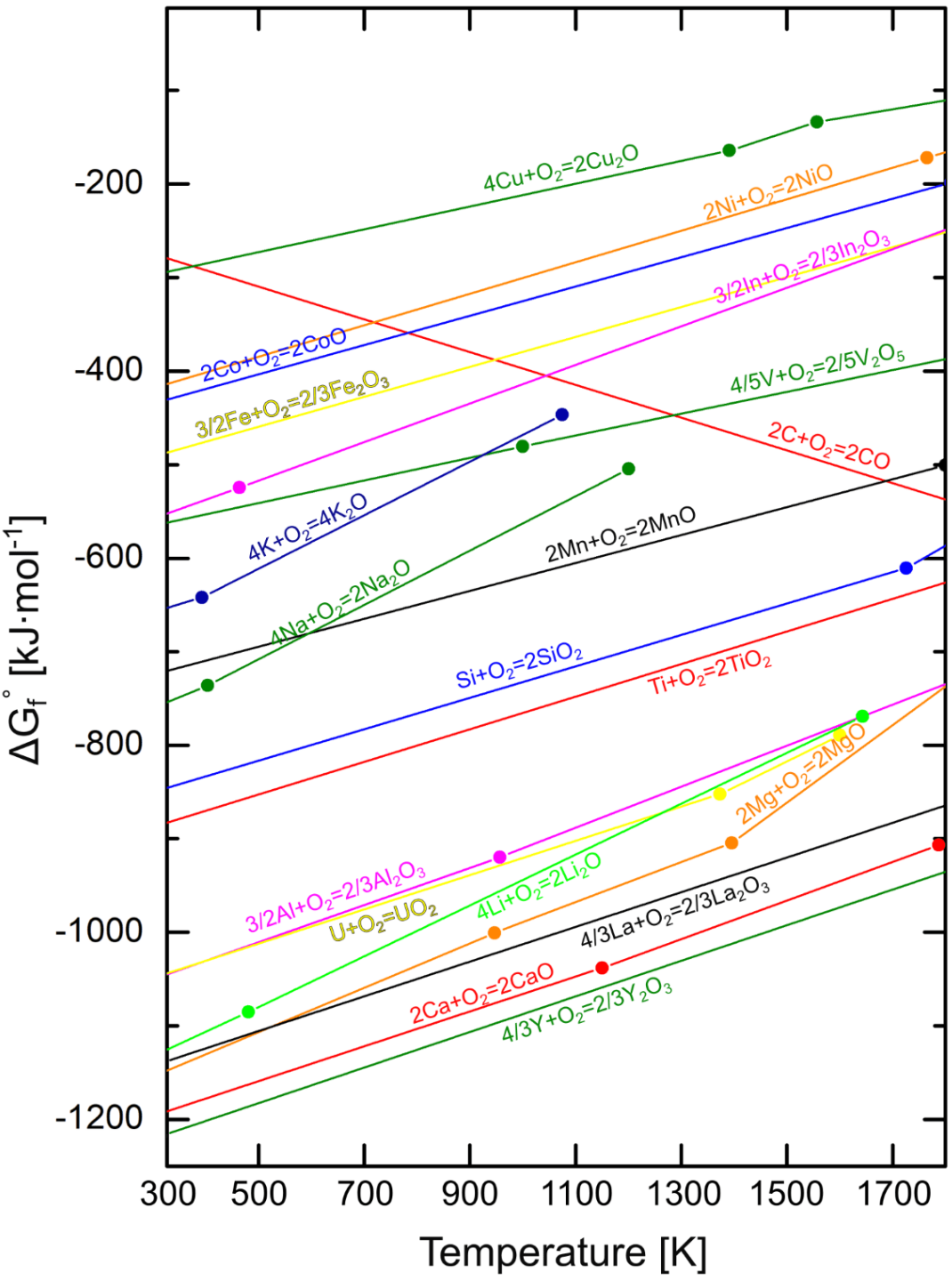

Figure 17: Ellingham diagrams of various metals taken from ref.[95]

Q can be appropriately varied by decreasing $a(\mathrm{M})$ or $a(\mathrm{M'A}_{x/y})$ and the variation amplified by a judicious choice of T in order to ensure a negative value for $\Delta \mathrm{G}_f$ even when $\Delta \mathrm{G}_f{}^\circ$ is positive. According to Le Chatelier principle, decreasing the values of $a(\mathrm{M})$ or $a(\mathrm{M'A}_{x/y})$ can be done, for example, by recovery of the reduced M as an alloy or the trapping of M in a complex slag of $\mathrm{M'A}_{x/y}$, respectively.

2.2 Industrial MRR methods

In the industry, MRR are almost exclusively used for the extraction of metals from purified ores. The desirable characteristics of the extraction processes have been summarized by C. Herget (1985)[87,96] as follows:

1. the reaction should occur quickly and give products with high yields;
2. the reaction products must be obtained in compact forms *e.g.* ingots or well-separated layers;
3. the reaction should be self-sustaining and once initiated should proceed without the need for additional external heating;
4. the products must be of high purity;
5. the reaction proceeds in an open atmosphere;
6. the reaction should proceed safely without risk;
7. the reaction should be carried out in commercially available reactors.

Moreover, the process must be as cost-effective and environment friendly as possible. The production of steel (Fe containing few % of C impurity) by carboreduction reaction in blast furnaces remains the most wild-spread extraction process and will thus be shortly described. Then, three different types of industrial MRR processes will be presented and their applicability with regard to the other extraction techniques will be discussed.

2.2.1 Carbothermic production of steel

Since the iron age, steel is elaborated by the carbothermic reduction of $\mathrm{Fe_2O_3}$ in blast furnaces according to the global reaction:

$$2\,\mathrm{Fe_2O_3} + 3\,\mathrm{C} \longrightarrow 4\,\mathrm{Fe} + 3\,\mathrm{CO_2} \tag{41}$$

Nowadays, the process is carried out in tens of meters tall reactors where $\mathrm{Fe_2O_3}$ and C are continuously injected at the top while melted steel is recovered at the bottom

(fig. 18). The CO_2 by-product is evacuated at the open top of the reactor. The temperature gradient and the reactions involved are quite complex inside the blast furnaces. Below 1163 K, the majority of Fe_2O_3 is successively reduced into Fe_3O_4, FeO and Fe by carbon monoxide. The later being produced *in situ* at the hottest part of the reactor from the reaction between C and O_2 according to the Boudouard equilibrium:

$$2\,C + O_2 = 2\,CO \tag{42}$$

Above 1163 K, the reduction of FeO by CO is no more thermodynamically allowed but FeO can be directly reduced by C. In addition, this process has the advantage of operating in continuous mode from inexpensive reducing agent which makes possible the mass-production of low-cost steel thus fulfilling most of the attributes listed by Herget. The steel production is about 1.2 10^6 tons per year from this process which represents 75% of the world annual production.[97] Ferroalloys (Fe + Si, Mn or Ni) can also be produced in this way. It should be noticed that blast furnaces are however progressively being replaced by less CO_2 emitting processes.

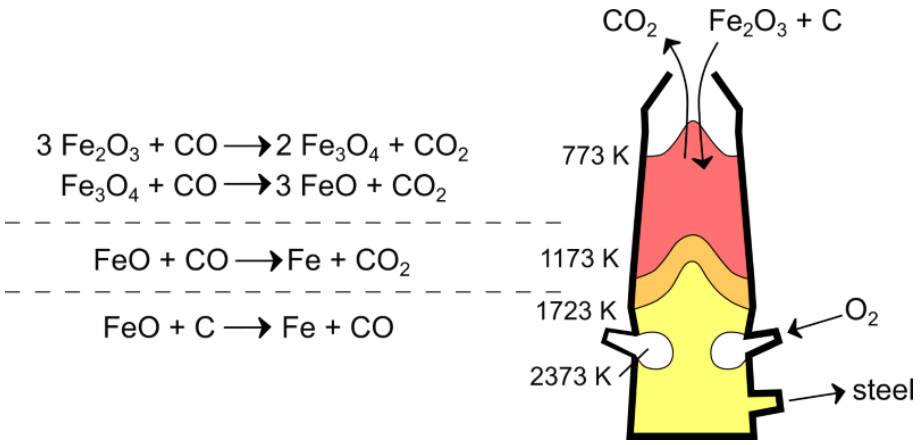

Figure 18: Schematic representation of the elaboration of steel in blast furnaces.

2.2.2 MRR processes

Such carbothermic process is not adapted to the extraction of all the metals. These include metals easily forming refractory carbides (Ti, Zr, U, rare earth elements) or highly stable metal salts which cannot be reduced by CO or C under conventional operating temperatures (Al). Moreover, it only enables the extraction of metals in the shape of ingots while powders are preferred for many industrial application thus requiring additional processing steps. For these reasons, some metals are currently extracted at the industrial scale using MRR. Compared to carbothermic reduction,

MRR present some advantages and drawbacks which are listed in the following:

Advantages:

- Lower temperatures thanks to more reactive reducing agents
- Good applicability to most of the metals
- Products in the shape of ingots, sponges or powder
- High yield and purity
- Very limited emission of greenhouse-gases

Drawbacks:

- Batch or semi-continuous processes
- More expensive reducing agents
- Separation of the metal from the slag may be challenging

MRR are often less attractive financially than carbothermic or electrolysis processes but they are competitive for the extraction of valuable metals or the fabrication of high added-value materials with high purity and specific morphology. MRR can be realized either in sealed reactors or in molten salts. Reaction in sealed reactor is the method used during my thesis work because it is easier to set up. Various reactors configurations are possible depending on the choice of reactants, reaction conditions and desired product forms. The reactors are however always made of refractory and chemically inert metals such as steel, tantalum or molybdenum. In the following, three main types of MRR will be described: (i) the industrial Kroll's process for the extraction of Ti, (ii) the industrial AMES process for the extraction of U and rare earth elements and (iii) preformed reduction processes for the production of metal powders.

The Kroll's process The Kroll's process consists in the magnesioreduction of $TiCl_4$ at 1100 K in airtight reactors (fig. 19a).[92] At this temperature, $TiCl_4$ is a gas (boiling point $\approx$ 400 K) and is reacted with molten Mg according to the highly exothermic reaction:

$$2\,Mg\,(l) + TiCl_4(g) \xrightarrow{1100\,K} 2\,MgCl_2(l) + Ti\,(s) \tag{43}$$

Magnesium is soluble only up to 1.5 at.% in Ti at 1100 K. The freshly reduced titanium particles sink in the molten $MgCl_2$ slag and stick to the reactor walls in

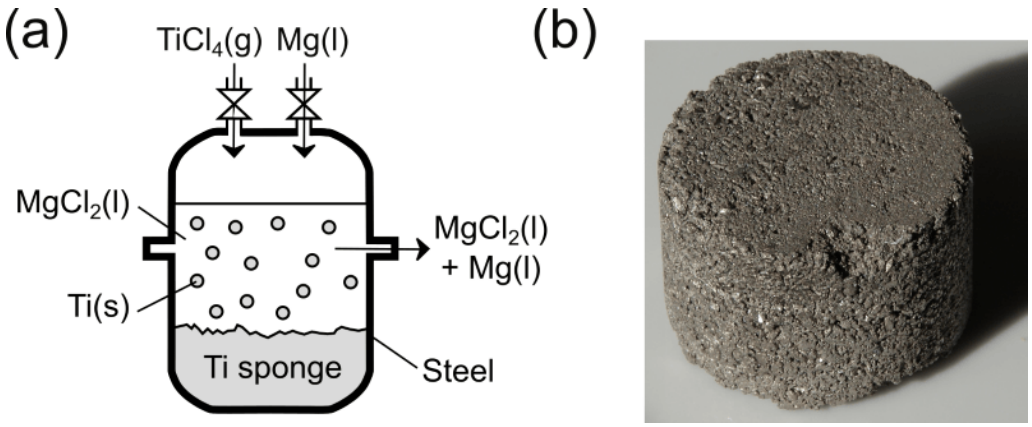

Figure 19: (a) Schematic representation of the industrial Kroll's process. (b) Picture of a titanium sponge obtained from this process (l: liquid, s: solid, g: gas).

the form of massive sponge (fig. 19b). $TiCl_4$ and Mg are regularly injected in order to keep the reaction self-sustained. Meanwhile, liquid $MgCl_2$ and Mg are removed from the reactor to set new space. The reaction can last for several days before the reactor is full of Ti sponges. The Kroll's process is said to be semi-continuous because the reactor must to be cut opened to recover the product. Mg and $MgCl_2$ impurities are removed by distillation before conventional refinement of Ti. A very similar method is used for the extraction of zirconium. The world productions of Ti and Zr represent about 50000 and 7000 tons per years, respectively.[98]

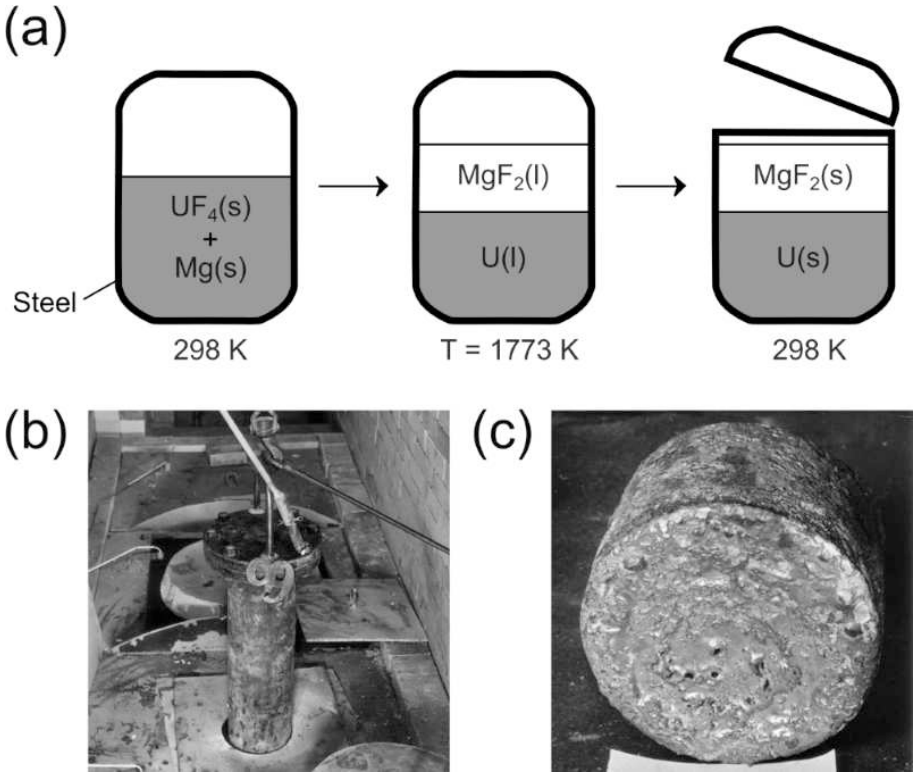

Figure 20: (a) Schematic representation of the AMES process. (b) Pictures of a reactor being removed from the furnace. (c) Picture of an uranium ingot.

The AMES process The AMES process was developed during the Manhattan project (1942 - 1946) for the large scale production of metallic uranium. It consists in the magnesioreduction of UF_4 at 1773 K in a sealed reactor vessel often called 'bomb' (fig. 20a and 20b). At this temperature, both reactants are in the gas phase and 'explode' forming liquid U and MgF_2 according to the reaction:

$$UF_4(g) + 2\,Mg\,(g) \xrightarrow{1773\,K} U\,(l) + 2\,MgF_2(l) \tag{44}$$

In the present case, magnesium is the ideal reducing agent since it is completely unreactive toward metallic uranium. Thanks to large density difference, uranium remains well-separated from the slag and forms a well-isolated metal ingot after the reactor is being cooled down (fig. 20c). The production is however relatively slow due to the batch nature of the process.

The AMES process was later adapted to the production of the rare earth elements. The rare earth trifluorides are commonly reduced with calcium according to the reaction (45). This process is still largely in use nowadays.[87]

$$2\,REF_3 + 3\,Ca \longrightarrow 2\,RE + 3\,CaF_2 \tag{45}$$

Preform reduction processes Metal powders are important for many industrial applications such as catalysis, electronic components manufacturing and the shaping of sintered pieces with improved mechanical properties. Powders are usually obtained by atomization, melt-spinning or milling techniques from purified metal ingots.[99]

Preform reduction processes (PRP) consist in the reduction of pressured or sintered preform metallic salts by vapor or liquid reducing metal (fig. 21a). The product is obtained as a metallic powder dispersed in a slag matrix. The slag in this case must be leached away to separate the metal powder. Mg and Ca are the most common reducing agents because of their large vapor pressure making them reactive even at low temperatures and their oxides can be easily removed with acids. The reaction conditions must however be carefully controlled in order to avoid the formation of Mg-containing compounds or contamination from the metallic preform holder or the melting/vaporization of the preform.

Various metals such as Ti[100–102], Ta[103,104], Nb[105,106], V[107,108] can be produced from oxides by this process. Most of the reactions last only few hours. After leaching with acid, pure submicronic powders are directly obtained. Moreover, the grain sizes and morphology could be controlled by adding a binder (carbonate, chloride...) to

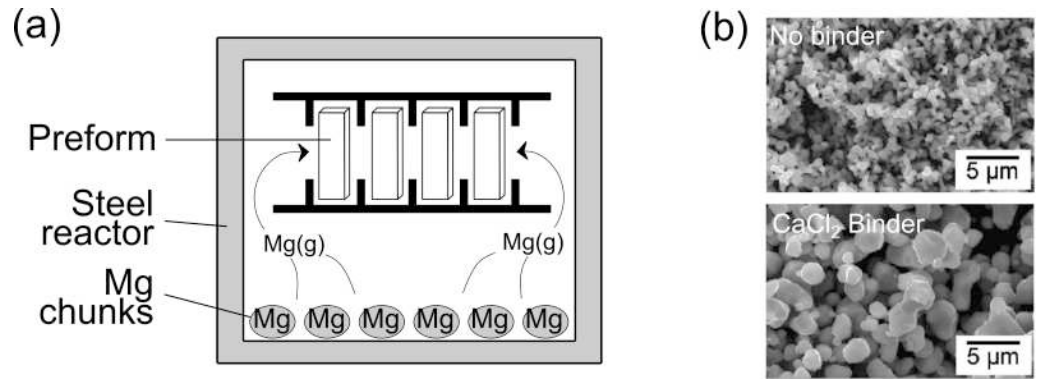

Figure 21: (a) Schematic representation of the PRP process. (b) Secondary electron SEM images of Ti powder obtained by PRP with (top) and without $CaCl_2$ binder (bottom). Taken from ref.[100]

the feed preform (fig. 21b).[100] This represents an interesting strategy to directly produce high purity metallic powders without going throught an additional costly and difficult powderization step.

2.3 MRR syntheses

Many researches have reported MRR syntheses in the recent years.[86] The MRR synthesis, or 'co-reduction synthesis', of the binary MM' compound consists in the simultaneous reduction of the metal salts MA_x and $M'A_y$ by a reducing metal R according to:

$$MA_x + M'A_y + z\,R \longrightarrow MM' + z\,RA_{(x+y)/z} \tag{46}$$

The MRR set-up and reaction conditions must be determined according to the characteristics of all the species involved in the reaction such as the oxidizing power, melting point, boiling point, vapor pressure, diffusion rate and chemical reactivity toward the reducing metal. Different configurations are possible to optimize the reactivity between the precursors and reducing agent (fig. 22). The precursor salts can be (i) mixed and pelletized separately from the reductant similarly to PRP,[109,110] (ii) mixed and pelletized along with the reductant[111–113] or (iii) directly ball-milled with the reductant.[114–116] In the cases (ii) and (iii) the reaction is expected to occur faster (and more vigorously) than in the case (i) since the reactants are directly in contact with the precursors. However, if the metal salts have different oxidizing power or affinity with the reducing agent, the chances to form undesired by-product are greatly enhanced.[111]

Careful preparation of the precursors mixture is essential to obtain pure and homogeneous products. The precursor preparation can be realized (i) by ball-milling

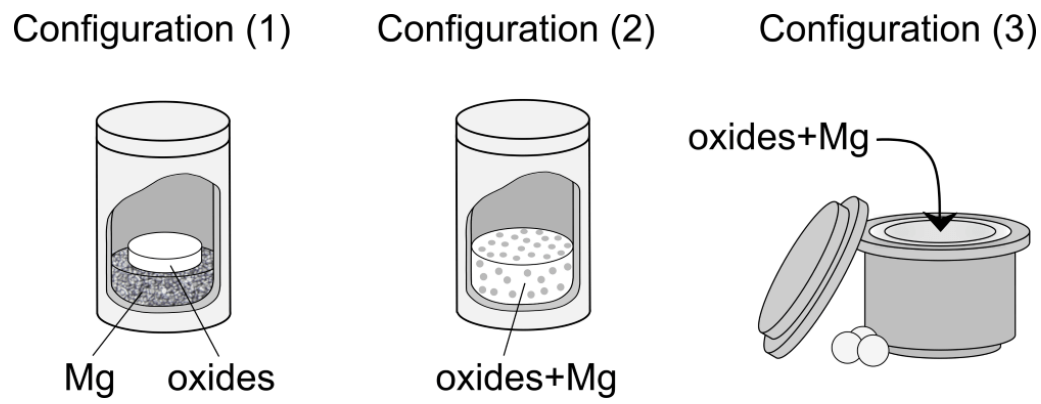

Figure 22: Schematic representation of the three possible configurations for MRR synthesis: (left) the oxides precursors are pelletized separately of Mg; (middle) the oxides are mixed and pelletized with Mg; (right) the oxides and Mg are reacting by ball-milling.

or mixing powders together in agate mortar[109,112] or (ii) by synthesizing a mixed metal salt precursor.[111,117,118] The case (ii) being clearly the most favorable option to obtain an intimate mixture of the metal atoms but it implies an additional synthesis step. The grain size of the precursor mixture is also of great importance since the smaller the grain size, the more reactive the synthesis but also the greater the chances to form side-products. For these reasons, it is of uttermost importance that all the reaction parameters are set in full adequacy when performing MRR syntheses to obtain pure products.

MRR have great advantages already listed in §2.2 which can be advantageously applied to the production of materials being difficult to synthesize by conventional 'fusion-solidification' methods. This includes materials constituted of elements with important differences in the physical properties (vapor pressures, melting points), having high synthesis temperature or low decomposition temperature. Some reports on MRR syntheses can be found in the literature and are summarized in table 1.

This review of the literature evidences that MRR have been predominantly used for the synthesis of refractory materials such as carbides, borides or silicides. Indeed, these materials are conventionally synthesized at very high temperature. Moreover, their important hardness and friability make good control of the powder morphology by milling difficult which is problematic for sintering. The magnesioreduction of the oxide precursors is generally realized around 1000 K in few hours only. It represents an important gain of energy and time compared to conventional high temperature syntheses. The products are isolated by leaching away the MgO by-product with hydrochloric or acetic acids. Typical product microstructure consists in powders composed of well-isolated crystallites with diameters in the 100 - 500 nm range. Such powders are perfectly suitable for sintering. Some authors attribute the relatively small crystallites sizes to the MgO formed during the reaction which is

playing the role of growth inhibitor.[86] Incorporation of MgO or CaO in the precursor mixture prior to the reaction was shown to be an option to control the product morphology.[117,118] L. Bai *et al.* were able to synthesize 1.25 kg of pure submicronic ZrC powder in one batch showing that MRR syntheses give good up-scaling perspectives.[113]

Table 1: Examples of MRR syntheses reported in the literature.

Materials	Precursors	Reducing Agent	Temperature [K]	Time [h]	Ref.
EuB_6	Eu_2O_3, B_2O_3	Mg	873	4	[112]
LaB_6	La_2O_3, B_2O_3	Ca	Ball-milling	3	[114]
ZrB_2	ZrO_2, B	Mg	1873	1.5	[113,119]
HfB_2	HfO_2, B_2O_3	Mg	1023	0.5	[119]
ReB_2	ReO_2, B_2O_3	Mg	923-1073	/	[120]
TiB_2	TiO_2, B_2O_3	Mg	923-1073	/	[120]
ZrC	ZrO_2, C	Mg	1873	1.5	[113]
$Si_{80}Ge_{20}$	$(Si_{0.8}Ge_{0.2})O_2$	Mg	923	6	[111]
SiC	SiO_2, C	Mg	1073	24	[121]
$FeSi_2$	SiO_2, Fe_2O_3	Mg	1073	6	[117,118]
$MoSi_2$	MoO_3, SiO_2	Al, C	Ball-milling	70	[122]
$U_{84}Mo_{16}$	UO_2, Mo	Mg	1023-1373	12-49	[109]
Nb_2Ti	$TiNb_2O_7$	Mg	1073	10	[123]
$LaNi_5$	La_2O_3, Ni	Mg	1173	9	[110]
$MmNi_5$	Mm_2O_3, Ni	Ca	1223-1323	/	[124]
Cu-Mo	CuO, MoO_3	Mg, C	Combustion		[125]
ZrCoSb FeNbSb ZrNiSn	Chloride/Bromide	Mg,Li	Ball-milling	2-5	[115]
$SmCo_5$	Sm_2O_3, Co_3O_4, Co	Ca	1373-1473	4	[126]
$Nd_2Fe_{14}B$	Nd_2O_3, Fe_2O_3, $Fe_{44}B_{56}$, Fe	Ca	1373-1473	4	[96]

MRR syntheses have also been applied to intermetallics or alloys whose properties can be greatly improved thanks to the uncommon morphology of the powders usually obtained from this process. This includes hydrogen-storage $LaNi_5$ (small grain size with high specific surface),[110] nuclear fuel $U_{84}Mo_{16}$ (chemical homogeneity and good-crystallinity)[109] and permanent magnets $SmCo_5$ and $Nd_2Fe_{14}B$ (small grain size for orientation).[96,126]

Two articles were found dealing with the magnesioreduction syntheses of thermoelectric (TE) materials. The first article by M. L. Snedaker *et al.* reported in 2013 the synthesis of B-doped $Si_{80}Ge_{20}$ high-temperature TE alloys.[111] In this article, the authors use the magnesioreduction process in order to reduce the reaction temperature and to shortcut the highly energy-consuming Si and Ge purification step ($\approx$ 2300 K). The procedure first consists in the realization of a sol/gel synthesis from tetraethylorthosilicate (TEOS), tetraethoxygermane (TEOG) and ethanolic

boric acid, and then in the calcination of the gel to obtain a mixed $(Si_{0.8}Ge_{0.2})O_2$ precursor. The precursor was directly mixed and pelletized with magnesium and the pellet is reacted at 923 K for 6 h under flowing Ar : H_2 (90 : 10) according to:

$$(Si_{0.8}Ge_{0.2})O_2 + 2\,Mg \xrightarrow[6\,h]{923\,K} Si_{0.8}Ge_{0.2} + MgO \tag{47}$$

At the end of the reaction, B-doped $Si_{80}Ge_{20}$ and MgO are obtained along with Mg_2(Si,Ge) and unreacted (Si,Ge)O_2. This is a typical example of the difficulty to obtain pure products by magnesioreduction process. While nanocrystalline mixed oxide precursor is needed because of the low reaction temperature and slow inter-diffusion rate of Si and Ge, it also makes the product more reactive toward Mg. The as-synthesized powder was leached with hydrochloric acid for 12 h to remove MgO and Mg_2(Si,Ge) and several times with diluted hydrofluoric acid to remove unreacted (Si,Ge)O_2. After sintering, the densified pellets with average crystallites size of about 500 nm is contaminated by a F and Mg rich secondary phase. A 10 % reduction of the thermal conductivity has been achieved for the optimally doped sample compared to the best 'bulk' Si-Ge alloys taken from the literature. However, the peak ZT could not be significantly improved due to lower PF which is attributed to the large amount of impurity.

The second article was written by H. Zhao *et al.* in 2017 and reports a novative magnesioreduction route to TE Half-Heusler alloys by ball-milling.[115] First the respective metal chlorides where ball-milled for 2 - 5 h with lithium or magnesium to obtain a mixture of metals nanoparticles and $MgCl_2$ or LiCl by-products. The mixture was then spark plasma sintered at 950 K for 4 h in order to (i) expel the $MgCl_2$ or LiCl by-product by evaporation, (ii) form the HH alloys by reaction of the metallic nanoparticles and finally (iii) to obtain a densified material. In the case of ZrCoSb, the global reaction equation is:

$$2\,ZrCl_4 + 2\,CoCl_2 + 2\,SbCl_3 + 9\,Mg \xrightarrow[2\text{-}5\,h]{B-M} \xrightarrow[950\,K]{SPS} 2\,ZrCoSb + 9\,MgCl_2 \tag{48}$$

The obtained pellets have average crystallites sizes varying from 200 to 500 nm depending on the sample and contain very high density of dislocation arrays. Reduction of the thermal conductivity of up to 40 % has been achieved by this method. However, as for the first article, the power factors are systematically lower than conventional materials leading to slightly lower ZT. This has been attributed to the presence of impurities such as $MgCl_2$/LiCl or metal oxides in the pellets.

3 Context and objectives

The efficiency of thermoelectric devices is directly related to the performances of the constituting materials (§1.2). Pb and Te containing alloys (§1.4.1) are currently the most efficient thermoelectric materials for mid-temperature region which corresponds, for example, to the exhaust line temperature of fuel engines. However, the scarcity, the high cost and the toxicity of these elements prevent the use of the materials for large scale applications. Extensive researches have thus been devoted to the development of alternative materials which respect the following conditions:

(1) The materials must preferentially be constituted of non-toxic and inexpensive elements;

(2) They must have good mechanical et chemical resistance properties in order to guarantee a long life time to the TEG;

(3) A large-scale, reliable and reproducible synthesis process must be available;

(4) The figure-of-merit ZT must be as high as possible (ideally $>$ 2 - 3).

I have selected two types of thermoelectric materials which are skutterudites (§1.4.3) and transition metal silicides (§1.4.4) because they possess good electrical properties (high PF) and they mostly fulfill the conditions (1) and (2). Skutterudites can reach figure-of-merit ZT above 1 thanks (i) to the possibility to insert heavy 'rattlers' in the large cages available in the structure and (ii) to the mass fluctuation phenomena made possible by the numerous chemical substitutions allowed on the various sites of the structure. Transition metal silicides, β-$FeSi_2$ and HMS, exhibit much smaller ZT figure-of-merit (typically below 0.5) but are composed of extremely abundant and low cost elements.

However, the synthesis of both classes of compounds by conventional fusion/solidification methods are very time- and energy-consuming since they are formed by peritectic or peritectoid reactions, thus requiring long annealing. Moreover, the improvement of their thermoelectric properties necessarily goes by the reduction of their thermal conductivities which can be realized thanks to nano-/mesostructuration (strategy 6 in §1.3.5). From the review of the literature data available on metallothermic reactions in §2, it seems that this unconventional synthesis route can be advantageously applied to these materials because (i) the reaction temperature can be reduced below the decomposition temperature of the phases and (ii) submicronic powders appropriate to the preparation of mesostrutured materials are directly obtained. In this way, the conditions (3) and (4) could be fulfilled in order to bring the materials to the industrial scale production. The present work is thus dedicated to the magnesioreduction syntheses of $CoSb_3$-based skutterudites, HMS and β-$FeSi_2$

thermoelectric materials. My investigations were:

1. The development of a magnesioreduction process optimized for the production of pure materials with controlled chemical composition;
2. The investigation of the structural and microstructural properties of the materials synthesized by magnesioreduction in respect of the ones obtained by melting/solidification synthesis and the study of how these properties affect the thermoelectric performances.

After a brief description of the experimental techniques used during this study, the results obtained will be presented in the form of four scientific articles, published in or submitted to peer-reviewed journals, followed by a critical discussion guided by the mentioned guidelines.

The first part is composed of two articles presenting the results on the magnesioreduction synthesis of $CoSb_3$-based skutterudites. The first article, published in *Journal of Alloys and Compound*, demonstrates the feasibility of the magnesioreduction synthesis of pristine $CoSb_3$, Ni-doped $Ni_{0.06}Co_{0.94}Sb_3$ and In-filled $In_{0.13}Co_4Sb_{12}$ skutterudites. The discussion is primarily focused of the particular morphology of the as-synthesized powders and the microstructure of the resulting sintered materials. The thermoelectric properties are presented and compared to 'bulk' and mesostructured materials with similar compositions from the literature. The second article, submitted to *Intermetallics*, focuses on the synthesis of $In_{0.25}Co_4Sb_{12}$. The aim of this article is to give a much more detailed analysis of the magnesioreduction mechanism which has been determined by X-ray diffraction and quantitative Rietveld analyses. This topic has been realized in collaboration with Dr. Eric Alleno (ICMPE, Thiais, France).

The second part is composed of two articles dealing with the magnesioreduction syntheses of Higher Silicides Manganese and β-$FeSi_2$ submitted to *Journal of Alloys and Compounds* and *ACS Applied Energy Materials*, respectively. In both articles, the magnesioreduction synthesis procedure and mechanism are first presented. Then, the advanced microstructural and structural analyses performed on both as-synthesized powders and densified pellets are discussed. Finally, the thermoelectric properties are compared to samples synthesized by conventional 'melting/annealing' methods and measured in similar conditions. This work has been realized in collaboration with Prof. Takao Mori (National Institute of Materials Sciences (NIMS), Tsukuba, Japon) and Dr. David Berthebaud (UMI-LINK, Tsukuba, Japon).

References

[1] D. Beretta, N. Neophytou, J. M. Hodges, M. G. Kanatzidis, D. Narducci, M. Martin-Gonzalez, M. Beekman, B. Balke, G. Cerretti, W. Tremelj, A. Zevalkink, A. I. Hofmann, C. Müller, B. Dörling, M. Campoy-Quiles, M. Caironi, *Mater. Sci. Eng. R Rep.* **2018**.

[2] S. P. Thompson, T. S. Phillips, *Dynamo-Electric Machinery; A Manual for Students of Electrotechnics* **2009**.

[3] S. I. Kim, K. H. Lee, H. A. Mun, H. S. Kim, S. W. Hwang, J. W. Roh, D. J. Yang, W. H. Shin, X. S. Li, Y. H. Lee, G. J. Snyder, S. W. Kim, *Science* **2015**, *348*, 109.

[4] J. P. Heremans, V. Jovovic, E. S. Toberer, A. Saramat, K. Kurosaki, A. Charoenphakdee, S. Yamanaka, G. J. Snyder, *Science* **2008**, *321*, 554–557.

[5] K. F. Hsu, S. Loo, F. Guo, W. Chen, J. S. Dyck, C. Uher, T. Hogan, E. K. Polychroniadis, M. G. Kanatzidis, *Science* **2014**, *303*, 818.

[6] S. R. Brown, S. M. Kauzlarich, F. Gascoin, G. J. Snyder, *Chem. Mater.* **2006**, *187*, 1873–1877.

[7] S. Sakurada, N. Shutoh, *Appl. Phys. Lett.* **2005**, *86*, 082105.

[8] A. Yamamoto, S. Ghodke, H. Miyazaki, M. Inukai, Y. Nishino, M. Matsunami, T. Takeuchi, *Jpn. J. Appl. Phys.* **2016**, *55*, 020301.

[9] G. Rogl, A. Grytsiv, P. Rogl, N. Peranio, E. Bauer, M. Zehetbauer, O. Eibl, *Acta Mater.* **2014**, *63*, 30–43.

[10] E. M. Levin, S. L. Bud'ko, K. Schmidt-Rohr, *Adv. Funct. Mater.* **2012**, *22*, 2766–2774.

[11] D. Cederkrantz, M. Nygren, A. E. C. Palmqvist, *J. Appl. Phys.* **2010**, *108*, 113711.

[12] C. B. Vining, W. Laskow, J. O. Hanson, R. R. Van der Beck, P. D. Gorsuch, *J. Appl. Phys.* **1991**, *69*, 4333.

[13] H. Ning, G. D. Mastrorillo, S. Grasso, B. Du, T. Mori, C. Hu, Y. Xu, K. Simpson, G. Maizza, M. J. Reece, *Mater. Chem. A* **2015**, *3*, 17426.

[14] D. L. Greeaway, G. Harbeke, *J. Phys. Chem. Solids* **1965**, *26*, 1585–1604.

[15] D. V. Lang, R. People, J. C. Bean, A. M. Sergent, *Appl. Phys. Lett.* **1985**, *47*, 1333.

[16] K. Koumoto, T. Mori, *Springer, Series in Materials Science* **2013**, *182*.

[17] J. A. Carruthers, T. H. Geballe, H. M. Rosenberg, J. M. Ziman, *Proc R Soc Lond A Math Phys Sci* **1957**, *238*, 502–514.

[18] S. K. Bux, R. G. Blair, P. K. Gogna, H. Lee, G. Chen, M. S. Dresselhaus, R. B. Kaner, J.-P. Fleurial, *Adv. Funct. Mater.* **2009**, *19*, 2445–2452.

[19] P. D. Maycock, *Solid State Electron.* **1967**, *10*, 161–168.

[20] G. J. Snyder, E. S. Toberer, *Nat. Mater.* **2008**, *7*, 105–114.

[21] T. Mori, *Small* **2017**, *13*, 1702013.

[22] W. Liu, J. Hu, S. Zhang, M. Deng, C.-G. Han, Y. Liu, *Mater. Today Phys.* **2017**, *1*, 50–60.

[23] L. Yang, Z.-G. Chen, M. S. Dargusch, J. Zou, *Adv. Energy Mater.* **2017**, *84*, 1701797.

[24] Y. Pei, H. Wang, G. J. Snyder, *Adv. Mater.* **2012**, *24*, 6125–6135.

[25] L. D. Hicks, T. C. Harman, M. S. Dresselhous, *Appl. Phys. Lett.* **1993**, *63*, 3230–3232.

[26] L. D. Hicks, M. S. Dresselhous, *Phys. Rev. B* **1993**, *47*, 8–11.

[27] A. Ioffe, *Semiconductor Thermoelements and Thermoelectric Cooling* **1957**.

[28] G. A. Slack, *MRS Proceedings* **1997**, *478*, 47.

[29] G. Rogl, P. Rogl, *Curr. Opin. Green Sustain. Chem.* **2017**, *4*, 50–57.

[30] J.-A. Dolyniuk, B. Owens-Baird, J. Wang, J. V. Zaikina, K. Kovnir, *Mater. Sci. Eng., R* **2016**, *108*, 1–46.

[31] T. Caillat, J. Fleurial, G.J.Snyder, *Solid State Sci.* **1999**, *1*, 535–544.

[32] C. W. Nan, R. Birringer, *Phys. Rev. B* **1998**, *14*, 8264–8268.

[33] H. S. Yang, G. Bai, L. Thompson, J. Eastman, *Acta Mater.* **2002**, *50*, 2309–2317.

[34] L. Weber, E. Gmelin, *Appl. Phys.* **1991**, *A 53*, 136–140.

[35] J. Yang, H.-L. Yip, A. K.-Y. Jen, *Adv. Energy Mater.* **2013**, *3*, 549–565.

[36] K. Biswas, J. He, I. D. Blum, C.-I. Wu, T. P. Hogan, D. N. Seidman, V. P. Dravid, M. G. Kanatzidis, *Nature* **2012**, *489*, 414–418.

[37] E. M. Levin, B. A. Cook, J. L. Harringa, S. L. Bud'ko, R. Venkatasubramanian, K. Schmidt-Rohr, *Adv. Funct. Mater.* **2011**, *21*, 441–447.

[38] Y. Pei, X. Shi, A. LaLonde, H. Wang, L. Chen, G. J. Snyder, *Nature* **2011**, *473*, 66.

[39] G. Tan, F. Shi, S. Hao, L.-D. Zhao, H. Chi, X. Zhang, C. Uher, C. Wolverton, V. P. Dravid, M. G. Kanatzidis, *Nat. Commun.* **2016**, *7*, 1.

[40] N. Chen, F. Gascoin, G. J. Snyder, E. Müller, G. Karpinski, C. Stiewe, *Science* **2005**, *87*, 171903.

[41] J. Androulakis, K. F. Hsu, R. Pcionek, H. Kong, C. Uher, J. J. D'Angelo, A. Downey, T. Hogan, M. G. Kanatzidis, *Adv. Mater.* **2006**, *18*, 1170–1173.

[42] T. Graf, C. Felser, S. S. Parkin, *Prog. Solid State Chem.* **2011**, *39*, 1–50.

[43] S. Bhattacharya, A. L. Pope, R. T. Littleton, T. M. Tritt, V. Ponnambalam, Y. Xia, S. J. Poon, *Appl. Phys. Lett.* **2000**, *77*, 2476.

[44] N. Shutoh, S. Sakurada, *J. Alloys Compd* **2005**, *389*, 204–208.

[45] L. Pauling, *J. Am. Chem. Soc.* **1932**, *54*, 3570–3582.

[46] Y. Tang, Z. M. Gibbs, L. A. Agapito, G. Li, H.-S. Kim, M. B. Nardelli, S. Curtarolo, G. J. Snyder, *Nature Mat.* **2015**, *97*, 1–6.

[47] G. Rogl, A. Grytsiv, K. Yubuta, S. Puchegger, E. Bauer, C. Raju, R. Mallik, P. Rogl, *Acta Matter.* **2015**, *95*, 201–211.

[48] G. Rogl, A. Grytsiv, P. Heinrich, E. Bauer, P. Kumar, N. Peranio, O. Eibl, J. Horky, M. Zehetbauerd, P. Rogl, *Acta Matter.* **2015**, *91*, 227–238.

[49] E. Alleno, E. Zehani, M. Gaborit, V. Orodniichuk, B. Lenoir, M. Benyahia, *J. Alloys Compd.* **2017**, *692*, 676–686.

[50] M. Benyahia, V. Ohorodniichuk, E. Leroy, A. Dauscher, B. Lenoir, E. Alleno, *J. Alloys Compd.* **2018**, *735*, 1096–1104.

[51] J. Leszczynski, V. D. Ros, B. Lenoir, A. Dauscher, C. Candolfi, P. Masschelein, J. Hejtmanek, K. Kutorasinski, J. Tobola, R. I. Smith, C. Stiewe, E. Müller, *J. Phys. D: Appl. Phys.* **2013**, *46*, 495106.

[52] G. Rogl, A. Grytsiv, P. Rogl, E. Bauer, M. Zehetbauer, *Intermetallics* **2011**, *19*, 546–555.

[53] H. Yang, P. Wen, X. Zhou, Y. Li, B. Duan, P. Zhai, Q. Zhang, *Scripta Mater.* **2019**, *159*, 68–71.

[54] X. Tang, Q. Zhang, L. Chen, T. Goto, T. Hirai, *J. Appl. Phys.* **2005**, *97*, 093712.

[55] C. Recknagel, N. Reinfried, P. Höhn, W. Schnelle, H. Rosner, Y. Grin, A. Leithe-Jasper, *Sci. Tech. Adv. Mater.* **2007**, *8*, 357–363.

[56] V. Trivedi, M. Battabyal, P. Balasubramanian, G. M. Muralikrishna, P. K. Jain, R. Gopalan, *Sustain. Energ. Fuels* **2018**, *2*, 2687–2697.

[57] L. Guo, G. Wang, K. Peng, Y. Yan, X. Tang, M. Zeng, J. Dai, G. Wangand, X. Zhou, *Scipta Mater.* **2016**, *116*, 26–30.

[58] S. Lee, K. H. Lee, Y.-M. Kim, H. S. Kim, G. J. Snyder, S. Baik, S. W. Kim, *Acta. Mater.* **2018**, *142*, 8–17.

[59] M. S. Toprak, C. Stiewe, D. Platzek, S. Williams, L. Bertini, E. Müller, C. Gatti,

Y. Zang, M. Rowe, M. Muhammed, *Adv. Funct. Mater.* **2004**, *14*, 1189–1196.

[60] Y. Li, C. Li, B. Wang, W. Li, P. Che, *J. Alloys Compd.* **2019**, *772*, 770–774.

[61] E. Godlewska, K. Mars, K. Zawadzka, *J. Solid State Chem.* **2012**, *193*, 109–113.

[62] L. Kong, X. Jia, Y. Zhang, B. Sun, B. Liu, H. Liu, C. Wang, B. Liu, J. Chen, H. Ma, *J. Alloys Compd.* **2018**, *734*, 36–42.

[63] L. Deng, J. Ni, L. Wang, X. Jia, J. Qin, B. Liu, *J. Alloys Compd.* **2017**, *712*, 477–481.

[64] G. Rogl, A. Grytsiv, R. Anbalagan, J. Bursik, M. Kerber, E. Schafler, M. Zehetbauer, E. Bauer, P. Rogl, *Acta Mater.* **2018**, *159*, 352–363.

[65] F. Gucci, T. G. Saunders, M. J. Reece, *Scripta Mater.* **2018**, *157*, 58–61.

[66] H. Okamoto, *J Phase Equilib.* **1991**, *12*, 244–245.

[67] Z. He, D. Platzek, C. Stiewe, H. Chen, G. Karpinski, E. Müller, *J. Alloys Compd.* **2007**, *438*, 303–309.

[68] Y. Arita, S. Mitsuda, T. Matsui, *J. Therm. Anal. Calorim.* **2002**, *69*, 821–830.

[69] G. Alekseeva, V. Zaitsev, A. Petrov, V. Tarasov, M. Fedorov, *Sov. Phys. Solid State* **1981**, *23*, 1685.

[70] Y. Ohishi, A. Mohamad, Y. Miyazaki, H. Muta, K. Kurosaki, S. Yamanaka, *J. Phys. Chem. Solids* **2015**, *87*, 153–157.

[71] A. Nozariasbmarz, A. Agarwal, Z. A. Coutant, M. J. Hall, J. Liu, R. Liu, A. Malhotra, P. Norouzzadeh, M. C. Öztürk, V. P. Ramesh, Y. Sargolzaeiaval, F. Suarez, D. Vashaee, *Jpn. J. Appl. Phys.* **2017**, *56*, 05DA04.

[72] W.-D. Liu, Z.-G. Chen, , J. Zou, *Adv. Energy Mater.* **2018**, *8*, 1800056.

[73] Y. Miyazaki, D. Igarashi, K. Hayashi, T. Kajitani, K. Yubuta, *Phys. Rev. B* **2008**, *78*, 214104.

[74] H. Yamane, T. Yamada, *J. Alloys Compd.* **2009**, *476*, 282–287.

[75] Y. Zheng, A. Taccoen, J. F. Petroff, *J. Appl. Cryst.* **1992**, *25*, 122–128.

[76] S. Vivès, C. Navone, E. Gaudin, S. Gorsse, *J. Mater. Sci.* **2017**, *52*, 12826–12833.

[77] O. Kubaschewski, *Phase Diagram of Binary Iron Alloys* **1993**, 380.

[78] Y. Miyazaki, H. Hamada, K. Hayashi, K. Yubuta, *J. Electron. Mater* **2017**, *46*, 2705.

[79] G. Skomedal, L. Holmgren, H. Middleton, I. Eremin, G. Isachenko, M. Jaegle, K. Tarantik, N. Vlachos, M. Manoli, T. Kyratsi, D. Berthebaud, N. Y. D. Truong, F. Gascoin, *Energy Convers. Manag.* **2016**, *110*, 13–21.

[80] Y. Thimont, Q. Lognoné, C. Goupil, F. Gascoin, E. Guilmeau, *J. Electron.*

Matter. **2014**, *43*, 2023–2028.

[81] K. S. Y. Saiga and, S. Deng, T. Yamamoto, Y. Kono, N. Ohya, T. Takabatake, *J. Alloys Compd.* **2010**, *507*, 1–5.

[82] Y. Saiga, B. Du, S. Deng, K. Kajisa, T. Takabatake, *J. Alloys Compd.* **2012**, *537*, 303–307.

[83] Y. Yan, X. Tang, P. Li, Q. Zhang, *J. Electron. Mater.* **2009**, *38*, 1278–1281.

[84] H. Anno, H. Yamada, T. Nakabayashi, M. Hokazono, R. Shirataki, *J. Solid State Chem.* **2012**, *193*, 94–104.

[85] G. S. Nolas, *Springer, Series in Materials Science* **2014**, *199*.

[86] Z. Xing, J. Lu, X. Ji, *Small Methods* **2018**, *2*, 1800062.

[87] N. Krishnamurthy, C. K. Gupta, *Extractive Metallurgy Of Rare Earth* **2016**.

[88] N. N. Greenwood, A. Earnshaw, *Chemie der Elemente* **1988**.

[89] F. Wöhler, *Annalen der Physik und Chemie* **1828**, *89*, 577–582.

[90] G. Flusin, *La Houille blanche* **1911**, 263–271.

[91] H. Goldschmidt, *Deutsche Reichs Patent no. 96317* **1895**.

[92] W. Kroll, *Z. Anorg. Allg. Chem.* **1940**, *234*, 42–50.

[93] F. H. Spedding, H. A. Wilhelm, W. H. Keller, *Patent US no. 2,830,894* **1947**.

[94] W. Klemm, H. Bommer, *Z. Anorg. Allg. Chem.* **1937**, *231*, 138–171.

[95] H. J. T. Ellingham, *J. Soc. Chem. Ind.* **1944**, *65*, 125.

[96] C. Herget, *Proc. 8th International Workshop on Rare Earth Magnets and their Applications,* **1985**, 407–422.

[97] World Steel Association, *Steel Statistical Yearbook 2018* **2018**, 15–16.

[98] *http://www.societechimiquedefrance.fr.*

[99] P. K. Samal, J. W. Newkirk, *ASM Handbook, Volume 7: Powder Metallurgy* **2015**.

[100] T. H. Okabe, T. Oda, Y. Mitsuda, *J. Alloys Compd.* **2004**, *364*, 156–163.

[101] H. Nersisyan, H. Won, C. Won, A. Joc, J. Kim, *Chem Eng J* **2014**, *235*, 67–74.

[102] C. Won, H. Nersisyan, H. Won, *Chem. Eng. J.* **2010**, *157*, 270–275.

[103] B. Yuan, T. H. Okabe, *J. Alloy Compd.* **2007**, *443*, 71–80.

[104] T. H. Okabe, N. Sato, Y. Mitsuda, S. Ono, *Mater. Trans.* **2003**, *44*, 2646–2653.

[105] B. Yuan, T. H. Okabe, *J. Alloy Compd.* **2008**, *454*, 185–193.

[106] K. Choi, H. Choi, H. Na, I. Sohn, *Mater. Lett.* **2016**, *183*, 151–155.

[107] D.-W. Lee, S.-H. Heoa, J.-T. Yeom, J.-P. Wang, *J. Kor. Powd. Met. Inst.*

2013, *20*, 43–47.

[108] A. Miyauchi, T. H. Okabe, *Mater. Trans.* **2010**, *51*, 1102–1108.

[109] G. Champion, J. Allenou, M. Pasturel, H. Noël, F. Charollais, M. Anselmet, X. Iltis, O. Tougait, *Adv. Eng. Mater.* **2013**, *15*, 257.

[110] G. Giresan, S. R. Sankaranarayanan, B. L. J, *J. Min. Metall. Sect. B-Metall.* **2016**, *52*, 171–175.

[111] M. L. Snedaker, Y. Zhang, C. S. Birkel, H. Wang, T. Day, Y. Shi, X. Ji, S. Kraemer, C. E. Mills, A. Moosazadeh, M. Moskovits, G. J. Snyder, G. D. Stucky, *Chem. Mater.* **2013**, *25*, 4867–4873.

[112] M. Aksu, E. Aydin, *J. Ceram. Process. Res.* **2013**, *14*, 4–7.

[113] L. Bai, Y. Wang, H. Chen, F. Yuan, *Cryst. Res. Technol.* **2016**, *51*, 428–432.

[114] D. Ağaoğullari, Özge Balci, M. L. Öveçoğlu, I. Duman, *Kona Powder Part J.* **2016**, *33*, 203–218.

[115] H. Zhao, B. Cao, S. Li, N. Liu, J. Shen, S. Li, J. Jian, L. Gu, Y. Pei, G. J. Snyder, Z. Ren, X. Chen, *Adv. Energy Mater.* **2017**, *1*, 713.

[116] M. Jalaly, M. Tamizifar, M. S. Bafghi, F. Gotor, *J. Alloys Compd.* **2013**, *81*, 782–787.

[117] S. Sen, N. Gogurla, P. Banerji, P. K. Guha, P. Pramanik, *Mater. Sci. Eng. B* **2015**, *200*, 28–39.

[118] S. Sen, P. K. Guha, P. Banerji, P. Pramanik, *RSC Adv.* **2016**, *6*, 68238.

[119] T. Ohkubo, T. Ono, K. Nishiyama, S. Niwa, H. Sakai, M. Koishi, M. Abe, *J. Jpn Soc. Powder Powder Metallurgy* **2005**, *52*, 664–669.

[120] K. Nishiyama, T. Nakamur, S. Utsumi, H. Sakai, M. Abe, *J. Phys.: Conf. Ser.* **2009**, *176*, 012043.

[121] W.-Y. Tsai, P.-C. Gao, P.-L. T. Barbara Daffos, C. R. Pérez, Y. Gogotsi, F. Favier, P. Simon, *Electrochem. Commun.* **2013**, *34*, 109–112.

[122] M. Zakeri, R. Yazdani-Rad, M. Enayati, M. Rahimipour, I. Mobasherpour, *J. Alloys Compd.* **2007**, *430*, 170–174.

[123] K. Choi, K. H. Lee, B. Ali, S.-H. Choi, K.-T. Park, I. Sohn, *Met. Mater. Int., Vol.* **2017**, *23*, 1037–1044.

[124] Z. Li, K. Yasuda, K. Itagaki, *J. Alloys Compd.* **1993**, *193*, 26–28.

[125] S. Aydinyan, H. Kirakosyan, S. Kharatyan, *Int. J. Refract. Met. H.* **2016**, *54*, 455–463.

[126] C. Herget, *Met. Powder. Rep.* **1982**, 34–36.

Part II

Experimentals

1 Magnesioreduction synthesis

The magnesioreduction syntheses were realized in molybdenum crucibles which are unreactive toward Mg. Molybdenum reactors are conventionally arc-welded sealed and break opened at the end of the reaction. This process is costly and the arc-welding is difficult to realize without partially evaporating Mg. Instead, a home-made clamping system was developed which keeps the reactor tightly closed with a lid (fig. 23a,b). In this way, the expensive Mo crucibles can be reused and the simplicity of the system considerably facilitated the synthesis preparation. The clamping system is made of refractory steel and consists in pressing the crucible and the lid between two blocks being hold tight with a screw. A graphite ring is used as a seal between the lid and the body of the crucible. Notice that carbides were never detected in the final products, highlighting the minor carbon contamination during the heat treatment using this set-up.

For the heat treatments, the crucible is placed at the bottom of an Inconel tube (fig. 23c). The pressure in the tube can be controlled during the synthesis by using the valves and the manometer placed on the top of the tube. Three vacuum/Ar purging cycles are performed and the tube is left under a small Ar over pressure (≈ 1.2 bar). The reaction is carried out under Ar atmosphere to prevent the molybdenum oxidation. The different thermal expansion coefficients of the materials constituting the reaction set-up allows maximum temperature of about 1323 K. The tube is heated along with the crucible and clamping system in a tubular furnace (fig. 23d). At the end of the reaction, the clamping system is unscrewed and the products can be easily recovered inside the crucible. The crucibles are washed with diluted hydrochloric acid (≈ 5 wt.%) and several times with distilled water, scoured using SiC polishing paper, sonicated in ethanol and dried in an oven.

Magnesioreduction products may contain MgO by-product which needs to be removed. This is realized by soaking the powder in diluted hydrochloric acid in order to dissolve MgO according to:

$$\mathrm{MgO\,(s)} + 2\,\mathrm{H^+(aq)} \longrightarrow \mathrm{Mg^{2+}(aq)} + \mathrm{H_2O\,(l)} \tag{49}$$

The slurry is sonicated several minutes and then centrifuged using a Hettich Rotofix 32 A apparatus. This process is repeated several times. Eventually, the powder is washed three times only with distilled water and once more with ethanol before being dried at about 363 K for several hours. Details of the MR syntheses will be given independently for each material in the following chapters.

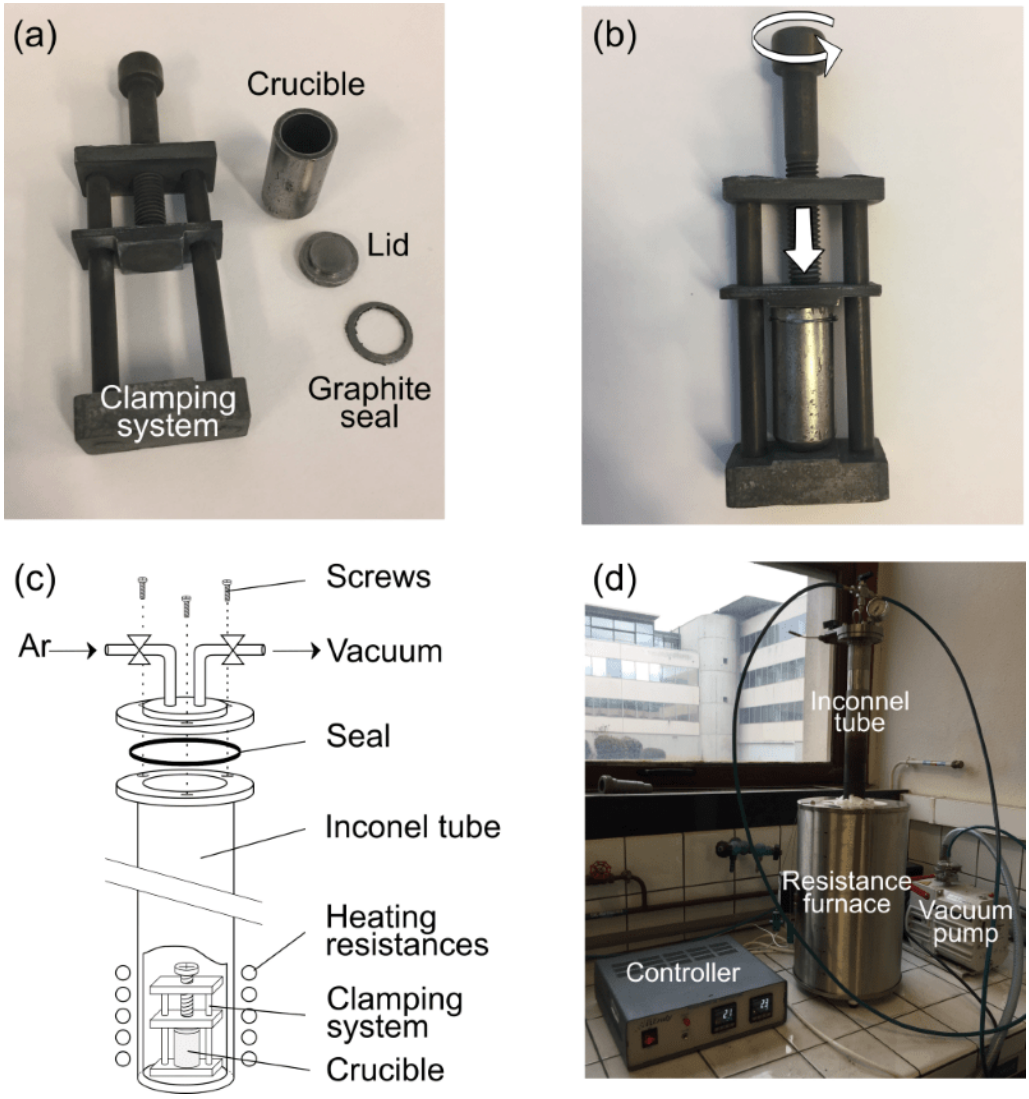

Figure 23: (a) Picture of the dismantled magnesioreduction reaction set-up. (b) Picture of the crucible locked in the clamping system. (c) Schematic representation of the Inconel reactor. (d) Picture of the whole experimental set-up.

2 Spark plasma sintering

Powders are directly obtained by magnesioreduction syntheses. Bulk materials suitable for thermoelectric characterizations have been obtained after densification by the spark plasma sintering (SPS) method. The set-up of the technique is illustrated in fig. 24. The powder is placed in a graphite die between two graphite punches. All the surfaces in contact with the powder are covered with 200 μm-thick carbon foil (Papyex ®) to facilitate the unmoulding and prevent the contamination of the mould by the proceed powder. A pulsed DC current and an uniaxial mechanical pressure (40 - 80 MPa) are applied during the sintering. The current with high intensity (up to 6 kA) crossing the matrix induces the self-heating Joule effect. For electrically conducting materials, the current is flowing through the powder and concentrate at the localized contacts between the powder particles inducing local overheat and accelerated diffusion of matter. The hypothetical formation of 'sparks'

and 'plasma' that are supposedly occurring in the voids between the particles during the process would further accelerate the densification process. Direct evidences of 'sparks' have however never been observed experimentally.[1] In the case of electrical insulators, the current is only crossing the graphite mould and the heat is transferred to the powder by classical diffusion routes. The SPS method enables much faster heating/cooling ramps (100 K min^{-1}) than conventional 'hot-pressing' methods due to the direct heating of the mould and powder. Consequently, faster sintering treatment (typically from 3 to 30 min during this study) and limited grain growth can be achieved. The later is of uttermost importance when considering the fabrication of densified nanostructured materials. The sintering condition were optimized to obtain materials with the highest possible density in order to favor good electrical resistivity. For my experimental work, a FCT HP-D-10 apparatus and Ø 10 mm graphite dies were used to densify the samples.

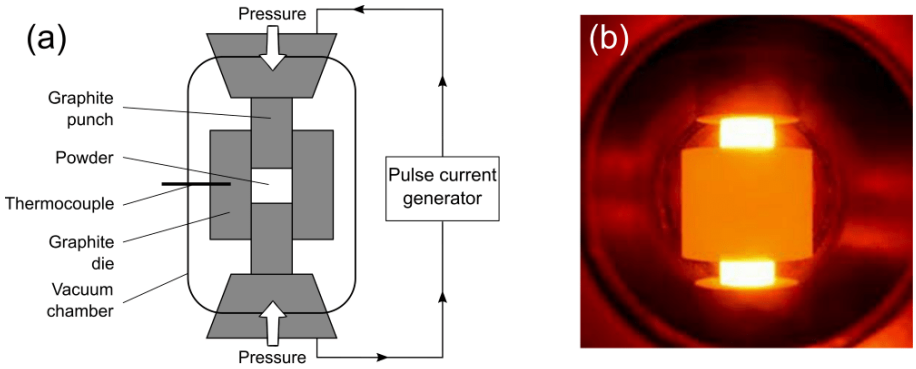

Figure 24: (a) Schematic set-up of the spark plasma sintering method. (b) Picture of the graphite die during the sintering.

3 Powder X-ray diffraction

X-ray diffraction (XRD) is a powerful technique to analyze the crystal (micro)structure and the purity of powders.[2] The powders obtained by magnesioreduction are composed of well-crystallized crystallites which are well-adapted to this technique. All analysed samples were considered as being composed of an infinite number of randomly oriented crystallites. For a given phase, the position 2θ of the hkl reflection is related to the interplanar distance d_{hkl} within the crystal structure and the wavelength λ by the Bragg relation:

$$\lambda = 2\, d_{hkl}\, sin(\theta) \tag{50}$$

Knowing the *hkl* indexing and diffraction angles for a set of reflections, it is possible to determine the lattice group symmetry and the lattice constants of a crystal.

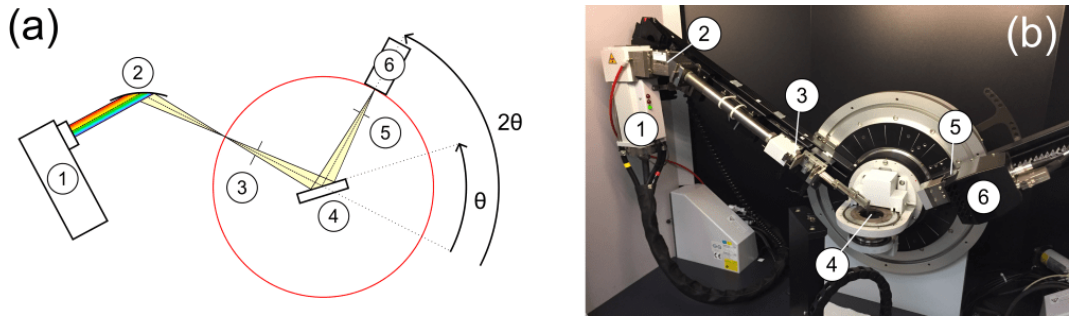

Figure 25: (a) Schematic representation of a X-ray diffractometer goniometer in the modified Bragg-Brentano geometry. (b) Picture of the Bruker D8 Advance diffractometer. The main components are (1) Cu X-ray tube, (2) curved Ge(111) monochromator, (3) divergence slits, (4) sample, (5) divergence slit and (6) detector.

For all the materials studied in this work, the structure was already known and the space group and atomic positions could be found in the literature.

The Le Bail method enables the refinement of the lattice constants without taking the atomic positions into consideration. For this, a model is refined by the least squares method to fit to the experimental data. The reflection intensities are determined by integration and set as constants. For the modeling, the peaks shapes are described using the Thompson-Cox-Hastings function which is a linear combination of a Lorentzian (L) and a Gaussian (G) peak each characterized by their respective full width at half maximum (FWHM). The FWHM_L and FWHM_G and their dependence with 2θ is described using the following relations:

$$FWHM_G^2 = U\,tan(\theta)^2 + V\,tan(\theta) + W + \frac{I_G}{cos^2\theta} \tag{51}$$

$$FWHM_L = X\,tan(\theta) + \frac{Y}{cos(\theta)} \tag{52}$$

where the coefficients U, V, W, I_G, X and Y are refined during the procedure. The 2θ dependence of the FWHM gives information about the origin of the peak broadening which can be lattice distortion ($\tan(\theta)$ dependence) or size effect ($1/\cos(\theta)$ dependence). The background was removed using a manually selected set of points. The effect of the sample height displacement on the positions of the diffraction peak was also taken into account using a constant. The quality of the fit can be estimated using reliability factors. For a pattern composed of N data points, two of them are:

$$\chi^2 = \frac{1}{N}\sum_{i=0}^{N}\frac{(y_{C,i}-y_{O,i})^2}{\sigma^2[y_{O,i}]} \qquad \text{and} \qquad R_{wp} = \frac{\sum_{i=0}^{N}(y_{C,i}-y_{O,i})^2}{\sum_{i=0}^{N} w_i (y_{O,i})^2} \tag{53}$$

where $y_{C,i}$ and $y_{O,i}$ are the computed and observed intensity values for the i^{th} data point, respectively, and $w_i = \frac{1}{\sigma[y_{O,i}]^2}$ a weighing factor with $\sigma[y_{O,i}]$ the standard deviation considered as $\sqrt{y_{O,i}}$.

The intensity *I(hkl)* of the reflection *hkl* is proportional to the square of the structure factor norm $|\boldsymbol{F}(hkl)|$ which corresponds to the Fourier transform of the electronic density of the crystal. For a unit cell containing n atoms, $\boldsymbol{F}(hkl)$ can be computed by the relation:

$$\boldsymbol{F}(hkl) \;=\; \sum_{j=1}^{n} g^j\, t^j(s)\, f^j(s)\, exp[2\pi i(hx^j + ky^j + lz^j)] \tag{54}$$

where g^j is the occupancy factor, $t^j(s)$ is the isotropic atomic displacement parameters, $f^j(s)$ is the diffusion factor with the norm of diffusion vector $s = \sin\theta/\lambda$ and x^j, y^j, z^j the relative coordinates of the atom j in the unit cell. The refined parameters were the same as for Le Bail refinement in addition of the scale factor, the atomic positions and the atomic displacement parameters. The Rietveld method is used to refined a structural model by fitting the whole experimental pattern. The procedure is similar to the Le Bail method except that *I(hkl)* is computed from $\boldsymbol{F}(hkl)$ according to:

$$I(hkl) \;=\; S\, N\, L\, |\boldsymbol{F}(hkl)|^2 \tag{55}$$

where S is the scale factor, N is the multiplicity of the reflection (determined by the crystal space group) and L is the Lorentz-Polarization factor. It is possible to perform phase quantification using the Rietveld method by considering the relative scale factors obtained for the different constituting phases. From these refinements the reaction mechanism have been identified by quantifying the phases in the sample at different times of the reaction.

The diffractometer used during my thesis was a Bruker D8 Advance equipped with a Cu X-ray tube and a curved Ge (111) monochromator selecting the Cu-$K_{\alpha 1}$ wavelength (λ = 1.54059 Å). The diffractometer is working in the modified Bragg-Brentano θ - 2θ geometry enabling the collection of the diffracted intensities over a large 2θ angular range (fig. 25a,b). The Co and Fe fluorescence signals were filtered

directly by the Bruker LynxEye fast detector. The XRD patterns (diffracted intensities *vs.* 2θ) were analyzed with the PowderCell software[3] for phase identification and with the FullProf Suite for conventional data modelization.[4] In the particular cases of HMS which is a composite crystal, the lattice and structural parameters were refined using a 3D+1 approach as described by Miyazaki *et al.*[5] with the software JANA2006[6]. The presence of stacking faults in β-$FeSi_2$ was reported in the literature[7] and leads to large broadening and displacement of some diffraction peaks. The stacking faults probabilities were refined by modelling the diffraction patterns using a Rietveld-like approach and the software FAULTS[8].

4 Electron microscopies

The principle of the electron microscopies is the observation and characterization of samples through the interaction with a high-energy electron beam. The short wavelength of the electrons ($\lambda = 0.027$ Å for an acceleration voltage of 200 kV) permit magnified imaging down to the atomic scale. In addition, secondary emissions resulting from by the electrons/matter interactions make numerous other structural, physical and chemical characterizations possible. Electronic microscopies can be realized in two operating modes: scanning (Scanning Electron Microscopy, SEM) or transmission mode (Transmission Electron Microscopy, TEM).

4.1 Scanning electron microscopy

SEM analyses aim at characterizing bulk samples by using secondary electrons (SE), backscattered electrons (BSE) and characteristic X-ray emitted near the surface.[9] Each of these different emissions gives complementary information about the sample characteristics. All SEM analyses are performed by scanning the selected area with a focused electron beam accelerated between 5 and 30 kV. The resolution is limited by the size of the interaction volume which corresponds to the volume of material producing the electron or X-ray emissions (fig. 26a). This volume strongly depends on the beam acceleration voltage and intensity, sample chemical composition, microscope optics and the types of emission considered. During my thesis, SEM analyses were realized using a JEOL JSM 7100F microscope equipped with a field-emission electron gun (FEG), an Oxford EDS SDD X-Max spectrometer and an EBSD HKL Advanced Nordlys Nano detector (fig. 26b).

Imaging with secondary electrons SE are low energy electrons (E < 50 eV) produced from inelastic interactions between the incident beam and valence electrons. They cannot easily escape from the surface due to their low energies and the interaction volume is consequently small ($\approx$ nm^3). Lateral resolution down to

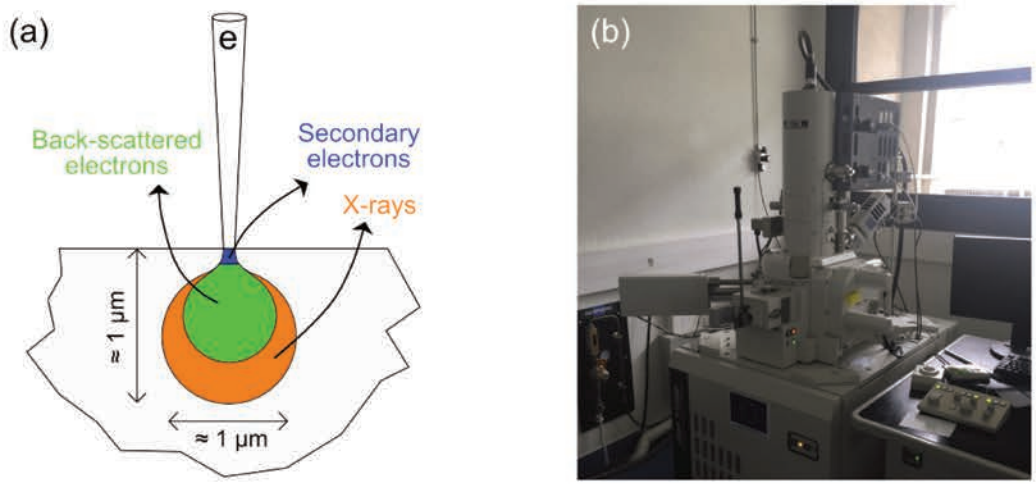

Figure 26: (a) Schematic representation of the interaction volume for secondary electron (SE, blue), backscattered electrons (BSE, green) and X-rays (orange). (b) Picture of the JEOL JSM 7100F scanning electron microscope used during my PhD work.

0.5 nm can be achieved with acceleration voltage of 5 - 10 kV. The SE emission rate is strongly dependent on the incident beam angle. For these reasons, they are used to realize high resolution images of the sample topography. However, they give no information on the chemical composition. Secondary electrons were notably used for the determination of the average grain size on loose powders and densified pellet cross-sections.

Imaging with back scattered electrons Electrons from the incident beam can be reflected or back scattered out of the surface by elastic interactions with the nuclei of atoms constituting the sample. Consequently, BSE interact much more strongly with heavy than light elements. They are used for the realization of chemically resolved images. They are much more energetic than SE and the interaction volume is consequently much bigger. Imaging lateral resolution varies from about 0.5 to 5 μm depending on the acceleration voltage (typically 20 - 30 kV) and the sample composition. Lower voltages and heavier chemical elements favor higher resolutions. BSE images were mostly used to evaluate the chemical homogeneity at the surface of a pellet.

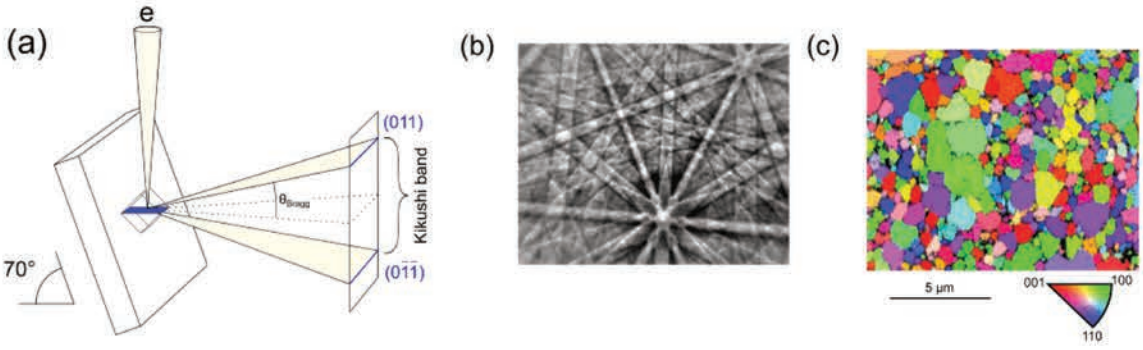

Figure 27: (a) Schematic representation of the EBSD principle. (b) Kikuchi diffraction pattern. (c) EBSD maps.

Electron Back Scattered Diffraction (EBSD) In Bragg condition, BSE can be diffracted by the crystal lattices. The principle of the EBSD method is presented in fig. 27a. The sample is tilted at an angle of 70° relatively to the incident beam to maximize the diffracted intensity and the diffraction pattern is collected using a CCD detector. Diffraction on the crystallographic planes results in the formation of two cones hkl and $\bar{h}\bar{k}\bar{l}$ with large openings due to the short wavelength of the electrons. Their intersections with the detector form Kikuchi bands as shown in fig. 27b. The indexing of these patterns using the crystallographic data of the phase in presence enables the determination of the crystal orientation. EBSD maps of the sample surface are obtained by scanning the area of interest and indexing the diffraction patterns for each pixel of the image (27c). The orientation of each crystal relatively to the normal surface is represented using a color code and an inverse pole figure. The interaction volume participating in the formation of the diffraction pattern is relatively small and spacial resolution down to about 50 nm can be achieved for acceleration voltage of 20 kV. The quality of the maps greatly depends on the preparation of the sample surface which must be mirror polished and free of oxide or amorphous layer. EBSD is a powerful tool to investigate the microstructural characteristic such as crystal size distribution, texturation, and defects density of bulk specimens. All data analyses were performed using the *Channel 5* software (HKL technology).

Energy Dispersive Spectroscopy (EDS) analyses The incident beam are energetic enough to expel core electrons from the sample atoms. Outer-shell electrons will then fill the created holes. This desexcitation is accompanied by the emission of X-ray with wavelength corresponding to the transition energies. The latter are characteristic of each element. The EDS method consists in analyzing the peaks of the X-ray fluorescence spectrum to (i) identify the elements in presence and (ii) determine the sample chemical composition. Indeed, quantitative analyses with a reasonable precision ($\approx$ 1 %) are possible using the corrective 'ZAF' method for elements with Z > 11. The interaction volume is relatively large ($\approx$ 1 μm^3) which strongly limits the lateral resolution of the technique. Acceleration voltages as high as 20 - 30 kV are typically required to excite the core electrons of the majority of the elements. The sample surface must be flat and well polished for performing accurate quantitative analyses.

4.2 Transmission electron microscopy

TEM analyses are realized by using a transmitted electron beam (fig. 28a).[10] Analyses are only possible if a substantial part of the incident beam manage to go through the sample without being adsorbed. This is generally achieved for specimen thinner than about 100 nm. The advantages of this technique are the extremely high

resolution (down to 0.5 - 2 Å, depending on the microscope resolution) enabling lattice-resolution imaging and the possibility to realize local electron diffraction. In the field of thermoelectrics, TEM are extensively used for microstructural characterizations at the micro- and nanometer scale to study grain sizes, defects or nanoprecipitates. TEM analyses were performed on a JEOL 2100 LaB_6 microscope operating at 200 kV (resolution 2.3 Å) and equipped with a high resolution Gatan US100 and an Orius SC 200D cameras (fig. 28b).

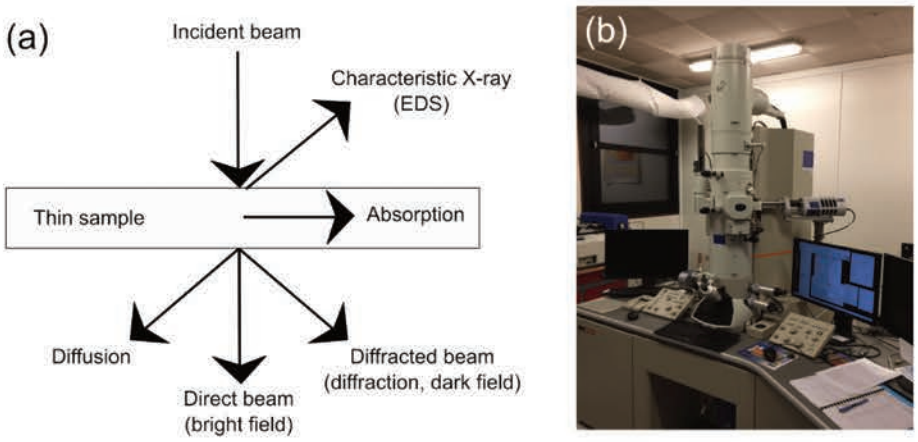

Figure 28: (a) Various signals generated by the interaction of the incident electron beam with thin specimen. (b) Picture of the JEOL 2100 LaB_6 TEM.

Electron diffraction Selected area electron diffraction can be realized on areas as small as few hundreds of nm^2. The diffraction condition is easily visualized with the Ewald sphere concept. Typical acceleration voltages are around 200 kV for conventional TEM which represents a wavelength of about 0.025 Å. The diameter of the Ewald sphere ($1/\lambda$) is thus extremely large and electron diffraction pattern can be seen as a cross-section of the crystal reciprocal space. The crystal symmetry and lattice constants can be readily determined from diffraction patterns taken along particular crystallographic directions. The reflection intensities are however subject to multiple scattering phenomena and cannot be used as-is. Electron diffraction is commonly used for studying faulty layered structure (diffuse streaks) or complex modulated structure (weak satellite reflections).

Imaging TEM images can be realized in brightfield mode using only the direct beam to form the image or in darkfield mode using diffracted beams. Contrasts in brightfield mode come from the scattering and absorption of the incident beam by the sample. Thicker areas of the sample or crystals in diffraction condition appears darker in this mode. Brightfield is the most common imaging mode because of its high luminosity which makes observations easier. In darkfield mode on the contrary, only the area in diffraction condition appears bright on the image while the

rest remains dark. High resolution mode is dedicated to the imaging of the lattice structure of the sample, depending on the resolution of the microscope.

EDS method Similarly to SEM, elemental EDS analyses can also be performed in the TEM. In the case of TEM samples, the interaction volume of the electrons is limited by the thickness of the sample which is much smaller than 1 μm. As a result, EDS lateral resolution is much higher for TEM than SEM.

5 Thermoelectric properties measurement

The figure-of-merit ZT is related to the thermoelectric performances of materials. It can be measured directly using the Harman method[11] but the measurement is difficult to realize and subject to large standard deviation and systematic errors especially at high temperatures.[12] Therefore, it is more common to individually measure ρ, α and κ and then calculated ZT from:

$$ZT = \frac{\alpha^2}{\rho\,\kappa}\,T \tag{56}$$

In addition, a better comprehension of the materials properties and more reliable comparison with literature results is possible from the knowledge of the individual parameters.

5.1 Electrical resistivity measurements

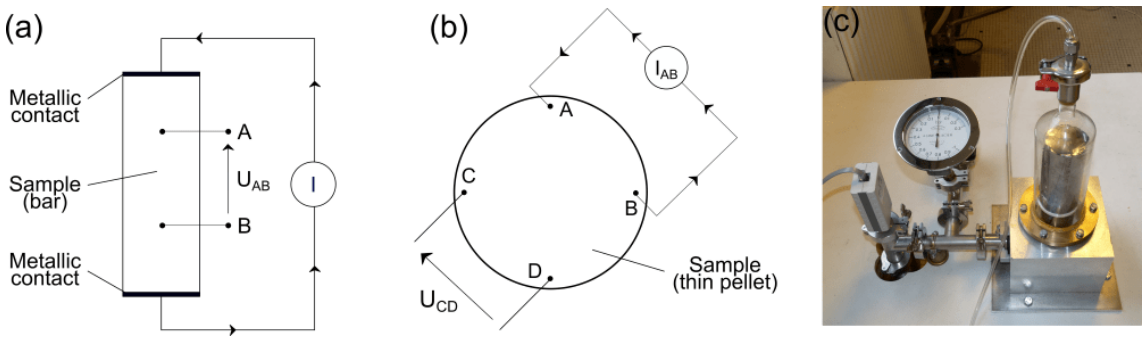

Figure 29: Schematic principle of (a) the 4-probes method and (b) the Van der Pauw method for the measurement of the electrical resistivity of densified samples with bar and pellet shapes, respectively. (c) Picture of the home-made apparatus used for the measurement of the electrical resistivity and Seebeck coefficient of skutterudites samples.

Two probes electrical resistivity measurement gives biased results because of the electric contact resistances. Two types of measurement methods were performed

during my thesis: the 4-probes and the Van der Pauw methods. The schematic set-up of the 4-probes method is presented in fig. 29a. It consists in applying an electrical current I [A] through a bar-shaped sample with known cross-section X [m^2]. The resistivity can be calculated from the voltage drop U_{AB} [V] measured between two probes spaced by a distance l [m] from the relation:

$$\rho = \frac{U_{AB}\, X}{I\, l} \tag{57}$$

This method was used for the measurements of the silicides at NIMS, Japan using a ZEM3 device which was also used for the Seebeck coefficient measurement. It is thus described in more details in the next section.

The electrical resistivity of the skutterudites were measured by the Van der Pauw method[13] using an home-made apparatus shown in fig. 29c and described in more details in ref.[14]. Four probes (A,B,C,D) are placed at the periphery of a pellet-shaped sample with thickness h and diameter D (fig. 29b). The resistance $R_{AB,CD} = U_{CD}/I_{AB}$ is obtained by injecting a current I_{AB} through A and B and measuring the voltage-drop U_{CD} between C and D. Similarly, $R_{AC,BD}$ is obtained from U_{BD} and I_{AC}. The resistivity of the material can be calculated from the relation:

$$\rho = \frac{\pi \cdot h}{\ln 2} \cdot \frac{R_{AB,CD} + R_{AC,BD}}{2} \cdot f \tag{58}$$

where the correcting factor $f \approx 1$ if $R_{AB,CD}/R_{AC,BD} < 2.5$. Accurate values are only obtained for pellets with $h \leq D/2$.[15] The shape of the sample and the spacing between the contacts do not need to be known accurately for using this method.

Whatever the method used, the sample must be measured in isothermal conditions in order to avoid the appearance of Seebeck voltage that could cause a bias in the measurement. For example, thermal gradient caused by Joule heat at the contacts can be removed by measuring twice with current flowing in opposite directions and taking into account the average value. The measurement of thermoelectric materials with large α is problematic since the current will induce large Peltier heat violating the isothermal conditions. The solution consists in measuring the voltage drop rapidly after application of the current (< 1 s). In this way, the Peltier effect contribution, which takes few seconds to become substantial due to relatively slow heat diffusion, is not taken into account in the measurement.

5.2 Seebeck coefficient measurement

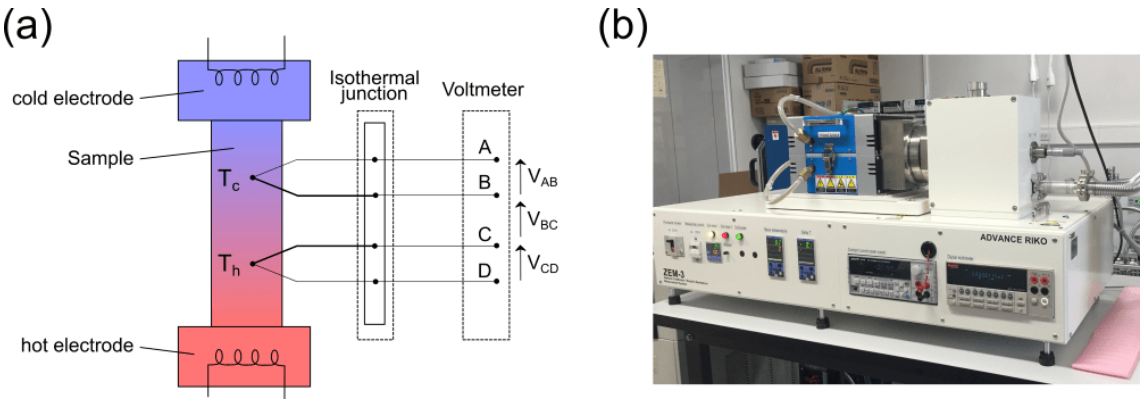

Figure 30: (a) Schematic set-up of the Seebeck coefficient measurement. The thick lines represent the thermocouple legs made of the reference metal. (b) Picture of the ZEM3 device used for the measurement of the electrical resistivity and Seebeck coefficient of the transition metal silicides.

As shown is chapter 1.1, a material placed in a thermal gradient generates a Seebeck voltage. The set-up of the Seebeck coefficient measurement is shown in fig. 30. The sample in the form of a bar is hold between two electrodes and two thermocouples are pressed on the bar. The two electrodes are heated differently by resistances so as to create a controlled thermal gradient in the material. The thermocouples measure, simultaneously, the materials temperature (T_c and T_h are given by V_{AB} and V_{CD}, respectively) and the Seebeck voltage (V_{BC}). The Seebeck coefficient can be calculated for the temperature $\bar{T} = (T_h - T_c)/2$ by:

$$-(\alpha(T) - \alpha_{ref}(T)) = \frac{V}{T_h - T_c} \tag{59}$$

For each temperature, the measurements are usually performed three times with different ΔT. This method does not directly give the absolute α since it is necessary to know α_{ref} of the reference metal constituting one side of the thermocouples. The absolute Seebeck coefficient for some metals have been determined from the measurement of the Thomson coefficient down to few K and using the 2^{nd} Kelvin relation.[16–18] In this way, an absolute scale could be established and serve as references for all measurements.

During my thesis, two types of devices were used for the Seebeck coefficient measurements. For skutterudites samples, the measurements were realized at ICMPE

(Thiais) under vacuum using the same home-made apparatus as for resistivity measurement and shown in fig. 29c.[14]. For the silicides samples, the Seebeck coefficients were measured at NIMS (Tsukuba, Japon) simultaneously to the electrical resistivity using the ZEM3 device under He atmosphere (Fig. 30b).

5.3 Thermal conductivity measurement

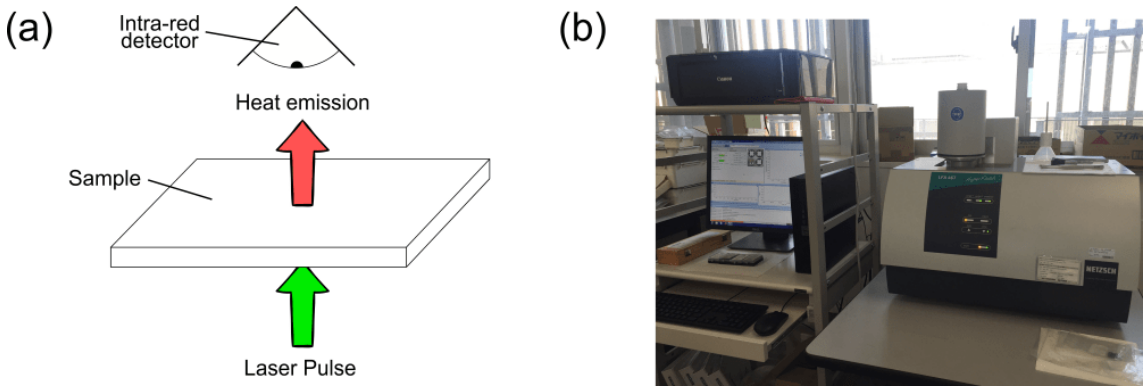

Figure 31: (a) Schematic representation of the LFA method used for thermal diffusivity measurements. (b) Picture of a Netzsch LFA 467 device.

The direct measurement of thermal conductivity is a difficult task at high temperature. For this reason, κ [W m^{-1} K^{-1}] is usually calculated from the thermal diffusivity D [m^2 s^{-1}] by:

$$\kappa = D\, C_p\, d \tag{60}$$

where C_p [J kg^{-1} K^{-1}] is the specific heat and d the density [kg m^{-3}] of the sample. The laser flash analysis (LFA) method is widely used to measure the thermal diffusivity of materials above room temperature. The principle of the LFA method is illustrated in fig. 31a. The sample in the shape of a pellet is placed inside a furnace under protective atmosphere and is irradiated by an energetic laser pulse (impulsion $<$ 1 ms) inducing an increase of the sample temperature. The time dependence of the sample temperature on the opposite side of the pellet is recorded with an infrared detector. After reaching a maximum just after the irradiation, the temperature slowly decreases to reach thermal equilibrium with the furnace. The half-time $t_{1/2}$ is defined as the time required for the sample to reach half of the temperature peak duing this cooling stage. The thermal diffusivity at a given temperature is determined from the half time $t_{1/2}$ [s] and the sample thickness h [m] according to:

$$D = 0.1388\, \frac{h^2}{t_{\frac{1}{2}}} \tag{61}$$

The sides of the pellet need to be perfectly parallel to obtain accurate results. Prior to measurement, the sample is coated with graphite in order to maximize the heat absorption during the irradiation. During my thesis two apparatus were used to measure the diffusivity: a Netzsch LFA 457 under Ar atmosphere (fig. 31b) for skutterudite at ICMMO (Orsay) and a Netzsch LFA 467 under N_2 atmosphere for silicides at NIMS (Tsukuba, Japan).

The specific heat C_p of skutterudites was calculated using the Dulong-Petit law:

$$C_p = n\,R\,T \tag{62}$$

where n is the number of atoms per formula unit. In the case of silicides, C_p was determined from the diffusivity of a Netzsch Pyroceram reference material measured in the same conditions as the samples.

References

[1] D. M. Hulbert, A. Anders, D. V. Dudina, J. Andersson, D. Jiang, C. Unuvar, U. Anselmi-Tamburini, E. J. Lavernia, A. K. Mukherjee, *J. Appl. Phys* **2008**, *104*, 033305.

[2] V. K. Pecharsky, P. Y. Zavalij, *Fundamentals of Powder Diffraction and Structure Characterization of Materials* **2009**.

[3] W. Kraus, G. Nolze, *J. Appl. Cryst.* **1996**, *29*, 301–303.

[4] J. Rodriguez-Carvajal, *Physica B* **1993**, *192*, 55.

[5] Y. Miyazaki, D. Igarashi, K. Hayashi, T. Kajitani, K. Yubuta, *Phys. Rev. B* **2008**, *78*, 214104.

[6] V. Petříček, M. Dušek, L. Palatinus, *Z. Kristall.* **2014**, *229*, 345.

[7] Y. Zheng, A. Taccoen, J. F. Petroff, *J. Appl. Crystallogr.* **1992**, *25*, 122–128.

[8] M. Casas-Cabanas, M. Reynaud, J. Rikarte, P. Horbach, J. Rodriguez-Carvajal, *J. Appl. Cryst.* **2016**, *49*, 2259–2269.

[9] F. Brisset, *Scanning Electron Microscopy and Microanalyses* **2006**.

[10] D. B. Williams, C. B. Carter, *Transmission Electron Microscopy: A Textbook for Materials Science* **2009**.

[11] T. Harman, *J. Appl.Phys.* **1958**, *29*, 1373–1374.

[12] K. Valset, *Mater. Today Proc.* **2015**, *2*, 721–728.

[13] L. J. Van Der Pauw, *Philips Tech. Rev.* **1958**, *20*, 220.

[14] O. Rouleau, E. Alleno, *Rev. Sci. Instrum.* **2013**, *84*, 105103.

[15] C. Kasl, M. J. R. Hoch, *Rev. Sci. Instrum.* **2005**, *76*, 033907.

[16] R. B. Roberts, *Philos. Mag.* **1977**, *36*, 91.

[17] R. B. Roberts, *Philos. Mag. B* **1981**, *43*, 1123.

[18] R. B. Roberts, *Philos. Mag. B* **1985**, *52*, 1147.

Innovative synthesis of mesostructured $CoSb_3$-based skutterudites by magnesioreduction

Sylvain Le Tonquesse,[a] Éric Alleno,[b] Valérie Demange,[a] Loic Joanny,[a] Vincent Dorcet[a] Carmelo Prestipino,[a] Olivier Rouleau,[b] and Mathieu Pasturel*[a]

[a] Univ Rennes, CNRS, ISCR-UMR6226/ScanMAT-UMS2001, F-35000, Rennes, France Tel: +33-2-23-23-58-61; E-mail: mathieu.pasturel@univ-rennes1.fr

[b] *Université Paris-Est, Institut de Chimie et des Matériaux Paris-Est, UMR 7182 CNRS - UPEC, 2 rue H. Dunant, 94320 THIAIS, France*

Published in *Journal of Alloys and Compound*, **796** (2019) 176 - 184

Abstract

High purity $CoSb_3$, $Ni_{0.06}Co_{0.94}Sb_3$ and $In_{0.13}Co_4Sb_{12}$ were synthesized from oxides by magnesioreduction. This novel synthesis route to $CoSb_3$-based skutterudites directly yields highly cristalline powders with submicronic grain size. Densified mesostructured pellets with an average grain size ranging between 550 and 800 nm were obtained by spark plasma sintering. The strong phonon scattering induced by the mesostructuration leads to a lattice thermal conductivity reduction up to 25 % for $CoSb_3$ and $Ni_{0.06}Co_{0.94}Sb_3$ at 300 K without significantly degrading the electronic properties. Consequently, maximum ZT figures-of-merit of 0.09, 0.60 and 0.75 are found for $CoSb_3$, $Ni_{0.06}Co_{0.94}Sb_3$ and $In_{0.13}Co_4Sb_{12}$, respectively, showing the ability of this scalable process to reach the best performances reported in literature for these compositions at moderate temperature and annealing duration.

Introduction

Thermoelectric materials (TM) enable the direct conversion of a temperature gradient into voltage, thus offering the opportunity to directly exchange wasted heat into electricity by highly reliable solid state power generators. However, TM-based technologies are still only used in niche applications because of the low performances, high cost or complex synthesis of the currently available materials[1]. Among them, $CoSb_3$-based skutterudites have attracted great attention as promising mid-temperature TM due to their high power factor $PF = \alpha^2/\rho$ (where α is the Seebeck coefficient and ρ the electrical resistivity), good mechanical properties and relatively abundant constituting chemical elements[2–5]. However its thermal conductivity κ is high - up to 9 W m^{-1} K^{-1} at 293 K in polycristalline $CoSb_3$[6] - mainly due to the lattice (phonon) contribution κ_L and much less to the charge carrier contribution κ_e, with $\kappa = \kappa_L + \kappa_e$.

Any attempt to improve the dimensionless thermoelectric figure-of-merit ZT, defined as:

$$ZT = \frac{\alpha^2}{\rho(\kappa_L + \kappa_e)}T \tag{63}$$

in $CoSb_3$ involves (i) the optimization of PF by adjusting the carrier concentration in the semiconducting material and (ii) the reduction of κ_L. The latter can be achieved by creating phonon scattering centers at different length scales in the materials:

(i) At the atomic scale, the most common strategy consists in partially filling the icosahedral *2a* crystallographic position of skutterudite structure with heavy atoms. The low energy phonons introduced by the filler atom as well as the mass fluctuation arising from its random occupancy both scatter the heat carrying phonons resulting in a strongly reduced κ_L[7–10]. Chemical doping on the Co- or Sb-sublattice, which is necessary to achieve optimal charge carrier concentration, has also been shown to affect the thermal conductivity via the mass fluctuation phenomenon[11,12].

(ii) At the microstructural scale, grain boundaries in bulk polycrystalline materials also act as effective phonon-scattering centers[13,14]. Their effect is highly intensified in nano- or mesostructured materials where κ_L can be reduced by more than 35 % compared to identical materials with much larger grain size[15,16]. As a result, it stimulates the development of alternative synthesis routes more suitable for the production of submicronic powders than traditional melting-annealing methods, such as ball-milling / spark plasma sintering (SPS)[17,18], severe plastic deformation[19],

melt spinning[20,21], combustion synthesis[22], flash-spark plasma sintering[23], high-pressure syntheses[24,25], gas atomization[26] or solution proceed[27,28]. Improvement of ZT by this approach can only be realized if the decrease of κ is not counterbalanced by a decrease of PF due to overly enhanced electron scattering at the grain boundaries.

Phonons being more likely scattered by defects with sizes close to their wavelengths, the creation of defects at different length scales in the material, often refereed as 'all-scale hierarchical architectures', offers the possibility to scatter phonons over a broader energy spectrum, thus reducing κ more efficiently[1,29–31]. Very recently, this multi-scale approach have been successfully employed with nanostructured filled-skutterudites[32,33], porous doped-skutterudites[34,35] or formation of nanoinclusions in filled- and doped-skutterudites[36,37].

With this approach in mind, we developed the magnesioreduction synthesis of pristine, Ni-doped and In-filled $CoSb_3$ according to the reaction:

$$\frac{1}{3}\,Co_3O_4 + \frac{3}{2}\,Sb_2O_4 + \frac{22}{3}\,Mg \xrightarrow[84\,h]{810\,K} CoSb_3 + \frac{22}{3}\,MgO \tag{64}$$

This new synthesis route to $CoSb_3$-based skutterudites, inspired from industrial pyrometallurgical processes (*e.g.* Kroll's process), yields powders with submicronic grain size that can be readily used for the sintering of mesostructured densified materials[38]. It offers other advantages such as the use of air stable and cheap oxides as precursors, relatively low temperature and short reaction time compared to conventional melting/annealing synthesis, good control of the chemical composition and high yield. In this article, the structural, microstructural and thermoelectric characterizations of these materials are reported and compared to literature data on similar materials (either mesostructured or not) prepared by conventional synthesis routes.

Experimental procedures

Synthesis of $CoSb_3$ by magnesioreduction

The first step of the synthesis consists in the preparation of an intimate mixture of Co_3O_4 (Sigma-Aldrich, 99.9 %) and Sb_2O_4 (Sigma-Aldrich, 99.995 %) with a molar ratio of 1:5.4 (20 % excess of Sb_2O_4) by thoroughly grinding the powders together in a vibrating mill (Retsch MM200) for 20 min at 25 Hz using tungsten carbide vial

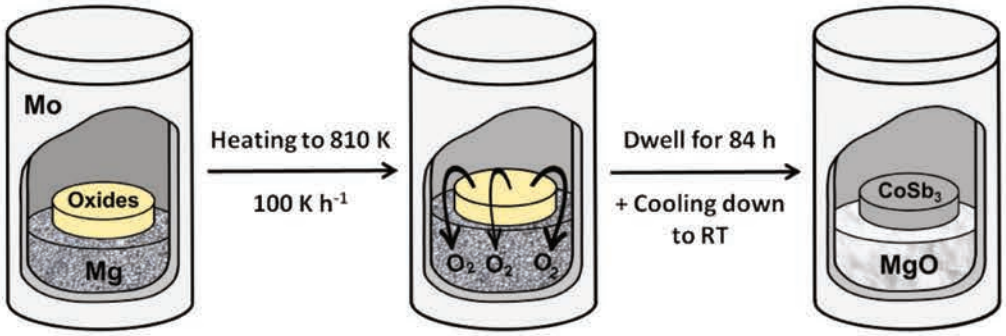

Figure 32: Experimental procedure for the synthesis of $CoSb_3$-based skutterudites by magnesioreduction of the corresponding (un-)doped Co_3O_4 and Sb_2O_4 oxide precursors (yellow pellet). See text for details.

and ball. The oxide mixture was then cold-pressed at 250 MPa into Ø 10 mm pellets with approximately 2 mm height. Two pellets were stacked together on top of a Mg chips bed (Strem, $\geq$ 99 %) lying at the bottom of a Mo crucible (fig. 32). The quantity of Mg needed to complete the reduction was determined from the masses of Co_3O_4 and Sb_2O_4 to be reduced plus an additional 2 - 3 % excess. The Mo crucible is then closed and placed in an argon-filled Inconel tube to prevent its oxidation during the thermal process. The reactor was heated up to 810 K at 100 K h^{-1} and held at this temperature for 84 h before being cooled down to room temperature. After the reaction, $CoSb_3$ remains in the shape of compact pellets and could easily be separated from the loose MgO. The powders were spark plasma sintered (FCT HP-D-10 system) in Ø 10 mm graphite dies at 910 K and 66 MPa for 5 min with heating/cooling ramps of 100 K min^{-1}.

Synthesis of $Ni_{0.06}Co_{0.94}Sb_3$ and $In_{0.13}Co_4Sb_{12}$ by magnesioreduction

The synthesis of Ni-doped and In-inserted $CoSb_3$ was attempted from a mixture of cobalt, nickel/indium and antimony oxides. Nevertheless, the primary formation of $NiSb_2$ and InSb during the magnesioreduction process did not allow to obtain pure samples in relatively fast and low temperature conditions. Mixed precursor oxides were thus prepared in order to start from an intimate mixture of metallic ions to speed up the process.

For the preparation of $Ni_{0.18}Co_{2.82}O_4$ precursor, $Co(NO_3)_2.6H_2O$ (Fluka, $\geq$ 98%) and $Ni(NO_3)_2.6H_2O$ (Fluka, $\geq$ 99%) were dissolved in distilled water with a molar ratio of about 16:1. The solution was stirred for 30 min and evaporated at 363 K. The slurry was ground before being decomposed in air at 573 K for 4 h leading to the formation of a black powder. The Bragg peaks of the X-ray diffraction

(XRD) patterns correspond to the Co_3O_4 structure ($Fd\bar{3}m$) with lattice parameter $a = 8.0905(5)$ Å (fig. SI 1), suggesting the insertion of Ni in Co_3O_4 ($a \approx 8.086$ Å). Accordingly, the metal ratio determined by X-ray energy dispersive spectroscopy (EDS) is in good agreement with the expected $Ni_{0.18}Co_{2.82}O_4$ composition.

For the preparation of $In_{0.10}Co_{2.90}O_4$ precursor, $CoCl_2.6H_2O$ (Prolabo, 99.9 %) and $In(NO_3)_3.xH_2O$ (home made by dissolving metallic indium in concentrated nitric acid) were dissolved in distilled water with a molar ratio of about 29:1 under vigorous stirring. Then a suitable amount (+20 % excess) of NaOH was added to form the metal hydroxides. The blue precipitate was then centrifuged, washed with water and ethanol, dried overnight at about 363 K and calcinated at 723 K to obtain the corresponding oxide. Powder XRD pattern (fig. SI 2) shows broad diffraction peaks corresponding to the Co_3O_4 structure. Le Bail refinement of the experimental pattern nevertheless converges to a cell parameter $a = 8.102(7)$ Å which could indicate the insertion of In on the Co-lattice in agreement with recent results by Ma *et al.*[39].

From these $Ni_{0.18}Co_{2.82}O_4$ and $In_{0.10}Co_{2.90}O_4$ precursors, $Ni_{0.06}Co_{0.94}Sb_3$ and $In_{0.13}Co_4Sb_{12}$ were synthesized using the same procedure as for $CoSb_3$, at identical temperature and duration.

These compositions have been selected as (i) the optimized carrier concentration for Ni-doped sample[40,41] and as (ii) a composition close to those usually presented in articles dealing with In-inserted skutterudites[42–47].

Materials characterization

The crystal structure and purity of the samples were checked by powder XRD using a Bruker D8 Advance diffractometer in the Bragg-Brentano geometry working with a monochromatized Cu Kα_1 radiation ($\lambda = 1.5406$ Å). The diffractometer is equipped with a 1D LynxEye detector with a photon energy discrimination around 20 % thus reducing the cobalt fluorescence signal. Lattice constants were determined by Le Bail refinements as implemented in the FullProf Suite software[48].

Scanning electron microscopy (SEM) images, energy dispersive spectroscopy (EDS) and electron backscattering diffraction (EBSD) were performed using a JEOL JSM 7100 F microscope equipped with an Oxford EDS SDD X-Max spectrometer and an EBSD HKL Advanced Nordlys Nano detector. Preparation of the powder samples for SEM analyses consisted in a mere deposition on carbon tape followed by metallization with carbon. As for the densified samples, the pellets were successively polished with SiC, diamond paste and colloidal silica and pasted on SEM holders using silver lacquer. Samples for the transmission electron microscopy were first thinned

by dimpling with colloidal silica and then by Ar ion milling using a Fischione Ion Mill 1010 operating at 4.5 kV and 5 mA. Transmission electron microscopy (TEM) analyses were performed on a JEOL 2100 LaB_6 instrument operating at 200 kV and equipped with a high resolution Gatan US1000 camera, and an Orius 200D camera.

The Seebeck coefficient α(T) and electrical resistivity ρ(T) measurements were realized using a home made apparatus described elsewhere[49]. Thermal diffusivities were measured in argon atmosphere with the laser flash method using a Netzsch LFA 457 equipment. The total thermal conductivity κ was determined by multiplying the thermal diffusivity, the specific heat calculated from the Dulong-Petit law and the experimental density of the samples.

Results and discussion

Structural and microstructural characterization of as-synthesized and SPSed materials

The powder XRD patterns of pristine and Ni-doped $CoSb_3$ (fig. 33) are fully indexed according to the skutterudite structure, revealing a single phase product. Only few traces of InSb ($F\bar{4}3m$) and Sb ($R\bar{3}m$) are visible on the XRD pattern of the indium containing compound. Le Bail fitting of the XRD patterns (fig. SI 3) result in cell parameters of a = 9.0350(2), 9.0434(1) and 9.0443(6) Å for $CoSb_3$, $Ni_{0.06}Co_{0.94}Sb_3$ and '$In_{0.13}Co_4Sb_{12}$', respectively, indicating an effective substitution by nickel on the cobalt site and insertion of indium in the cages of the structure[44,51,52]. By comparison with literature data, one can expect chemical compositions close to $Ni_{0.06}Co_{0.94}Sb_3$ and $In_{0.10}Co_4Sb_{12}$ from these lattice parameter values[40,53]. The discrepancy with the targeted In-concentration could be explained by some residual InSb binary compound in the sample. The diffraction peaks exhibit very narrow profiles characteristic of well-crystallized matter which may favor the electrical transport in these materials. Surprisingly, no traces of MgO are visible on these patterns which is quite unusual for such a process[54–56] and may result either from the absence of this by-product or from its amorphous nature, the reaction being carried out at a relatively low temperature.

SEM examination of the obtained powders reveals faceted submicronic grains (fig. 34). The grain size ranges from 300 nm to 1 μm for $CoSb_3$ and its Ni-doped counterpart and from 100 nm to 1 μm for the In-inserted skutterudite. Such small particles are required to lower the thermal conductivity and are usually obtained by high energy ball-milling with both risks of contamination from the milling material and

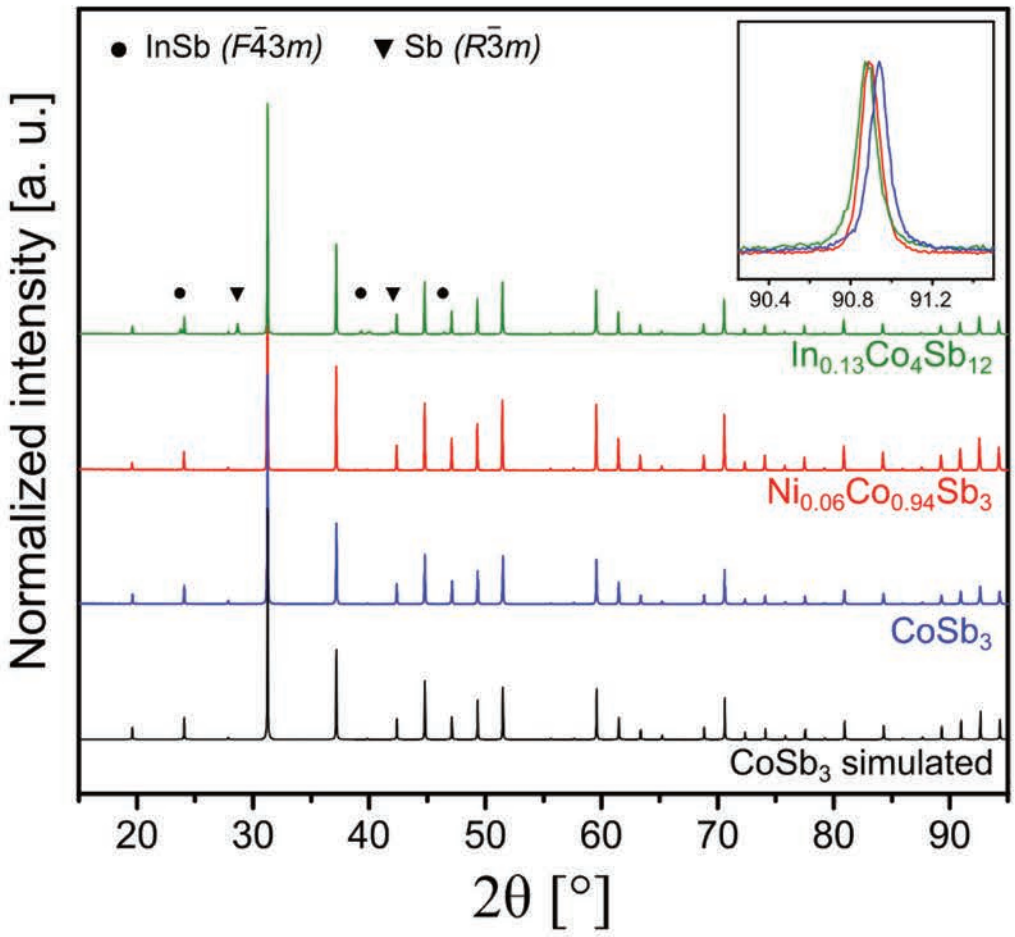

Figure 33: Experimental XRD patterns of the as-synthesized skutterudite powders and theoretical one calculated with FullProf[48] from cell parameters and atomic positions given in[50] and peak profile function from the utilized diffractometer. The inset shows the shift of the (653) diffraction peak of the $CoSb_3$ structure (systematic peak shift due to sample displacement is corrected) revealing the lattice parameter evolution among the samples.

decomposition of the phase. In agreement with the narrow XRD peaks, the shape of most of the grains clearly indicates their single crystalline nature. EDS analyses of the Ni-doped $CoSb_3$ powders confirm the presence of Ni in the sample with a concentration of $\approx$ 1 at.%. On the other hand, no characteristic X-ray emission peaks of In could be detected for the filled skutterudite and this could be explained by the low concentration of the element in the material ($<$ 1 at.%) being below the detection limit of the technique. No signal of Mg is visible on the X-ray emission spectra from all the samples.

Both XRD and EDS analyses indicate the absence of MgO in the as-synthesized products. In addition, TEM observations coupled with EDS analyses did not reveal any traces of Mg or MgO particles in the samples. Together with the retention of both mixed-oxide pellet and magnesium turning shapes, and based on the Ellingham diagram[57] for the metals in presence, we hypothesize solid-gas driven reduction reactions at 810 K: Mg consumes the residual O_2 atmosphere in the crucible

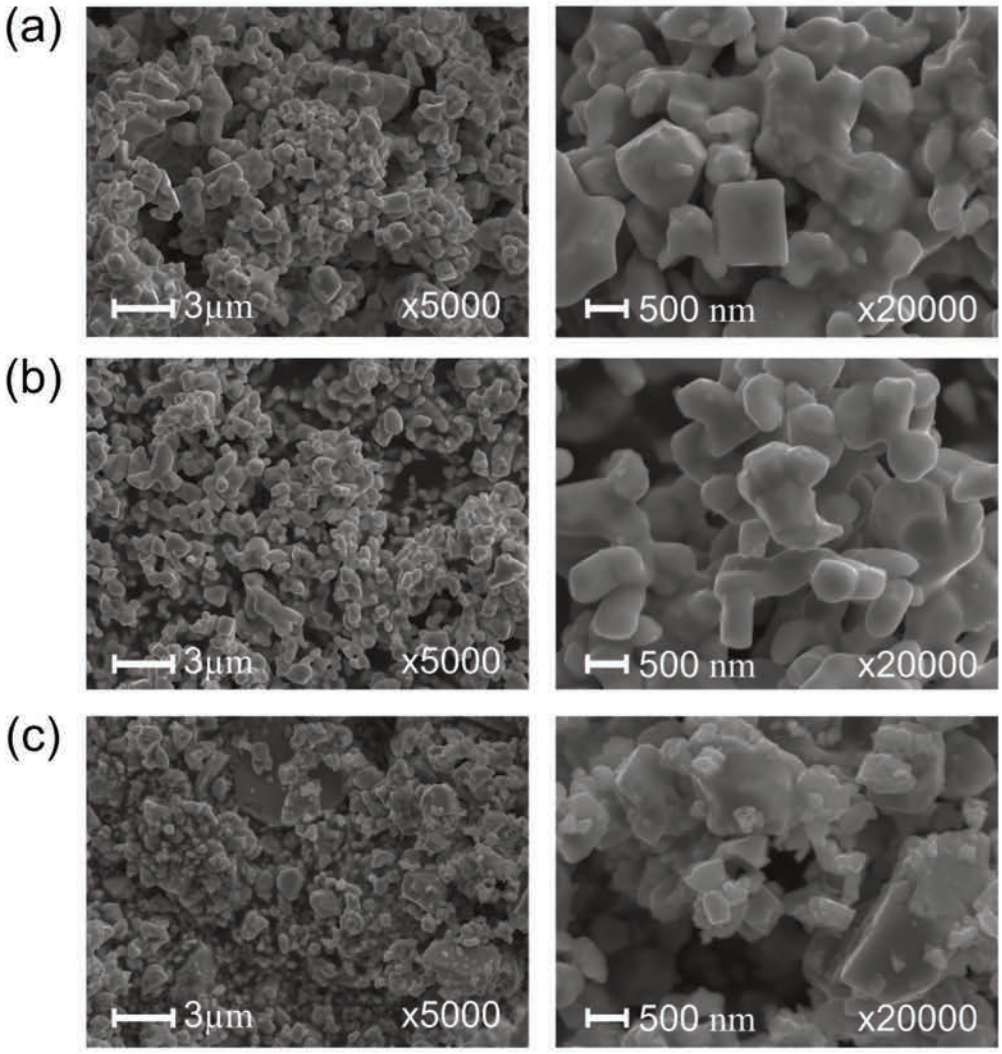

Figure 34: Secondary electron SEM images of the as-synthesized (a) $CoSb_3$ (b) $Ni_{0.06}Co_{0.94}Sb_3$ and (c) $In_{0.13}Co_4Sb_{12}$ at two different magnifications.

($p_{eq}(O_2) = 10^{-63}$ Pa) inducing the decomposition of Co_3O_4 ($p_{eq}(O_2) = 10^{-19}$ Pa) and Sb_2O_4 ($p_{eq}(O_2) = 10^{-14}$ Pa) into native metals that readily react together to form the skutterudite phase.

Spark plasma sintering was used to prepare the skutterudite pellets because it can achieve high densities in short sintering times thus limiting grain growth during the densification process. With the sintering conditions given in 2.1, relative densities ranging from 96 to 97 % were obtained (table 2).

Le Bail fitting of the XRD patterns measured on sintered pellets polished surfaces (fig. 35 and fig. SI 4) do not show significant evolution of the unit cell parameter for $CoSb_3$ and $Ni_{0.06}Co_{0.94}Sb_3$ ($a = 9.0361(2)$ and $9.0428(1)$ Å, respectively). A significant increase up to $a = 9.0482(3)$ Å is observed for $In_{0.13}Co_4Sb_{12}$, which, together with the disappearance of the InSb Bragg peaks, is attributed to a higher insertion of indium in the cages available in the skutterudite structure. Considering the low

melting point (789 K) reported for InSb[58], its reactivity with the skutterudite matrix during the sintering process performed above this melting point was expected. Only a very small amount of antimony ($R\bar{3}m$) could be detected by XRD after sintering and it was found to represent less than 1 wt.% of the sample. The latter cell parameter corresponds to the composition $In_xCo_4Sb_{12}$ with $0.13 \leq x \leq 0.15$, depending on the literature data[42,53].

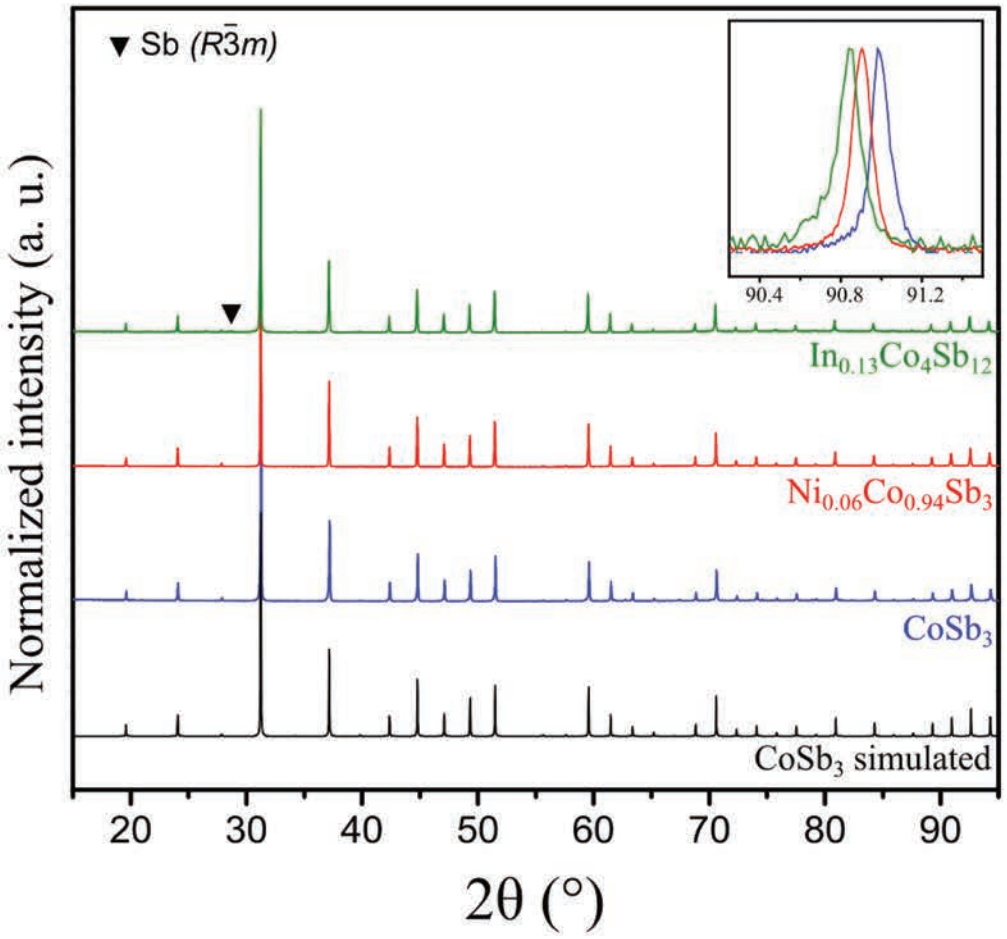

Figure 35: Experimental XRD patterns of the sintered skutterudite pellets and theoretical one calculated with FullProf[48] from cell parameters and atomic positions given in[50] and peak profile function from the utilized diffractometer. The inset shows the shift of the (653) diffraction peak of the $CoSb_3$ structure (systematic peak shift due to sample displacement is corrected) revealing the lattice parameter evolution among the samples.

SEM-EDS analyses performed on several spots of the polished surfaces gives a mean Ni concentration of 1.5 at.% for the Ni-doped samples, which is in good agreement with the targeted and crystallographic compositions. This composition is homogeneous through the analyzed polished surface and no concentration gradient is observed. As for the powders, no significant In or Mg content could be detected on any samples by EDS analyses which means that those elements are in concentration below the detection limit of the technique.

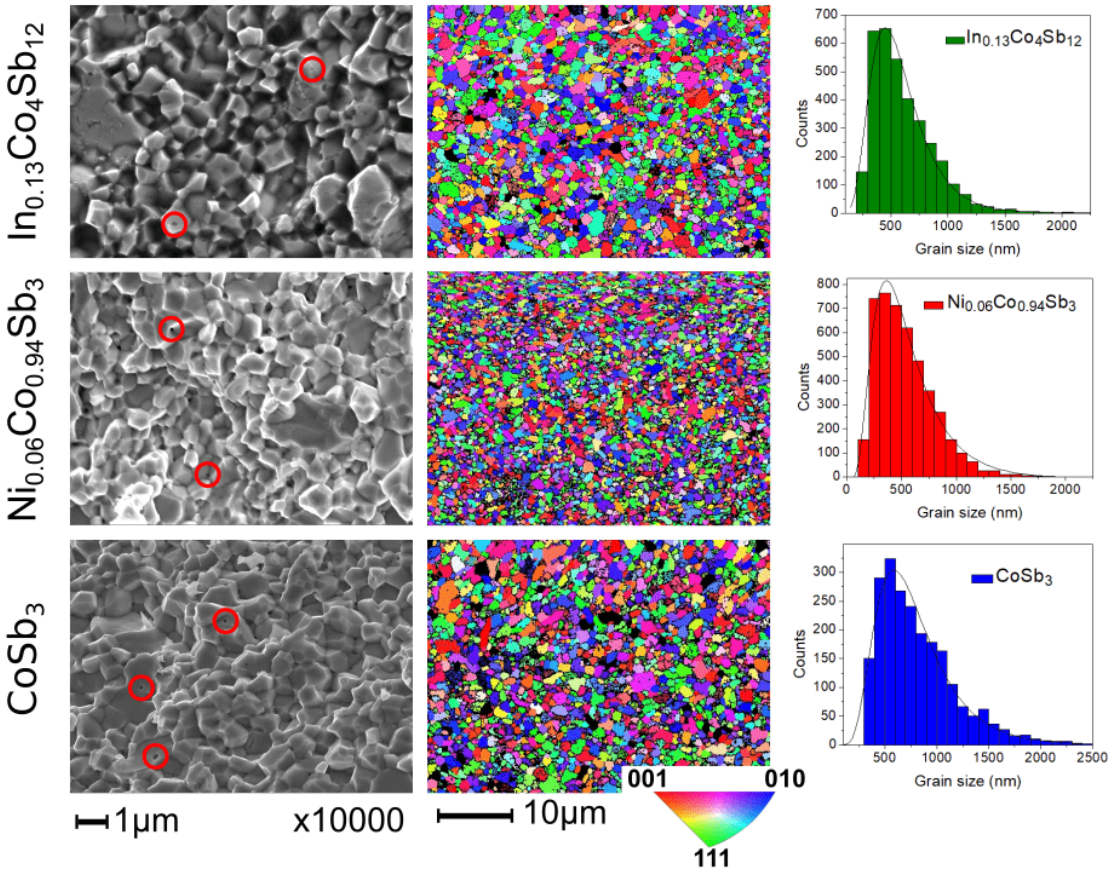

Figure 36: Secondary electron SEM images of the pellet cross-sections (left) showing some residual porosity (circled in red). EBSD mappings (middle) of the polished pellet surfaces and histograms (right) showing the distribution of grain sizes determined from EBSD maps for the SPSed $CoSb_3$ (bottom), $Ni_{0.06}Co_{0.94}Sb_3$ (middle) and $In_{0.13}Co_4Sb_{12}$ (top) skutterudites.

In order to check how sintering affects grain size, electron backscattering diffraction (EBSD) and SEM imaging (fig. 36) were performed on polished surfaces and on broken cross-sections of the pellets, respectively. SEM imaging reveals some closed porosity (encircled in red) which is responsible for the full densification deviation. EBSD mappings were realized on a 1750.5 $\pm$ 9.5 μm^2 area with a step size of 100 nm for $CoSb_3$ and $In_{0.13}Co_4Sb_{12}$ and 50 nm for $Ni_{0.06}Co_{0.94}Sb_3$ to distinguish better smaller grains. Kikuchi lines were well indexed using the skutterudite structure and cell parameters obtained from XRD, and only a few non-indexed areas were found on the 3 pellets. First of all, one can notice a random distribution of the grains orientation throughout the analyzed areas. Then submicronic particles are found to cover the majority of the surface in all cases, with apparent smaller sizes for the Ni-doped antimonide compared to the other two compounds.

In order to quantify these observations, image analyses were performed using the *Channel 5* software (HKL Technology) by considering all the diffracting domains

Table 2: Summary of the main structural and microstructural features of the sintered skutterudite pellets used for the thermoelectric characterizations

Nominal composition	a [Å]	Impurity [wt.%]	Average grain size [nm]	Relative density [%]
$CoSb_3$	9.0362(4)	None	784 ± 376	96
$Ni_{0.06}Co_{0.94}Sb_3$	9.0428(3)	None	580 ± 336	97
$In_{0.13}Co_4Sb_{12}$	9.0482(3)	Sb (<1)	617 ± 292	97

containing at least 7 pixels (*i.e.* ∼0.07 μm^2) for $CoSb_3$ and $In_{0.13}Co_4Sb_{12}$ and at least 14 pixels (*i.e.* ∼0.035 μm^2) for $Ni_{0.06}Co_{0.94}Sb_3$. The particles size distribution (diameter of an equivalent circle with equal surface, Fig. **??**) clearly shows a majority of submicronic particles. This distribution has been fitted using a log-normal distribution function:

$$f(x) = \frac{A}{x\sigma\sqrt{2\pi}}.exp(-\frac{[ln(x)-\mu]^2}{2\sigma^2}) \tag{65}$$

where A, μ and σ are the fitting parameters. From μ and σ values, the average grain size D and its standard deviation SD can be calculated using the formulae:

$$D = exp(\mu + \frac{\sigma^2}{2}) \tag{66}$$

$$SD = [(exp(\sigma^2)-1).exp(2\mu+\sigma^2)]^{\frac{1}{2}} \tag{67}$$

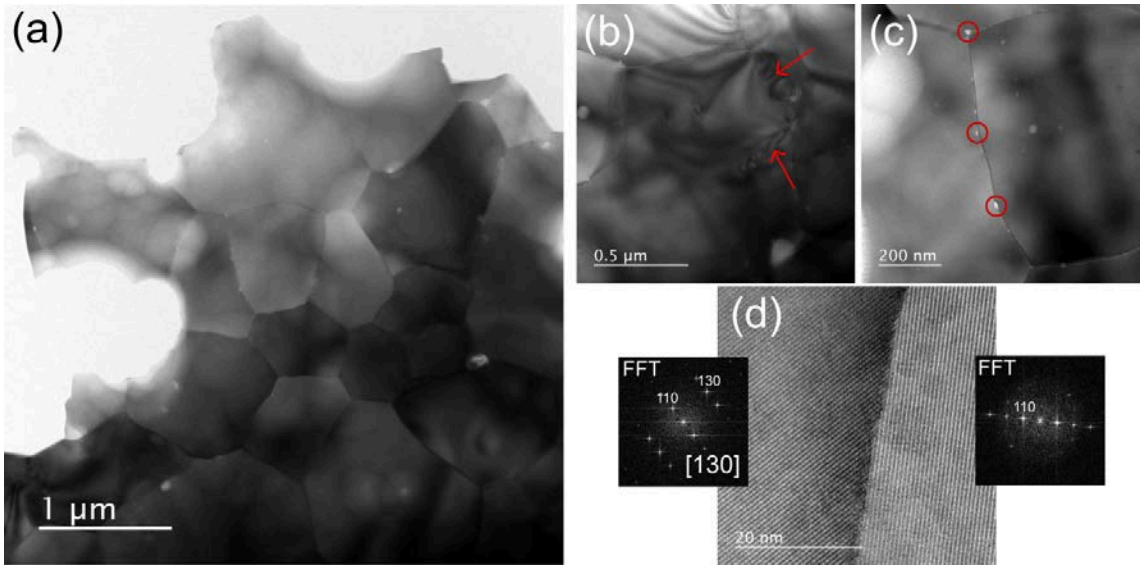

Figure 37: TEM brightfield images of thinned $CoSb_3$ sintered pellet. (a) Typical global area, (b) strips indicating lattice distortions originating from dislocations high density at the grain boundaries (red arrows), (c) nano-scale porosities (encircled in red) and (d) HRTEM image showing the crystallinity of the grain boundaries

The average grain sizes are found to range from 780 nm for $CoSb_3$ down to 580 nm for $Ni_{0.06}Co_{0.94}Sb_3$ with intermediate values for the In-inserted phase (table 2).

Such small grain sizes induce numerous grain boundaries, which along the presence of defects due to crystal orientation mismatches might be efficient to decrease the lattice thermal conductivity. It was shown that dislocations or nanoscale porosity/precipitate can efficiently reduce the skutterudites thermal conductivity by phonon scattering[30,59,60]. In order to demonstrate the existence of such defects in our materials, $CoSb_3$ sintered pellet grains boundaries have been investigated by TEM. Figure 37a shows a typical area of the thinned pellet where the observations were realized. At this magnification, proper tilting of the sample reveals stripes originating from boundaries and propagating inside the grains (fig. 37b). Contrast between those stripes arises from slight deviation from the diffraction condition and evidences large lattice constraints in the crystal. These are common to sintered materials as they originate from high density of dislocations, which are in the present case, mostly located close to or at the grain boundaries (red arrows). HRTEM examination of such grain boundaries (fig. 37d) reveals that they are well-crystallized and free of any amorphous layer. Two major kinds of defects are evidenced in fig. SI 5a taken on a semi-coherent lattice interface. Typical dislocations appear inside the grains (fig. SI 5b) while two dimensional analogues of dislocations[61] are created at the interface between the grains (fig. SI 5c), both types being able to scatter mid-wavelength phonons.

As shown in fig. 37c, some porosity with nanometric size (encircled in red) is also observed at the grain boundaries and can also act as efficient phonon scattering centers.

All these observations are quite common for sintered materials and are not a special feature resulting from the magnesioreduction synthesis. However, an exacerbated effect on the thermal conductivity is expected in MR-materials because of the high grain boundary concentration leading to an elevated defect concentration.

Thermoelectric characterizations

The electrical resistivities, Seebeck coefficients and thermal conductivities have been determined in the temperature range 300 - 800 K where skutterudites usually present their maximum ZT value.

The electrical resistivity and Seebeck coefficient of the three pellets are shown in fig. 38a and 38b. $CoSb_3$ shows a semiconducting shape of $\rho(T)$ in the 300 - 800 K temperature range and the $\alpha(T)$ evolves from strongly negative at room temperature

to positive at 800 K with a sign change at 600 K attributed to the intrinsic regime caused by holes activation through the band gap[43,62,63]. The electrical resistivity of the Ni-doped and In-inserted skutterudites are strongly reduced to respectively 14.5 and 16.0 $\mu\Omega$.m at 300 K confirming the insertion of these elements in the crystal structure. The n-doping is confirmed by the stabilized negative value of $\alpha(T)$ in both cases, ranging between -120 and -200 μV K^{-1} for $Ni_{0.06}Co_{0.94}Sb_3$ and between -180 and -240 μV K^{-1} for $In_{0.13}Co_4Sb_{12}$ in the investigated temperature range. The electrical resistivities and Seebeck coefficients are in very good agreement with those reported for similar compositions of Ni-doped[41,64] and In-filled[44,65] $CoSb_3$. These values lead to an increase of the maximum PF (fig. 38c) from about 1 mW m^{-1} K^{-2} at 400 K for $CoSb_3$ to 3 and 3.5 mW m^{-1} K^{-2} for $Ni_{0.06}Co_{0.94}Sb_3$ at 700 K and $In_{0.13}Co_4Sb_{12}$ at 600 K, respectively. The small grain sizes and thus a high concentration of grain boundaries do not seem to alter the sample transport properties that are dominated by the high crystallinity of the powder particles.

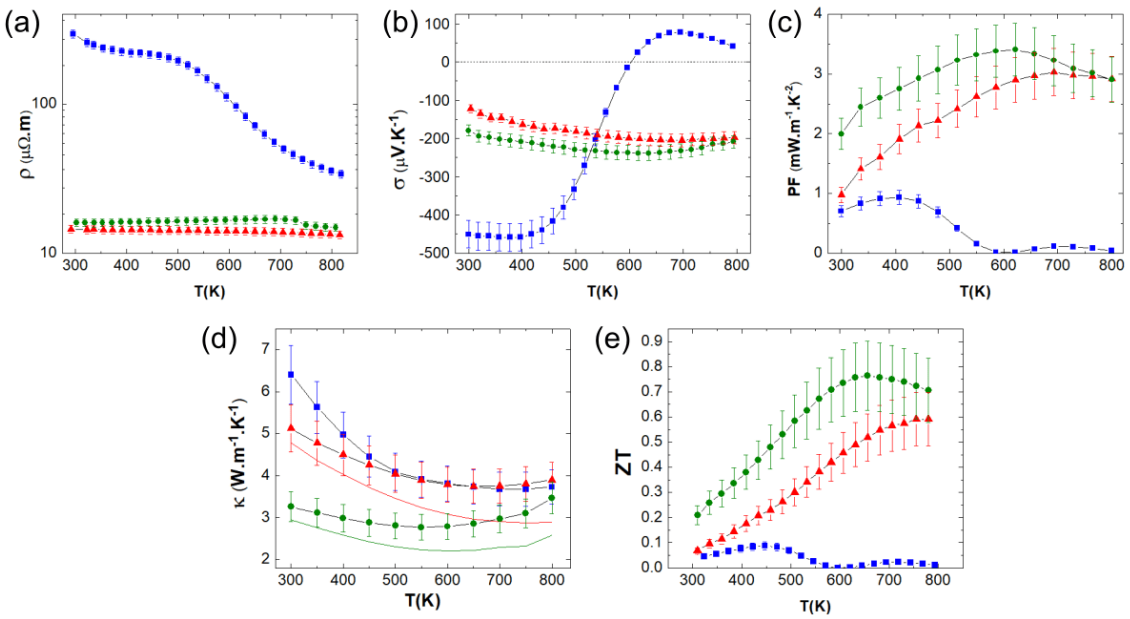

Figure 38: High-temperature dependence of (a) the electrical resistivity, (b) Seebeck coefficient, (c) power factor, (d) total (symbols) and lattice (solid colored lines) thermal conductivity and (d) figure-of-merit ZT of (■) $CoSb_3$, (▲) $Ni_{0.06}Co_{0.94}Sb_3$ and (●) $In_{0.13}Co_4Sb_{12}$. Standard deviations have been estimated to 6 %, 8 %, 13 %, 11 % and 18 % for electrical resistivity, Seebeck coefficient, power factor, thermal conductivity and figure-of-merit ZT, respectively, according to[66]

The thermal diffusivity of the three synthesized skutterudites has been measured on sintered pellets and converted to thermal conductivity (fig. 38d) using the densities of the pellets and the Dulong and Petit specific heat which usually applies for skutterudites in this temperature range. The overall shape of $\kappa(T)$ for pristine $CoSb_3$ corresponds to that usually reported for this material[44]. Nevertheless, it ranges from 6.5 W m^{-1} K^{-1} at 300 K down to 3.7 W m^{-1} K^{-1} at 800 K. Values reported for

Table 3: Measured total thermal conductivity and calculated lattice thermal conductivity in W m^{-1} K^{-1} of $CoSb_3$, $Ni_{0.06}Co_{0.94}Sb_3$ and $In_{0.13}Co_4Sb_{12}$ at 300 K and 800 K compared to the thermal conductivities of macrostructured compounds with similar compositions reported in literature.

		MR samples		Literature data	
		300 K	800 K	300 K	800 K (700 K*)
$CoSb_3$	κ	6.5	3.7	11.1[43], 9.2[44]	7.5*[43], 4.9[44]
	κ_L	6.5	3.4	11.1[43], 9.0[44]	7.2*[43], 4.6[44]
$Ni_{0.06}Co_{0.94}Sb_3$	κ	5.1	3.9	6.7[41]	4.4[41]
	κ_L	4.7	2.9	6.3[41]	3.4[41]
$In_{0.13}Co_4Sb_{12}$	κ	3.3	3.5	3.5[44], 4.6[65]	3.0[44], 3.2*[65]
	κ_L	2.9	2.6	3.1[44], 3.9[65]	2.3[44], 2.5*[65]

similar materials which were synthesized by conventional melting-annealing routes and being mostly composed of crytallites much larger than 1 μm are between 9 - 11 down to 5 - 7.5 W m^{-1} K^{-1} at 300 K and 700 K, respectively[43,44,64]. This corresponds to a reduction of the thermal conductivity of at least 25 % on the whole temperature range for the metalloreduced samples. The here presented values are in better agreement with those observed for 'nano'-engineered materials with comparable densities[67,68]. A direct correlation can be made between the decrease of the thermal conductivity measured for $CoSb_3$ and the high concentration of grain boundaries and associated defects which were evidenced by EBSD/SEM and TEM analyses and act as efficient phonons scattering centers.

Because of the larger electronic contribution to the total thermal conductivity in the Ni-doped and In-filled samples and to compare more significantly with literature data, the lattice thermal conductivities κ_L were calculated by subtracting κ_e to κ_{tot} (table 3 and solid lines in fig. 38d). The Wiedmann-Franz law, κ_e=LT/ρ, was used to obtain κ_e using the measured electrical resistivity and a Lorenz number of 1.6×10^{-8} and 1.7×10^{-8} W Ω K^{-2} for $Ni_{0.06}Co_{0.94}Sb_3$ and $In_{0.13}Co_4Sb_{12}$, respectively[41,44].

The total thermal conductivity of $Ni_{0.06}Co_{0.94}Sb_3$ is 20 % lower than that of pristine $CoSb_3$ at 300 K and reaches similar values from 450 up to 800 K. This reduction of $\kappa(T)$ at room temperature could be explained (i) by the smaller particle size and thus higher density of grain boundaries and associated defects and (ii) by the higher mass fluctuation on the 'disordered' transition metal sublattice, both enhancing the scattering of phonons and decreasing $\kappa_L(T)$. The beneficial effect of the mesostructuration is more apparent when κ_L is compared to the values reported for conventionally synthesized macrostructured materials and where a reduction of $\approx$ 25 % is noticed at 300 K (table 3). At higher temperature, the mesostructuration seems to become less and less efficient so that at 800 K the reduction of κ_L falls to

$\approx$ 15 %. Again, the measured trend and values are in good agreement with reported mesostructured samples with a similar doping level[41,69].

With the insertion of indium rattlers in the structure, the total thermal conductivity of $In_{0.13}Co_4Sb_{12}$ is further lowered to 3.2 and 3.5 W m^{-1} K^{-1} at 300 and 800 K, respectively, with a minimum of 2.8 W m^{-1} K^{-1} at about 550 K. These correspond to κ_L of 2.9 W m^{-1} K^{-1} at 300 K and 2.6 W m^{-1} K^{-1} at 800 K. Comparisons with literature data are rather difficult due to the wide span of (effective) rattler concentration and pellet densities encountered and to the relatively large standard deviations inherent to thermal diffusivity measurements. However the presently investigated sample seems to have a slighly lower κ_L than reported value but without strong effect from the mesostructuration opposite to our observations on the two previous compositions. According to Benyahia *et al.*[70] who investigated the influence of grain size on $In_{0.25}Co_4Sb_{12}$ lattice thermal conductivity, the reduction of $\kappa_L(T)$ by mesostructuration would have a stronger effect from room temperature to $\approx$ 580 K while at higher temperature scattering by the rattler would become dominant. This could explain why magnesioreduced samples have a low κ_L at 300 K compared to those reported in literature but is only in the average at 700 K. Furthermore, in the above mentioned article, a modified Nan and Birringer law[71,72] was used to estimate the reduction of κ_L according to the reciprocal of the crystallite size in $In_{0.25}Co_4Sb_{12}$ at 300 K. Applying here this law and considering a mean crystallite size of 600 nm, a reduction of κ_L(300 K) of only $\approx$ 10% is estimated compared to macrostructured materials. This must be taken as a rough estimate since the synthesis routes and the methods for grain size determination are different, but it would support the reduction of $\kappa_L(T)$ thanks to mesostructuration especially near room temperature in $In_{0.13}Co_4Sb_{12}$.

The measured physical properties enable to calculate the figure-of-merit ZT of these materials (fig. 38e). The ZT values of pristine $CoSb_3$ are small due to the combined high electrical resistivity and the occurrence of the bipolar effect around 500 K. The obtained values for the Ni-doped and In-filled $CoSb_3$ increase ZT up to 0.6 at 800 K and 0.75 at 650 K, respectively. In the case of Ni-doped $CoSb_3$, this result is very similar to the improved ZT reported for mesostructured $Ni_{0.06}Co_{0.94}Sb_3$ where the reduction of the grain sizes and consequently of the thermal conductivities was realized by high energy ball-milling[41,69]. In the case of $In_{0.13}Co_4Sb_{12}$, the reduction of κ by mesostructuration is less effective due to the elevated phonon diffusion by In-rattlers and the calculated ZT corresponds well to materials synthesized by conventional melting/annealing methods[43,44,65].

Conclusions

Pure, Ni-doped and In-filled $CoSb_3$ were synthesized from metal oxides in only 84 h at temperature as low as 810 K by a magnesioreduction process. As-synthesized powders are directly composed of well-crystallized submicronic particles. After spark plasma sintering, pellets with excellent purities and high densities were obtained. XRD and SEM analyses show that the dopant and rattler concentrations are very close to the targetted ones, indicating that a good control of the chemical composition is possible with this process. After sintering, the average grain size are found to be 780, 580 and 620 nm for $CoSb_3$, $Ni_{0.06}Co_{0.94}Sb_3$ and $In_{0.13}Co_4Sb_{12}$, respectively. Such small grain size along with the presence of crystal defects and nanoporosity at the grain boundaries were shown to decrease the lattice thermal conductivity of the samples especially for $CoSb_3$ and $Ni_{0.06}Co_{0.94}Sb_3$ where strong κ_L reduction of 25 % were observed at 300 K. The electrical resistivity and Seebeck coefficient measurements show no degradation of the transport properties due to the reduction of grain sizes. This synthesis route thus directly leads to materials approaching the 'phonon glass-electron crystal' state[73]. It results in ZT_{max} of 0.09 at 450 K, 0.60 at 800 K and 0.75 at 650 K for $CoSb_3$, $Ni_{0.06}Co_{0.94}Sb_3$ and $In_{0.13}Co_4Sb_{12}$, respectively. These values are close to those reported in literature for similar compositions but after multistep high temperature syntheses followed by various mesostructuration steps. This industrializable process is thus promising for the preparation of thermoelectric materials and will be applied to more complex (multi-doped and -filled) skutterudites but also to other intermetallic thermoelectric materials such as clathrates, (half-)Heusler phases or transition metal silicides.

Acknowledgements

Francis Gouttefangeas is acknowledged for SEM images and EDS analyses performed on the CMEBA platform. TEM experiments were performed on THEMIS platform. Both platforms belong to the ScanMAT unit (UMS 2001, University of Rennes 1) which received a financial support from the European Union (CPER-FEDER 2007-2014).

Laura Paradis-Fortin is acknowledged for her careful reading of the article and correction of language errors.

References

[1] L. Yang, Z.-G. Chen, M. S. Dargusch, J. Zou, *Adv. Energy Mater.* **2018**, *8*, 1701797.

[2] B. C. Sales, D. Mandrus, R. K. Williams, *Science* **1996**, *272*, 1325–1328.

[3] G. S. Nolas, D. T. Morelli, T. M. Tritt, *Annu. Rev. Mater. Sci.* **1999**, *29*, 89–116.

[4] S. LeBlanc, S. K. Yee, M. L. Scullin, C. Dames, K. E. Goodson, *Renew. Sust. Energ. Rev.* **2014**, *84*, 313–327.

[5] G. Rogl, P. Rogl, *Curr. Opin. Green Sustainable Chem.* **2017**, *4*, 50–57.

[6] M. Puyet, C. Candolfi, L. Chaput, V. D. Ros, A. Dauscher, B. Lenoir, J. Hejtmanek, *J. Phys.:Condens. Matter* **2006**, *18*, 11301–11308.

[7] G. S. Nolas, J. Yang, H. Takizawa, *Appl. Phys. Lett.* **2004**, *84*, 5210–5212.

[8] X. Y. Zhao, X. Shi, L. D. Chen, W. Q. Zhang, W. B. Zhang, Y. Z. Pei, *J. Appl. Phys.* **2006**, *99*, 053711.

[9] G. Rogl, A. Grytsiv, K. Yubuta, S. Puchegger, E. Bauer, C. Raju, R. C. Mallik, P. Rogl, *Acta Mater.* **2015**, *95*, 201–211.

[10] J. Gainza, F. Serrano-Sánchez, J. Prado-Gonjal, N. M. Nemes, N. Biskup, O. J. Dura, J. L. Martínez, F. Fauth, J. A. Alonso, *J. Mater. Chem. C* **2019**, *7*, 4124–4131.

[11] K. Wojciechowski, J. Tobola, J. Leszczynski, *J. Alloys Compd.* **2003**, *361*, 19–27.

[12] J. Mi, X. Zhao, T. Zhu, J. Ma, *J. Alloys Compd.* **2008**, *452*, 225–229.

[13] Y. Lan, A. J. Minnich, G. Chen, Z. Ren, *Adv. Funct. Mater.* **2010**, *20*, 357–376.

[14] X. Meng, Z. Liu, B. Cui, D. Qin, H. Geng, W. Cai, L. Fu, J. He, Z. Ren, J. Sui, *Adv. Energy Mater.* **2017**, *7*, 1602582.

[15] G. Joshi, H. Lee, Y. Lan, X. Wang, G. Zhu, D. Wang, R. W. Gould, D. C. Cuff, M. Y. Tang, M. S. Dresselhaus, G. Chen, Z. Ren, *Nano Lett.* **2008**, *8*, 4670–4674.

[16] L. Yang, Z. G. Chen, M. Hong, G. Han, J. Zou, *ACS Appl. Mater. Interfaces* **2015**, *7*, 23694–23699.

[17] C. Recknagel, N. Reinfried, P. Höhn, W. Schnelle, H. Rosner, Y. Grin, A. Leithe-Jasper, *Sci. Tech. Adv. Mater.* **2007**, *8*, 357–363.

[18] V. Trivedi, M. Battabyal, P. Balasubramanian, G. M. Muralikrishna, P. K. Jain, R. Gopalan, *Sustain. Energ. Fuels* **2018**, *2*, 2687–2697.

[19] G. Rogl, A. Grytsiv, R. Anbalagan, J. Bursik, M. Kerber, E. Schafler, M. Zehetbauer, E. Bauer, P. Rogl, *Acta Mater.* **2018**, *159*, 352–363.

[20] L. Guo, G. Wang, K. Peng, Y. Yan, X. Tang, M. Zeng, J. Dai, G. Wangand, X. Zhou, *Scipta Mater.* **2016**, *116*, 26–30.

[21] S. Lee, K. H. Lee, Y.-M. Kim, H. S. Kim, G. J. Snyder, S. Baik, S. W. Kim, *Acta. Mater.* **2018**, *142*, 8–17.

[22] E. Godlewska, K. Mars, K. Zawadzka, *J. Solid State Chem.* **2012**, *193*, 109–113.

[23] F. Gucci, T. G. Saunders, M. J. Reece, *Scripta Mater.* **2018**, *157*, 58–61.

[24] L. Kong, X. Jia, Y. Zhang, B. Sun, B. Liu, H. Liu, C. Wang, B. Liu, J. Chen, H. Ma, *J. Alloys Compd.* **2018**, *734*, 36–42.

[25] L. Deng, J. Ni, L. Wang, X. Jia, J. Qin, B. Liu, *J. Alloys Compd.* **2017**, *712*, 477–481.

[26] A. Sesselmann, G. Skomedal, H. Middleton, E. Müller, *J. Electron. Mater.* **2015**, *45*, 1397–1407.

[27] M. S. Toprak, C. Stiewe, D. Platzek, S. Williams, L. Bertini, E. Müller, C. Gatti, Y. Zang, M. Rowe, M. Muhammed, *Adv. Funct. Mater.* **2004**, *14*, 1189–1196.

[28] Y. Li, C. Li, B. Wang, W. Li, P. Che, *J. Alloys Compd.* **2019**, *772*, 770–774.

[29] K. Biswas, J. He, I. D. Blum, C.-I. Wu, T. P. Hogan, D. N. Seidman, V. P. Dravid, M. G. Kanatzidis, *Nature* **2012**, *489*, 414–418.

[30] X. Meng, Z. Liu, B. Cui, D. Gin, H. Geng, W. Cai, L. Fu, J. He, Z. Ren, J. Sui, *Adv. Energy Mater.* **2017**, *7*, 642–651.

[31] W. Li, J. Wang, Y. Xie, J. L. Gray, J. J. Heremans, H. B. Kang, B. Poudel, S. T. Huxtable, S. Priya, *Chem. Mater.* **2019**, *31*, 862–872.

[32] G. Rogl, A. Grytsiv, P.Rogl, E. Bauer, M. B. Kerber, M. Zehetbauer, S. Puchegger, *Intermetallics* **2010**, *18*, 2435–2444.

[33] M. Matsubara, Y. Masuoka, R. Asahi, *J. Alloys Compd.* **2019**, *774*, 731–738.

[34] H. Yang, P. Wen, X. Zhou, Y. Li, B. Duan, P. Zhai, Q. Zhang, *Scripta Mater.* **2018**, *159*, 68–71.

[35] A. U. Khan, K. Kobayashi, D.-M. Tang, Y. Yamauchi, K. Hasegawa, M. Mitome, Y. Xue, B. Jiang, K. Tsuchiya, D. Golberg, Y. Bando, T. Mori, *Nano Energy* **2017**, *31*, 152–159.

[36] H. Li, X. Su, X. Tang, Q. Zhang, C. Uher, G. J. Snyder, U. Aydemir, *J. Materiomics* **2017**, *3*, 273–279.

[37] P. Chen, Z. Zhou, W. Jiang, WeiLuo, J. Yang, J. Zhu, L. Wang, Y. Fan, *Scripta Mater.* **2018**, *146*, 136–141.

[38] H. Zhao, B. Cao, S. Li, N. Liu, J. Shen, S. Li, J. Jian, L. Gu, Y. Pei, G. J. Snyder, Z. Ren, X. Chen, *Adv. Energy Mater.* **2017**, *7*, 1700446.

[39] L. Ma, C. Y. Seo, X. Chen, K. Sun, J. W. Schwank, *Appl. Catal. B-Environ.* **2018**, *222*, 44–58.

[40] E. Alleno, E. Zehani, O. Rouleau, *J. Alloys Compd.* **2013**, *572*, 43–48.

[41] E. Alleno, E. Zehani, M. Gaborit, V. Orodniichuk, B. Lenoir, M. Benyahia, *J. Alloys Compd.* **2017**, *692*, 676–686.

[42] T. He, J. Chen, H. D. Rosenfeld, M. A. Subramanian, *Chem. Mater.* **2006**, *18*, 759–762.

[43] R. C. . Mallik, J. Y. Jung, S. C. Ur, I. H. Kim, *Met. Mater. Int.* **2008**, *14*, 223–228.

[44] J. Leszczynski, V. D. Ros, B. Lenoir, A. Dauscher, C. Candolfi, P. Masschelein, J. Hejtmanek, K. Kutorasinski, J. Tobola, R. I. Smith, C. Stiewe, E. Müller, *J. Phys. D: Appl. Phys.* **2013**, *46*, 495106.

[45] R. C. Mallik, C. Stiewe, G. Karpinski, R. Hassdorf, E. Müller, *J. Electron. Mater.* **2009**, *38*, 1337–1339.

[46] G. Li, K. Kurosaki, Y. Ohishi, H. Muta, S. Yamanaka, *J. Electron. Mater.* **2013**, *42*, 1463–1468.

[47] E. Visnow, C. P. Heinrich, A. S. andJ. de Boor, P. Leidich, B. Klobes, R. P. Hermann, W. E. Müller, W. Tremel, *Inorg. Chem.* **2015**, *54*, 7818–7827.

[48] J. Rodriguez-Carvajal, *Physica B* **1993**, *192*, 55–69.

[49] O. Rouleau, E. Alleno, *Rev. Sci. Instrum.* **2013**, *84*, 105103.

[50] D. G. Mandrus, A. Migliori, T. W. Darling, M. F. Hundley, E. J. Peterson, J. D. Thompson, *Phys. Rev. B* **1995**, *52*, 4926–4931.

[51] M. Christensen, B. B. Iversen, L. Bertini, C. Gatti, M. Toprak, M. Muhammed, E. Nishibori, *J. Appl. Phys.* **2004**, *96*, 3148–3157.

[52] W. Zhao, P. Wei, Q. J. Zhang, H. Peng, W. T. Zhu, D. G. Tang, J. Yu, H. Y. Zhou, Z. Y. Liu, X. Mu, D. Q. He, J. C. Li, C. L. Wang, X. F. Tang, J. H. Yang, *Nat. Commun.* **2015**, *6*, 6197.

[53] A. Grytsiv, P. Rogl, H. Michor, E. Bauer, G. Giester, *J. Electron. Mater.* **2013**, *42*, 2940–2952.

[54] G. Champion, J. Allenou, M. Pasturel, H. Noël, F. Charollais, M. Anselmet, X. Iltis, O. Tougait, *Adv. Eng. Mater.* **2013**, *15*, 257–261.

[55] K. Choi, H. Choi, H. Na, I. Sohn, *Mater. Lett.* **2016**, *183*, 151–155.

[56] C. Won, H. Nersisyan, H. Won, *Chem. Eng. J.* **2010**, *157*, 270–275.

[57] H. J. T. Ellingham, *J. Soc. Chem. Ind.* **1944**, *63*, 125–160.

[58] R. C. Sharma, T. L. Ngai, Y. A. Chang, *Bull. Alloy Phase Diagrams* **1989**, *10*, 657–664.

[59] G. Rogl, A. Grytsiv, P. Rogl, E. Royanian, E. Bauer, J. Horky, D. Setman,

E. Schafler, M. Zehetbauer, *Acta. Mater.* **2013**, *61*, 6778–6789.

[60] L. Yang, J. Wu, L. Zhang, *J. Alloys Compd.* **2004**, *364*, 83–88.

[61] J. Friedel, *Dislocations*, 1. Aufl., Pergamon Press, **1964**.

[62] Y. Kawaharada, K. Kurosaki, M. Uno, S. Yamanaka, *J. Alloys Compd.* **2001**, *315*, 193–197.

[63] J. W. Sharp, E. C. Jones, R. K. Williams, P. M. Martin, B. C. Sales, *J. Appl. Phys.* **1995**, *78*, 1013–1018.

[64] H. Kitagawa, M. Wakatsuki, H. Nagaoka, H. Noguchi, Y. Isoda, K. Hasezaki, Y. Noda, *J. Phys. Chem. Solid.* **2005**, *66*, 1635–1639.

[65] A. Sesselmann, B. Klobes, T. Dasgupta, O. Gourdon, R. Hermann, E. Müller, *Phys. Stat. Sol. A* **2016**, *213*, 766–773.

[66] E. Alleno, D. Berardan, C. Byl, C. Candolfi, R. Daou, R. Decourt, E. Guilmeau, S. Hebert, J. Hejtmanek, B. Lenoir, P. Masschelein, V. Ohorodnichuk, M. Pollet, S. Populoh, D. Ravot, O. Rouleau, M. Soulier, *Rev. Sci. Instrum.* **2015**, *86*, 011301.

[67] E. Alleno, L. Chen, Chubilleau, B. Lenoir, O. Rouleau, M. Trichet, B. Villeroy, *J. Electron. Mater.* **2010**, *39*, 1966–1970.

[68] A. Khan, M. Saleemi, M. Johnsson, L. Han, N. Nong, M. Muhammed, M. Toprak, *J. Alloys Compd.* **2014**, *612*, 293–300.

[69] Q. He, Q. Hao, X. Wang, J. Yang, Y. Lan, X. Yan, B. Yu, Y. Ma, B. Poude, G. Joshi, D. Wang, G. Chen, Z. Ren, *J. Nanosci. Nanotechnol.* **2008**, *8*, 4003–4006.

[70] M. Benyahia, V. Ohorodniichuk, E. Leroy, A. Dauscher, B. Lenoir, E. Alleno, *J. Alloys Compd.* **2018**, *735*, 1096–1104.

[71] C. W. Nan, R. Birringer, *Phys. Rev. B* **1998**, *14*, 8264–8268.

[72] H. S. Yang, G. Bai, L. Thompson, J. Eastman, *Acta Mater.* **2002**, *50*, 2309–2317.

[73] G. A. Slack, *MRS Proceedings* **1997**, *478*, 47.

Innovative synthesis of mesostructured $CoSb_3$-based skutterudites by magnesioreduction: supplementary informations

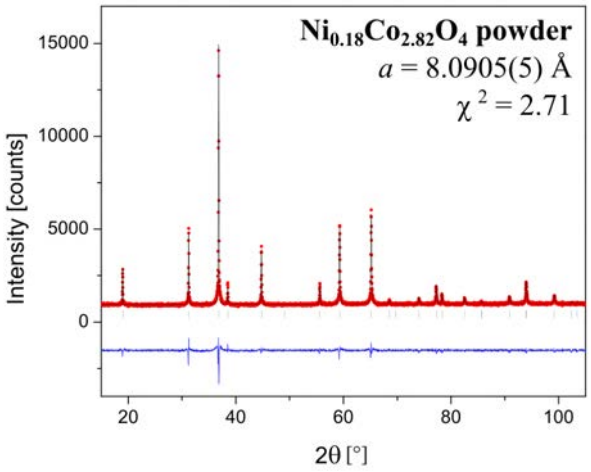

Figure SI 1: Le Bail refined XRD pattern of $Ni_{0.18}Co_{2.82}O_4$. The experimental data are plotted in red symbols, the calculated one in black line and the difference in blue line. The vertical ticks indicate the theoretical Bragg peak positions.

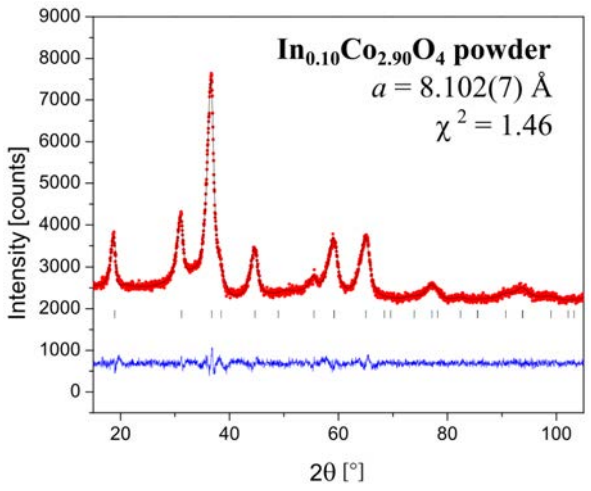

Figure SI 2: Le Bail refined XRD pattern of $In_{0.10}Co_{2.90}O_4$. The experimental data are plotted in red symbols, the calculated one in black line and the difference in blue line. The vertical ticks indicate the theoretical Bragg peak positions.

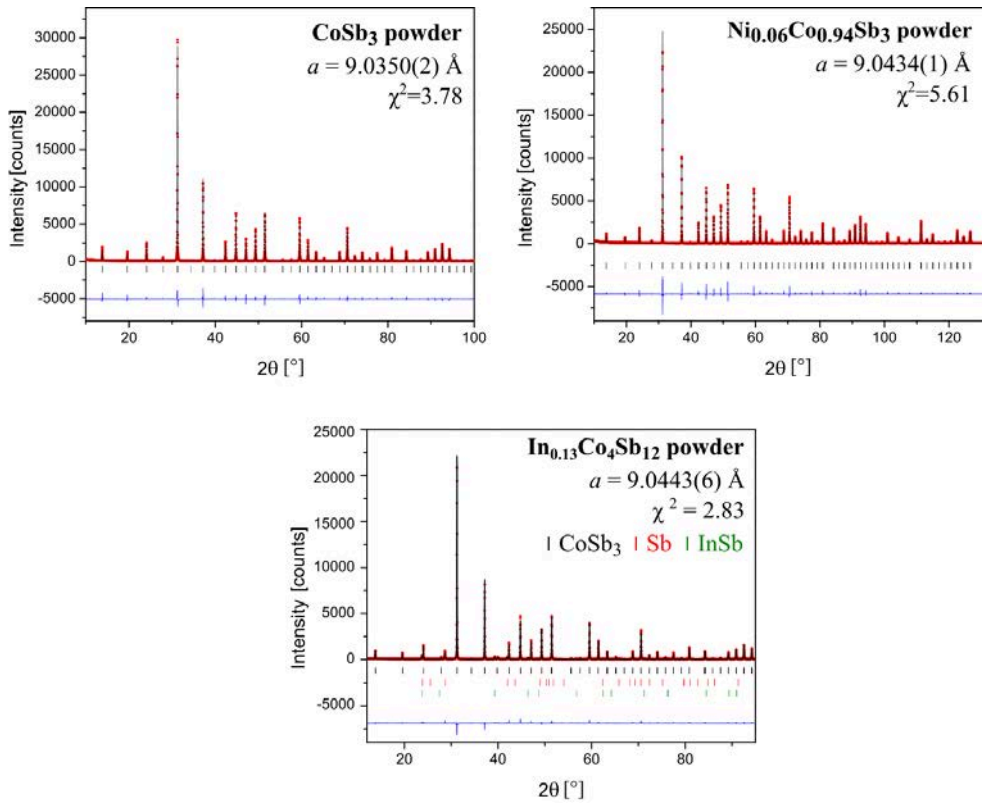

Figure SI 3: Le Bail refined XRD patterns of as-syntesized $CoSb_3$ (up left), $Ni_{0.06}Co_{0.94}Sb_3$ (up right) and $In_{0.13}Co_4Sb_{12}$ (down). The experimental data are plotted in red symbols, the calculated one in black line and the difference in blue line. The vertical ticks indicate the theoretical Bragg peak positions.

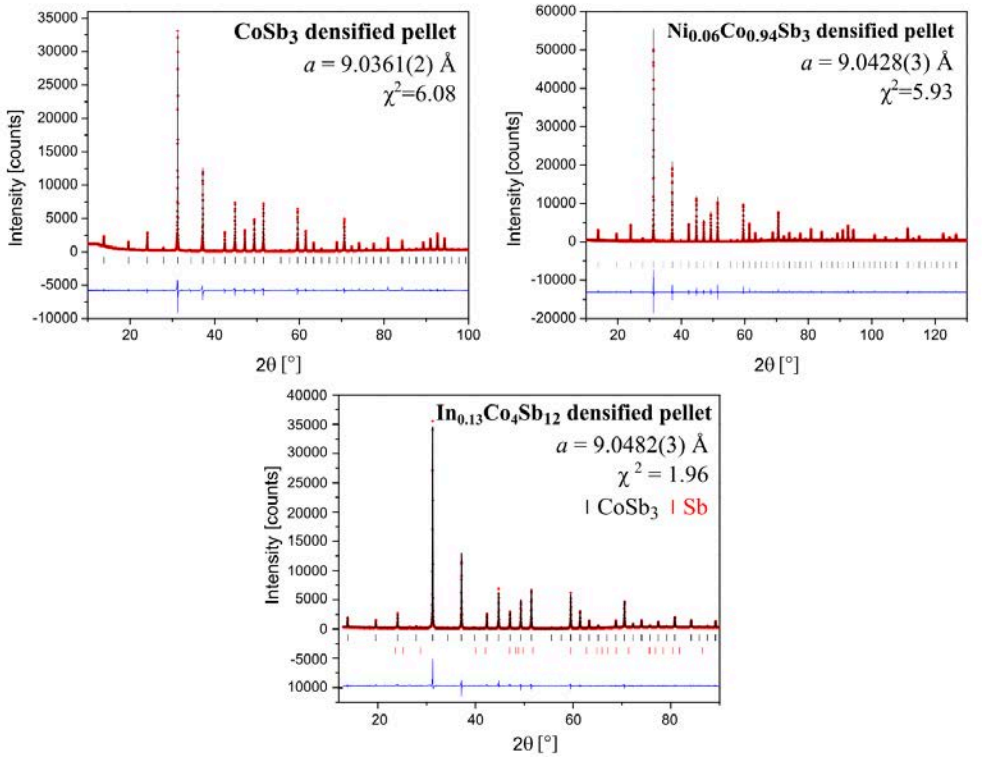

Figure SI 4: Le Bail refined XRD patterns of the sintered pellets of $CoSb_3$ (up left), $Ni_{0.06}Co_{0.94}Sb_3$ (up right) and $In_{0.13}Co_4Sb_{12}$ (down). The experimental data are plotted in red symbols, the calculated one in black line and the difference in blue line. The vertical ticks indicate the theoretical Bragg peak positions.

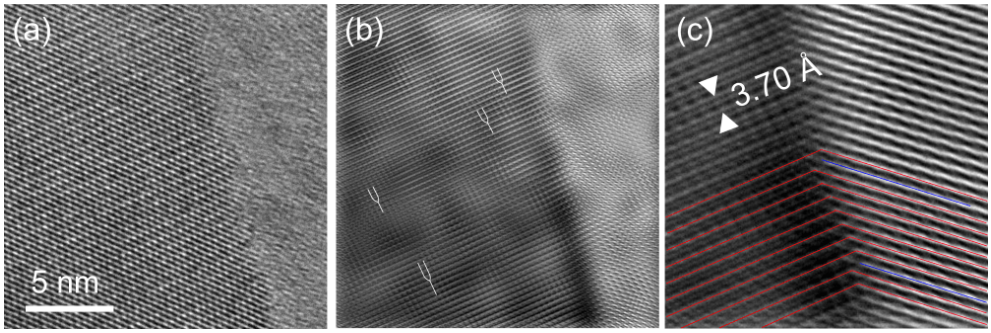

Figure SI 5: (a) HRTEM image of a semi-coherent grain boundary in a spark plasma sintered pellet of $CoSb_3$ prepared by magnesioreduction and (b) its inversed filtered FFT image highlighting the presence of intra-grain dislocations (white lines). (c) Zoomed area of the inversed filtered FFT image showing the grain coherence (red lines) and analogues to dislocations (blue line) at the semi-coherent interface.

Reaction mechanism and thermoelectric properties of $In_{0.22}Co_4Sb_{12}$ prepared by magnesiothermy

Sylvain Le Tonquesse,[a] Éric Alleno,[b] Valérie Demange,[a] Carmelo Prestipino,[a] Olivier Rouleau,[b] and Mathieu Pasturel*[a]

[a] Univ Rennes, CNRS, ISCR-UMR6226/ScanMAT-UMS2001, F-35000, Rennes, France. Tel: +33-2-23-23-58-61;
E-mail: mathieu.pasturel@univ-rennes1.fr

[b] Université Paris-Est, Institut de Chimie et des Matériaux Paris-Est, UMR 7182 CNRS - UPEC, 2 rue H. Dunant, 94320 THIAIS, France.

Published in *Materials Today Chemistry*

Abstract

The magnesioreduction synthesis of $In_{0.22}Co_4Sb_{12}$ with high In-rattler content from In-doped Co_3O_4 and Sb_2O_4 is reported. By this process, a submicronic powder is directly obtained in a single step of 96 h at 810 K. The reaction mechanism has been investigated by stopping the reaction at different times of the process and by quantifying the phases in presence by X-ray diffraction and Rietveld refinements. The precursors are first reduced in CoO and Sb_2O_3 lower oxides, then form $CoSb_2O_6$ and $CoSb_2O_4$ intermediates which are finally reduced in $In_xCo_4Sb_{12}$. A powder with 350 nm average size and mostly composed of In-filled skutterudite phase with composition close to $In_{0.17}Co_4Sb_{12}$ is obtained. Upon spark plasma sintering, small residual amount of InSb reacts with the skutterudite matrix to form a single-phase densified pellet with true composition close to $In_{0.22}Co_4Sb_{12}$. The resulting densified material with 1.8 μm average grain size shows a ZT_{max} of 0.95 at 750 K.

Introduction

Thermoelectrics (TE) materials enable the direct conversion of heat into electricity thanks to the Seebeck effect. The conversion efficiency is directly related to the figure of merit ZT defined as:

$$ZT = \frac{\alpha^2}{\rho\left(\kappa_L + \kappa_e\right)} T \tag{68}$$

with α the Seebeck coefficient, ρ the electrical resistivity, κ_L and κ_e the lattice and electronic contributions to the total thermal conductivity κ and T the temperature. $CoSb_3$ - based skutterudites are well known TE materials with a band gap of about 0.2 eV.[1] They are considered as promising candidates for mid-temperature (600 - 800 K) TE applications because of their excellent electronic properties, good mechanical properties and relatively abundant constituting elements. Large power factors, $PF = \alpha^2/\rho$, reaching 4 - 5 W m^{-1} K^{-2} can be obtained for compositions with optimized charge carrier concentration. In order to achieve high ZT, the intrinsic high thermal conductivity ($\approx$ 9 W m^{-1} K^{-1} at 298 K for $CoSb_3$[2]) must be reduced as much as possible without simultaneously degrading the electronic properties. This can be effectively done by partially filling the empty isocahedral voids of the structure with rare-earth, alkaline metal or III - IV group element.[1] The additional mass contrast induced by the partial occupancy as well as the 'rattling' behavior of the filling atoms in the oversized voids effectively scatter acoustic heat-carrying phonons. For example, lattice thermal conductivities as low as 1 - 2 and $\approx$ 0.5 W m^{-1} K^{-1} were reported for single Ba-, Ca- and Yb-filled[3–5] and nanostructured multi-filled skutterudites[6], respectively.

Indium is among the most studied filler atom for n-type skutterudite because (i) it acts as an electron donor enabling large increase of PF and (ii) it efficiently reduces κ_L thanks to its high atomic mass. While some controversy exists about its true solubility limit ($0.16 < x < 0.27$),[7–9] all authors agree that the best performances are obtained by maximizing the In concentration.[2,10] ZT_{max} of about 1.1 are usually reported for microns sized grains materials with composition close to $In_{0.25}Co_4Sb_{12}$.[2,11,12] Further κ reduction were attempted by *in situ* formation of InSb nanoprecipitates[13–15] or the design of mesostructured materials with oxide nanoinclusions.[11,16] Unconventional routes such as hydrothermal synthesis[17] or melt-spinning/reactive spark plasma sintering[18] were developed to achieved nanostructured $In_xCo_4Sb_{12}$ materials with high concentration of interfaces and lattice thermal conductivity as low as 1.5 W m^{-1} K^{-1}. These alternative synthesis routes offer the additional advantage to avoid long post-synthesis annealing (> 96 h) which is required after conventional melting/annealing process due to the slow peritectoid

formation of $CoSb_3$ below 876 K. However, nanostructured materials often suffer from largely higher electrical resistivity due to enhanced charge carriers scattering at the numerous interfaces/defects considerably reducing the beneficial effect of the microstructure on *ZT*.

In a previous article[19], we reported a new magnesioreduction synthesis for $In_xCo_4Sb_{12}$ with x = 0.13 according to the reaction:

$$2\,(\mathrm{In})Co_3O_4 + 9\,Sb_2O_4 + 44\,Mg \xrightarrow[96\,h]{810\,K} 6\,(\mathrm{In})CoSb_3 + 44\,MgO \qquad (69)$$

This process possesses many advantages such as the direct synthesis of skutterudite powders with submicronic average grain sizes without additional long annealing or milling step, high yield, relatively low reaction temperature and the use of cheap and air-stable oxide precursors. In the present article, this magnesioreduction process is adapted to the synthesis of optimized $In_{0.22}Co_4Sb_{12}$. The discussion will mainly focus on the comprehension of the relatively complex reaction mechanism which was investigated by X-ray diffraction. Finally, the thermoelectric properties were measured and compared to reference samples from the literature.

Experimental procedures

The detailed procedure for the magnesioreduction synthesis of In-filled skutterudites according to reaction (69) is described in a previous work[19]. For preparation of the '$In_{0.19}Co_{2.81}O_4$' precursor, stoichiometric amount of $CoCl_2{\cdot}6H_2O$ (Prolabo, 99.9 %) and $In(NO_3)_3{\cdot}xH_2O$ (home made by dissolving In in concentrated HNO_3) are dissolved in distilled water and then precipitated using NaOH. The precipitate is washed with water and ethanol several times, dried at 363 K and calcined at 723 K for 4 h in air. XRD pattern (fig. SI 6) shows broad diffraction peaks corresponding to Co_3O_4 and In_2O_3. Rietveld refinement converges to a lattice parameter $a = 8.137(9)$ Å significantly larger than for pristine Co_3O_4, $a = 8.076$ Å[20], suggesting the insertion of In the structure[21]. However, the presence of In_2O_3 indicates that the solubility limit has been reached. A mixture of this precursor and Sb_2O_4 (Sigma-Aldrich, 99.995 %) with 1:5.4 molar composition is thoroughly milled in an agate mortar. The oxide mixture is cold-pressed at 250 MPa into Ø 10 mm pellets with about 2 mm height. The pellets (usually 2 stacked on top of each other) are placed with Mg chunks (2 - 3 % excess) in a sealed Mo crucible. The crucible is heated to 810 K for 96 h under protective Ar atmosphere before being cooled down to room temperature. After the reaction, the skutterudite remains in the shape of compact pellets and can easily be separated from the loose MgO. Pictures of the sample at various stages of the synthesis is shown in fig. 39. The powder is then

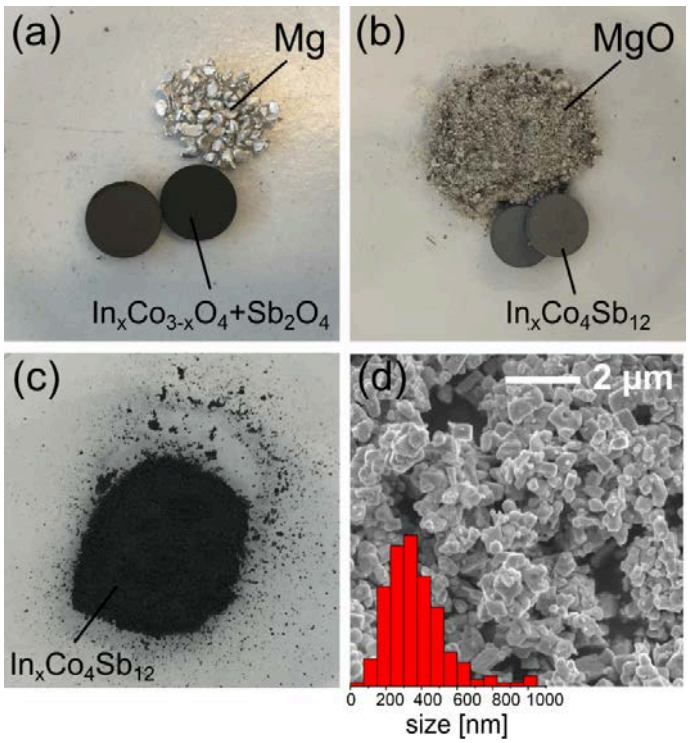

Figure 39: Pictures of (a) the reaction precursors, (b) reaction products after 96 h at 810 K and (c) crushed as-synthesized $In_xCo_4Sb_{12}$ pellets. (d) Secondary electron SEM image of the as-synthesized powder with histogram showing the grain size distribution.

spark plasma sintered (FCT system HP-D-10) in Ø 10 mm graphite dies at 1000 K and 66 MPa for 10 min.

Powder X-ray diffraction is realized on a Bruker D8 Advance diffractometer in the modified Bragg-Brentano geometry working with a monochromatized Cu Kα_1 radiation ($\lambda = 1.5406$ Å). The LynxEye detector enables photon energy discrimination around 20 % thus reducing the cobalt fluorescence signal. Lattice parameters and phase concentrations are refined by the Rietveld method using the FullProf software[22]. Scanning electron microscopy (SEM) images and energy dispersive spectroscopy (EDS) are performed on a JEOL JSM 7100 F microscope equipped with an Oxford EDS SDD X-Max spectrometer. Transport properties measurements are realized using a home-made apparatus described elsewhere[23]. Thermal diffusivity measurements are performed using a Netzsch LFA 457 equipment under Ar atmosphere. The thermal conductivity is determined from $\kappa = D\ C_p\ d$ with D the thermal diffusivity, C_p the specific heat of the sample calculated using the Dulong-Petit law and d the sample density determined by the Archimede method in absolute ethanol.

Results and discussion

Reaction mechanism and skutterudite characterizations

$In_xCo_4Sb_{12}$ (targeted x = 0.25) has been synthesized, along with some InSb and Sb impurities, from Sb_2O_4 and In-doped Co_3O_4 after 96 h heat treatment at 810 K in presence of Mg. To elucidate the reaction mechanism, the synthesis was repeated several times and stopped every twelve hours. Each time, the phases in the samples were quantified with the Rietveld method and their relative concentrations are represented in fig. 40. Figure 41 shows some selected XRD patterns while all refined patterns and parameters can be found in supplementary information (fig. SI 7, tables SI. 1 - 9). Up to 6 different phases have been identified in some patterns indicating a complex reaction mechanism. The full reduction of the precursors is realized in three steps: (i) the partial reduction of the precursors in lower oxides (0 h - 24 h), (ii) the formation of $CoSb_2O_6$ and $CoSb_2O_4$ intermediates (0 h - 48 h) and (iii) the complete reduction of the intermediates and the formation of $In_xCo_4Sb_{12}$ (38 h - 96 h).

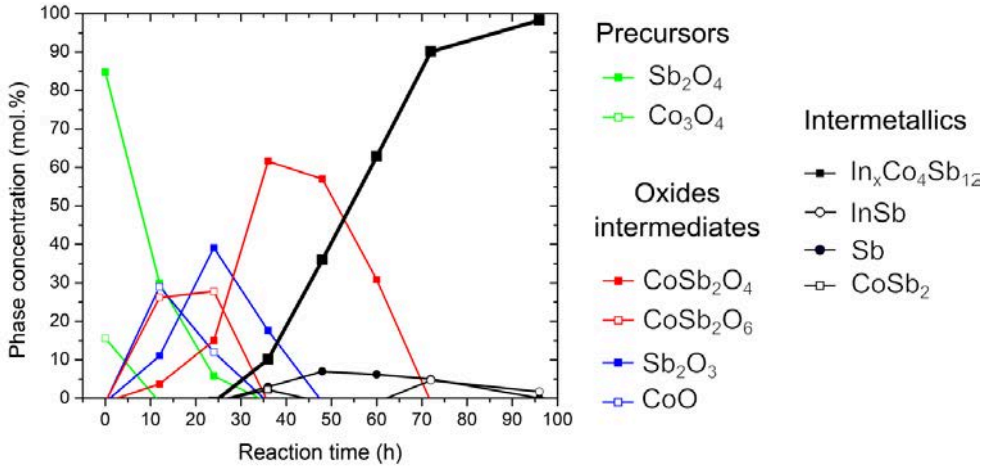

Figure 40: Evolution of the sample composition during the magnesioreduction synthesis of $In_xCo_4Sb_{12}$, determined by the Rietveld method, as a function of the reaction time. In the present case and according to[24], the relative standard deviation on the concentrations are considered to be well below 5 %.

The precursors mixture is initially composed of Sb_2O_4 [Sb^{5+}, Sb^{3+}] and Co_3O_4 [Co^{2+}, Co^{3+}]. After 24 h at 813 K, Co_3O_4 and Sb_2O_4 almost completely disappeared. Instead, freshly formed CoO [Co^{2+}] and Sb_2O_3 [Sb^{3+}] represent almost 50 % of the reaction media. This suggests the partial reduction of the precursors in lower oxides by Mg according to the reactions:

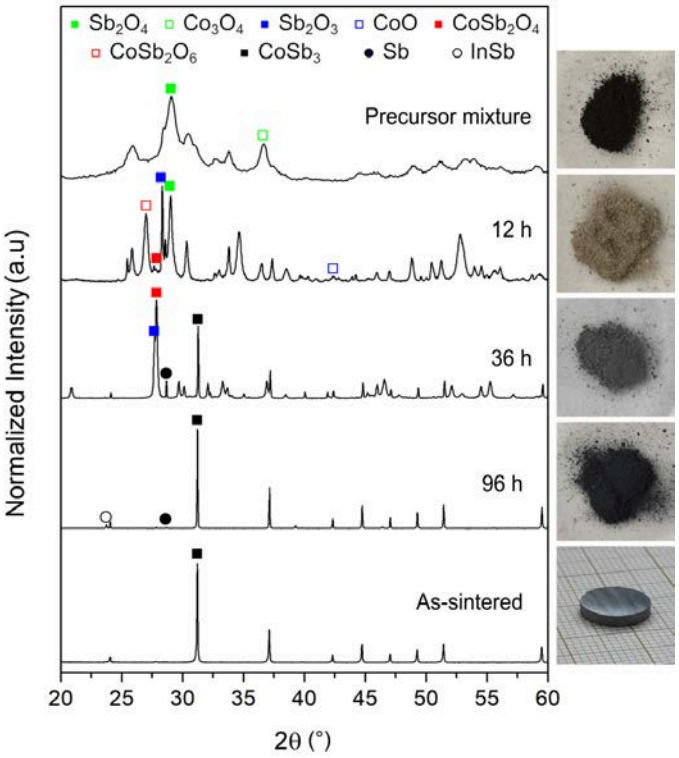

Figure 41: XRD patterns of the $In_xCo_4Sb_{12}$ magnesioreduction synthesis after 0 h, 12 h, 36 h, 96 h reaction time and after spark plasma sintering. The symbols indicate the most intense reflection of each constituting phases. The images shows the evolution of the product color with the reaction time.

$$Co_3O_4 + Mg \xrightarrow[12\,h]{810\,K} 3\,CoO + MgO \qquad \Delta G_r(810\ K) = \text{-}512.3\ kJ\ mol^{-1}\,[25] \qquad (70)$$

$$Sb_2O_4 + Mg \xrightarrow[12\,h]{810\,K} Sb_2O_3 + MgO \qquad \Delta G_r(810\ K) = \text{-}396.4\ kJ\ mol^{-1}\,[25] \qquad (71)$$

These reductions are thermodynamically possible at 810 K as indicated by the large negative Gibbs free energy of reaction. In addition, $CoSb_2O_6$ [Co^{2+}, Sb^{5+}] ($P4_2/mnm$) and $CoSb_2O_4$ [Co^{2+}, Sb^{3+}] ($P4_2/mbc$) intermediates are formed most likely by solid-state reactions between the various metal oxides in presence. This is supported by several works reporting the synthesis of these mixed oxides by conventional solid-state reaction starting from CoO and Sb_2O_3/Sb_2O_5 powders between 973 and 1073 K[26–28].

After 36 h, no trace of $CoSb_2O_6$ remains on the XRD pattern (fig. 41) and $CoSb_2O_4$ is the major phase representing 60 mol.% of the sample. According to the simultaneous decrease of $CoSb_2O_6$ and increase of $CoSb_2O_4$ contents, one might expect

$CoSb_2O_4$ to be formed from the reduction of $CoSb_2O_6$ according to:

$$CoSb_2O_6 + 2\,Mg \longrightarrow CoSb_2O_4 + 2\,MgO \tag{72}$$

More interestingly, skutterudite starts forming (≈ 10 %) and the lattice parameter of $a = 9.0384(8)$ Å corresponds well to $In_xCo_4Sb_{12}$ with low In-content ($x < 0.05$) [7,8]. At this point of the reaction, no more Sb^{5+} and Co^{3+} are present in the reaction media and Sb^{3+} and Co^{2+} are consecutively reduced in metallic Co and Sb.

The complete reduction of $CoSb_2O_4$ and Sb_2O_3 in $CoSb_3$ takes 60 more hours according to:

$$2\,CoSb_2O_4 + Sb + 11\,Mg \longrightarrow 2\,CoSb_3 + 11\,MgO \tag{73}$$

Traces of InSb appear on the diffraction patterns after 72 h. We hypothesize that In was solubilized in $CoSb_2O_4$ because (i) the formation of InSb corresponds to the total reduction of $CoSb_2O_4$, (ii) the refined lattice parameters of the latter, $a = 8.5078(5)$ Å and $c = 5.9316(5)$ Å, are significantly larger that literature data, $a = 8.49285(7)$ Å and $c = 5.92449(5)$ Å [26] and (iii) other elements such as Pb^{2+} can substitute Sb to a great extent in $CoSb_2O_4$ [26]. In presence of InSb, the lattice parameter of In_xCoSb_3 increases from 9.0384(2) Å at 48 h to 9.04872(4) Å at 96 h. This can be explained by the insertion of In in the $CoSb_3$ structure according to:

$$Co_4Sb_{12} + xInSb \longrightarrow In_xCo_4Sb_{12} + xSb \tag{74}$$

The slow diffusion of In in $CoSb_3$ was already stressed out by Grytsiv *et al.* [8]. After 96 h, the reaction media is mostly composed of $In_xCo_4Sb_{12}$ with $a = 9.04872(4)$ Å which corresponds to x = 0.17 - 0.18 [7,8] and of a small amount of InSb (≈ 4 mol.%) and Sb (≈ 2 mol.%). No traces of MgO or Mg containing compound are visible at any time on the diffraction patterns. For this reason, we hypothesize that the reduction reactions occurs *via* the slow oxidation of the Mg chunks by the equilibrium O_2 vapor pressure of the oxides. This is consistent with the general aspect of the Mg chunks between 24 h to 48 h which are clearly oxidized at the surface (powdery and white) but remain metallic and relatively shinny at the core.

The as-synthesized powder was spark plasma sintered to obtain pellets with 97 % relative density. The XRD pattern of the as-sintered pellet (fig. 41) is fully indexed

with the skutterudite structure type. Rietveld refinement results in a lattice parameter $a = 9.0527(2)$ Å which is significantly larger than for the as-synthesized powder. Along with the disappearance of the InSb secondary phase, whose melting point (789 K) is lower than the sintering temperature, this suggests that InSb reacts with the skutterudite matrix during the sintering step thus increasing the inserted In content. According to literature data, this lattice parameter corresponds to a true $In_xCo_4Sb_{12}$ composition close to x = 0.20 - 0.22[7,8]. The scenario is very similar to the synthesis of $In_{0.13}Co_4Sb_{12}$ where about 20 % of In was inserted in the structure during the sintering step[19].

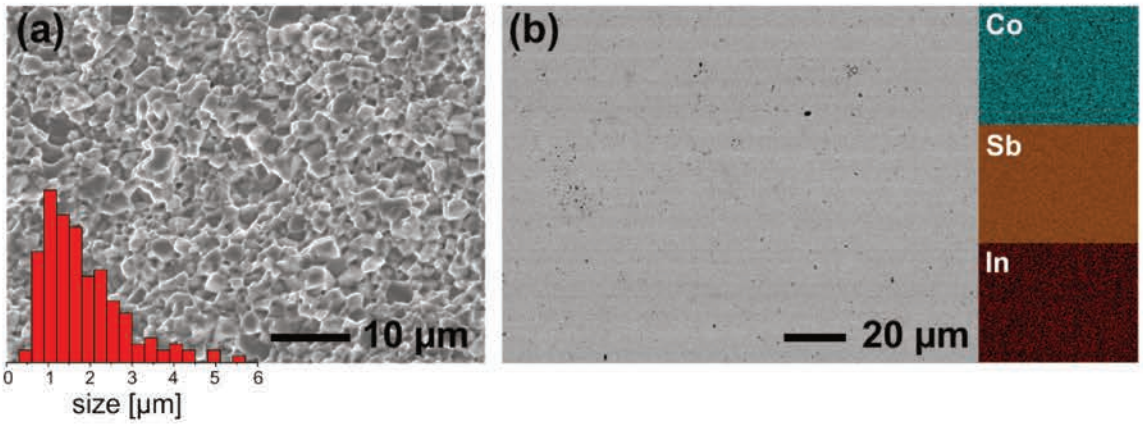

Figure 42: (a) Secondary electrons SEM image of a broken cross-section of a densified $In_{0.22}Co_4Sb_{12}$ pellet and histogram showing the distribution of the apparent grain size. (b) Backscattered electrons SEM image and corresponding EDS elementary mappings of the pellet polished surface.

Backscattered electron image and SEM-EDS mapping of the pellet (fig. 42b) reveal homogeneous chemical composition. Indium filling fraction could however not be accurately quantified by EDS because of its low concentration and the partial overlapping of the In L_α and the intense Sb L_α peaks. The magnesioreduction synthesis of $In_{0.30}Co_4Sb_{12}$ was also attempted but InSb in excess leaked out of the die during sintering and the resulting skutterudite lattice parameter remained close to $a = 9.053$ Å. As a result, $In_{0.22}Co_4Sb_{12}$ would be In-richest composition accessible by magnesioreduction synthesis in this reaction conditions. It is in agreement with the solubility limit usually reported for In-filled $CoSb_3$ prepared by conventional melting/annealing synthesis[8]. The SEM secondary electrons image of the broken cross-section of a pellet is shown in fig. 42a. The microstructure is typical for magnesioreduced skutterudite with well-faceted grain and size distribution characterized by an average value of 1.8 μm. The present grain size is significantly larger than our previous work[19]. This is mostly attributed to the 90 K higher sintering temperature found necessary to complete the reaction. Also the higher content of liquid InSb might have favored grain growth by accelerating matter transport during the sintering[29].

Thermoelectric properties

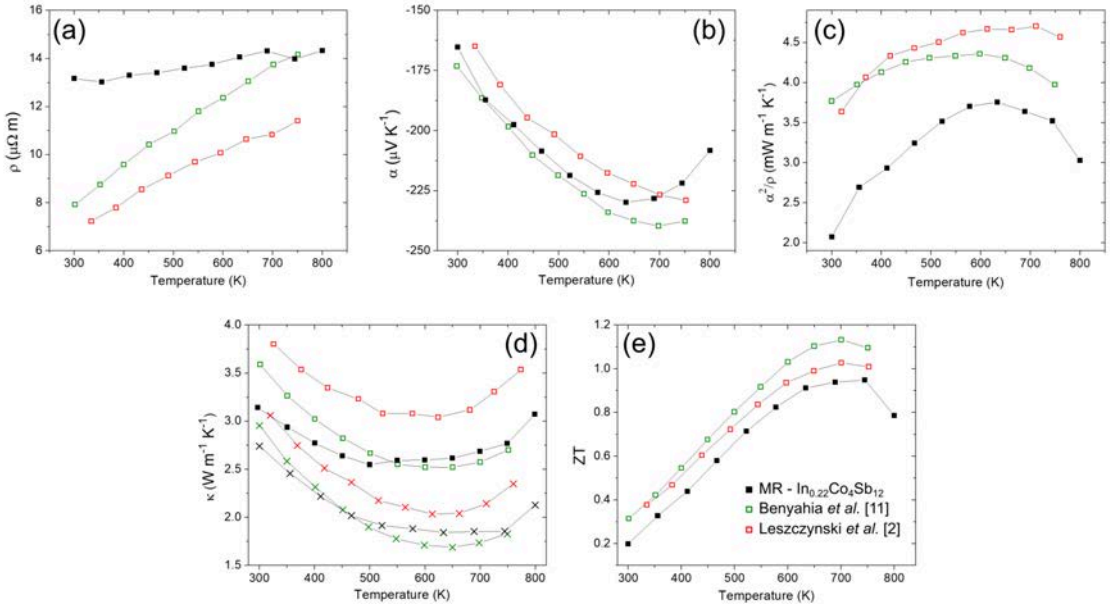

Figure 43: High-temperature dependence of (a) the electrical resistivity, (b) Seebeck coefficient, (c) power factor, (d) total (squares) and lattice (crosses) thermal conductivities and (d) figure-of-merit ZT of $In_{0.22}Co_4Sb_{12}$ synthesized by magnesioreduction (filled black squares) along with literature data for $In_{0.25}Co_4Sb_{12}$ taken from[11] (green empty squares) and $In_{0.28}Co_4Sb_{12}$ taken from[2] (red empty squares).

The thermoelectric properties of $In_{0.22}Co_4Sb_{12}$ is shown in fig. 43 and compared to literature data with similar compositions. Data reported by Benyahia *et al.*[11] and Leszczynski *et al.*[2] were obtained for materials synthesized by melting/annealing/sintering method. Although the Seebeck coefficient of our sample compares well to literature data, the resistivity is more elevated, especially near room temperature. As a direct consequence, the PF_{max} is 7 to 20 % lower at 750 K. Despite its good purity and density, small cracks appeared on our sample upon thermal cycles that could explain the higher measured resistivity. No clear reasons could be found to explain such deterioration.

The room temperature thermal conductivity of MR sample is about 3.2 W m^{-1} K^{-1} and reaches its minimum value of 2.6 W m^{-1} K^{-1} in the 450 - 650 K range. The simultaneous decrease of α and upturn of κ at about 650 K is attributed to the bipolar effect *i.e.* to the contribution of two types of charge carriers to the material transport properties. The lattice thermal conductivity was determined by subtracting κ_e to κ and κ_e was calculated using the the Wiedermann-Franz law $\kappa_e = L\ T/\rho$ with L taken from[2] as 1.7. 10^{-8} W Ω K^{-2}. The κ_L of the magnesiosynthesized sample corresponds well to the lower κ_L values of the literature over the entire temperature

range. No significant decrease of κ_L is measured at room temperature contrary to our previous work on $In_{0.13}Co_4Sb_{12}$ certainly because of the larger average grain size 1.8 μm and 600 nm, respectively, and the stronger influence of the rattlers over the mesostructure at such elevated concentration. As a consequence of the lower *PF*, a ZT_{max} of 0.95 at 750 K is obtained which remains 5 and 15 % lower than the reference samples made by conventional melting/annealing process.

Conclusions

The investigation of the reaction mechanism for the magnesioreduction synthesis of In-filled skutterudite from Sb_2O_4 and In-doped Co_3O_4 evidenced a complex scenario involving intermediate species: CoO, Sb_2O_3, $CoSb_2O_6$ and $CoSb_2O_4$. The formation of $CoSb_3$ precedes the insertion of In-rattler in the cage. After spark plasma sintering, the resulting material is single phase skutterudite with composition close to $In_{0.22}Co_4Sb_{12}$ which corresponds to the In-richest composition which could be synthesized by this technique in this conditions. A ZT_{max} of 0.95 is measured at 750 K due to limited *PF* resulting from elevated ρ caused by microcracks appearing in the pellets. In addition to important energy and time saving, the relatively mild reaction conditions used in this process prevent high Mg vapors pressure inside the reactor thus avoiding the formation of deleterious Mg-containing side-products which often limits the up-scaling perspectives of magnesioreduction processes. Finally, the knowledge gained on the reaction mechanism will be a precious help for the development of optimized reaction conditions (multi-step heat treatment, mixed oxide precursors) enabling the insertion of other filler atoms (*e.g.* Ba, rare earths elements) whose respective oxides are often too stable to be reduced by Mg in the present reaction conditions.

Acknowledgements

Loic Joanny and Francis Gouttefangeas are acknowledged for SEM images and EDS analyses performed on the CMEBA platform belonging to the ScanMAT unit (UMS 2001, University of Rennes 1) which received a financial support from the European Union (CPER-FEDER 2007-2014).

References

[1] G. Rogl, P. Rogl, *Curr. Opin. Green Sustainable Chem.* **2017**, *4*, 50–57.

[2] J. Leszczynski, V. D. Ros, B. Lenoir, A. Dauscher, C. Candolfi, P. Masschelein, J. Hejtmanek, K. Kutorasinski, J. Tobola, R. I. Smith, C. Stiewe, E. Müller, *J. Phys. D: Appl. Phys.* **2013**, *46*, 495106.

[3] X. Li, Q. Zhang, Y. Kang, C. Chen, L. Zhang, D. Yu, Y. Tian, B. Xu, *J. Alloys Compd.* **2016**, *677*, 61–65.

[4] Y. Kang, F. Yu, C. Chen, Q. Zhang, H. Sun, L. Zhang, D. Yu, Y. Tian, B. Xu, *J. Mater. Sci.: Mater. Electron.* **2017**, *28*, 8771–8776.

[5] G. S. Nolas, M. Kaeser, R. T. Littleton, T. M. Tritt, *Appl. Phys. Lett.* **2000**, *77*, 1855.

[6] G. Rogl, A. Grytsiv, K. Yubuta, S. Puchegger, E. Bauer, C. Raju, R. Mallik, P. Rogl, *Acta Mater.* **2015**, *95*, 201–211.

[7] Y. Tang, Y. Qiu, L. Xi, X. Shi, W. Zhang, L. Chen, S.-M. Tseng, S. wen Chend, G. J. Snyder, *Energy Environ. Sci.* **2014**, *7*, 812.

[8] A. Grytsiv, P. Rogl, H. Michor, E. Bauer, G. Giester, *J. Electron. Mater.* **2013**, *42*, 2940–2952.

[9] E. Visnow, C. P. Heinrich, A. Schmitz, J. de Boor, P. Leidich, B. Klobes, R. P. Hermann, W. E. Müller, W. Tremel, *Inorg. Chem.* **2015**, *54*, 7818–7827.

[10] R. C. Mallik, J. Y. Jung, S. C. Ur, I. H. Kim, *Met. Mater. Int.* **2008**, *14*, 223.

[11] M. Benyahia, V. Ohorodniichuk, E. Leroy, A. Dauscher, B. Lenoir, E. Alleno, *J. Alloys Compd.* **2018**, *735*, 1096–1104.

[12] T. He, J. Chen, H. D. Rosenfeld, M. A. Subramanian, *Chem. Mater.* **2006**, *18*, 759–762.

[13] J. Eilertsen, S. Rouvimov, M. Subramanian, *Acta Mater.* **2012**, *60*, 2178–2185.

[14] G. Li, K. Kurosaki, Y. Ohishi, H. Muta, S. Yamanaka, *J. Electron. Mater.* **2013**, *42*, 1463.

[15] H. Li, X. Su, X. Tang, Q. Zhang, C. Uher, G. J. Snyder, U. Aydemir, *J Materiomics* **2017**, *3*, 273–279.

[16] C. Chubilleau, B. Lenoir, C. Candolfi, P. Masschelein, A. Dauscher, E. Guilmeau, C. Godart, *J. Alloys Compd.* **2014**, *589*, 513–523.

[17] A. Gharleghi, P.-C. Hung, F.-H. Lin, C.-J. Liu, *ACS Appl. Mater. Interfaces* **2016**, *8*, 35123–35131.

[18] S. Lee, K. H. Lee, Y.-M. Kim, H. S. Kim, G. J. Snyder, S. Baik, S. W. Kim, *Acta Mater.* **2018**, *142*, 8–17.

[19] S. Le Tonquesse, E. Alleno, V. Demange, V. Dorcet, L. Joanny, C. Prestipino, O. Rouleau, M. Pasturel, *J. Alloys Compd.* **2019**, *796*, 176–184.

[20] E. Antolini, M. Ferretti, *J. Solid State Chem.* **1995**, *117*, 1–7.

[21] L. Ma, C. Y. Seo, X. Chen, K. Sun, J. W. Schwank, *Appl. Catal. B-Environ.* **2018**, *222*, 44–58.

[22] J. Rodriguez-Carvajal, *Physica B* **1993**, *192*, 55–69.

[23] O. Rouleau, E. Alleno, *Rev. Sci. Instrum.* **2013**, *84*, 105103.

[24] H. Toraya, *J. Appl. Cryst.* **2000**, *33*, 1324–1328.

[25] O. Knacke, O. Kubaschewski, K. Hesselmann, *Thermo-chemical Properties of Inorganic Substances*.

[26] B. P. de Laune, C. Greaves, *J. Solid State Chem.* **2012**, *187*, 225–230.

[27] D. Larcher, A. S. Prakash, L. Laffont, M. Womes, J. C. Jumas, J. Olivier-Fourcade, M. S. Hedge, J.-M. Tarascon, *J. Electrochem. Soc.* **2006**, *153*, A1778–A1787.

[28] J. N. Reimers, J. E. Greedan, C. V. Stager, R. Kremer, *J. Solid State Chem.* **1989**, *83*, 20–30.

[29] S.-J. L. Kang, *Sintering: Densification, Grain Growth and Microstructure* **2004**.

Reaction mechanism and thermoelectric properties of $In_{0.22}Co_4Sb_{12}$ prepared by magnesiothermy: supplementary information

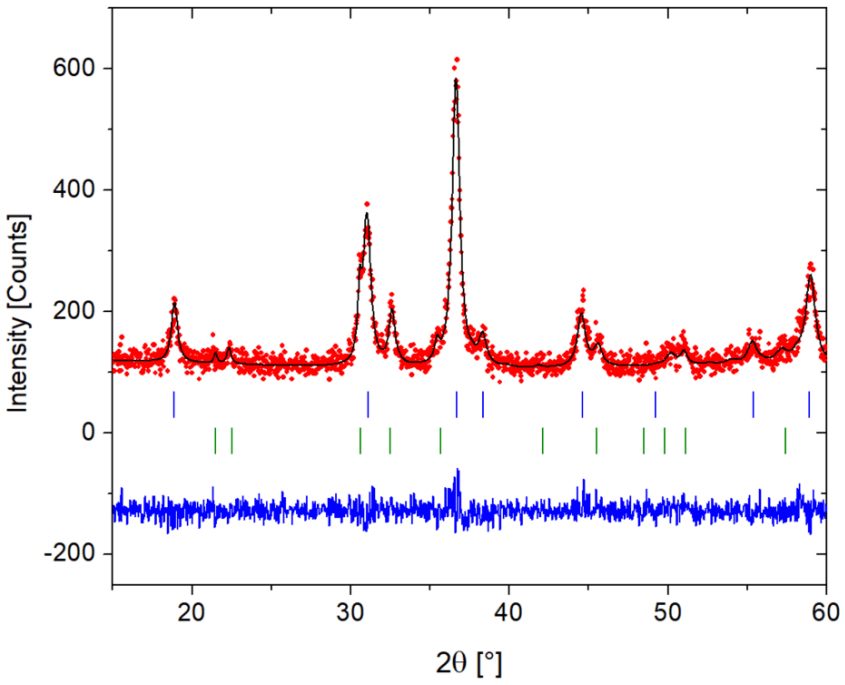

Figure SI 6: Rietveld refined XRD pattern of '$In_{0.19}Co_{2.81}O_4$'. The experimental data are plotted in red symbols, the calculated one in black line and the difference in blue line. The vertical ticks indicate the theoretical Bragg peak positions of Co_3O_4 (blue) and In_2O_3 (green).

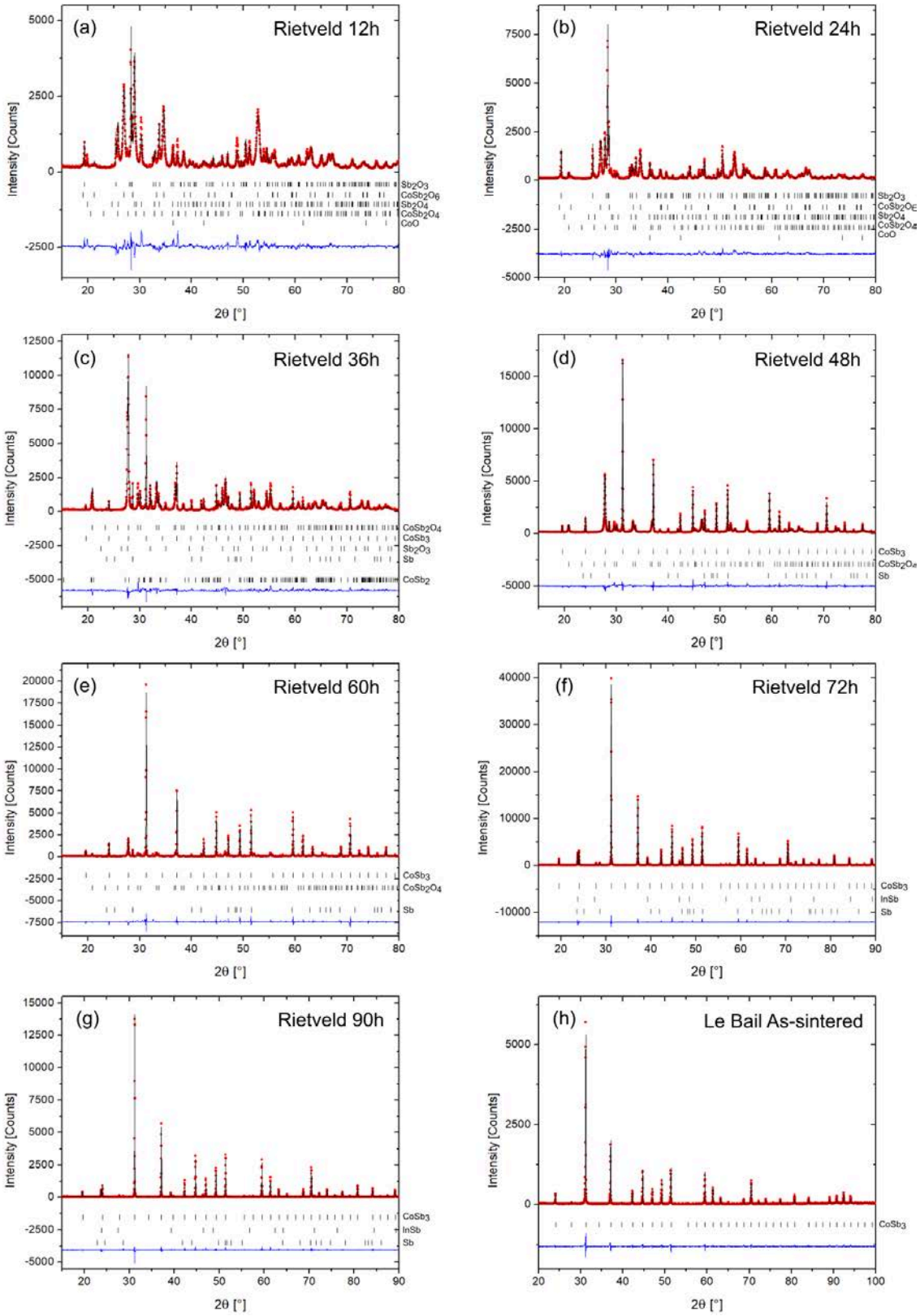

Figure SI 7: Rietveld refined XRD patterns of the reaction media after (a) 12 h, (b) 24 h, (c) 36 h, (d) 48 h, (e) 60 h, (f) 72 h, (g) 96 h during the MR synthesis of $In_{0.22}Co_4Sb_{12}$. (h) The Le bail refined XRD pattern of the $In_{0.22}Co_4Sb_{12}$ pellet after spark plasma sintering. The experimental data are plotted in red symbols, the calculated one in black line and the difference in blue line. The vertical ticks indicate the theoretical Bragg peak positions of the different phases in presence.

Table SI 1: Structural parameters for $CoSb_3$ (space group $Im\bar{3}$) used for the Rietveld refinement of the patterns in fig. SI 7. The isotropic atomic displacement parameters were set to 0.3 Å^2 for Co/Sb atoms and 1.5 Å^2 for In atoms. The In occupancies were set to fit the composition determined from the lattice parameters and [1,2].

		Co ($8c$)			Sb ($24g$)			In ($2a$)			
Pattern	a (Å)	x	y	z	x	y	z	x	y	z	Occ.
(c)	9.0384(8)	1/4	1/4	1/4	0	0.1587(4)	0.3359(7)	0	0	0	0
(d)	9.0384(2)	1/4	1/4	1/4	0	0.1577(4)	0.3340(4)	0	0	0	0
(e)	9.0396(1)	1/4	1/4	1/4	0	0.1572(6)	0.3342(2)	0	0	0	0
(f)	9.0475(4)	1/4	1/4	1/4	0	0.1574(4)	0.3342(4)	0	0	0	0.29
(g)	9.04872(4)	1/4	1/4	1/4	0	0.1575(4)	0.3347(4)	0	0	0	0.34
(h)	9.0527(1)	/	/	/	/	/	/	/	/	/	/

Table SI 2: Lattice parameters for $CoSb_2O_4$ (s.g. $P4_2/mbc$) used for the Rietveld refinement of the patterns in fig. SI 7. The isotropic atomic displacement parameters were set to 0.3 Å^2 for Co atoms, 0.6 Å^2 for Sb atoms and 2 Å^2 for O atoms. The structural parameters where taken from [3]: Co ($4d$) $x = 0$, $y = 1/2$, $z = 1/4$; Sb ($8h$) $x = 0.1610$, $y = 0.1765$, $z = 0$; O ($8h$) $x = 0.1412$, $y = 0.4052$, $z = 0$; O ($8g$) $x = 0.1803$, $y = 0.6803$, $z = 1/4$.

Pattern	a (Å)	c (Å)
(a)	8.63(2)	5.79(2)
(b)	8.5086(9)	5.9290(9)
(c)	8.5071(5)	5.9319(5)
(d)	8.5061(4)	5.9305(4)
(e)	8.5098(8)	5.9297(8)

Table SI 3: Lattice parameters for $CoSb_2O_6$ (s.g. $P4_2/mnm$) used for the Rietveld refinement of the patterns in fig. SI 7. The isotropic atomic displacement parameters were set to 0.3 Å^2 for Co atoms, 0.6 Å^2 for Sb atoms and 2 Å^2 for O atoms. The structural parameters where taken from [4]: Co ($2a$) $x = 0$, $y = 0$, $z = 0$; Sb ($4e$) $x = 0$, $y = 0$, $z = 0.3358$; O ($4f$) $x = 0.3082$, $y = 0.3082$, $z = 0$; O ($8j$) $x = 0.3026$, $y = 0.3026$, $z = 0.3264$.

Pattern	a (Å)	c (Å)
(a)	4.6706(5)	9.324(2)
(b)	4.6663(4)	9.316(1)

Table SI 4: Lattice parameters for Sb_2O_4 (s.g. $Pna2_1$) used for the Rietveld refinement of the patterns in fig. SI 7. The isotropic atomic displacement parameters were set to 0.3 Å^2 for Sb atoms and 1.5 Å^2 for O atoms. The structural parameters where taken from [5]: Sb ($4e$) $x = 0$, $y = 0.2209$, $z = 1/4$; Sb ($4c$) $x = 1/4$, $y = 1/4$, $z = 0$; O ($8f$) $x = 0.4007$, $y = 0.3950$, $z = 0.0165$; O ($8f$) $x = 0.3258$, $y = 0.0520$, $z = 0.32637$.

Pattern	a (Å)	b (Å)	c (Å)
(a)	5.442(8)	4.813(8)	11.781(7)
(b)	5.44(1)	4.81(1)	11.77(1)

Table SI 5: Lattice parameters for Sb_2O_3 (s.g. *Pccn*) used for the Rietveld refinement of the patterns in fig. SI 7. The isotropic atomic displacement parameters were set to 0.3 Å^2 for Sb atoms and 1 Å^2 for O atoms. The structural parameters where taken from [6]: Sb ($8e$) $x = 0.0415$, $y = 0.1275$, $z = 0.1784$; O ($8e$) $x = 0.3480$, $y = 0.0591$, $z = 0.3554$; O ($4c$) $x = 1/4$, $y = 1/4$, $z = 0.0229$.

Pattern	a (Å)	b (Å)	c (Å)
(a)	4.921(3)	12.490(6)	5.422(3)
(b)	4.917(3)	12.480(8)	5.419(3)
(c)	4.922(4)	12.48(1)	5.434(4)

Table SI 6: Lattice parameters for CoO (s.g. $Fm\bar{3}m$) used of the Rietveld refinement of the patterns in fig. SI 7. The isotropic atomic displacement parameters were set to 0.3 Å^2 for Co atoms and 1 Å^2 for O atoms. The structural parameters where taken from [7]: Co ($4a$) $x = 0$, $y = 0$, $z = 0$; O ($4b$) $x = 1/2$, $y = 1/2$, $z = 1/2$

Pattern	a (Å)
(a)	4.265(2)

Table SI 7: Lattice parameters for InSb (s.g. $F\bar{4}3m$) used for the Rietveld refinement of the patterns in fig. SI 7. The isotropic atomic displacement parameters were set to 0.3 Å^2 for In atoms and 0.3 Å^2 for Sb atoms. The structural parameters where taken from [8]: In ($4a$) $x = 0$, $y = 0$, $z = 0$; Sb ($4c$) $x = 1/4$, $y = 1/4$, $z = 1/4$

Pattern	a (Å)
(f)	6.4834(1)
(g)	6.4833(2)

Table SI 8: Lattice parameters for Sb (s.g. $R\bar{3}m$) used for the Rietveld refinement of the patterns in fig. SI 7. The isotropic atomic displacement parameters were set to 0.3 Å^2 for Sb atoms. The structural parameters where taken from [9]: Sb ($6c$) $x = 0$, $y = 0$, $z = 0.2271$

Pattern	a (Å)	c (Å)
(c)	4.3087(3)	11.28(2)
(e)	4.3074(2)	11.28(1)
(f)	4.3055(3)	11.31(1)

Table SI 9: Lattice parameters for $CoSb_2$ (s.g. $P12_1/c1$) used for the Rietveld refinement of the patterns in fig. SI 7. The isotropic atomic displacement parameters were set to 0.3 Å^2 for Sb atoms. The structural parameters where taken from [10]: Co ($4e$) $x = 0.2299$, $y = 0.0005$, $z = 0.2183$, Sb ($4e$) $x = 0.1534$, $y = 0.6431$, $z = 0.3325$, Sb ($4e$) $x = 0.3511$, $y = 0.3607$, $z = 0.1329$

Pattern	a (Å)	b (Å)	c (Å)	β
(d)	6.512(2)	6.388(2)	6.543(2)	117.62(3)

References

[1] A. Grytsiv, P. Rogl, H. Michor, E. Bauer, G. Giester, *J. Electron. Mater.* **2013**, *42*, 2940–2952.

[2] Y. Tang, Y. Qiu, L. Xi, X. Shi, W. Zhang, L. Chen, S.-M. Tseng, S. wen Chend, G. J. Snyder, *Energy Environ. Sci.* **2014**, *7*, 812.

[3] P. Norby, M. Roelsgaard, M. Sondergaard, B. B. Iversen, *Cryst. Growth Des.* **2016**, *16*, 834–841.

[4] J. N. Reimers, J. E. Greedan, C. V. Stager, R. Kremer, *J. Solid State Chem.* **1989**, *83*, 20–30.

[5] K. Ok, N. Bhuvanesh, P. Halasyamani, *J. Solid State Chem.* **2001**, *161*, 57–62.

[6] C. Svensson, *Acta Crystallogr. B* **1974**, *30*, 458–461.

[7] R. Kannan, M. Seehra, *Phys. Rev. B: Condens. Matter* **1987**, *35*, 6847–6853.

[8] T. Abaeva, V. Bublik, A. Morozov, A. Pereverzev, *Inorg. Mater.* **1987**, *23*, 171–173.

[9] Y. Ugai, E. Goncharov, A. Samoilov, N. Malkin, *Inorg. Mater.* **1984**, *20*, 1084–1086.

[10] T. Siegrist, F. Hulliger, *J. Solid State Chem.* **1986**, *63*, 23–30.

Mesostructure - thermoelectric properties relationships in $V_xMn_{1-x}Si_{1.74}$ (x = 0, 0.04) Higher Manganese Silicides prepared by magnesiothermy

Sylvain Le Tonquesse,[a] Vincent Dorcet,[a] Loic Joanny,[a] Valérie Demange,[a] Carmelo Prestipino,[a] Quansheng Guo,[b,c] David Berthebaud,[b] Takao Mori[c] and Mathieu Pasturel*[a]

[a] Univ Rennes, CNRS, ISCR-UMR6226/ScanMAT-UMS2001, F-35000, Rennes, France. Tel: +33-2-23-23-58-61; E-mail: mathieu.pasturel@univ-rennes1.fr

[b] CNRS - Saint-Gobain - NIMS, UMI3629, Laboratory for Innovative Key Materials and Structures (LINK), National Institute for Materials Science, 1-1 Namiki, Tsukuba, Ibaraki 305-0044, Japan

[c] National Institute for Materials Science (NIMS), WPI-MANA and CFSN, Tsukuba, Japan

Published in *Journal of Alloys and Compound*

Abstract

The synthesis of pure pristine and vanadium-doped $MnSi_\gamma$ (γ = 1.74) powder by a relatively fast, 'low temperature' and high yield magnesioreduction process is described. The powder obtained by this innovative route is composed of well-crystallized grains with sizes ranging from 20 to 500 nm and free from any MnSi precipitates. Mesostructured densified pellets with average grain sizes as small as 550 nm are obtained by spark plasma sintering (SPS). Detailed structural and microstructural characterization of the samples were realized at every stage of the process, highlighting a high concentration of defects such as orientational or spacing anomalies of the Nowotny phase, γ variations within a single grain and dislocations. Accordingly a significant decrease of the lattice thermal conductivity is evidenced in comparison to conventionally synthesized (arc-melting/SPS) samples having similar density and (V/)Mn/Si stoichiometry. The thermoelectric properties of these materials are discussed in regard of their complex microstructure.

Introduction

Thermoelectric (TE) materials are being extensively investigated for their potential of energy-saving and dynamical energy harvesting through solid state conversion of heat into electricity[1,2]. Higher Manganese Silicides (HMS) with chemical formula $MnSi_\gamma$ ($1.72 < \gamma < 1.75$) are widely considered as a promising thermolectrical material because of their potential in industrial application. Indeed, HMS are low density materials composed of non-hazardous and inexpensive elements and they possess very good mechanical properties and oxidation resistance. HMS are currently used as *p*-type material for industrial thermoelectric generator (TEG) prototypes operating at mid-temperature[3,4]. However, a large scale industrial implementation of such materials is limited by their moderate thermoelectric properties usually evaluated by the figure-of-merit ZT defined as:

$$ZT = \frac{\alpha^2}{\rho(\kappa_L + \kappa_e)}T \tag{75}$$

where α is the Seebeck coefficient, ρ the electrical resistivity, κ_L and κ_e the lattice and electronic contribution to the total thermal conductivity κ and T the operating temperature.

Improvement of their TE properties can be achieved through various strategies enhancing ZT[5,6]. Many studies have been focused on chemical doping of $MnSi_\gamma$ to increase the power factor $PF = \alpha^2/\rho$[7,8] or on fabrication of elaborated microstructures with the aim to decrease κ_L *via* synthesis routes such as ball-milling[9], melt-spinning[10,11], fast combustion[12] or reactive sintering[13,14]. For example, ZT_{max} exceeding unity has been obtained for Re supersaturated HMS realized by liquid quenching[15,16] at the expense of industrial scalability and elevated price of Re.

Investigation of HMS is rather difficult because these materials are characterized by a high structural, microstructural and synthesis complexity. This includes (i) the difficulty to obtain pure samples due to the incongruent melting of $MnSi_\gamma$ [17] and the high vapor pressure of Mn at elevated temperature[18], (ii) the formation of metallic MnSi precipitates inside HMS grains which can severely affect the TE[19,20] and mechanical[21] properties, (iii) the incommensurate chimney-ladder crystal structure which is often unsatisfactorily described as a series of commensurate Mn_ySi_x structures (x, y are natural numbers)[22], and (iv) the anisotropic transport properties which can bias the comparison of performances in the case of crystallographically textured samples[23].

Recently, we reported on the synthesis of high purity mesostructured TE skutterudites by magnesioreduction of oxides[24]. This scalable process based on cheap and air-stable oxides leads to the formation at moderate temperature of well-crystallized submicronic powders with elevated TE properties. Similar process was attempted to obtain HMS powders by Girard *et al.*[25] starting from nanosilica and MnO_2 in molten salt fluxes but the information on such process is limited to a single conference abstract and, to the best of our knowledge, no peer-review article has ever been published. We have thus applied a flux-free magnesioreduction process employing MnO and Si as reactants for the synthesis of pure and vanadium doped $MnSi_{1.74}$. The structural and microstructural characterizations, using X-ray diffraction Rietveld refinements in a composite crystal structure model, electron backscattering diffraction and scanning/transmission electron microscopy on both as-synthesized powders and spark plasma sintered pellets are presented thereafter. The thermal dependence of the electrical resistivity, Seebeck coefficient and thermal conductivity have been measured in the temperature range 300-800 K and subsequent thermoelectric performances are discussed in terms of structure-microstructure-properties relationships. These results are compared to equivalent HMS prepared by conventional melting-solidification-annealing method.

Experimental procedure

For the magnesioreduction (MR) synthesis of $MnSi_{1.74}$ and $V_{0.04}Mn_{0.96}Si_{1.74}$, precursor mixtures first need to be prepared by ball-milling of V_2O_5 (Merck, 99 %), MnO (Alfa Aesar, 99 %) and Si (Ventron, 99.9 %) with a molar ratio of $0 : 1 : 1.74$ and $0.02 : 0.96 : 1.74$, respectively, under air in a planetary mill (Retsch PM100) for 3 h at 650 rpm in a WC vial filled with Ø 10 mm WC balls (fig 44a). A small ball-to-powder ratio of 5 : 1 is used in order to avoid contamination by WC during the milling process. The obtained precursor mixture is cold-pressed at 65 MPa into Ø 10 mm pellets with about 4 mm height. Each pellet is placed in a Mo-crucible with Mg turnings (Strem Chemicals, $\geq$ 99 %) equally distributed under and on top of the pellet (fig. 44b). Such distribution of Mg helps to maximize the surface contact between Mg and the pellets in order to promote a homogeneous reduction and was found compulsory to avoid the presence of Mg_2Si by-product. A 25 % excess Mg is empirically needed to complete the magnesioreduction reaction:

$$\mathrm{MnO} + 1.74\ \mathrm{Si} + \underset{(+25\%)}{\mathrm{Mg}} \longrightarrow \mathrm{MnSi_{1.74}} + \mathrm{MgO} \tag{76}$$

A graphite seal is inserted between the crucible and the lid and the system is held tight with a clamping system. This set-up is placed in an Inconel tube filled with Ar to avoid the Mo-crucible oxidization. The whole is heated up to 1173 K at a

rate of 60 K h^{-1} in a tubular furnace and held at this temperature for 8 h before being cooled down by switching off the furnace (fig. 44c). At the end of the reaction the product still in the shape of a pellet can be easily separated from loose MgO powder (fig. 44d). A black powder composed of $MnSi_{\gamma}$ is obtained by softly crushing the pellet in an agate mortar. The MgO by-product is removed by soaking the as-synthesized powder twice in diluted hydrochloric acid (2 wt.%) for 5 - 10 minutes and washing three times with distilled water and once more with ethanol before being dried at 353 K overnight (fig.44e). The washed $MnSi_{\gamma}$ powder is then densified by spark plasma sintering (SPS) in Ø 10 mm graphite dies at 1273 K and 75 MPa for 20 min with 100 K min^{-1} heating/cooling rates using a FCT HP-D-10 apparatus.

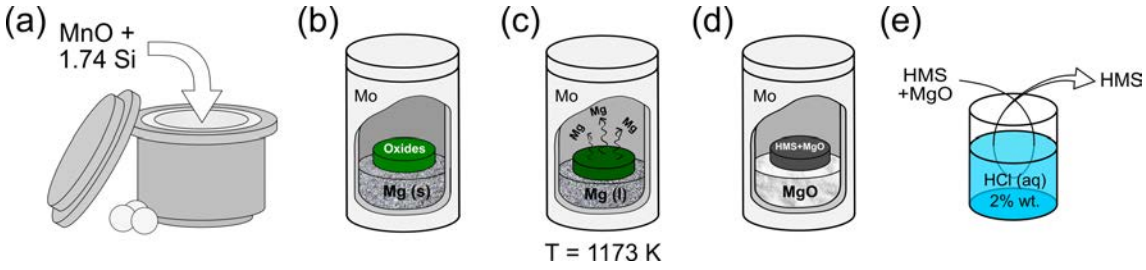

Figure 44: Main steps of the magnesioreduction synthesis: (a) MnO and Si are ball-milled in WC vial; (b) pellets of MnO/Si mixture are sealed with the adequate amount of Mg in a Mo crucible; (c) Mg vapor reduces the oxides during the heat treatment at 1173 K; (d) the reduction is completed after 8 h at 1173 K; (e) MgO is removed from the product by soaking the powder in diluted HCl.

In order to investigate how magnesiothermy synthetic route affects the final thermolectric properties, $MnSi_{1.74}$ has also been synthesized by conventional fusion solidification method. Stoichiometric amounts of the elements are arc-melted (AM) three times to ensure homogenization and the obtained ingot was annealed for 100 h at 1273 K in evacuated silica tubes. The annealed ingot was finely ground in an agate mortar and the powder was densified by SPS in Ø 10 mm graphite dies at 1238 K and 80 MPa for 5 min.

The crystal structure and purity of the samples were checked by powder X-ray diffraction (PXRD) using a Bruker D8 Advance diffractometer in the Bragg-Brentano geometry working with a monochromatized Cu Kα_1 radiation (λ = 1.5406 Å) and equipped with a LynxEye detector. Structural parameters were determined by Rietveld refinement of the PXRD patterns using JANA2006[26]. Scanning electron microscopy (SEM) images, energy dispersive spectroscopy (EDS) and electron backscattering diffraction (EBSD) were performed using a JEOL JSM 7100F microscope equipped with an Oxford EDS SDD X-Max spectrometer and an EBSD HKL Advanced Nordlys Nano detector. TEM analyses were performed on a JEOL 2100 LaB_6 instrument operating at 200 kV and equipped with an Oxford EDS SDD 80 mm^2 spectrometer and high resolution Gatan US1000 and Orius 200D cameras.

Preparation of the powder samples for SEM analyses consisted in their deposition on carbon tape followed by metallization with carbon. For transmission electron microscopy (TEM), a small amount of powder was sonicated in absolute ethanol and deposited for drying on a carbon coated copper grid. For EBSD and EDS analyses, densified pellets were consecutively mirror polished with 320 down to 1200 grit SiC papers, diamond paste (3 and 1 μm) and colloidal silica. EBSD mappings were analyzed using the *Channel 5* software (HKL Technology). Thin foils of densified pellet for TEM analyses were obtained by dimpling a 100 μm thick pellet down to 10 μm with diamond paste (3 and 1 μm) followed by Ar-ion milling using a Fischione Ion Mill 1010 operating at 4.5 kV and 4.5 mA.

The thermal diffusivity (D) has been measured by the laser flash method on Ø 10 mm and 2 mm thick samples coated with graphite using a Netzsch LFA 467 HyperFlash equipment under N_2 atmosphere. The thermal conductivity could be calculated by the $\kappa = \mathrm{D}\, C_p d$ relation with C_p the specific heat of the sample determined thanks to a Netzsch Pyroceram reference sample and d the density measured by the Archimede method. The Seebeck coefficient and electrical resistivity were measured simultaneously on 6×2×2 mm bars using a ZEM3 device (ULVAC-RIKO Inc., Yokohama, Japan) under He atmosphere.

Results and discussion

Magnesioreduction synthesis

The XRD pattern of the precursor mixture obtained by high energy ball-milling of MnO and Si is shown in fig. 45. Interestingly, MnSi and $MnSi_\gamma$ readily start to form in the milling vial indicating the reduction of manganese. According to the Ellingham diagram[27,28] the reduction of MnO by Si :

$$2\ \mathrm{MnO} + \mathrm{Si} \longrightarrow 2\ \mathrm{Mn} + \mathrm{SiO_2} \qquad \Delta G_r^\circ(298\ \mathrm{K}) = \text{-}136.5\ \mathrm{kJ.mol^{-1}} \qquad (77)$$

is thermodynamically possible. The activation energy for this reaction is probably overcome locally in the milling vial when highly energetic shocks occur. Upon further milling, metallic Mn would then react with unreacted Si to form $MnSi_\gamma$ and MnSi as already reported by different groups[29–31]. SiO_2 must be present in the mixture but could not be detected by XRD due to its probable amorphous nature. At the end of the milling step, a very intimate mixture of Mn- and Si-containing species is produced according to:

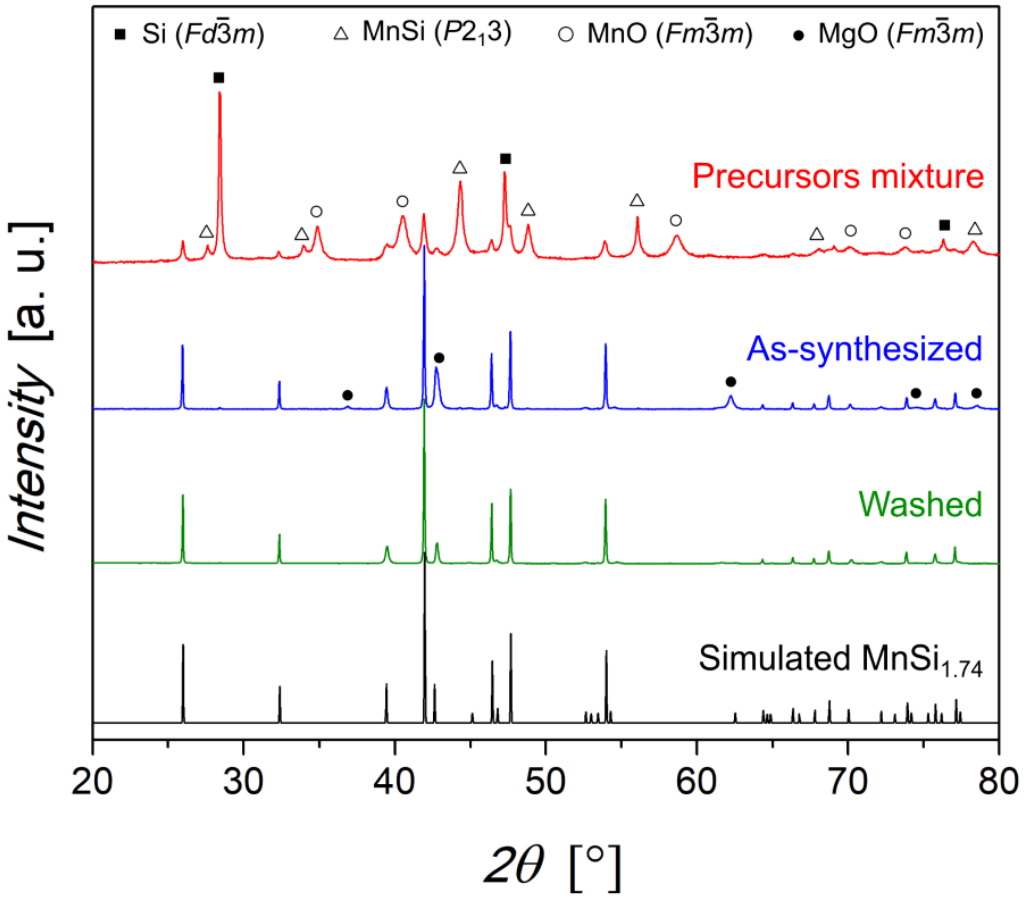

Figure 45: XRD patterns of the precursors mixture (red), as-synthesized HMS powder (blue), HCl washed HMS powder (green) and simulated pattern for $MnSi_{1.74}$ with first order satellite peaks [22] (black). Some weak intensity satellite reflections in the simulated pattern might not be visible in the experimental ones because of their large broadening (see text for details).

$$\mathrm{MnO} + 1.74\,\mathrm{Si} \xrightarrow[3\,\mathrm{h}]{650\,\mathrm{rpm}} \underset{51\%}{\mathrm{Si}} + \underset{20\%}{\mathrm{MnO}} + \underset{18\%}{\mathrm{MnSi}} + \underset{11\%}{\mathrm{MnSi_\gamma}}\ (+\,\mathrm{SiO_2}) \tag{78}$$

where the molar concentrations are determined from Rietveld refinement (see fig. SI 8 and tables SI 8-12).

The precursors mixture is then reacted with Mg according to:

$$\underset{51\%}{\mathrm{Si}} + \underset{20\%}{\mathrm{MnO}} + \underset{18\%}{\mathrm{MnSi}} + \underset{11\%}{\mathrm{MnSi_\gamma}}\ (+\mathrm{SiO_2}) + \mathrm{Mg} \xrightarrow[8\,\mathrm{h}]{1123\,\mathrm{K}} \mathrm{MnSi_\gamma} + \mathrm{MgO} \tag{79}$$

and XRD on the as-synthesized powders (fig. 45, blue curve) confirms that the product is only composed of $MnSi_\gamma$ and MgO.

Magnesioreduction was attempted at several temperatures and a lower limit of 1073 K has been found to initiate this reaction. The high vapor pressure of Mg at these elevated temperatures is expected to easily penetrate inside the pellet to induce the reduction of the oxides and subsequent interdiffusion of native metals to form the targeted silicide. Additionally, the reduction of MnO and SiO_2 by Mg is highly exothermic at 1123 K with ΔH_r = - 346.9 and - 344.0 kJ mol^{-1} respectively[27,28]. The heat released locally inside the pellet may accelerate the reaction and a scenario close to a combustion synthesis[32,33] cannot be ruled out.

Microstructure of the magnesioreduced $MnSi_\gamma$ powders

Figure 46a and 46b show secondary electron SEM images of an as-synthesized MR HMS powder containing $MnSi_\gamma$ and MgO. It is composed of grains with sizes ranging from about 50 nm to several hundreds of nm, some of them forming aggregates with micrometric sizes. According to EDS elemental analyses, MgO constitute 60 at.% of the as-synthesized powder. Moreover, they give a Si/Mn metal ratio of about 1.7 which is in agreement with the targeted $MnSi_{1.74}$ composition.

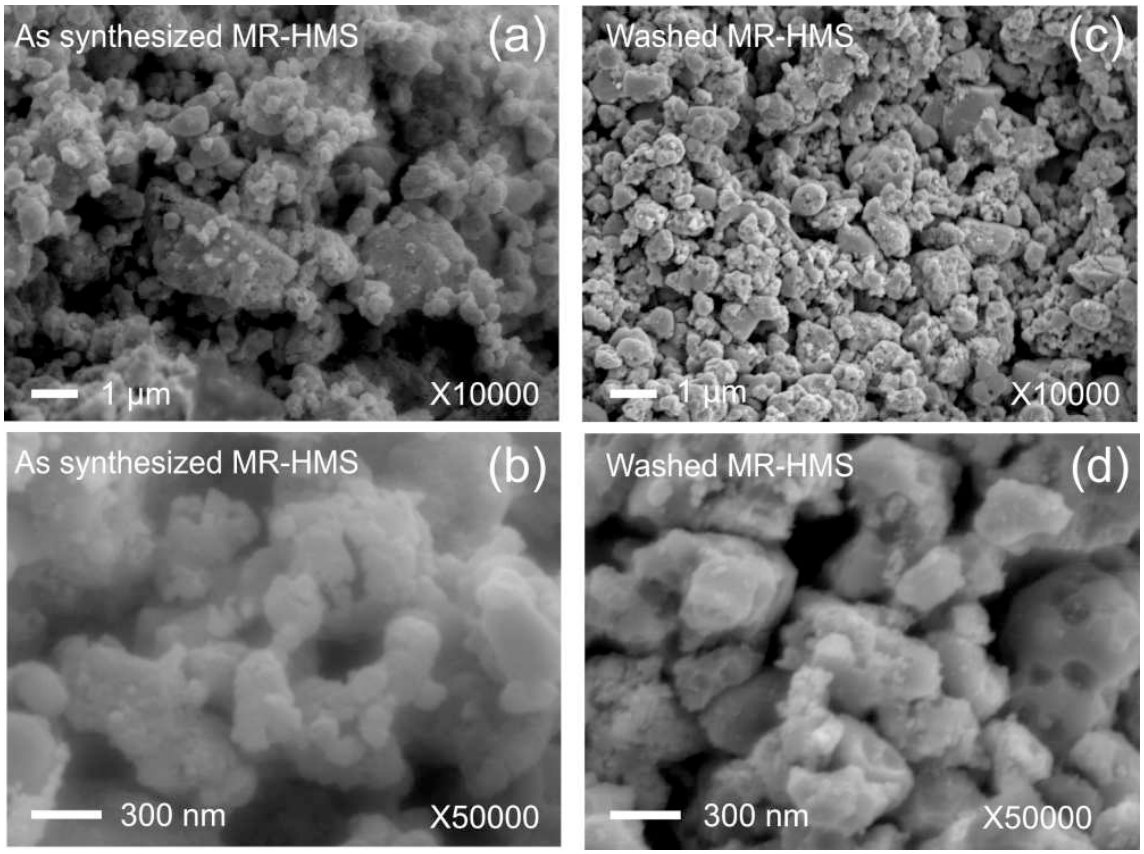

Figure 46: Secondary electron SEM images of (a)(b) as-synthesized MR HMS powder composed of $MnSi_{1.74}$ and MgO and (c)(d) MR HMS powder after acidic washing containing only $MnSi_{1.74}$, at two different magnifications.

The HMS + MgO composite microstructure has been investigated by TEM. A typ-

ical brightfield image of the as-synthesized HMS powder is shown in fig. 47a. EDS analyses and selected area electron diffraction realized on several areas of the sample assign the electron-opaque grains to $MnSi_\gamma$ while the more electron-transparent matrix is mainly composed of much smaller MgO crystals. These observations are consistent with the much broader XRD Bragg peaks ascribed to MgO compared to those of HMS (fig. 45). We hypothesize here that the MgO matrix formed during the MR reaction and surrounding the $MnSi_\gamma$ grains plays a significant role by limiting the silicide particle growth at the rather elevated reaction temperature and thus helps stabilizing the powder submicronic size.

After acidic washing, powder XRD (fig. 45) shows that MgO is eliminated, at least down to the detection limit of the technique. The absence of Mg K_α emission line on SEM-EDS analyses and the detection of only traces of Mg on TEM-EDS confirm that MgO was almost entirely removed from the sample. Without the surrounding MgO matrix, the morphology of the HMS grains is fully revealed and typical SEM and TEM images are shown in fig. 46c,d and 47b, respectively. The grains have relatively isotropic shapes with sizes ranging from about 50 to few hundreds of nm. Based on their relatively faceted shape, most of the grains look single crystalline. Interestingly, high resolution transmission electron microscopy (HRTEM) does not reveal any MnSi precipitates inside the grains as is usually seen in samples obtained by crystallization from a liquid melt. It should also be noticed that HRTEM observations of the surface of the grains before and after the acidic washing (not shown here) do not reveal any trace of chemical erosion of the grains by the acid. Electron diffraction patterns (fig. 47c) can be fully indexed using 4 Miller indices *hklm* with the $MnSi_\gamma$ composite crystal structure described in details in the next section. Noticeable orientation and spacing anomalies as already reported and described by Ye and Amelinckx[34] are clearly visible along the $[00l]$ rows and will be further discussed in section 5.3.

Structural analysis of the MR-$MnSi_\gamma$ powders

$MnSi_\gamma$ crystallizes in a composite tetragonal 'Chimney-Ladder' structure-type - also known as Nowotny phase - in which a 'ladder' subsystem of Si-atoms (s.g. $P4/nnc$) is penetrating a 'chimney' subsystem of Mn (s.g. $I4_1/amd$)[35–37] (fig. 48).

As mentioned above, HMS were originally described as a large family of stoichiometric compositions with formula Mn_ySi_x where x and y are natural numbers and $\gamma = x/y$ is ranging between ≈ 1.727 and 1.75. Accordingly, they were described as commensurate structure with c increasing from 17.4 Å for the simplest Mn_4Si_7 ($\gamma = 1.75$) to $c = 117.9$ Å for $Mn_{27}Si_{47}$ ($\gamma \approx 1.741$). Miyazaki *et al.* have proposed a

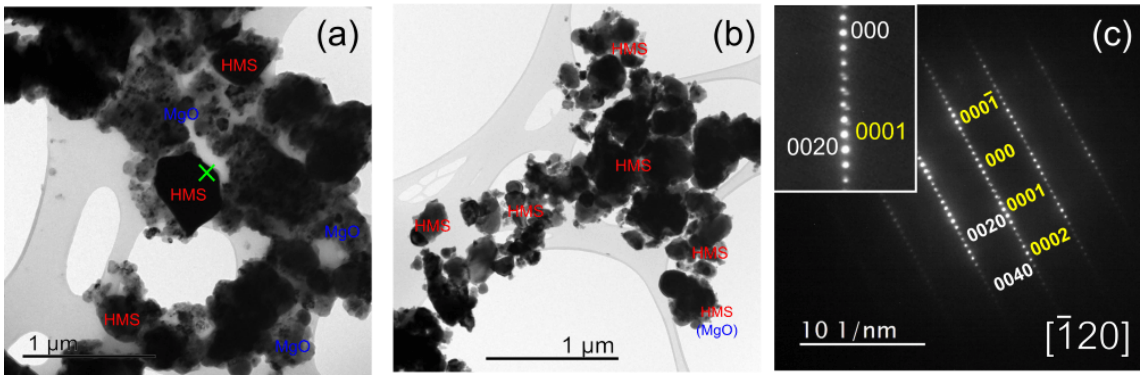

Figure 47: TEM brightfield images of the (a) as-synthesized MR-$MnSi_{\gamma}$ + MgO powder and (b) HCl-washed $MnSi_{\gamma}$ powder. Annotations on the images correspond to the main phase deduced from EDS analyses performed on different spots of the observed area. (c) Selected area electron diffraction patterns taken at the green cross in (a) and indexed with the composite crystal structure of $MnSi_{1.74}$ described in section 3.3 and pictured in fig.48. For clarity reason, only strong reflections corresponding to the two basic subsystems are indicated along the [00l] row but all satellite reflections could be indexed with $00lm$ indices. *hkl0* (white) and *hk0m* (yellow) Miller indices correspond to the Mn- and Si-subsystems, respectively. The inset shows a close-up view of the orientation anomaly along the [00l] direction.

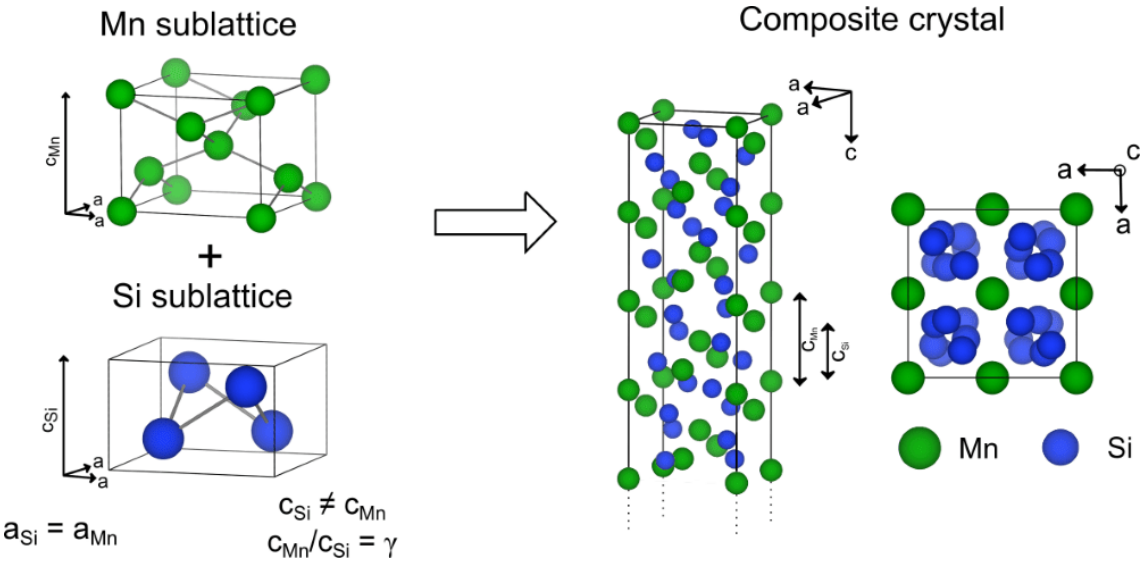

Figure 48: Crystal structure description of $MnSi_{\gamma}$ showing the interpenetrating tetragonal Mn- and Si-subsystems with identical a- but different c-lattice parameters (left). The interaction between the two subsystems leads to a composite $MnSi_{\gamma}$ unit-cell (right) where $\gamma = c_{Mn}/c_{Si}$.

more general approach, describing $MnSi_{\gamma}$ as a composite structure with a restrained domain of stability for γ[22]. In this approach, the structure is composed of two incommensurately modulated subsystems, where the modulation results from interactions between mutually incommensurate, periodic subsystems[38,39]. In the case of $MnSi_{\gamma}$, each subsystem is described by only one atom in the asymmetric unit (four equivalent in the basic cell). They have identical a lattice parameters of about 5.53 Å, while the c lattice parameters are different ($c_{Si} \approx 2.5$ Å and $c_{Mn} \approx 4.4$ Å) with a non-rational ratio $\gamma = c_{Mn}/c_{Si}$ that corresponds to the Si/Mn stoichiometry

of the compound in the case of full chemical occupancy.

In this context, the 3D lattice periodicity is replaced by a 3D+1 one. The symmetry elements present in the structure are described using a $I4_1/amd(00\gamma)00ss$ superspace group and four *hklm* Miller indices are required for the complete indexing of the diffraction patterns[40]. In this superspace description, the reciprocal basis vectors of the Mn and Si-sublattices in $MnSi_\gamma$ are described from the basis vectors of the composite crystal lattice via the W matrices:

$$W_{Mn} = \begin{pmatrix} 1 & 0 & 0 & 0 \\ 0 & 1 & 0 & 0 \\ 0 & 0 & 1 & 0 \\ 0 & 0 & 0 & 1 \end{pmatrix} \qquad W_{Si} = \begin{pmatrix} 1 & 0 & 0 & 0 \\ 0 & 1 & 0 & 0 \\ 0 & 0 & 0 & 1 \\ 0 & 0 & 1 & 0 \end{pmatrix} \tag{80}$$

In this setting, the diffraction patterns of $MnSi_\gamma$ are composed of *hk00* reflections common to both subsystem, *hkl0* reflections relative to the basic Mn-subsystem, *hk0m* reflections relative to the basic Si-subsystem and *hklm* satellite reflections with contribution of the incommensurate modulations. In incommensurately modulated structures, the displacement vector $\boldsymbol{u}^\mu(x,y,z)$ of the μ-atom relative to its base structure position $\bar{\boldsymbol{x}}^\mu(x,y,z)$ is described by the modulation vector function $\boldsymbol{u}^\mu(\nu_\mu)$. The argument ν_μ of the modulation function is the fourth 3D+1 superspace coordinate of μ in the basic structure. From the respective W matrices, ν_{Mn} and ν_{Si} are defined by the relations:

$$\begin{aligned} \nu_{Mn} &= t + \gamma x_3 \\ \nu_{Si} &= t + 1/\gamma x_4 \end{aligned} \tag{81}$$

where t is a real number corresponding to the initial phase of $\boldsymbol{u}^\mu(\nu_\mu)$.

As the modulation $\boldsymbol{u}^\mu(\nu_\mu)$ is periodic in 3D+1 superspace, it can be decomposed by Fourier series according to:

$$\boldsymbol{u}^\mu(\nu_\mu) = \sum_{k=1}^{n} \boldsymbol{A}_\mu^k sin(2\pi k\nu_\mu) + \boldsymbol{B}_\mu^k cos(2\pi k\nu_\mu) \tag{82}$$

where the amplitudes $\boldsymbol{A}_\mu^k$ and $\boldsymbol{B}_\mu^k$ are refined to fit to the experimental data.

The experimental XRD are satisfactorily fitted by Rietveld refinements using this approach as shown *e.g.* in fig. 49a for a HCl-washed $MnSi_\gamma$ powder with refined

lattice parameters, modulation vector and atomic displacement parameters summarized in Table 4 and fig. 50. The refined γ value of 1.7416(2) is in agreement with the synthesized and EDS determined compositions, confirming the ability of the synthesis technique to produce composition controlled materials.

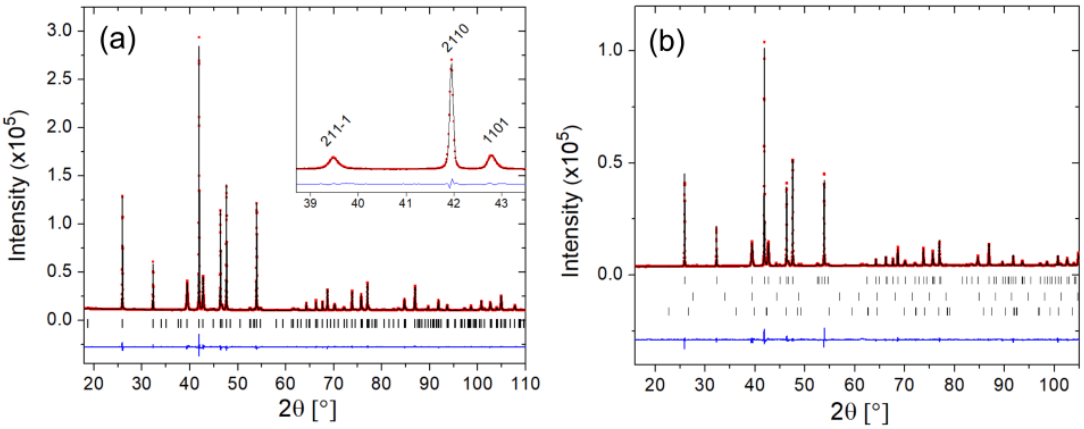

Figure 49: Rietveld refined XRD patterns of (a) washed $MnSi_{1.74}$, with enlarged view in inset, and (b) $V_{0.04}Mn_{0.96}Si_{1.74}$ powders prepared by magnesioreduction. The experimental data are plotted in red symbols, the calculated one in black line and the difference with a blue line. The vertical ticks indicate the theoretical $V_xMn_{1-x}Si_{1.74}$ (x = 0, 0.04) Bragg positions up to the 2^{nd} order satellite reflections. In (b), the second and third rows indicate the theoretical Bragg positions of VSi_2 and MnSi impurities.

Table 4: Structural parameters obtained by Rietveld refinement of washed $MnSi_{1.74}$ and $V_{0.04}Mn_{0.96}Si_{1.74}$ XRD patterns.

		$MnSi_{1.74}$	$V_{0.04}Mn_{0.96}Si_{1.74}$
Mn	$\bar{\boldsymbol{x}}^{Mn}$ (x,y,z)	0 0 0 [1]	0 0 0
	a (Å)	5.52908(2)	5.5301(1)
	c_{Mn} (Å)	4.36749(4)	4.3696(1)
	γ	1.7416(2)	1.7394(2)
	U_{iso} (Å^2)	0.0069(8)	0.001(2)
Si	$\bar{\boldsymbol{x}}^{Si}$ (x,y,z)	0.25 0.25 0.25 [1]	0.25 0.25 0.25
	a (Å)	5.52908(2)	5.5301(1)
	c_{Si} (Å)	2.5077(1) [2]	2.5121(3)
	U_{iso} (Å^2)	0.0033(4)	0.004(2)

[1] Average position coordinates of Mn and Si are constrained
[2] Calculated as c_{Mn}/γ

In the present case, the collected XRD data allowed satellite reflections up to the 2^{nd} order to be considered in the refinement procedure as many of them were found to have intensities just above the background level. The modulation functions were described using Fourier coefficients up to $n = 2$ and $n = 4$ for Mn and Si subcells, respectively. The large number of refined Fourier coefficients used to describe the Si

modulation is imposed by the crystal symmetry, the first coefficient describing the z component of the modulation - B^4 - being non null for $n = 4$. Refined Fourier coefficients are tabulated in Table 5 while the resulting modulation functions are plotted in fig. 50. On the one hand, the displacement of Mn around its average position $\bar{\boldsymbol{x}}^{Mn} = (0,0,0)$ has a small maximum amplitude along z of about 0.04 Å while no displacement is found in the (x,y) plane. On the other hand, Si-atoms at $\bar{\boldsymbol{x}}^{Si} = (\frac{1}{4}, \frac{1}{4}, \frac{1}{4})$ show much larger sinusoidal displacements reaching a maximum of $x = y \approx 0.2$ Å and $z \approx 0.08$ Å. The large displacement modulations induce the formation of Si-atom helices around the $(\frac{1}{4},\frac{1}{4},z)$ axis as shown in the projection of the crystal structure along the c-axis (fig. 48). All these refined values are in very good agreement with those reported by Miyazaki *et al.* obtained on high resolution neutron powder diffraction data of $MnSi_{\approx 1.736}$ synthesized by conventional melting/annealing method[22].

Table 5: Refined coefficients of the modulation functions of Mn (top) and Si (bottom) for washed $MnSi_{1.74}$ and $V_{0.04}Mn_{0.96}Si_{1.74}$

	$MnSi_{1.74}$			$V_{0.04}Mn_{0.96}Si_{1.74}$		
Mn	$x\ (=x_1)$	$y\ (=x_2)$	$z\ (=x_3)$	$x\ (=x_1)$	$y\ (=x_2)$	$z\ (=x_3)$
B^2	0	0	-0.019(1)	0	0	-0.017(3)
Si	$x\ (=x_1)$	$y\ (=x_2)$	$z\ (=x_4)$	$x\ (=x_1)$	$y\ (=x_2)$	$z\ (=x_4)$
A^1	0.0764(3)	0.0764(3)	0	0.0773(4)	0.0773(4)	0
B^1	0.0764(3)	-0.0764(3)	0	0.0773(4)	-0.0773(4)	0
A^3	0.0099(6)	0.0099(6)	0	0.0107(7)	0.0107(7)	0
B^3	-0.0099(6)	0.0099(6)	0	-0.0107(7)	0.0107(7)	0
B^4	0	0	-0.041(3)	0	0	-0.049(4)

As illustrated in the inset to fig. 49 with the intense (2110) and (1101) Bragg peaks, *hk0m* reflections of the Si subsystem are much broader than the relatively narrow *hkl0* reflections of the Mn subsystem. From the diffractogram refinement point of view, this strong peak shape anisotropy between the different families of reflections has been managed using a strain tensor implemented in JANA2006. This could be attributed to higher disorder on the Si subsystem as confirmed by HRTEM observations that are discussed in next section. This strain tensor also avoids the implementation of an extra Si-position in the structural model proposed by Akselrud *et al.* to describe the disordered Si-subsystem[41].

The XRD pattern of washed $V_{0.04}Mn_{0.96}Si_{1.74}$ powder was also fitted using the same approach (fig. 49b, tables 4,5). The lattice parameters are slightly larger and γ slightly smaller in the case of the V-doped sample. On the other hand, the

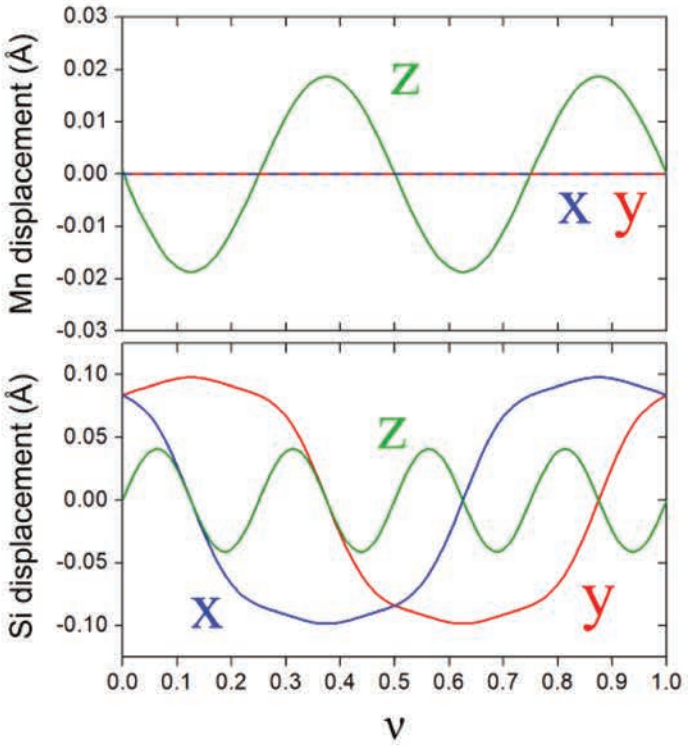

Figure 50: Coordinates of the displacement vector relative to the average position for Mn (top) and Si (bottom) as a function of the fourth space parameter ν for washed $MnSi_{1.74}$

Fourier coefficient of the modulation functions remains relatively similar. It should be noticed that VSi_2 and MnSi impurities represent 1 and 2 wt.% of the sample, respectively. The presence of VSi_2 suggest that V was not entirely inserted in the structure during the magnesioreduction process.

Microstructure of sintered $MnSi_\gamma$ pellets

$MnSi_{1.74}$ and $V_{0.04}Mn_{0.96}Si_{1.74}$ pellets with densities of 96 % according to the Archimede weighing were produced by spark plasma sintering. After the sintering step, both samples are single phase according to XRD (fig. 51 and SI 9), indicating that most of the residual VSi_2 and MnSi reacted during the heat treatment for the doped sample. Accordingly, a significant decrease of γ from about 1.74 for the as-synthesized MR powder to 1.73 for the as-sintered pellet is obtained by Rietveld refinements (fig. SI 9), reaching a value close to the arc-melted (AM) samples. Generally, the lattice and structural parameters (table 6) of each composition made by both MR and AM synthesis routes are quite equivalent. Upon V-doping, a moderate increase of a and c_{Mn} is consistent with the slightly larger vanadium metallic radius (r_V = 1.346 Å, r_{Mn} = 1.264 Å[42]) while a much larger increase of c_{Si} from about 2.515 to almost 2.53 Å is in agreement with Miyazaki's results[20]. As can be seen from the 2θ shift of the $(211\bar{1})$ reflection toward low 2θ angles, this increase of c_{Si} is associated to a significantly smaller γ value for V-doped samples.

Interestingly, the $(211\bar{1})$ and (1101) reflections of the AM samples are much less affected by the broadening than MR samples. In the case of the MR V-doped sample, the (1101) peak even seems to be composed of the sum of three peaks. This suggests some level of heterogeneity of c_{Si} and thus of γ in the MR samples, in agreement with similar observations reported by Miyazaki *et al.* in V- and Ge-doped HMS prepared by conventional methods[20].

EDS mapping on polished surfaces of the SPSed pellets (SI 10) confirms a homogeneous concentration of Mn and Si (within the resolution of the technique) on the analyzed areas of the $MnSi_{1.74}$ sample, while in the case of $V_{0.04}Mn_{0.96}Si_{1.74}$, a few vanadium-rich areas with diameters below 1 μm could be attributed to small amounts of residual VSi_2 impurity (not visible on XRD patterns). As a consequence, the V-concentration in this $V_xMn_{1-x}Si_{1.74}$ may be slightly below the nominal x = 0.04 value.

Residual porosity with average size of approximately 100 nm and located at the grain boundaries is visible for samples prepared by MR and AM syntheses (fig. 52). Similar residual porosity after spark plasma sintering is reported in samples prepared by other processes such as ball-milling[43], melt-spinning[10] or solid-state diffusion[44] and seems thus intrinsic to this material densified by SPS.

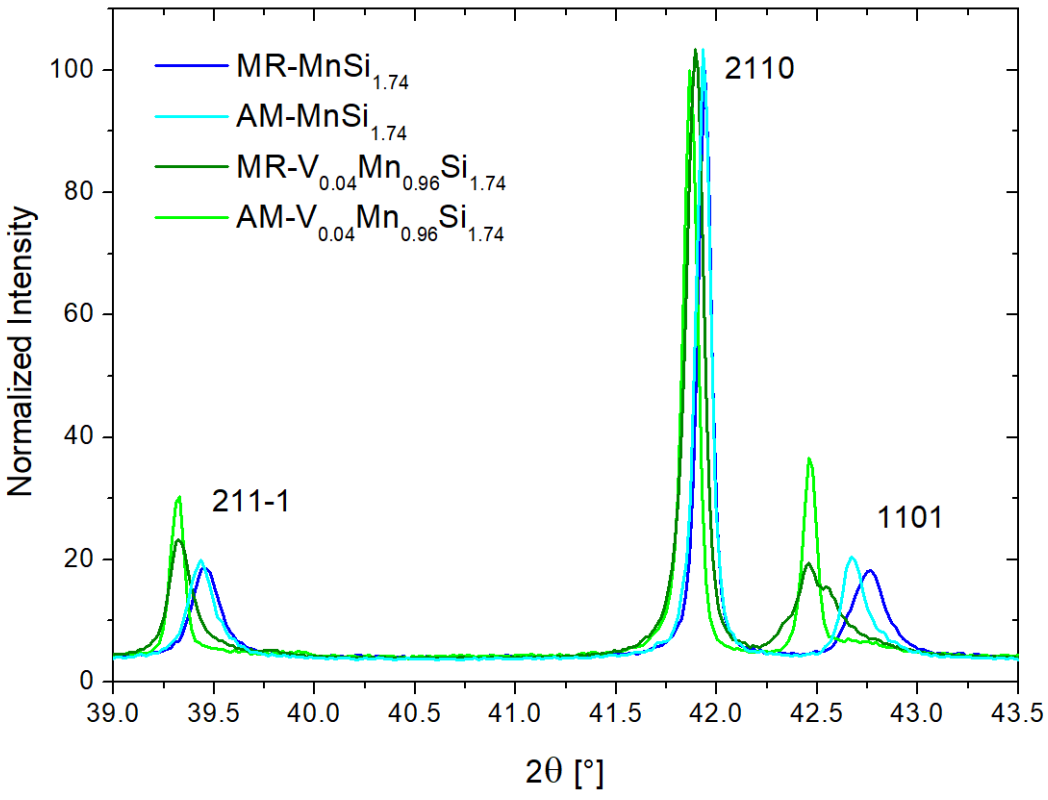

Figure 51: XRD patterns of MR $MnSi_{1.74}$ (dark blue), MR $V_{0.04}Mn_{0.96}Si_{1.74}$ (dark green), AM-$MnSi_{1.74}$ (bright blue) and AM-$V_{0.04}Mn_{0.96}Si_{1.74}$ (bright green) showing the relative peaks shifts among the samples

Further microstructural characterization of the sintered pellets was realized by elec-

Table 6: Main structural and microstructural characteristics of the SPSed MR and AM $V_xMn_{1-x}Si_{1.74}$ (x = 0 and 0.04) samples used for the TE characterizations

		MR $MnSi_{1.74}$	AM $MnSi_{1.74}$	MR $V_{0.04}Mn_{0.96}Si_{1.74}$	AM $V_{0.04}Mn_{0.96}Si_{1.74}$
	a (Å)	5.5295(3)	5.52954(6)	5.5308(4)	5.5319(1)
	c_{Mn} (Å)	4.3696(3)	4.36834(8)	4.3710(3)	4.3746(1)
	c_{Si} (Å)	2.5156(3)	2.5110	2.5265	2.5291
	γ	1.7370(3)	1.7397(3)	1.7300(6)	1.7297(1)
	$A^1(x)$	0.0768(8)	0.0769(8)	0.0758(8)	0.0753(6)
Si	$A^2(x)$	0.010(1)	0.013(1)	0.012(1)	0.014(1)
	$A^3(z)$	-0.049(8)	-0.064(7)	-0.042(7)	-0.050(6)
	$U_{iso}(Å^2)$	0.004(3)	0.008(2)	0.001(2)	0.007(2)
Mn	$A^2(z)$	-0.017(4)	-0.009(5)	-0.013(4)	-0.009(3)
	$U_{iso}(Å^2)$	0.001(2)	0.001(1)	0.001(1)	0.001(1)
Impurity	Si	/	2	/	1
(wt. %)	MnSi	/	1	/	1

tron back-scattering diffraction (EBSD, fig.52). EBSD maps have been obtained by scanning the area with a 50 nm step and by indexing the Kikuchi lines using the commensurate Mn_4Si_7 structure ($P\bar{4}c2$, $a = 5.52$ Å , $c = 17.46$ Å). Orientation analysis of the maps do not reveal any crystallographic texturation of the pellets which could have been caused by the uniaxial pressing during the sintering process[23]. TE properties of the pellets will thus be considered as isotropic. The grain size distributions (fig. 52) have been obtained from EBSD maps by considering all diffracting domains containing at least 12 pixels (*i.e.* $\sim$0.03 μm^2). It follows a log-normal law with average values of 580 nm and 606 nm for the sintered undoped and V-doped MR samples, respectively. Such small grain sizes logically lead to a much higher density of grain boundaries than a conventionally synthesized AM sample with average grain size estimated at 13 μm using the same procedure. Enhanced scattering of the phonons at the grain boundaries and reduced lattice thermal conductivity are expected from such microstructure.

Fig. 53a shows a typical low magnification brighfield TEM image of the MR $MnSi_{1.74}$ densified sample. The shape and size distribution of the grains are in good agreement with the EBSD analysis. The residual porosity due to incomplete densification is confirmed at the grain boundaries. As for the as-synthesized powder, no MnSi precipitates are observed inside the grains after sintering.

As shown on the HRTEM images (fig 53b,c), the great majority of the grain boundaries looks well crystalline and free of amorphous layer. Proper sintering of nanometric powders can be quite challenging because of oxidation layers or residual absorbed species at the surface of the particles which often result in much higher electrical

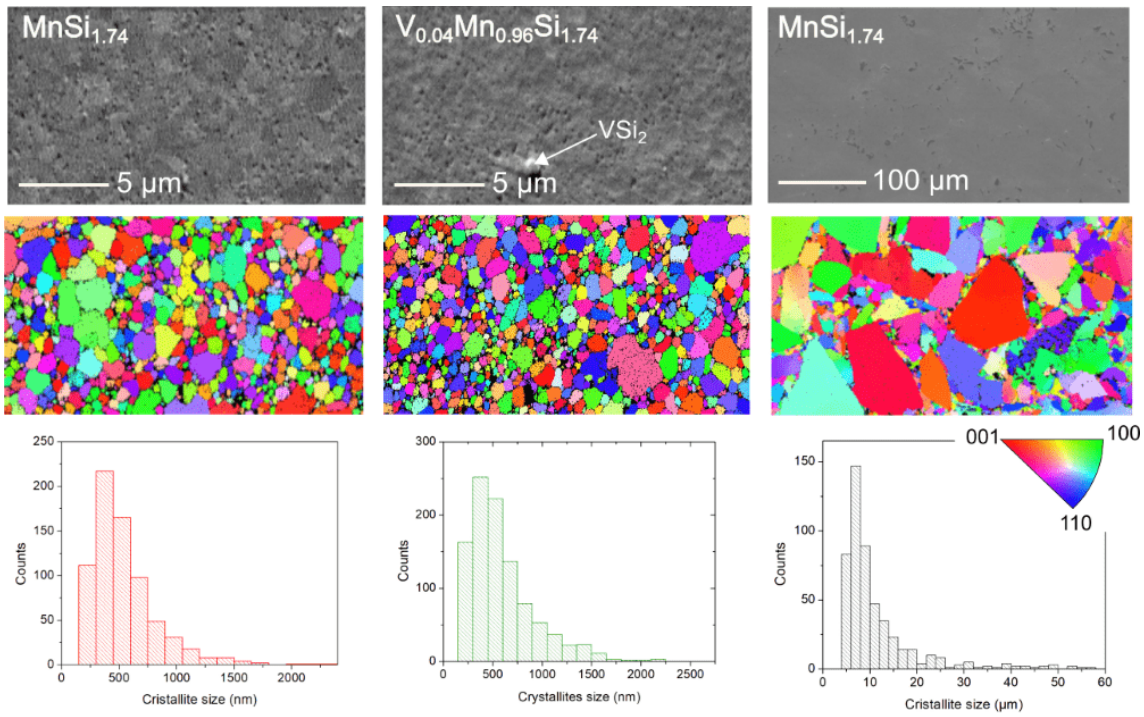

Figure 52: EBSD microstructural analyses of SPSed pellets of MR $MnSi_{1.74}$ (left), MR $V_{0.04}Mn_{0.96}Si_{1.74}$ (middle), and AM $MnSi_{1.74}$ (right). The top, middle and bottom rows correspond to backscattered electron images of the analyzed areas, EBSD maps and histograms of the grain size distribution, respectively

resistivity compared to bulk[45]. In the present case, the good crystallinity of the grain boundaries is expected to prevent exceedingly large decrease of the charge carriers transport while still acting as efficient phonon scattering centers.

Typical electron diffraction patterns along the $[\bar{1}20]$ zone axis obtained on a MR $MnSi_{1.74}$ sintered pellet (fig. 53d) are significantly different than those obtained on the as-synthesized powder (fig. 53c). The 'orientation' anomalies affecting the Si and satellite rows of reflections are no more visible. This evolution is attributed to the heat treatment during the sintering and seems correlated to the variation of the modulation vector observed by XRD. Such influence of the temperature on the microstructural properties of $MnSi_{\gamma}$ have already been reported, *e.g.* by Kikuchi *et al.* who reported a linear decrease of γ with temperature above 770 K associated to a VEC change[46]. In addition, careful examination of the diffraction pattern obtained on several areas of the sample reveals some degree of structural heterogeneity between different crystals. As an example, fig. 53e and 53f are diffraction patterns taken along the $[\bar{1}10]$ zone axis on two different crystals. While in fig. 53e the arrangement of the satellite peaks is equally spaced but slightly misoriented along the c-axis, fig. 53f shows on the contrary a split in satellite spot position in agreement with a variation of the modulation vector. A clear explanation of the origin of such microstructural effects is not available in literature and moreover out of the scope of the present work. However it is worth to underline that such effects are not ho-

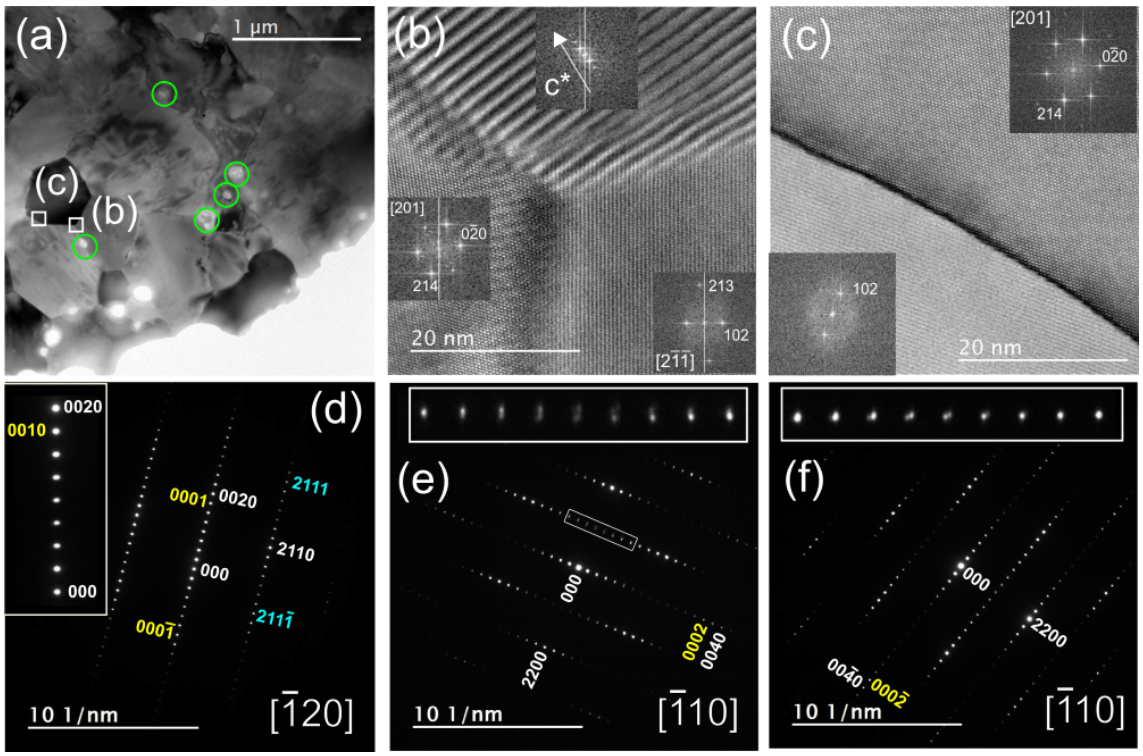

Figure 53: Low magnification brightfield TEM images of typical thinned undoped $MnSi_{1.74}$ pellet showing (a) the residual porosity (encircled in green) and the areas chosen for (b) and (c) HRTEM images showing the high crystallinity of the grain boundaries. FFT in insets indicate the crystal orientation of the grains. (d) Typical electron diffraction pattern taken along the [$\bar{1}$20] zone axis. (e) and (f) Electron diffraction patterns obtained on two different crystals along the [$\bar{1}$10] zone axis showing different anomalies.

mogeneous at the micrometer scale throughout the samples and are a characteristic of HMS that should be taken into account during theoretical modeling of the system.

An important contrast inside the crystals can be observed in brightfield mode (fig. 53a) and are attributed to local deviations from the diffraction condition due to large lattice distortions. Magnified images of this area are shown in fig. 54a and 54b revealing high concentration of dislocation-like defects propagating lattice distortion up to a distance of 50 nm in the crystal. A more detailed study of lattice defects was realized by high resolution imaging on thin crystals oriented along the [$\bar{1}$20] zone axis. A defect-free area is shown in fig. 54(c) revealing two types of structural features: (i) large fringes with approximately 17.46 Å periodicity along the [001] direction corresponding to the *c*-axis of the commensurate structure of Mn_4Si_7 and generated by Moiré interferences between the two Mn- and Si-subsystems of the composite crystal and (ii) atomic rows spaced by approximately 2.53 Å along the [211] direction and corresponding to the Mn-Mn distance in the [$\bar{1}$20] projection of the structure (fig. 54c). The schematic representation of the crystal structure projection along the [$\bar{1}$20] direction illustrates the formation of the Moiré fringes by interaction of the two sublattices (fig. 54c). As assumed by the structural model, the orientation of the Moiré fringes and the Mn rows are both parallel to the [211]

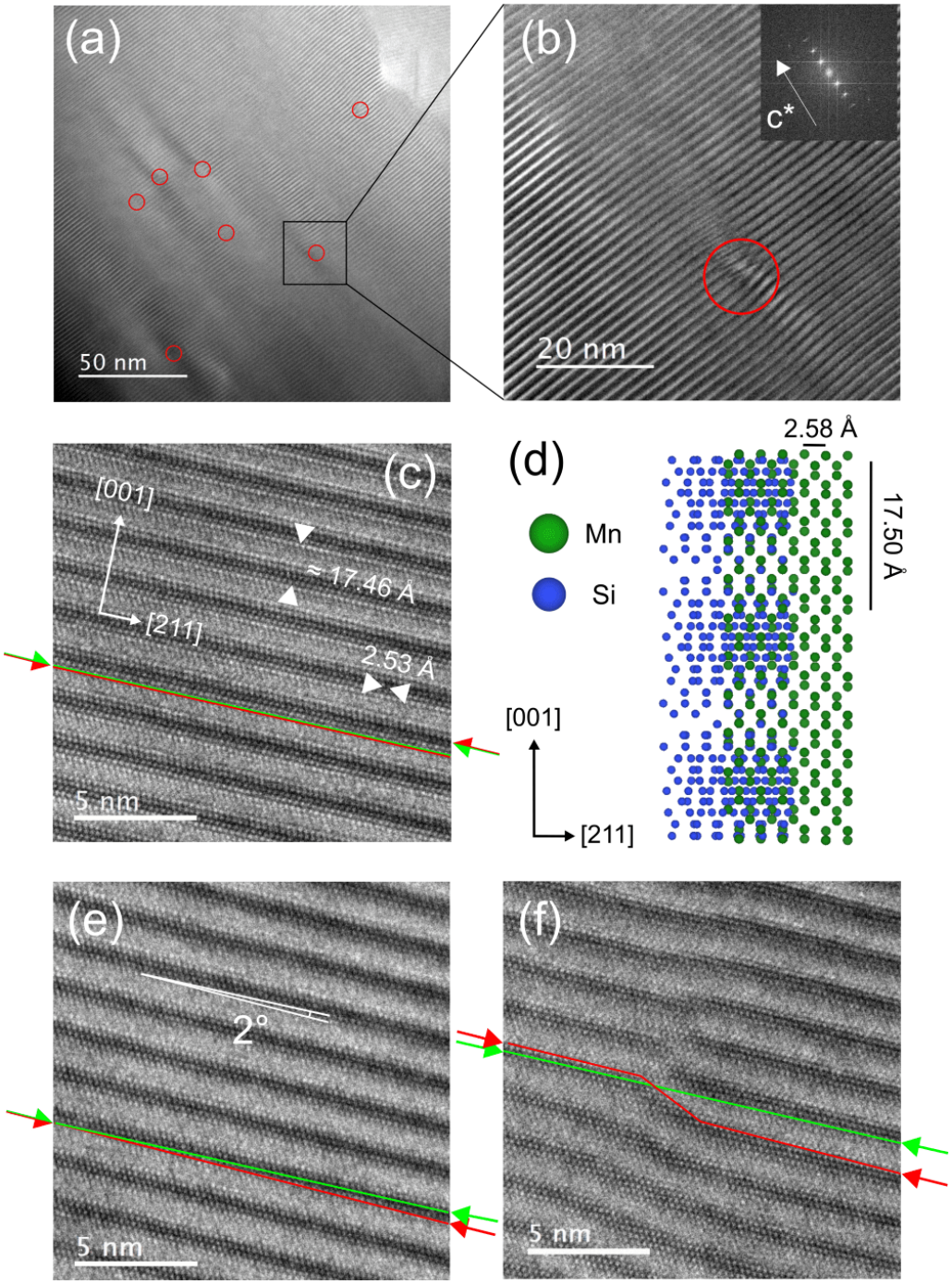

Figure 54: (a) and (b) Brightfield images of MR $MnSi_{1.74}$ sintered pellet showing dislocation-like defects (encircled in red) at two different magnifications. (c) Typical HRTEM image of a defect-free area of a $MnSi_{1.74}$ crystal taken along the $[\bar{1}20]$ zone axis with average characteristic distances of the lattice determined from the corresponding FFT image. The orientations of the Moiré fringes and the Mn atomic rows are emphasized on the images with red and green lines, respectively. (d) Scheme of the formation of Moiré-like fringes along the $[\bar{1}20]$ direction by interaction of the Si-sublattice (left side) and Mn-sublattice (right side). (e) and (f) HRTEM images showing the tilting of the Moiré fringes relatively to the [211] direction and a dislocation-like defect, respectively.

direction because of the existence of lattice translation symmetry in the (001) plane. Surprisingly, the situation is somewhat different in fig. 54e taken in a different area of the same crystal, where the Moiré fringes are found to be tilted by about 2°

with respect to the Mn row itself. Ye and Amelinckx reported similar observations and explained it as a small systematic 'phase-shift' of the Si helical arrangement inside the columnar Mn-sublattice resulting in the tilting of the Moiré fringes[34]. According to these authors, the loss of the tetragonal symmetry in the area of the crystal affected by the Si helices 'phase-shift' explains the 'orientation' anomalies visible on the electron diffraction patterns. Similar type of images taken on the dislocation-like defects (fig. 54f) reveals that only the Moiré fringes are deformed on these areas of the crystal. As shown by the green line, the Mn rows remains well oriented and defect-free throughout the analyzed area and even close to the lattice defect where severe distortion is expected. From these observations, the Si sublattice can be described as highly deformed by numerous defects while on the contrary the Mn lattice remains well crystallized and less affected by Si sublattice disorder. It should be noticed that this more 'realistic' description of the HMS structure is consistent with the peak shape broadening of the Si *hk0m* reflections clearly visible on the powder XRD patterns and supports the use of the strain tensor applied in our Rietveld refinements.

The presence of numerous defects and heterogeneities within the submicronic grains of MR $MnSi_{1.74}$ might act as efficient scattering centers for phonons and thus might strongly influence the thermal conductivity of the materials. In the next section, the thermoelectric properties of pristine and V-doped MR $MnSi_{1.74}$ are thus presented and compared to conventionally synthesized AM counterparts. The objective is to discuss the effect of the different synthesis routes and microstructures on the TE properties of comparable polycrystalline $MnSi_{1.74}$ samples.

Thermoelectric properties of MR and AM $MnSi_{1.74}$ and - $V_{0.04}Mn_{0.96}Si_{1.74}$

The TE properties of $MnSi_{1.74}$ and $V_{0.04}Mn_{0.96}Si_{1.74}$ synthesized by magnesioreduction or arc-melting were measured from room temperature up to 800 K (fig. 55). Measurements of the electronic properties were cycled twice and showed good reversibility within a time span of few hours at high temperature.

The electrical resistivity of MR $MnSi_{1.74}$ (fig. 55a) increases from 23 $\mu\Omega$.m at 320 K to 39 $\mu\Omega$.m at 750 K, in agreement with the behavior expected for a heavily degenerated semiconductor. In the same temperature range, its positive Seebeck coefficient (fig. 55b) increases accordingly from 135 to 230 $\mu V.K^{-1}$. The electronic properties of AM $MnSi_{1.74}$ were measured in the same conditions: at room temperature, the electrical resistivity and Seebeck coefficient are found to be 17 % and 2 % lower for the AM $MnSi_{1.74}$ sample in comparison to MR sample. At higher temperature, the difference in electrical resistivity becomes less and less significant, which is at-

tributed to the apparition of the bipolar effect arising at slightly lower temperature (700-750 K) in the case of the MR sample. This effect corresponds to the thermal activation of minor carriers across the band gap (electrons in this case) leading to the simultaneous decrease of the electrical resistivity and the Seebeck coefficient. Maximum power factor PF of 1.3 mW m^{-1} K^{-2} at 740 K and 1.4 mW m^{-1} K^{-2} at 700 K (fig. 55c) are found for MR and AM $MnSi_{1.74}$, respectively. This corresponds to a 5 % reduction of the maximum PF which can be attributed in a large extent to the higher resistivity of the MR sample. Since the two samples mainly differ in their microstructure, the higher ρ in the 'mesostructured' sample most likely arises from increasing the scattering of charge carriers at the numerous grains boundaries.

Fig. 55d shows the temperature dependence of the total $\kappa_{tot}(T)$ and lattice $\kappa_L(T)$ thermal conductivities calculated by substracting to $\kappa_{tot}(T)$ the electronic contribution $\kappa_e(T)$ calculated using the Wiedemann-Franz law $\kappa_e(T) = L\ T/\rho(T)$ with $L = 2.4.10^{-8}$ W Ω K^{-2}. The lattice thermal conductivity of MR $MnSi_{1.74}$ amounts to 2.3 W m^{-1} K^{-1} at 320 K, which corresponds to a 13 % decrease compared to AM $MnSi_{1.74}$ at the same temperature. The beneficial reduction of the lattice thermal conductivity in MR $MnSi_{1.74}$ is attributed to the smaller grain sizes and the high concentration of defects as evidenced by EBSD and TEM analyses. However, the effect of mesostructuration becomes less and less efficient with increasing temperature and the lattice thermal conductivities of the two samples ultimately reach similar value at 750 K corresponding to the temperature with the highest PF. Equivalent maximum ZT of about 0.4 is achieved at 750 K which is in good agreement with the best performances reported for undoped HMS synthesized by conventional melting/annealing/SPS[47,48]. No improvement of the ZT could be achieved because the beneficial effect of the mesostructuration on κ_{tot} is counterbalanced by the deterioration of PF resulting in equivalent ZT values over the whole temperature range. Concordant experimental results show that highly-densified nanostructured HMS (average grain size around 200 nm) synthesized by ball milling followed by SPS did not improve the ZT also because of the drop of the power factor[9]. It suggests that any attempt to reduce the grain size down to few hundreds of nm is inefficient to improve ZT in the case of $MnSi_{1.74}$.

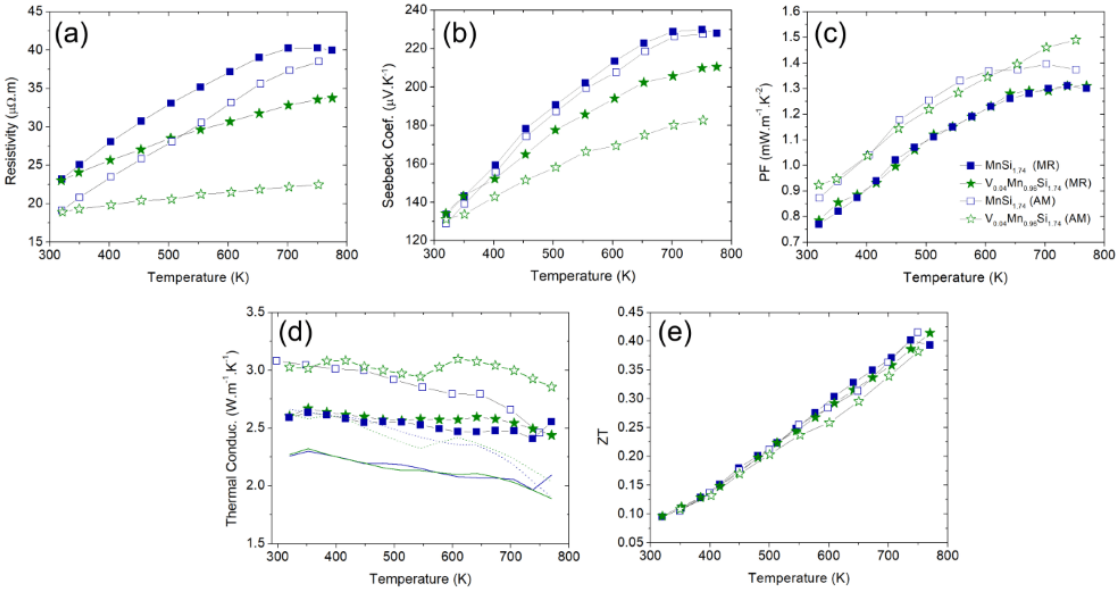

Figure 55: High temperature thermoelectric properties of $MnSi_{1.74}$ (blue squares) and $V_{0.04}Mn_{0.96}Si_{1.74}$ (green stars) synthesized by magnesioreduction (MR, filled symbols) and conventional arc-melting (AM, empty symbols): thermal dependence of (a) electrical resistivity, (b) thermopower, (c) power factor, (d) total (symbols) and lattice (solid lines for MR $MnSi_{1.74}$ and dotted lines for AM $MnSi_{1.74}$) thermal conductivities and (e) resulting figure-of-merit.

Increasing *PF* of MR-HMS was attempted by partially substituting manganese with vanadium up to 4 %. Vanadium-doping was reported to effectively improved the power factor of $MnSi_\gamma$ while employing a relatively abundant element compared to other commonly used dopant such as Ge or Re[49]. In addition, V_2O_5 can be reduced relatively easily by Mg in the synthesis condition unlike other very stable oxides such as Al_2O_3. As for undoped $MnSi_{1.74}$, TE measurements were realized on both MR and AM $V_{0.04}Mn_{0.96}Si_{1.74}$. The electrical resistivity and the Seebeck coefficient of both samples decrease with the insertion of vanadium in the structure. This is consistent with an increase of the holes concentration in the materials resulting from the substitution of Mn by an electron-poorer element. The less pronounced effect of the doping on the MR sample could be explained by the probable smaller amount of V effectively substituting Mn due to the residual VSi_2 precipitates observed by EDS mapping. However, doping the MR sample do not improve *PF* while for the AM sample it leads only to a small improvement of about 8 % above 700 K. Similarly, doping do not induce significant improvement of the lattice thermal conductivity which remain identical to the undoped sample over the whole temperature range. Neither the mass fluctuation scattering of thermal phonons at the disordered Mn/V sites, nor the submicrometric VSi_2 precipitates present in the materials seem to significantly influence κ_L. As a consequence, no improvement of ZT_{max} has been achieved in our case by vanadium doping.

Conclusion

A new magnesioreduction synthesis for high purity $MnSi_{1.74}$ is reported. This method offers many advantages over conventional melting/annealing syntheses such as the use of cheap and air-stable precursors (MnO and Si), relatively fast heat treatment at moderate temperature and the possibility to produce doped compounds. Additionnally, a finely divided powder is directly obtained, which is suitable for the sintering of mesostructured materials with average grain size of about 500 nm. The inflence of the microstructure, investigated by means of EBSD and TEM, on the thermoelectric properties was evaluated by comparison with a sample synthesized by a conventional arc-melting/annealing/sintering process and composed of much larger grains. The thermal conductivity is decreased by up to 25% at 300 K thank to the mesotructuration and associated crystal defect density. However, this beneficial effect is counterbalanced by a decrease of the power factor, resulting eventually in materials with similar $ZT_{max} \simeq 0.4$ at 750 K. The present results suggest that microstructure engineering alone might not be a sufficient strategy to improve the TE properties of HMS.

Acknowledgements

Francis Gouttefangeas is acknowledged for SEM images and EDS analyses performed on the CMEBA platform. TEM experiments were performed on THEMIS platform. Both platforms belong to the ScanMAT unit (UMS 2001, University of Rennes 1) which received a financial support from the European Union (CPER-FEDER 2007-2014). The authors acknowledge support from CREST JPMJCR15Q6 and JSPS KAKENHI JP17H02749, JP16H06441.

References

[1] L. E. Bell, *Science* **2008**, *321*, 1457–1461.

[2] I. Petsagkourakis, K. Tybrandt, X. Crispin, I. Ohkubo, N. Satoh, T. Mori, *Sci. Technol. Adv. Mater.* **2018**, *19*, 836–862.

[3] L. Aixala, C. de Vaulx, *3rd Thermoelectrics Applications Workshop* **2012**, *Baltimore, USA*, –.

[4] G. Skomedal, L. Holmgren, H. M. andI.S. Eremin, G. Isachenko, M. Jaegle, K. Tarantik, N. Vlachos, M. Manoli, T. Kyratsi, D. Berthebaud, N. Y. D. Truong, F. Gascoin, *Energy Convers. Manag.* **2016**, *110*, 13–21.

[5] T. Mori, *Small* **2017**, *13*, 1702013.

[6] J. Mao, Z. Liu, J. Zhou, H. Zhu, Q. Zhang, G. Chen, Z. Ren, *Adv. Phys.* **2018**, *67*, 69–147.

[7] D. N. Truong, D. Berthebaud, F. Gascoin, H. Kleinke, *J. Electron. Mater.* **2015**, *44*, 3603–3611.

[8] V. Ponnambalam, D. T. Morelli, *Mater. Res. Express* **2018**, *6*, 025507.

[9] X. Chen, L. Shi, J. Zhou, J. B. Goodenough, *J. Alloys Compd.* **2015**, *641*, 30–36.

[10] S. Muthiah, R. C. Singh, B. D. Pathak, P. K. Avasthi, R. Kumar, A. Kumar, A. K. Srivastava, A. Dhar, *Nanoscale* **2018**, *10*, 1970–1977.

[11] W. Luo, H. Li, F. Fu, W. Hao, X. Tang, *J. Electron. Mater.* **2011**, *40*, 1233–1237.

[12] X. She, X. Su, H. Du, T. Liang, G. Zheng, Y. Yan, R. Akram, C. Uher, X. Tang, *J. Mater. Chem. C* **2015**, *3*, 12116–12122.

[13] Y. Thimont, L. Presmanes, V. Baylac, P. Tailhades, D. Berthebaud, F. Gascoin, *Mater. Lett.* **2018**, *214*, 236–239.

[14] S. Vivès, C. Navone, E. Gaudin, S. Gorsse, *J. Mater. Sci.* **2017**, *52*, 12826–12833.

[15] A. Yamamoto, S. Ghodke, H. Miyazaki, M. Inukai, Y. Nishino, M. Matsunami, T. Takeuchi, *Jpn. J. Appl. Phys.* **2016**, *55*, 020301.

[16] T. Homma, T. Kamata, N. Saito, S. Ghodke, T. Takeuchi, *J. Alloys Compd.* **2019**, *776*, 8–15.

[17] A. Berche, E. Ruiz-Théron, J.-C. Tedenac, R. Ayral, F. Rouessac, P. Jund, *J. Alloys Compd.* **2014**, *615*, 693–702.

[18] W. M. Haynes, D. R. Lide, T. J. Bruno, *CRC Press Ed.* **2015-2016**, 6–91.

[19] S. N. Girard, X. Chen, F. Meng, A. Pokhrel, J. Zhou, L. Shi, S. Jin, *Chem. Mater.* **2014**, *26*, 5097–5104.

[20] Y. Miyazaki, H. Hamada, K. Hayashi, K. Yubuta, *J. Electron. Mater.* **2017**, *46*, 2705–2709.

[21] S. S. Ravazi-Tousi, Y.-C. Tseng, *J. Alloys Compd.* **2018**, *764*, 745–754.

[22] Y. Miyazaki, D. Igarashi, K. Hayashi, T. Kajitani, K. Yubuta, *Phys. Rev. B* **2008**, *78*, 214104.

[23] Y. Sadia, Z. Aminov, D. Mogilyansky, Y. Gelbstein, *Intermetallics* **2016**, *68*, 71–77.

[24] S. Le Tonquesse, E. Alleno, V. Demange, V. Dorcet, L. Joanny, C. Prestipino, O. Rouleau, M. Pasturel, *J. Alloys Compd.* **2019**, *796*, 176.

[25] S. N. Girard, T. J. Slade, X. Chen, F. Meng, L. Shi, S. Jin, *Abstract book of the 33th Internationnal Conference on Thermoelectrics* **2014**, *Nashville, USA*.

[26] V. Petříček, M. Dušek, L. Palatinus, *Z. Kristall.* **2014**, *229*, 345–352.

[27] H. J. T. Ellingham, *J. Soc. Chem. Ind.* **1944**, *65*, 125–160.

[28] O. Knacke, O. Kubaschewski, K. Hesselmann, *Springer Ed.* **1991**, *vol. II*, –.

[29] Z. Zamanipour, X. Shi, M. Mozafari, J. S. Krasinski, L. Tayebi, D. Vashaee, *Ceram. Int.* **2013**, *39*, 2353–2358.

[30] M. Saleemi, A. Famengo, S. Fiameni, S. Boldrini, S. Battiston, M. Johnsson, M. Muhammed, M. Toprak, *J. Alloys Compd.* **2015**, *619*, 31–37.

[31] Y. Sadia, L. Dinnerman, Y. Gelbstein, *J. Electron. Mater.* **2013**, *42*, 1926–1931.

[32] C. Won, H. Nersisyan, H. Won, *Chem. Eng. J.* **2010**, *157*, 270–275.

[33] H. Nersisyan, H. Won, C. Won, A. Joc, J. Kim, *Chem. Eng. J.* **2014**, *235*, 67–74.

[34] H. G. Ye, S. Amelinckx, *J. Solid State Chem.* **1986**, *61*, 8–39.

[35] O. Schwomma, H. Nowotny, A. Wittmann, *Monatsh. Chem.* **1963**, *94*, 681–685.

[36] G. Flieher, H. Völlenkle, H. Nowotny, *Monatsh. Chem.* **1967**, *98*, 2173–2179.

[37] H. Knott, M. Mueller, L. Heaton, *Acta Crystallogr.* **1967**, *23*, 549–555.

[38] S. van Smaalen, *Phys. Rev. B* **1991**, *43*, 11330–11341.

[39] V. Petricek, K. Maly, P. Coppens, X. Bu, I. Cisarova, A. Frost-Jensen, *Acta Crystallogr. A* **1991**, *47*, 210–216.

[40] P. M. D. Wolff, T. Janssen, A. Janner, *Acta Crystallogr. A* **1981**, *37*, 625–636.

[41] L. Akselrud, R. C. Gil, M. Wagner-Reetz, Y. Grin, *Acta Crystallogr. B* **2015**, *71*, 707–712.

[42] E. Teatum, K. Gschneidner, J. Waber, *Los Alamos Scientific Laboratory* **1960**, *LA-2345*, –.

[43] Y.-G. Lee, M.-K. Choi, I.-H. Kim, S.-C. Ur, *J. Ceram. Process. Res.* **2012**, *13*, 816–819.

[44] X. Chen, A. Weathers, D. Salta, L. Zhang, J. Zhou, J. B. Goodenough, L. Shi, *J. Appl. Phys.* **2013**, *114*, 173705.

[45] A. Khan, M. Saleemi, M. Johnsson, L. Han, N. Nong, M. Muhammed, M. Toprak, *J. Alloys Compd.* **2014**, *612*, 293–300.

[46] Y. Kikuchi, T. Nakajo, K. Hayashi, Y. Miyazaki, *J. Alloys Compd.* **2014**, *616*, 263–267.

[47] W. Luo, H. Li, Y. Yan, Z. Lin, X. Tang, Q. Zhang, C. Uher, *Intermetallics*

2011, *19*, 404–408.

[48] T.-H. An, S.-M. Choi, W.-S. Seo, C. Park, I.-H. Kim, S.-U. Kim, *Jpn. J. Appl. Phys.* **2013**, *52*, 10MC11.

[49] Y. Miyazaki, H. Hamada, H. Nagai, K. Hayashi, *Materials* **2018**, *11*, 926.

Mesostructure - thermoelectric properties relationships in $V_xMn_{1-x}Si_{1.74}$ (x = 0, 0.04) Higher Manganese Silicides prepared by magnesiothermy: supplementary information

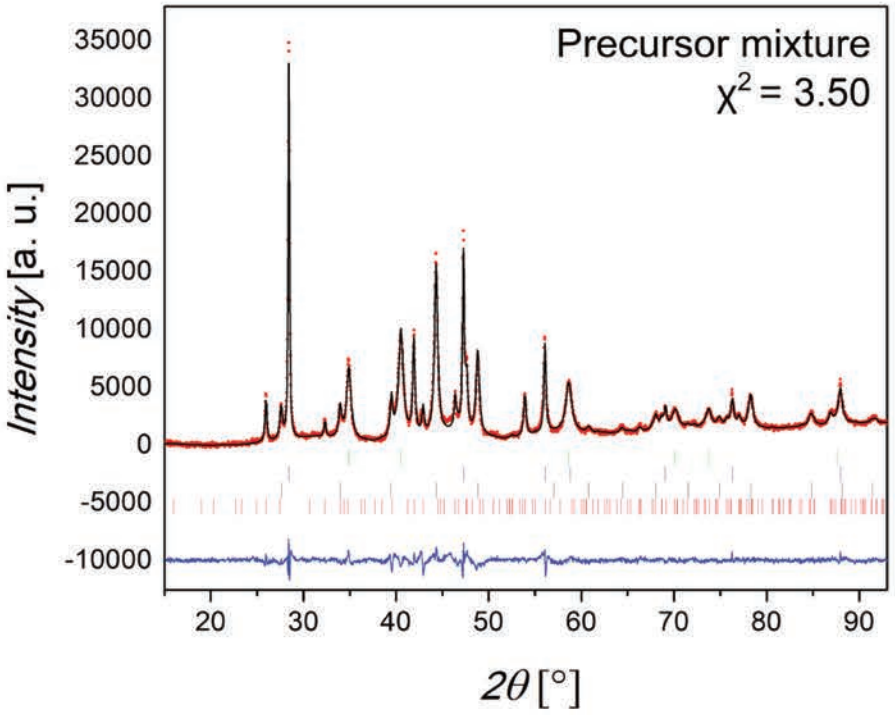

Figure SI 8: Rietveld refined XRD pattern of a ball-milled MnO + Si precursor mixture. The experimental data are plotted in red symbols, the calculated one in black line and the difference with a blue line. The vertical ticks indicate the theoretical Bragg positions of MnO (green), Si (blue), MnSi (black) and $MnSi_\gamma$ (red).

Table SI 10: Structural parameters for Si (s.g. $Fd\bar{3}m$) obtained from the Rietveld refinement of the precursor mixture in fig. SI 8. For this phase, the scale factor, lattice parameters and coefficient for peak profile functions were the refined parameters. The atomic coordinates were taken from [1] while the isotropic atomic displacement parameter were set at 0.5 Å^2 for Si.

		Si ($8a$)		
a (Å)	Vol. Fraction (%)	x	y	z
5.434(1)	27(1)	1/8	1/8	1/8

Table SI 11: Structural parameters for MnO (s.g. $Fm\bar{3}m$) obtained from the Rietveld refinement of the precursor mixture in fig. SI 8. For this phase, the scale factor, lattice parameters and coefficient for peak profile functions were the refined parameters. The atomic coordinates were taken from [2] while the isotropic atomic displacement parameters were set at 0.5 Å^2 for Mn and O.

		Mn ($4a$)			O ($4b$)		
a (Å)	Vol. Fraction (%)	x	y	z	x	y	z
4.4490(5)	26(1)	0	0	0	1/2	1/2	1/2

Table SI 12: Structural parameters for MnSi (s.g. $P2_13$) obtained from the Rietveld refinement of the precursor mixture in fig. SI 8. For this phase, the scale factor, lattice parameters and coefficient for peak profile functions were the refined parameters. The atomic coordinates were taken from [3] and fixed while the isotropic atomic displacement parameters were set at 0.5 Å^2 for Mn and Si.

			Mn ($4a$)	Si ($4a$)
Pattern	a (Å)	Vol. Fraction (%)	x,y,z	x,y,z
(a)	4.5657(5)	26(1)	0.3883	0.0961

Table SI 13: The approximate commensurate structure Mn_4Si_7 (s.g. $P\bar{4}c2$) was used to describe the Bragg peaks corresponding to HMS in the Rietveld refinement of the precursor mixture in fig. SI 8. For this phase, the scale factor, lattice parameters and coefficients for peak profile functions were the refined parameters. The atomic coordinates were taken from [4] and fixed while the isotropic atomic displacement parameters were set at 0.5 $Å^2$ for Mn and Si.

a(Å)		b(Å)		c(Å)		Vol. Fraction (%)		
5.533(1)		5.533(1)		17.484(2)		21(1)		
	Mn ($2a$)			Mn ($4c$)			Mn ($4h$)	
x	y	z	x	y	z	x	y	z
0	0	1/4	0	0	0	1/2	1/2	1/8
	Mn ($4i$)			Mn ($4i$)			Si ($8j$)	
x	y	z	x	y	z	x	y	z
0	1/2	1/16	0	1/2	5/16	0.3436	0.2279	0.5409
	Si ($8j$)			Si ($8j$)			Si ($4e$)	
x	y	z	x	y	z	x	y	z
0.1933	0.1507	0.1129	0.1627	0.6791	0.1815	1/3	1/3	1/4

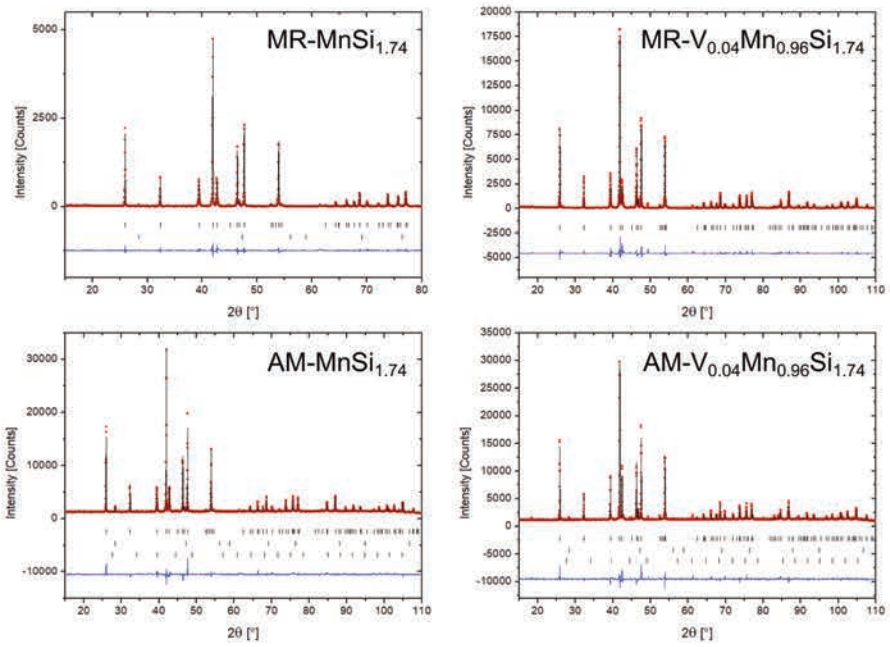

Figure SI 9: Rietveld refined XRD patterns of the as-sintered MR-$MnSi_{1.74}$, MR-$V_{0.04}Mn_{0.96}Si_{1.74}$, AM-$MnSi_{1.74}$ and AM-$V_{0.04}Mn_{0.96}Si_{1.74}$ pellets. The experimental data are plotted in red symbols, the calculated one in black line and the difference with a blue line. The vertical ticks indicate the theoretical Bragg positions for HMS (1^{st} row), Si (2^{nd} row) and MnSi (3^{rd} row)

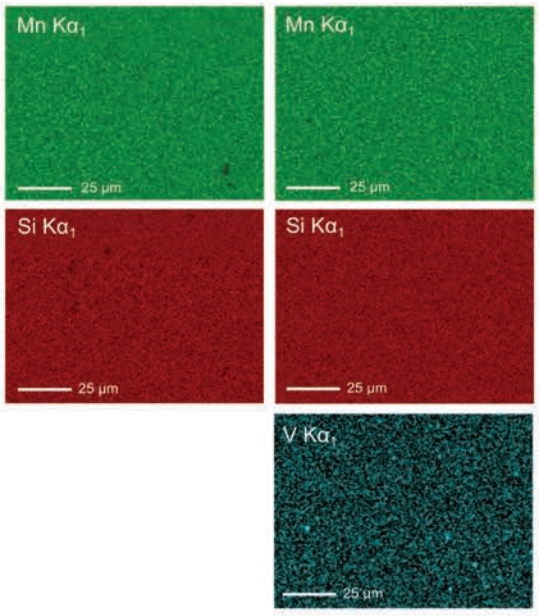

Figure SI 10: SEM-EDS maps of the surface of the polished surface of as-sintered MR-$MnSi_{1.74}$ (left) and MR-$V_{0.04}Mn_{0.96}Si_{1.74}$ (right)

References

[1] J. Dismukes, L. Ekstrom, R. Paff, *J. Phys. Chem.* **1964**, *68*, 3021–3027.

[2] C. A. Barrett, E. B. Evans, *J. Am. Ceram. Soc.* **1964**, *47*, 533.

[3] M. I. Gasik, O. I. Polyakov, *Russ. Metall.* **1982**, *4*, 177–185.

[4] H. Knott, M. Mueller, L. Heaton, *Acta Crystallogr.* **1967**, *23*, 549–555.

Magnesioreduction synthesis (Co-doped) β-$FeSi_2$: mechanism, microstructure and improved thermoelectric properties

Sylvain Le Tonquesse,[a], Zelia Verastegui [a], Helene Huynh [b], Vincent Dorcet [a], Quansheng Guo [b], Valérie Demange,[a] Carmelo Prestipino,[a], David Berthebaud [b], Takao Mori [c], and Mathieu Pasturel*[a]

[a] Univ Rennes, CNRS, ISCR-UMR6226/ScanMAT-UMS2001, F-35000, Rennes, France. Tel: +33-2-23-23-58-61; E-mail: mathieu.pasturel@univ-rennes1.fr

[b] CNRS - Saint-Gobain - NIMS, UMI3629, Laboratory for Innovative Key Materials and Structures (LINK), National Institute for Materials Science, 1-1 Namiki, Tsukuba, Ibaraki 305-0044, Japan

[c] National Institute for Materials Science (NIMS), WPI-MANA and CFSN, Tsukuba, Japan

Published in *ACS Applied Energy Materials*.

Abstract

β-$FeSi_2$ and β-$Co_{0.07}Fe_{0.93}Si_2$ thermoelectric silicides were synthesized from Fe_2O_3 and Si powders using a magnesiothermic process. Detailed study of the synthesis reaction mechanism by X-ray diffraction analyses of the products reveals that liquid Mg is mandatory to initiate the reduction reaction. After completion of the reaction in relatively short time (10 h at 1173 K), the magnesiosynthesized iron disilicide are characterized as powders with grain sizes ranging from 30 to 400 nm and containing a high concentration of (100)[011]/2 stacking faults quantified for the first time using a dedicated Rietveld refinement software. The thermoelectric properties of spark plasma sintered pellets with submicrometric grain sizes, high stacking faults density and residual micro- to nanoporosities are presented. To better appreciate the influence of the original microstructure on the thermoelectric properties, corresponding materials synthesized by conventional arc-melting process are characterized under the same conditions and used for comparison. Strong thermal conductivity reduction of 20 % at 773 K has been achieved thanks to the mesostructuration induced by the magnesioreduction synthesis. It results in an improved maximum figure-of-merit ZT reaching 0.18 at 773 K for β-$Co_{0.07}Fe_{0.93}Si_2$.

Introduction

Thermoelectric (TE) materials are being extensively investigated because they enable the direct conversion of (wasted) heat into electricity, and *vice versa*, through highly reliable solid state devices.[1,2] The material performances are directly related to the TE figure-of-merit ZT defined as:

$$ZT = \frac{\alpha^2}{\rho \cdot (\kappa_L + \kappa_e)} \cdot \mathrm{T}$$

where α is the Seebeck coefficient, ρ the electrical resistivity, κ_L and κ_e the lattice and electronic contributions to the total thermal conductivity κ and T the absolute temperature. Large enhancement of ZT and subsequent conversion yield is however challenging due to interrelated physical components. Common strategies consist on the one hand in the optimization of the power factor, $PF = \alpha^2/\rho$, essentially *via* doping and band engineering,[3] and on the other hand in the reduction of κ_L *via* nanostructuration, porosity/defects engineering and complex alloying.[4–6] In the past twenty years, these strategies successfully resulted in TE materials with ZT much higher than 1.[7–9] Most of these materials, including clathrates,[10] Pd/Te-based alloys[11] or Hf-containing Heusler phases,[12] are however hardly industrializable candidates because of time and energy consuming syntheses, low mechanical properties and most importantly chemical compositions including toxic and/or expensive constituting elements.[13]

From these points of view, β-$FeSi_2$ is considered as a reasonable candidate for large scale application due to its extremely abundant and ecofriendly constituting elements, excellent mechanical properties and oxidation resistance. However, the intrinsic TE properties of pristine $FeSi_2$ are poor, especially due to its high thermal conductivity (16 - 17 W m^{-1} K^{-1} at 273 K) and electrical resistivity (5 - 10 mΩ m at 273 K).[14] Doping with Co[14,15], Al[15], Mn[16] or Cr[14] efficiently improves the maximum ZT to about 0.15. Moreover, the synthesis of β-$FeSi_2$ (space group $Cmce$) by conventional metallurgical routes is facing the peritectoid decomposition in ϵ-FeSi (S. G. $P2_13$) and α-$Fe_{1-\delta}Si_2$ (S. G. $P4/mmm$) above 1255 K,[17] implying long annealing at high-temperature to recover the β-phase. For such reasons, extensive research has been devoted to the development of alternative synthesis routes for nanostructured silicides with reduced thermal conductivity adapted to large scale production. For example, mechanical alloying[14,18,19] or melt spinning[20] followed by reactive sintering were used for the fabrication of mesostructured and highly substituted β-$FeSi_2$. Recently, several studies reported the synthesis of β-$FeSi_2$/Si(Ge) nanocomposites by the eutectoid decomposition of α-$Fe_{1-\delta}Si_2$.[21–23] The resulting

microstructure consists in 10 to 200 nm Si(Ge) inclusions well-dispersed inside a β-$FeSi_2$ matrix allowing a κ reduction up to 50 %. Controlled doping remains however difficult by this approach resulting in materials with peak ZT rarely exceeding 0.1.[24–27] More exploratory synthesis routes such as laser sintering[28,29] or gas-phase reaction[30] were successful to obtain β-$FeSi_2$ but they still remain more adapted to laboratory scale production.

Sen *et al.* reported an innovative synthesis of (doped) β-$FeSi_2$ nanopowders by magnesioreduction of mixed oxide mixtures prepared by sol-gel method from tetraethyl orthosilicate ($Si(OC_2H_5)_3$) and ferric nitrate ($Fe(NO_3)_3{\cdot}9H_2O$).[31,32] The high reducing power of Mg allows the reaction to be carried out in short reaction time (6 h) and at relatively low temperature (1073 K) thus avoiding the post-synthesis annealing step. In addition, the powder obtained by this process has grain sizes as small as 50 nm, which might be suitable for the preparation of nanostructured thermoelectrics. However, the as-reported synthesis procedure remains hardly compatible with industrial scale production, mainly due to the numerous steps involved (up to 6) including a time-consuming preparation of mixed oxide mixture (2 steps totaling 18 h) from highly hygroscopic reactants.

In the present article, a modified magnesioreduction synthesis for thermoelectric β-$FeSi_2$ and β-$Co_{0.07}Fe_{0.93}Si_2$ powders with 30 - 400 nm grain sizes is described. The preparation of the oxide precursor mixture is realized in a single step by ball-milling (Co-doped) Fe_2O_3 and Si. This offers many advantages such as a higher scalability perspective, the use of cheap, air stable and non-hazardous precursors and a final yield greater than 98 %. The chemical reactivity has been followed by powder X-ray diffraction during the whole process to optimize the temperature/duration of the thermal treatment. The crystal structure, refined for the first time using a stacking faults dedicated software, and the microstructure, characterized by scanning and transmission electron microscopies, are presented on as-synthesized powders and spark plasma sintered pellets. Finally the improved TE properties are discussed toward the influence of the microstructure and compared to similar materials synthesized by conventional arc-melting/sintering/annealing route.

Experimental methods

The experimental set-up for the magnesioreduction synthesis (MR) is described in more details in our previous articles.[33,34] For undoped β-$FeSi_2$, a precursors mixture is first prepared by ball-milling stoichiometric amounts of Fe_2O_3 (Merck, $>$ 99 %) and Si powder (Ventron, 99.9 %) using WC vial and balls (ball-to-powder ratio of 5 : 1) with rotation speed of 650 rpm for 4 h. Good control of milling conditions of

precursors was found essential to prevent contamination by WC during the milling and formation of side-products (FeSi, Fe_3Si, unreacted Si) during the magnesioreduction process. The precursor mixture is cold pressed (100 MPa) in Ø 10 mm pellets with 2 mm height and placed with adequate amount of Mg turnings according to:

$$Fe_2O_3 + 4\,Si + \underset{(+25\%)}{3\,Mg} \longrightarrow \beta\text{-}FeSi_2 + 3\,MgO$$

in a clamped Mo crucible. The latter is heated under Ar protective atmosphere at a rate of 100 K h^{-1} up to 1173 K, maintained at this temperature for 10 h and cooled down to room temperature by switching off the furnace. The reaction product is recovered by opening the crucible and MgO by-product is removed by soaking the as-synthesized powder twice in diluted hydrochloric acid (2 wt.%) and washing three times with distilled water and once more with ethanol before being dried at 353 K overnight. Densified β-$FeSi_2$ pellets are obtained by spark plasma sintering (SPS, FCT HP-D-10 apparatus) the 'washed' powders in Ø 10 mm graphite dies at 1323 K - 80 MPa for 30 min followed by 24 h annealing at 1100 K in an evacuated silica tube.

For the synthesis of β-$Co_{0.07}Fe_{0.93}Si_2$, the addition of Co_3O_4 to Fe_2O_3 and Si during the ball-milling preparation of the precursor mixture leads to the formation of $CoSi_2$ during the magnesioreduction process. This is attributed to an uneven distribution of Co in the mixture. Much better results are obtained starting from properly doped $Co_{0.14}Fe_{1.86}O_3$ where Fe and Co are homogeneously distributed at the atomic scale in the precursor and the probability to form side-products is greatly reduced. $Co_{0.14}Fe_{1.86}O_3$ is synthesized by dissolving $Co(NO_3)_2{\cdot}6H_2O$ (Fluka, $\geq$ 98 %) and $Fe(NO_3)_2{\cdot}9H_2O$ (Fluka, $\geq$ 98 %) in a minimum amount of distilled water and by calcinating the mixture at 773 K for 6 h in air. According to X-ray diffraction (XRD), the obtained red powder is single phase α-$Co_xFe_{2-x}O_3$ ($R\bar{3}c$) with a = 5.0327(1) Å and c = 13.7413(4) Å as refined by the Le Bail method (fig. SI 11). The lattice parameters are significantly different from those reported for pure α-Fe_2O_3 (a = 5.0368(1) Å and c = 13.7601(3) Å[35]) and energy dispersive spectroscopy (EDS) elementary analyses indicate a Co concentration of approximately 2 at.% in agreement with the targeted composition. This precursor is used instead of Fe_2O_3 in the above procedure for the magnesioreduction synthesis of $Co_{0.07}Fe_{0.93}Si_2$. The conventional synthesis of β-$FeSi_2$ and β-$Co_{0.07}Fe_{0.93}Si_2$ consisted in arc-melting (AM) stoichiometric amounts of the metallic elements three times to ensure homogenization. The resulting ingots are milled, SPS sintered at 1223 K and 90 MPa for 5 min and finally annealed for 72 h at 1073 K in evacuated silica tubes.

The crystal structure and purity of the samples are checked by powder XRD using a Bruker D8 Advance diffractometer working in the modified Bragg-Brentano geometry with a monochromatized Cu Kα_1 radiation (λ = 1.54059 Å) and equipped with a LynxEye fast detector. Structural parameters are determined by Rietveld refinements of the XRD patterns using the FullProf or FAULTS softwares[36,37] included in the FullProf Suite package.[38] Scanning electron microscopy (SEM) in secondary and backscattered electrons modes and EDS are performed on a JEOL JSM 7100 F microscope equipped with an Oxford EDS SDD X-Max spectrometer. Transmission electron microscopy (TEM) is performed on a JEOL 2100 LaB_6 instrument operating at 200 kV and equipped with high resolution Gatan US1000 and Orius SC 200D cameras and EDS Oxford 20 mm^2 SDD spectrometer. Preparation of the powder samples for SEM analyses consists in the deposition of powder on carbon tape followed by metallization with carbon while for TEM analyses small amount of the powder is sonificated in absolute ethanol and deposited for drying on a carbon coated copper grid.

The thermal diffusivity (D) is measured by the laser flash analysis (LFA) method on Ø 10 mm and 2 mm thick samples coated with graphite using a Netzsch LFA 467 HyperFlash equipment under N_2 atmosphere. The thermal conductivities are then calculated by the relation $\kappa = D \cdot C_p \cdot d$ with C_p the specific heat of the sample determined thanks to a Netzsch *Pyroceram* reference and the density d determined by the Archimede method in absolute ethanol. Measurements of the Seebeck coefficient and electrical resistivity are realized simultaneously on 6x2x2 mm^3 bars using a ZEM3 (ULVAC-RIKO Inc., Yokohama, Japan) equipment under He atmosphere.

Result and discussion

Magnesioreduction process

The XRD pattern of the precursors mixture obtained by ball-milling Fe_2O_3 and Si is shown in fig. 56. Up to six crystalline phases have been identified indicating a reactive milling. The relative concentrations (mol.%) of the products in the precursors mixture are determined by Rietveld refinement (fig. SI 12a):

$$Fe_2O_3 + 4\,Si \xrightarrow[4\,h]{650\,rpm} \underset{42\%}{Si} + \underset{23.5\%}{FeSi} + \underset{18\%}{\alpha\text{-}Fe} + \underset{11.5\%}{\alpha\text{-}Fe_{1-\delta}Si_2} + \underset{2.5\%}{FeO} + \underset{2.5\%}{Fe_2SiO_4}$$

Interestingly, Fe^{3+} (Fe_2O_3) is entirely reduced in Fe^{2+} (FeO, Fe_2SiO_4) or metallic Fe (Fe, FeSi, α-$Fe_{1-\delta}Si_2$) during the milling process. Solid state redox reactions occur

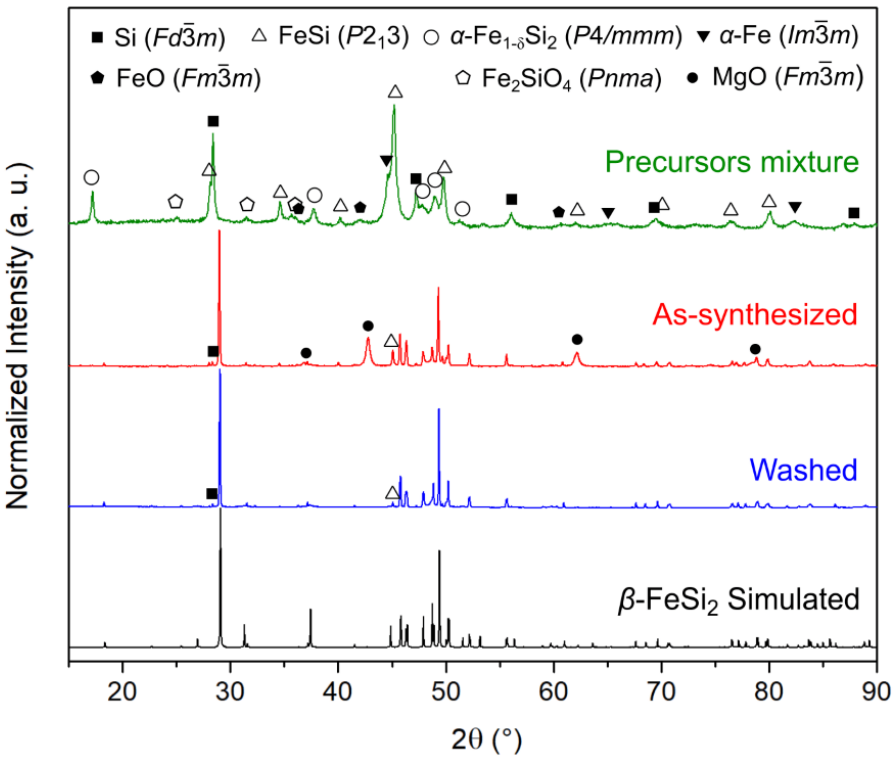

Figure 56: XRD patterns of the precursor mixture (green), as-synthesized (red) and HCl-washed (blue) MR β-$FeSi_2$ powders, as well as simulated pattern for β-$FeSi_2$ [39] (black). Intensity discrepancies between some peaks in the experimental and theoretical β-$FeSi_2$ patterns are linked to the presence of (100)[011]/2 stacking faults in the crystals (see text for details)

with Si playing the role of reducing agent most probably according to:

$$2\,Fe_2O_3 + Si \longrightarrow 4\,FeO + SiO_2 \qquad \Delta G_r^\circ(300\ K) = \text{-}353.3\ kJ\ [40]$$

$$2\,FeO + Si \longrightarrow 2\,Fe + SiO_2 \qquad \Delta G_r^\circ(300\ K) = \text{-}444.4\ kJ\ [40]$$

Both reductions are thermodynamically possible at room temperature in view of their large negative Gibbs free energies. The activation energies are overcome by the highly energetic shocks occurring in the milling vial. Analogous reaction are reported for higher manganese silicides where MnO is reduced by Si in similar milling conditions.[34]

As a result, SiO_2 has to be present in the precursor mixture. Its amorphous nature is suggested by the broad deviation of the background of XRD patterns around 22° associated to silica glass[41]. The Si/Fe atomic ratio of 1.5 determined from Rietveld

refinement is much smaller than the value of about 2 expected from the reactant quantities and confirmed by SEM-EDS analyses. A SiO_2 concentration of about 23 mol.% in the precursor mixture can thus be estimated. Moreover, freshly reduced metallic Fe is expected to react with Si by mechanical alloying forming FeSi and α-$Fe_{1-\delta}Si_2$ as already reported in the literature.[18,42,43] The formation of the high temperature allotrope of the disilicide upon milling highlights the energetic conditions in the vial during the milling. Fe_2SiO_4 is probably formed in a similar manner from FeO and SiO_2. SiO_2, FeO and Fe_2SiO_4 are the remaining oxide phases to be reduced by Mg during the magnesioreduction process.

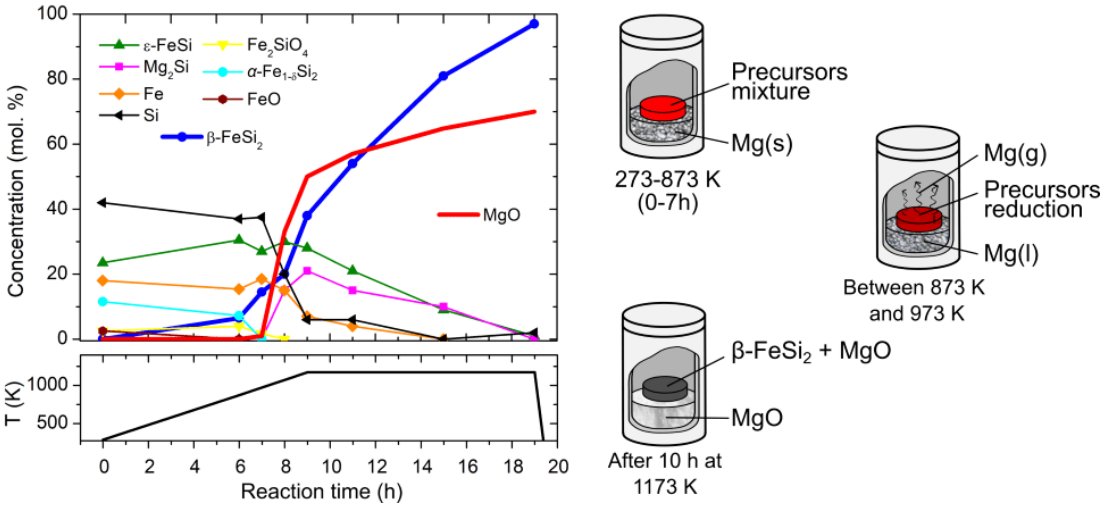

Figure 57: (left) Evolution of the sample composition during the magnesioreduction synthesis of β-$FeSi_2$ determined by Rietveld refinements. The relative deviation on the concentrations is estimated to be well below 5 % according to measurement conditions, quality of the fits and ref[44]. (right) Schemes of the crucible at three important stages of the reaction: heating-up (top), melting of Mg and reduction of the precursor mixture (middle), completed reaction after 19 h (right). (s: solid, l: liquid, g: gas)

The thermal cycle used for the magnesiothermic reaction consists in a heating ramp up to 1173 K in 9 h followed by a 10 h isothermal plateau. In order to better understand the reaction mechanism, the reactor was quenched in cold water at different times of the process and the phases in presence were quantified by Rietveld refinement of XRD patterns. The evolution of phase concentrations (excluding MgO) as a function of the reaction time is presented in fig. 57 with symbols while the overall content in MgO in the reaction media is displayed with a red line. The fitted XRD pattern and refined structural parameters and details about the refinement procedure can be found in fig. SI 12a-h and tables SI. 13-22.

During the first 6 hours of the reaction, no significant changes can be observed indicating that Mg is quite unreactive below 873 K toward the species in presence. Only α-$Fe_{1-\delta}Si_2$ slowly transforms in β-$FeSi_2$ which is the thermodynamically stable allotrope in this temperature range. At Between 873 and 973 K, the reduction process

starts as indicated by the formation of MgO (1 mol.%). Interestingly, it corresponds well to the melting temperature of Mg (melting point T_m = 922 K) and suggests that liquid Mg with high vapor pressure (383 Pa at T_m) is required to initiate the reduction.[45] At 1073 K, MgO and newly formed Mg_2Si intermetallic represent as much as 33 and 16 mol.% of the whole reaction media, respectively. The heat produced locally by the highly exothermic reduction of SiO_2 by Mg (ΔH_r(1200 K) = -344 kJ mol^{-1} [40]) is expected to intensify the reactivity of Mg and to enhance the reaction rate in a scenario close to a combustion synthesis.[46,47] The β-$FeSi_2$ concentration strongly increases (+23 %) between 873 K and 1173 K which is mostly attributed to the solid-state reaction between Fe (-17 %) and Si (-30 %).

At 1173 K, the reaction media is composed of β-$FeSi_2$, FeSi, Mg_2Si and some unreacted Si and Fe giving an overall Si/Fe metal ratio of 1.8. This is higher than the 1.5 ratio determined for the precursor mixture but still lower than the expected value of 2. This suggests that the reduction of amorphous SiO_2 is not yet completed at the end of the heating ramp. As indicted by the decrease of Mg_2Si content and the increase of Si/Fe ratio during the isothermal plateau, amorphous SiO_2 is slowly reduced by highly reactive Mg_2Si[48,49] according to the reaction:

$$SiO_2 + Mg_2Si \xrightarrow{1173\,K} 2\,Si + 2\,MgO \qquad \Delta G_r(1200\ K) = \text{-}252.0\ kJ\ [40]$$

Finally, after 10 h at 1173 K, XRD patters shows that MgO and β-$FeSi_2$ are the major phases in the reduced pellets with only small amounts of residual Si and FeSi.

Weighing the pellets before the reaction and the powders after HCl-washing to remove residual MgO enables to calculate the reaction yields that are typically higher than 98 % using this process.

MR-powder microstructure

SEM images of the as-synthesized MR β-$FeSi_2$ powder (fig. 58a) reveal aggregated particles with sizes below 400 nm. SEM-EDS elementary analyses confirm the Si/Fe metal ratio of 2 and the presence of Mg (60 at.%) ascribed to MgO. Typical TEM brightfield image of an aggregate is shown in fig. 58c. According to TEM-EDS analyses, the large darker areas at the center are mostly composed of Fe and Si while the surrounding brighter area corresponds to MgO. In addition, electron diffraction pattern in fig 58c shows diffuse rings indexed as MgO (s.g. $Fm\bar{3}m$, a = 4.21 Å)[50]

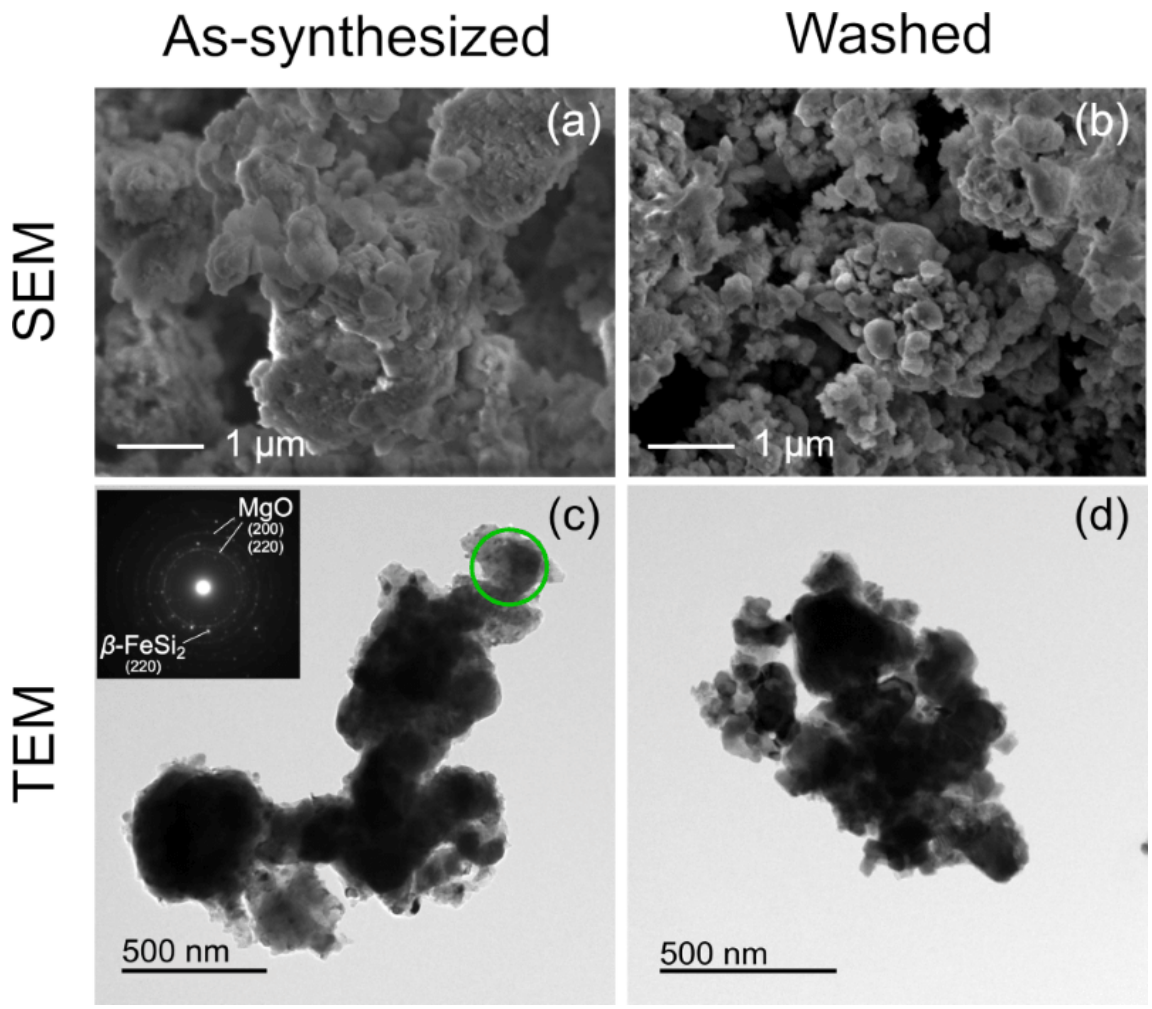

Figure 58: (a-b) Secondary electron SEM and (c-d) brightfield TEM images of the as-synthesized (left) and HCl-washed (right) MR β-$FeSi_2$ powder. The electron diffraction pattern shown in inset was taken at the green circle in (c).

while sharp spots are indexed as β-$FeSi_2$ [39]. In light of these observations, the aggregate irregular shape of as-synthesized powder, derives from the association of well-crystallized β-$FeSi_2$ particles (darker areas) being embedded inside a nanocrystalline MgO matrix (bright area). We hypothesize here that the MgO layer surrounding the β-$FeSi_2$ grains plays a significant role during the heat treatment to limit the grain growth and stabilize the submicronic size of the silicide.

After the washing step with diluted hydrochloric acid, the diffraction peaks of MgO disappear on the XRD patterns indicating its elimination at least below the detection level of the technique (fig. 56). The almost entire dissolution of MgO as well as the homogeneous insertion of cobalt in the doped samples are confirmed by SEM/TEM-EDS analyses.

Removal of the MgO layer reveals the morphology of the β-$FeSi_2$ particles (fig. 58b,d) having sizes ranking from 30 nm to about 400 nm. The average size of the MR β-$FeSi_2$ powders obtained in the present magnesioreduction process is slightly

larger than that obtained by Sen *et al.*.[31] We attribute it to smaller oxide particles, lower reaction temperature (-100 K) and presence of MgO diluent in their precursor mixture. In our case, adding MgO diluent was found to considerably reduce the reaction kinetics.

Crystal structure

As reported by Dusausoy *et al.*,[39] β-$FeSi_2$ crystallizes in the orthorhombic *Cmce* space group with lattice parameters $a = 9.8774(3)$ Å, $b = 7.8128(3)$ Å and $c = 7.8272(3)$ Å. This structure type derives from the fluorite-type structure by strongly distorting the [Si_8] cubes into irregular prisms where Fe-atoms occupy alternatively one half of the central sites (fig. 59a,b). In this initial description of the crystal structure, two independent Fe-sites are distributed over two kind of layers stacked along the *a*-axis (fig. 59a): the layer 1 contains the Fe1 atoms in *8d* Wyckoff site surrounded by a [Si_8] trapezoid-based prisms, the layer 2 contains the Fe2 atoms in *8f* Wyckoff site coordinated by similar [Si_8] trapezoid-based prisms with additional torsion angle between the rectangular faces. This structure of β-$FeSi_2$ can also be described as another layered structure with ABAB stacking mode along the [100] direction as shown in fig. 59a. While the individual layers are structurally identical, the layer A transforms into the layer B by the translation vector $x + 1/2$, $y + 1/2$, z as represented in the projections along the *a*-axis of the layers in fig. 59c. In this description, each layer is composed of the layer 1 (fig. 59b) sandwiched between two half of the layer 2. In this representation, the pseudo-cubic layer 2 is build from the interaction of the A and B layers.

However, the crystal structure is known to accommodate high concentration of intrinsic stacking faults with displacement vector (100)[011]/2 as reported by Zheng *et al.*[51] and confirmed by Yamane *et al.*[52] In other words, the expected AB stacking is randomly replaced by a second AB* one where the B* layer is obtained by a x+1/2, y, z+1/2 translation of the A-layer (fig. 59c). A consequence of these stacking faults is the formation of a third type of Fe@[Si8] network (layer 3 in fig. 59b) at the defect which can be considered as a twinned version of the layer 2,[51] with minor differences in the Fe-atom coordination sphere.

In the case of the magnesioreduced powders, the presence of the stacking faults (SF) is highlighted by an important XRD peak shape broadening of *hkl* reflections with $k+l \neq 2n$ (fig. 56) corresponding to diffuse streaks observed in the electron diffraction pattern for this condition along the a^*-direction (fig. 60a). Dark field images obtained from the diffuse streaks of a crystal oriented along the [$0\bar{1}2$] zone axis (fig. 60b) clearly reveal a high density of planar defects. High resolution TEM image of this defective structure (fig. 60c) shows 4.9 Å *(i.e.* $a/2$) thick layers perpendicular

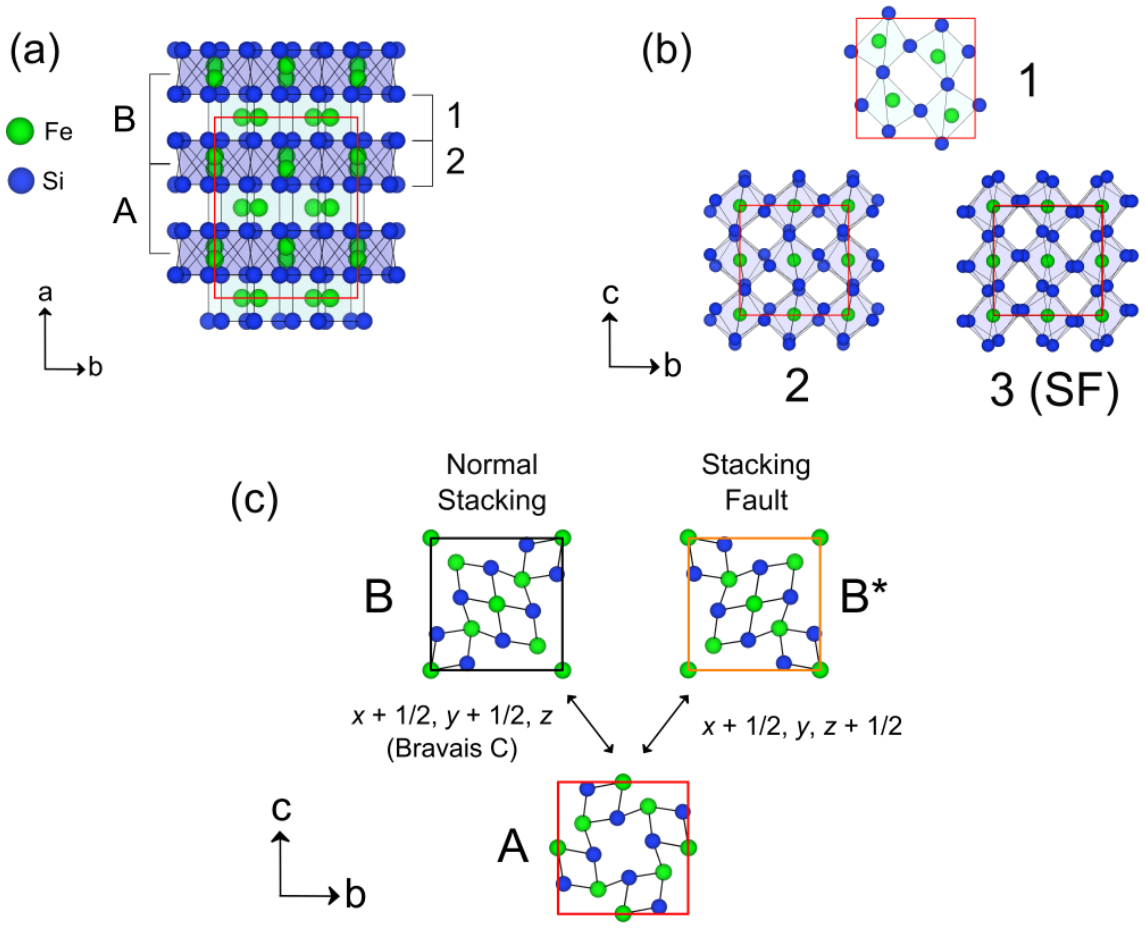

Figure 59: (a) c-axis projection of the crystal structure of β-$FeSi_2$ reported by Dusausoy *et al.*[39] showing the Fe@[Si_8] networks and the $ABAB$ stacking mode; (b) a-axis projections of the pseudo-cubic networks CN1, CN2 and CN3; (c) a-axis projections of the normal stacking A and B layers and alternative stacking layer B* along with related displacement vectors.

to the [100] direction and AB or AB* stacking.

As pointed out by Yamane *et al.*[52], the density of SF in β-$FeSi_2$ is strongly dependent on the synthesis method. Indeed, pulverized crystals grown in relatively mild conditions, *e.g.* metal flux or chemical transport methods, are found to be relatively free of SF while polycrystalline sample prepared for example by conventional fusion/solidification or powder metallurgical methods are more affected. In order to quantify the probability of SF in our samples, Rietveld refinements have been undertaken on both pristine and Co-doped β-$FeSi_2$ prepared by magnesioreduction.

The SF have been taken into account in the modeling of the X-ray diffraction data using the dedicated FAULTS software included in the Full Prof Suite[36–38]. For this, half a unit cell along the a-axis, corresponding to a single layer A (fig. 59), was considered along with two possible displacement vectors, $x + 1$, $y + 1/2$, z and $x + 1$, y, $z+ 1/2$ corresponding to the normal and faulty stacking , respectively. Using this approach, the patterns were refined by the Rietveld method optimizing the stacking

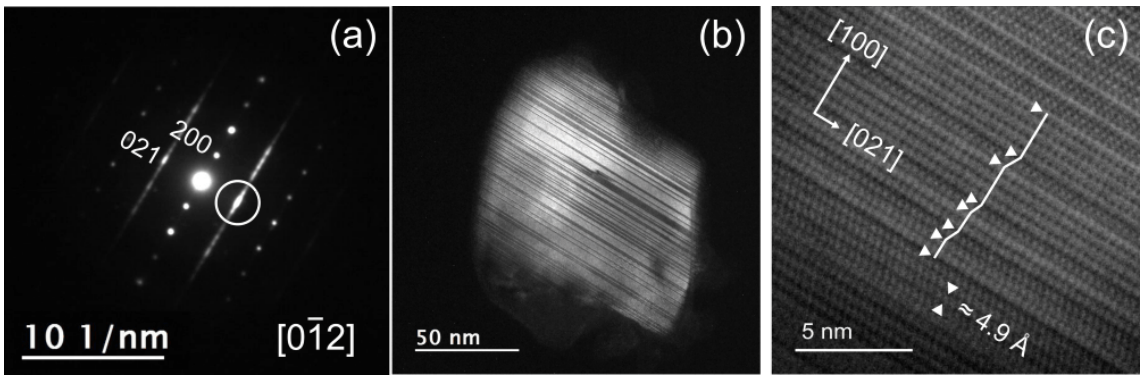

Figure 60: (a) Electron diffraction pattern of MR β-$FeSi_2$ taken along the [0$\bar{1}$2] zone axis showing diffuse streaks for *hkl* reflections with $k+l \neq 2n$. (b) Dark field image taken at a diffuse streak (white circle) revealing high density of planar defects in MR $FeSi_2$(c) HRTEM image showing the stacking faults indicated with white arrows.

fault probability, the lattice and atomic parameters and the peak profile function. Refined XRD are shown in fig. 61 and refined structural parameters summarized in table 7. The atomic coordinates remain almost unchanged compared to Dusausoy's structural model and the atomic displacement parameters have regular values for intermetallic compounds. The SF probabilities were found to be close to 15 % for both compositions. This value compares well with the ratios reported by Yamane *et al.* for β-$FeSi_2$ samples synthesized by powder metallurgy methods.[52] As pointed out by Zheng *et al.*[51], the layer 3 exhibits a twin-like structure, as if the b and c axes were exchanged in the defect layer. Thus with increasing the SF concentration, one expects the b and c lattice parameters to converge to an average value between those in the regular lattice. Accordingly, the b and c lattice parameters in the MR powders are rather close from each other. Interestingly, the lattice constant a of the Co-doped sample increasing from 9.88240(2) Å to 9.89838(8) Å seems to be the only structural parameter affected by the insertion of Co in the structure. This is consistent with Hesse's work[53] reporting a linear increase of a with increasing Co substitution and an expected value of about $a = 9.905$ Å for β-$Co_{0.07}Fe_{0.93}Si_2$.

Densified pellet microstructure

Any attempts to obtain densified pellets by spark plasma sintering below the decomposition temperature of β-$FeSi_2$ resulted in materials with poor relative density (< 85 %) and were consequently abandoned. Opposite, pellets with 94 % and 97 % relative density were prepared from magnesioreduced (MR) and arc-melted (AM), respectively, β-$FeSi_2$ and β-$Co_{0.07}Fe_{0.93}Si_2$ powders by SPS at 1323 K followed by 24 h annealing at 1100 K to recover the desired β-phase. Backscattered electron SEM images and EDS mappings of polished pellet surfaces obtained from the MR process reveal relatively homogeneous chemical composition (fig. 62) with the exception of small amount of FeSi impurity as well as a few WSi_2 particles certainly coming from WC contamination during the early precursor milling. SEM-EDS elementary

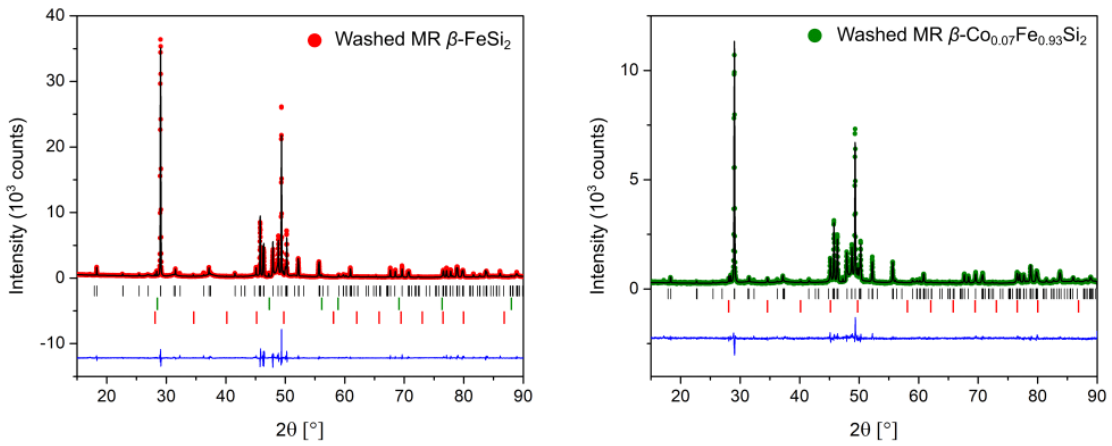

Figure 61: Rietveld refinement of the washed MR β-$FeSi_2$ (left) and MR β-$Co_{0.07}Fe_{0.93}Si_2$(right) powder XRD. The experimental data are plotted in colored symbols, the calculated one with a black line and the difference with a blue line. The vertical ticks indicate the Bragg peak positions for β-$FeSi_2$ (black), FeSi (red) and Si (green).

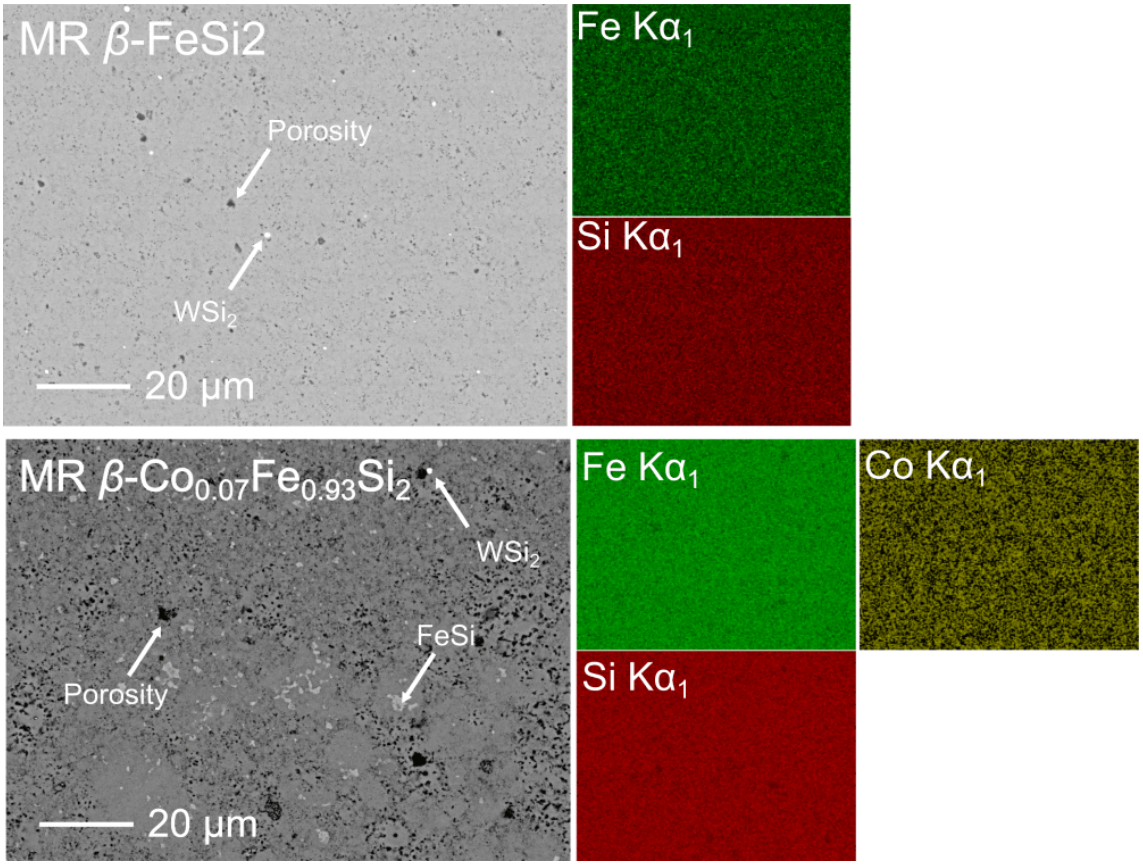

Figure 62: Backscattered electron SEM images and corresponding EDS mappings of the polished surface of undoped MR β-$FeSi_2$ (top) and MR β-$Co_{0.07}Fe_{0.93}Si_2$ (bottom) densified pellets

analyses realized on the Co-doped samples synthesized by MR or conventional AM routes give a similar global Co concentration of about 2 at.% in good agreement with the targeted composition.

SEM secondary electrons images of the broken cross-section of undoped β-$FeSi_2$

Table 7: Lattice parameters, atomic coordinates, isotropic thermal displacement parameters and stacking fault propability (SF) extracted from the Rietveld refinement of the HCl-washed MR β-$FeSi_2$ and MR β-$Co_{0.07}Fe_{0.93}Si_2$XRD patterns

		MR β-$FeSi_2$	MR β-$Co_{0.07}Fe_{0.93}Si_2$
	a (Å)	9.88240(2)	9.89838(8)
	b (Å)	7.81651(2)	7.81778(8)
	c (Å)	7.83428(2)	7.82839(8)
	x	0.129(1)	0.128(1)
Si ($16g$)	y	0.273(1)	0.276(1)
	z	0.049(1)	0.045(1)
	x	0.124(1)	0.124(1)
Si ($16g$)	y	0.049(1)	0.046(1)
	z	0.272(1)	0.273(1)
	B_{iso} (Å^2)	0.4(1)	0.2(1)
Fe2 ($8f$)	y	0.309(1)	0.310(1)
	z	0.312(1)	0.310(1)
Fe1 ($8d$)	x	0.216(1)	0.216(1)
	B_{iso} (Å^2)	0.2(1)	0.1(1)
	SF (%)	14.8(1)	18.5(3)

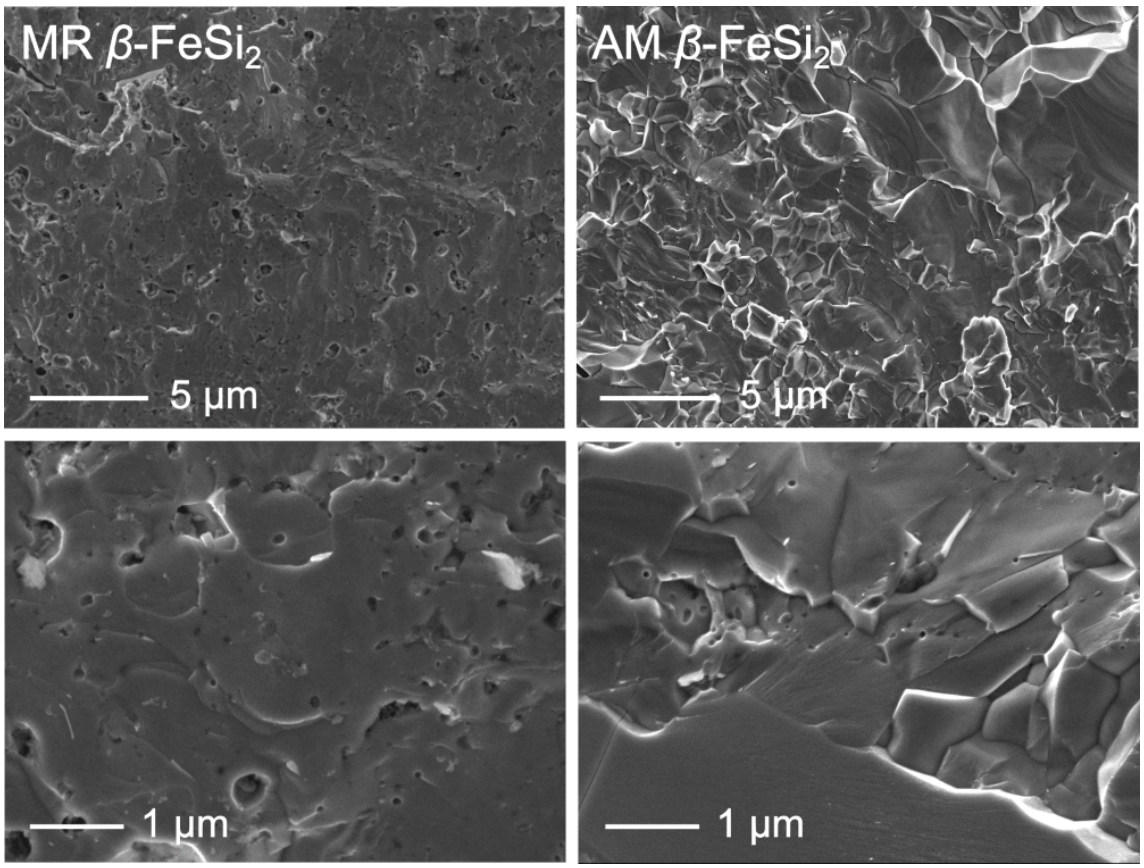

Figure 63: Secondary electron SEM images of broken cross-sections of MR- (left side) and AM $FeSi_2$ (right side) at two different magnifications.

densified pellets are shown in fig. 63 for MR and AM samples. The microstructure of the AM sample is relatively common to sintered iron silicides prepared by fusion-solidification techniques[15,18] and the particle sizes are ranging from 1 μm to tens of μm. Porosity is hardly visible and only a few submicronic pores are visible at high magnification in agreement with the elevated density (97 %) measured by the Archimede method. In the case of the MR samples, the microstructure is significantly different with less well-faceted particles. They also have smaller average grain size with the majority of them being in the 500 nm - 1 μm range. By analogy with our previous report on higher manganese silicides and TEM analysis (fig. 58d) prior to SPS, we assume here that these MR particles are single crystalline. As a consequence of the submicronic grain sizes, numerous residual porosities with sizes ranging from 500 nm down to few tens of nanometers are observed for MR samples which is consistent with the larger deviation from full densification (94 %).

XRD realized on crushed pellets are presented in fig. 64a for undoped and in fig. SI 13 for Co-doped samples. Lattice and structural parameters extracted by Rietveld refinements are presented in table 8 and table SI 23. The lattice constants and atomic coordinates are comparable for the corresponding compositions. More particularly, the similar a-parameters for the doped samples suggests equivalent Co substitution in agreement with SEM-EDS results. The SF probability is however systematically higher for MR ($\approx$ 10 %) than for AM samples ($\approx$ 3 %). The density of SF in the samples can be directly appreciated by comparison of the (312) Bragg reflections (fig. 64b) which become significantly less intense and broader with increasing SF probability. This result confirms that the synthesis route has a strong influence on the SF density in β-$FeSi_2$ even after high-temperature sintering/annealing steps.

Table 8: Lattice parameters, stacking fault probability and impurity content for spark plasma sintered MR $FeSi_2$, AM $FeSi_2$, MR $Co_{0.07}Fe_{0.93}Si_2$, AM $Co_{0.07}Fe_{0.93}Si_2$ obtained by Rietveld refinements, together with their relative density obtained by the Archimede method.

	MR $FeSi_2$	AM $FeSi_2$	MR $Co_{0.07}Fe_{0.93}Si_2$	AM $Co_{0.07}Fe_{0.93}Si_2$
a (Å)	9.89104(6)	9.87518(4)	9.91176(8)	9.91200(4)
b (Å)	7.81612(3)	7.79980(3)	7.81410(4)	7.81500(4)
c (Å)	7.84209(3)	7.83727(2)	7.84084(5)	7.84060(3)
SF (%)	10.7(2)	3.7(1)	10.4(1)	3.2(1)
Rel. density (%)	94	97	94	97
Impurities (wt.%)	1 (FeSi)	1 (FeSi) 2.5 (Si)	2 (FeSi)	5 (FeSi)

Despite the phase transition from of β-$FeSi_2$ to α-$_{1-\delta}Si_2$ during the sintering process and back to β-form after annealing, the microstructures of the densified materials remain significantly different for the two synthesis routes. The MR samples are char-

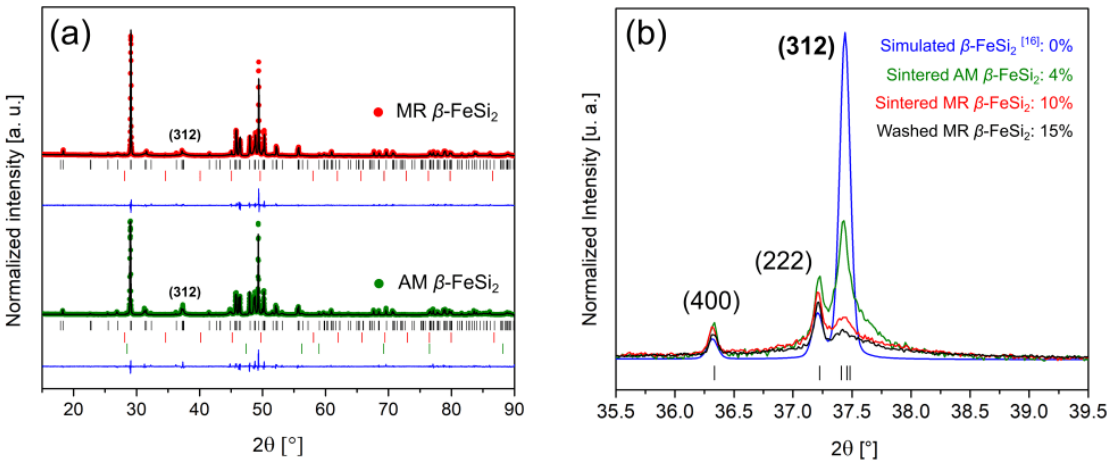

Figure 64: (a) Rietveld refined powder XRD patterns of sintered MR β-$FeSi_2$ (red) and AM β-$FeSi_2$ (green). The experimental data are plotted in colored symbols, the calculated one with a black line and the difference with a blue line. The vertical ticks indicate the Bragg peak positions for β-$FeSi_2$ (black), FeSi (red) and Si (green). (b) Influence of the stacking fault density on the (312) diffraction peak profile and intensity.

acterized by smaller average particle sizes and higher density of grain boundaries, of porosities and higher concentration of SF. All these defects acting at different scales in the materials are expected to scatter efficiently the phonons over a broad energy spectrum and thus to reduce the thermal conductivity of $FeSi_2$. The influence of this microstructure on the thermoelectric properties of this material is thus presented in the following.

Thermoelectric properties

The TE properties of β-$FeSi_2$ and β-$Co_{0.07}Fe_{0.93}Si_2$ synthesized by magnesioreduction and arc-melting were investigated from room temperature up to 773 K. Measurements of the electronic properties were cycled twice and showed good reversibility. Undoped MR β-$FeSi_2$ samples have elevated electrical resistivity (14 mΩ m) (fig. 65a) and Seebeck coefficient (550 μV K^{-1}) (fig. 65b) at room temperature which is in agreement with the relatively low charge carrier concentration (10^{17} - 10^{18} cm^{-3}) reported for this semiconductor.[54,55] Interestingly, the Seebeck coefficients are positive for MR and negative for AM samples indicating n-type and p-type conductions, respectively. Experimental data from the literature report p-type[56] as well as n-type[14,25] bulk materials. The conduction type change is often attributed to the presence of impurities or defects (*e.g.* Fe or Si vacancies) which strongly depends on the synthesis route.[57] Chu *et al.* also reported change from p- to n-type conduction on a β-$FeSi_2$ thin film after prolonged annealing at 1163 K.[58] These results suggest that the synthesis routes as well as the high-temperature treatment can strongly influence the transport properties of β-$FeSi_2$ materials and possibly explain the different conduction types measured in the present work. Due to the high electrical

resistivity and despite the higher Seebck coefficient, the *PF* of the MR β-$FeSi_2$ sample is found far superior to the AM sample one on the whole temperature range reaching a maximum value of 0.2 mW m^{-1} K^{-2} at 650 K (fig. 65c).

Upon Co doping, the electrical resistivities of both MR and AM samples significantly drop while the Seebeck coefficient stabilizes around -180 μV K^{-1}. This can be explained by the creation of donor levels in the band gap increasing the estimated charge carriers concentration up to 10^{20} - 10^{21} cm^{-3} according to literature data.[56,59,60] The electrical resistivity of the MR sample is however systematically 35 % higher than the AM sample on the whole temperature range which can be partially explained by the lower density of the MR material.[16] The resulting *PF* are increased to values as high as 0.9 and 1.0 mW m^{-1} K^{-2} at 773 K foe the MR and AM β-$Co_{0.07}Fe_{0.93}Si_2$, respectively.

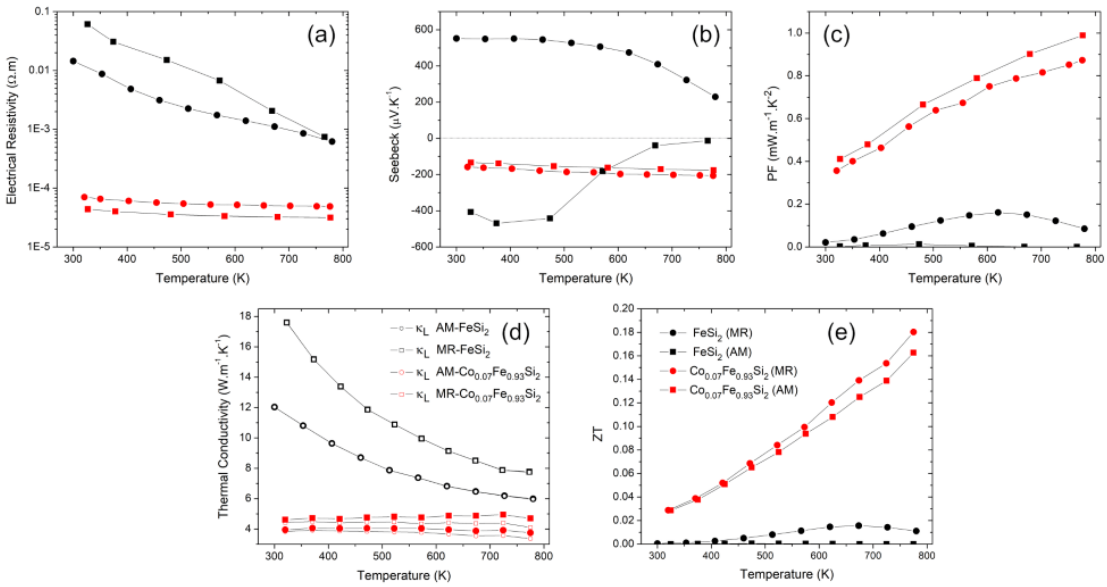

Figure 65: High temperature thermoelectric properties of β-$FeSi_2$ (black symbols) and β-$Co_{0.07}Fe_{0.93}Si_2$ (red symbols) synthesized by magnesioreduction (MR, circles) and conventional arc-melting (AM, squares). Thermal dependence of (a) the electrical resistivity, (b) the thermopower, (c) the power factor (*PF*), (d) the total (filled symbols) and lattice (empty symbols) thermal conductivity and (e) resulting figure-of-merit *ZT*.

The thermal conductivities of AM β-$FeSi_2$ and β-$Co_{0.07}Fe_{0.93}Si_2$ (fig. 65d) equal 17.5 and 4.7 W m^{-1} K^{-1} at room temperature which is in good agreement with most literature data.[14,15,53,56] The lower thermal conductivity of the doped sample is attributed to the mass fluctuation phenomenon at the mixed Fe/Co sites. The thermal conductivities of the respective MR synthesized samples are comparatively lower by 32 % and 15 % at 320 K. At the highest temperature, the thermal conductivity reduction reaches 23 % for both compositions. The lattice thermal conductivity of all the samples were estimated by subtraction of κ_E calculated with the Wiedermann-Franz law $\kappa_e(T) = L \cdot T/\rho(T)$ with the commonly used L = $2.4.10^{-8}$ W Ω K^{-2} to

the total thermal conductivity. The lower κ measured for MR samples can thus be mostly attributed to κ_L reduction reaching 24 % and 17 % at 773 K for the undoped and Co-doped sample, respectively. The MR and AM samples having similar elementary composition, the reduction of κ_L is attributed to the enhanced acoustic phonon scattering at the porosities, grain boundaries and stacking faults higher density evidenced in the MR materials. Eventually, maximum figure-of-merit ZT of 0.015 at 673 K and 0.18 at 773 K could be calculated for the undoped and doped MR samples, respectively (fig. 65e). In the case of MR β-$FeSi_2$, ZT has been improved compared to the AM sample mostly because of the reduced thermal conductivity but it remains low due to the exceedingly large electrical resistivity. On the other hand, MR β-$Co_{0.07}Fe_{0.93}Si_2$ has a much higher maximum ZT which corresponds to a 12 % improvement compared to the conventionally synthesized sample thanks to the mesostructuration. This is to the best of our knowledge the highest ZT value reported at this temperature for Co-doped β-$FeSi_2$.[15,61]

Conclusions

An optimized magnesioreduction synthesis of β-$FeSi_2$ and β-$Co_{0.07}Fe_{0.93}Si_2$ powders from (Co-doped) Fe_2O_3 and Si has been developed. It offers many advantages over more conventional synthesis routes such as the use of air-stable and inexpensive precursors, short heat treatment below the decomposition temperature of β-$FeSi_2$, very high yield ($>$ 98 %) and a satisfying control of the chemical composition including dopant concentration. Detailed study of the reaction mechanism by means of XRD pattern Rietveld refinements enabled to determine the reduction starting temperature as 973 K, the formation of Mg_2Si intermediate during the process, and a total duration of the thermal treatment of 19 h at 1173 K to achieve a total reaction. After removal of MgO by-product by diluted HCl washing, the as-synthesized silicide powders are composed of well crystallized grains with sizes ranging between 30 and 400 nm. TEM observations reveal high concentration of stacking faults evaluated at 15 - 18 % by Rietveld refinement of the XRD pattern using a dedicated software. The high temperature TE properties of MR/SPS/annealed densified pellets were measured up to 773 K and compared to conventionally arc-melted/SPS/annealed samples with similar compositions. The higher densities of grain boundaries, stacking faults and porosities in the magnesioreduced materials lead to strongly reduced lattice thermal conductivities. As a result, the TE figure of merit ZT of the two compositions are improved even reaching 0.18 at 773 K in the case of β-$Co_{0.07}Fe_{0.93}Si_2$.

Conflicts of interest

There are no conflicts to declare.

Acknowledgements

Loic Joanny and Francis Gouttefangeas are acknowledged for SEM images, and EDS analyses performed on the CMEBA platform. The TEM analyses were performed on THEMIS platform. Both platforms belong to the ScanMAT unit (UMS 2001, University of Rennes 1) which received a financial support from the European Union (CPER-FEDER 2007-2014).

References

[1] L. E. Bell, *Science* **2008**, *321*(5895), 1457–1461.

[2] I. Petsagkourakis, K. Tybrandt, X. Crispin, I. Ohkubo, N. Satoh, T. Mori, *Sci. Technol. Adv. Mater* **2018**, *19*(1), 836–862.

[3] Y. Pei, H. Wang, G. J. Snyder, *Adv. Mater.* **2012**, *24*(46), 6125–6135.

[4] L. Yang, Z.-G. Chen, M. S. Dargusch, J. Zou, *Adv. Energy Mater.* **2018**, *8*, 1701797.

[5] Y. Pei, G. Tan, D. Feng, L. Zheng, Q. Tan, X. Xie, S. Gong, Y. Chen, J.-F. Li, J. He, M. G. Kanatzidis, L.-D. Zhao, *Advanced Energy Materials* **2017**, *7*, 1601450.

[6] T. Mori, *Small* **2017**, *13*, 1702013.

[7] Z. Luo, X. Zhang, X. Hua, G. Tan, T. P. Bailey, J. Xu, C. Uher, C. Wolverton, V. P. Dravid, Q. Yan, M. G. Kanatzidis, *Adv. Funct. Mater.* **2018**, *28*, 1801617.

[8] G.Rogl, J.Bursik, A.Grytsiv, S.Puchegger, V.Soprunyuk, W.Schranz, X.Yan, E.Bauer, P.Rogl, *Acta Mater.* **2018**, *145*, 359–368.

[9] L. Hu, Y. Zhang, H. Wu, Y. Liu, J. Li, J. He, W. Ao, F. Liu, S. J. Pennycook, X. Zeng, *Adv. Funct. Mater.* **2018**, *28*, 1803617.

[10] J.-A. Dolyniuk, B. Owens-Baird, J. Wang, J. V. Zaikina, K. Kovnir, *Mater. Sci. Eng. R* **2016**, *108*, 1–46.

[11] Y. Pei, X. Shi, A. LaLonde, H. Wang, L. Chen, G. J. Snyder, *Nature* **2011**, *473*, 66.

[12] N. Shutoh, S. Sakurada, *J. Alloys Compd* **2005**, *389*, 204–208.

[13] S. LeBlanc, S. K. Yee, M. L. Scullin, C. Dames, K. E. Goodson, *Renew. Sust. Energ. Rev.* **2014**, *84*, 313.

[14] S. Kim, M. Cho, Y. Mishima, D. Choi, *Intermetallics* **2003**, *11*, 399–405.

[15] Z. He, D. Platzek, C. Stiewe, H. Chen, G. Karpinski, E. Müller, *J. Alloys Compd.* **2007**, *438*, 303–309.

[16] C. Gayner, D. Prakash, A. Ballal, *J. Alloys Compd.* **2017**, *698*, 164–169.

[17] T. Massalski, *Binary Alloy Phase Diagrams* **1990**.

[18] X. Qu, S. Lü, J. Hu, Q. Meng, *J. Alloys Compd.* **2011**, *509*, 10217–10221.

[19] V. Poddar, N. Dhokey, R. Garbade, S. Butee, D. Prakash, R. Purohit, *Mat. Sci. Semicon. Proc.* **2017**, *71*, 477–481.

[20] L. Han, T. Xin-Feng, C. Wei-Qiang, Z. Qing-Jie, *Chinese Phys. B* **2009**, *18*, 287–923.

[21] U. Ail, S. Gorsse, S. Perumal, M. Prakasam, A. Umarji, S. Vivès, P. Bellanger, R. Decourt, *J. Mater. Sci.* **2015**, *50*, 6713–6718.

[22] N. Liu, W. A. Jensen, M. Zebarjadi, J. A. Floro, *Mater. Today Phys.* **2018**, *4*, 19–27.

[23] W. A. Jensen, N. Liu, E. Rosker, B. F. Donovan, B. Foley, P. E. Hopkins, J. A. Floro, *J. Alloys Compd.* **2017**, *721*, 705–711.

[24] F. L. B. M. Redzuan, I. Mikio, T. Masatoshi, *J. Mater. Sci.* **2018**, *10*.

[25] P. Rajasekar, A. M. Umarji, *Intermetallics* **2017**, *89*, 57–64.

[26] R. Parasuraman, Y. Wu, J. Ordonez-Miranda, S. Volz, A. M. Umarji, *Sustain. Energ. Fuels.* **2018**, *2*, 1764.

[27] F. L. B. M. Redzuan, M. Ito, M. Takeda, *Intermetallics* **2019**, *108*, 19–24.

[28] H. Wu, B. Hu, N. Tian, Q. Zheng, *Mater. Lett.* **2011**, *65*, 2877–2879.

[29] Y. Kinemuchi, M. Mikami, I. Terasaki, W. Shin, *Mater. Des.* **2016**, *106*, 30–36.

[30] R. Bywalez, H. Orthner, E. Mehmedovic, R. Imlau, A. Kovacs, M. Luysberg, H. Wiggers, *J. Nanopart. Res.* **2013**, *15*, 1878.

[31] S. Sen, N. Gogurla, P. Banerji, P. K. Guha, P. Pramanik, *Mater. Sci. Eng. B* **2015**, *200*, 28–39.

[32] S. Sen, P. K. Guha, P. Banerji, P. Pramanik, *RSC Adv.* **2016**, *6*, 68238.

[33] S. Le Tonquesse, E. Alleno, V. Demange, V. Dorcet, L. Joanny, C. Prestipino, O. Rouleau, M. Pasturel, *J. Alloys Compd.* **2019**, *796*, 176–184.

[34] S. Le Tonquesse, V. Dorcet, L. Joanny, V. Demange, C. Prestipino, Q. Guo, D. Berthebaud, T. Mori, M. Pasturel, *in preparation*.

[35] F. J. Pérez-Alonso, M. L. Granados, M. Ojeda, P. Terreros, S. Rojas, T. Herranz, J. L. G. Fierro, M. Gracia, J. R. Gancedo, *Chem. Mater.* **2005**, *17*, 2329.

[36] M. Casas-Cabanas, M. Reynaud, J. Rikarte, P. Horbachb, J. Rodriguez-Carvajal, *J. Appl. Cryst.* **2016**, *49*, 2259–2269.

[37] M. M. J. Treacy, J. M. Newsam, M. W. Deem, *Proc. R. Soc. London Ser. A* **1991**, *433*, 499–520.

[38] J. Rodriguez-Carvajal, *Physica B* **1993**, *192*, 55–69.

[39] P. Dusausoy, J. Protas, R.Wandji, B. Roques, *Acta Cryst. B* **1971**, *27*, 1209.

[40] O. Knacke, O. Kubaschewski, K. Hesselmann, *Thermo-chemical Properties of Inorganic Substances*.

[41] X. Wang, S. Wang, W. Hu, J. Cai, L. Zhang, L. Dong, L. Zhao, Y. He, *Mater. Lett.* **2014**, *115*, 53–56.

[42] I. Dézsia, C. Fetzera, L. Bujdosób, J. Brötzc, A. Baloghc, *J. Alloys Compd.* **2010**, *508*, 51–54.

[43] H. Nagai, *Mater. Trans., JIM* **1995**, *36*, 365–372.

[44] H. Toraya, *J. Appl. Cryst.* **2000**, *33*, 1324–1328.

[45] *CRC Handbook of Chemistry and Physics*.

[46] C. Won, H. Nersisyan, H. Won, *Chem. Eng. J.* **2010**, *157*, 270–275.

[47] H. Nersisyan, H. Won, C. Won, A. Joc, J. Kim, *Chem Eng J* **2014**, *235*, 67–74.

[48] Z. Xing, J. Lu, X. Ji, *Small Methods* **2018**, *2*, 1800062.

[49] S. Haouli, S. Boudebane, I. J. Slipper, S. Lemboub, P. Gebara, S. Mezrag, *Phosphorus Sulfur Silicon Relat. Elem.* **2018**, *193*, 280–287.

[50] B. A. . Wechsler, A. Navrotsky, *J. Solid State Chem.* **1984**, *55*, 165–180.

[51] Y. Zheng, A. Taccoen, J. F. Petroff, *J. Appl. Cryst.* **1992**, *25*, 122–128.

[52] H. Yamane, T. Yamada, *J. Alloys Compd.* **2009**, *476*, 282–287.

[53] J. Hesse, R. Bucksch, *J. Mater. Sci.* **1970**, *5*, 272.

[54] E. Arushanov1, K. G. Lisunov, *Jpn. J. Appl. Phys.* **2015**, *54*, 07JA02.

[55] E. Arushanov, H. Lange, J. Werner, *phys. Stat. Sol.* **1998**, *166*, 853.

[56] J. ichi Tani, H. Kido, *Jpn. J. Appl. Phys.* **2001**, *40*, 3236–3239.

[57] J. Tani, H. Kido, *J. Alloys Compd* **2003**, *352*, 153–157.

[58] S. Chu, T. Hirohada, H. Kan, *Jpn. J. Appl. Phys.* **2002**, *41*, 299.

[59] S. Brehme, G. Behr, A. Heinrich, *J. Appl. Phys.* **2001**, *89*, 3798.

[60] J.-I. Tani, H. Kido, *J. Appl. Phys.* **1998**, *84*, 1408.

[61] A. Nozariasbmarz, A. Agarwal, Z. A. Coutant, M. J. Hall, J. Liu, R. Liu, A. Malhotra, P. Norouzzadeh, M. C. Öztürk, V. P. Ramesh, Y. Sargolzaeiaval, F. Suarez, D. Vashaee, *Jpn. J. Appl. Phys.* **2017**, *56*, 05DA04.

Magnesioreduction synthesis (Co-doped) β-$FeSi_2$: mechanism, microstructure and improved thermoelectric properties: supplementary information

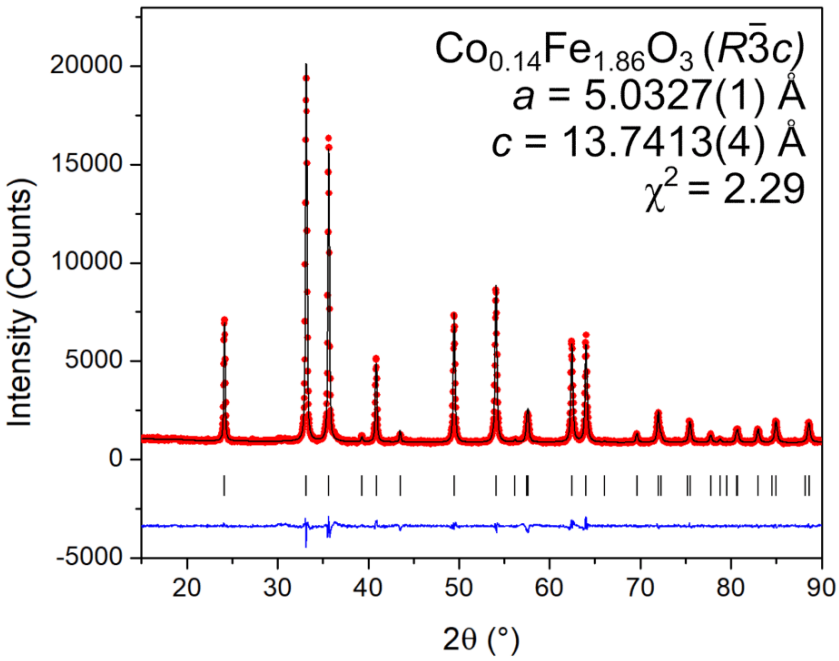

Figure SI 11: Le Bail refined powder XRD pattern of $Co_{0.14}Fe_{1.86}O_3$. The experimental data are plotted in red symbols, the calculated one in black line and the difference in blue line. The vertical ticks indicate the theoretical Bragg peak positions of Fe_2O_3.

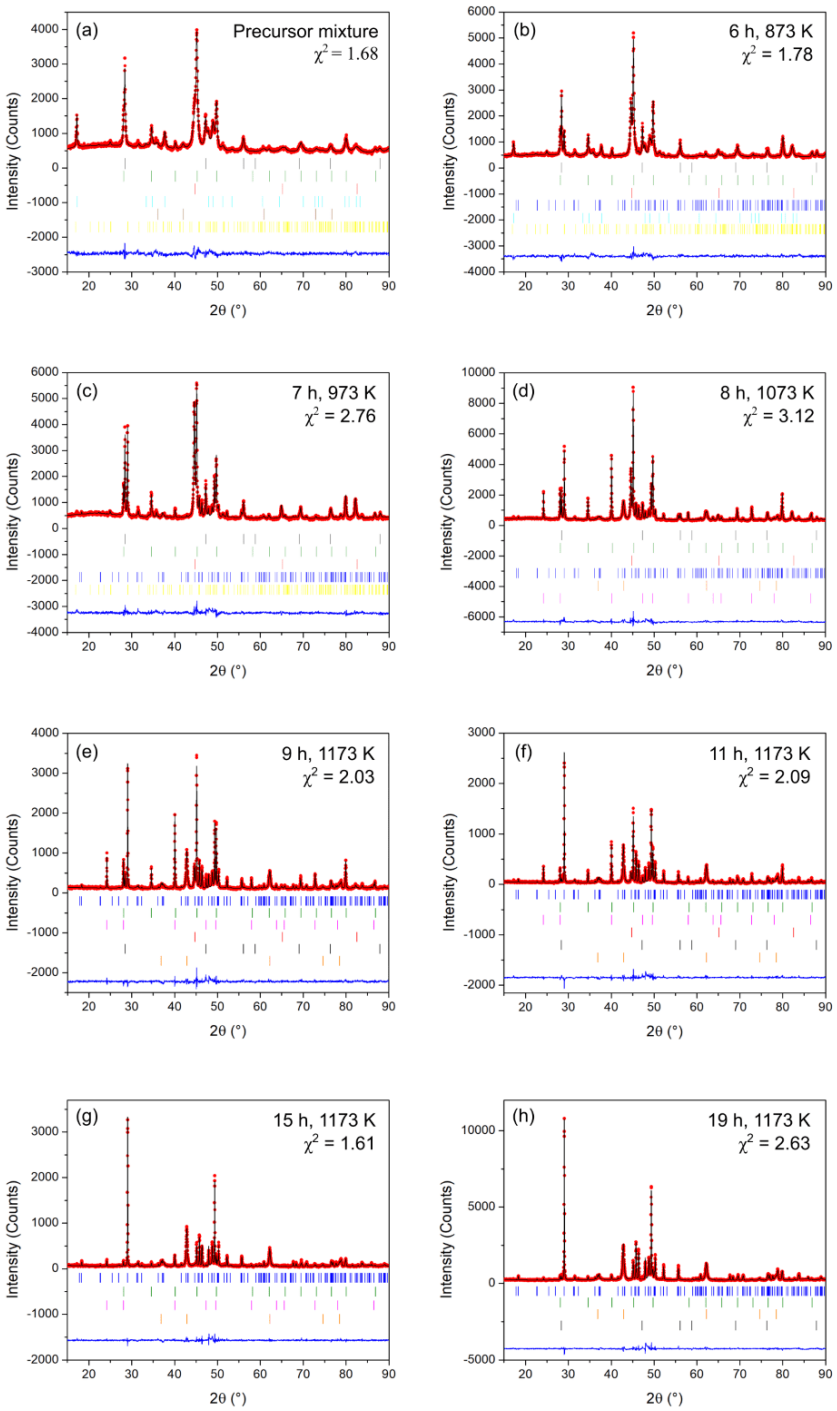

Figure SI 12: Rietveld refined XRD patterns of the magnesioreduced β-$FeSi_2$ samples at various stage of the reaction: (a) the precursor mixture and the reaction media after (b) 6 h, (c) 7 h, (d) 8 h, (e) 9 h, (f) 11 h, (g) 15 h and (h) 19 h. The experimental data are plotted in red symbols, the calculated one in black line and the difference in blue line. The vertical ticks indicate the theoretical Bragg peak positions for Si (black), Fe (red), FeSi (green), α-$Fe_{1-\delta}Si_2$ (bright blue), β-$FeSi_2$ (dark blue), FeO (purple), Mg_2Si (pink), Fe_2SiO_4 (yellow), MgO (orange)

Table SI 14: Structural parameters for β-$FeSi_2$ (s.g. *Cmce*) obtained from the Rietveld refinement of the XRD patterns in fig. SI 12. For Patterns (a) to (f), the scale factor, lattices parameters and peak profile coefficients are the only refined parameters. The thermal coordinates are taken from ref.[1] while the isotropic atomic displacement parameters are set to 0.2 $Å^2$ for Fe- and Si-atoms. For patterns (g) and (h), the atomic coordinates are refined and the peak shape of the reflection fulfilling the condition $k+l\neq 2n$ have been broadened using an individual refined coefficients.

Pattern	a(Å)	b(Å)	c(Å)	Vol. Fraction (%)
(b)	9.921(3)	7.812(3)	7.835(3)	11(1)
(c)	9.912(1)	7.818(2)	7.830(1)	26(1)
(d)	9.9032(6)	7.8144(6)	7.8280(6)	26(1)
(e)	9.9000(5)	7.8131(5)	7.8267(5)	32(1)
(f)	9.8994(5)	7.8119(5)	7.8265(5)	41(1)
(g)	9.9007(4)	7.8098(4)	7.8291(4)	52(1)
(h)	9.8979(4)	7.8130(4)	7.8255(4)	54(1)

	Si (16g)			Si (16g)			Fe (8d)	Fe (8f)	
Pattern	x	y	z	x	y	z	x	y	z
(b)	0.1273	0.0450	0.2739	0.1282	0.2746	0.0512	0.2146	0.3086	0.3149
(c)	0.1273	0.0450	0.2739	0.1282	0.2746	0.0512	0.2146	0.3086	0.3149
(d)	0.1273	0.0450	0.2739	0.1282	0.2746	0.0512	0.2146	0.3086	0.3149
(e)	0.1273	0.0450	0.2739	0.1282	0.2746	0.0512	0.2146	0.3086	0.3149
(f)	0.1273	0.0450	0.2739	0.1282	0.2746	0.0512	0.2146	0.3086	0.3149
(g)	0.124(2)	0.043(2)	0.276(2)	0.126(2)	0.275(2)	0.0489(2)	0.216(1)	0.306(2)	0.311(2)
(h)	0.124(3)	0.042(3)	0.274(3)	0.127(3)	0.273(3)	0.051(3)	0.216(1)	0.309(2)	0.313(2)

Table SI 15: Structural parameters for Fe (s.g. $Im\bar{3}m$) obtained from the Rietveld refinement of the XRD patterns in fig. SI 12. The scale factor, lattices parameters and peak profile coefficients are the only refined parameters. The atomic coordinates are taken from ref.[2] while the isotropic thermal displacement parameter is set to 0.3 Å^2.

Pattern	a (Å)	Vol. Fraction (%)	Fe ($2a$) x,y,z
(a)	2.8603(4)	17(1)	0
(b)	2.8681(3)	13(1)	0
(c)	2.8691(1)	19(1)	0
(d)	2.8694(2)	9(1)	0
(e)	2.867(1)	3(1)	0
(f)	2.867(1)	(2)	0

Table SI 16: Structural parameters for Si (s.g. $Fd\bar{3}m$) obtained from the Rietveld refinement of the XRD patterns in fig. SI 12. The scale factor, lattices parameters and peak profile coefficients are the only refined parameters. The atomic coordinates are taken from ref[3] while the isotropic thermal displacement parameters are set to 0.5 Å^2.

Pattern	a (Å)	Vol. Fraction (%)	Si ($8a$) x, y, z
(a)	5.435(4)	20(1)	1/8
(b)	5.4308(4)	16(1)	1/8
(c)	5.4304(3)	16(1)	1/8
(d)	5.431(1)	6(1)	1/8
(e)	5.431(1)	4(1)	1/8
(f)	5.430(1)	1(1)	1/8
(h)	5.431(1)	1(1)	1/8

Table SI 17: Structural parameters for FeSi (s.g. $P2_13$) obtained from the Rietveld refinement of the XRD patterns in fig. SI 12. The scale factor, lattices parameters and peak profile coefficients are the only refined parameters. The atomic coordinates are taken from ref.[4] while the isotropic thermal displacement parameters are set to 0.2 Å^2 for Fe- and Si-atoms.

Pattern	a (Å)	Vol. Fraction (%)	Fe ($4a$) x,y,z	Si ($4a$) x,y,z
(a)	4.4813(4)	33(1)	0.3860	0.0917
(b)	4.4804(4)	39(1)	0.3860	0.0917
(c)	4.4849(5)	32(1)	0.3860	0.0917
(d)	4.4867(1)	26(1)	0.3860	0.0917
(e)	4.4851(2)	18(1)	0.3860	0.0917
(f)	4.4844(2)	12(1)	0.3860	0.0917
(g)	4.4839(2)	4(1)	0.3860	0.0917
(h)	4.4848(2)	4(1)	0.3860	0.0917

Table SI 18: Structural parameters for MgO (s.g. $Fm\bar{3}m$) obtained from the Rietveld refinement of the XRD patterns in fig. SI 12. The scale factor, lattices parameters and peak profile coefficients are the only refined parameters. The atomic coordinates are taken from ref.[5] while the isotropic thermal displacement parameters are set to 0.3 Å^2 for Mg- and O-atoms.

Pattern	a (Å)	Vol. Fraction (%)	Mg ($4a$) x, y, z	O ($4b$) x, y, z
(c)	4.215(3)	1(1)	0	1/2
(d)	4.2134(4)	22(1)	0	1/2
(e)	4.2149(1)	31(1)	0	1/2
(f)	4.2152(3)	37(1)	0	1/2
(g)	4.2157(3)	40(1)	0	1/2
(h)	4.2160(6)	40(1)	0	1/2

Table SI 19: Structural parameters for Mg_2Si (s.g. $Fm\bar{3}m$) obtained from the Rietveld refinement of the XRD patterns in fig. SI 12. The scale factor, lattices parameters and coefficients for peak profile functions are the only refined parameters. The atomic coordinates are taken from ref.[6] while the isotropic thermal displacement parameters are set to 0.3 Å^2 for Mg- and Si-atoms.

Pattern	a (Å)	Vol. Fraction (%)	Mg ($8c$) x,y,z	Si ($4a$) x,y,z
(d)	6.357(1)	12(1)	1/4	0
(e)	6.357(1)	12(1)	1/4	0
(f)	6.357(1)	8(1)	1/4	0
(g)	6.360(1)	4(1)	1/4	0
(h)	6.356(1)	1(1)	1/4	0

Table SI 20: Structural parameters for FeO (s.g. $Fm\bar{3}m$) obtained from the Rietveld refinement of the XRD patterns in fig. SI 12. The scale factor, lattices parameters and peak profile coefficients are the only refined parameters. The atomic coordinates are taken from ref.[7] while the isotropic thermal displacement parameters are set to 0.3 Å^2 for Fe- and O-atoms.

Pattern	a (Å)	Vol. Fraction (%)	Fe ($4a$) x,y,z	O ($4b$) x,y,z
(a)	4.299(2)	3(1)	0	1/2

Table SI 22: Structural parameters for α-$FeSi_2$ (s.g. $P4/mmm$) obtained from the Rietveld refinement of the XRD patterns in fig. SI. 2. The scale factor, lattices parameters and peak profile coefficients are the only refined parameters. The atomic coordinates are taken from ref.[9] while the isotropic thermal displacement parameters are set to 0.3 Å^2 for Si- and Fe-atoms. Relative occupancy of the Fe ($1a$) position is set to 0.8.

Pattern	a (Å)	c (Å)	Vol. Fraction (%)	Fe ($1a$)[0.8] x,y,z	Si ($2h$) x,y	z
(a)	2.6855(4)	5.145(1)	19(1)	0	1/2	0.27
(b)	2.6882(6)	5.138(1)	10(1)	0	1/2	0.27

Table SI 21: Structural parameters for Fe_2SiO_4 (s.g. $Fd\bar{3}m$) obtained from the Rietveld refinement of the XRD patterns in fig. SI 12. The scale factor, lattices parameters and peak profile coefficients are the only refined parameters. The atomic coordinates are taken from[8] while the isotropic thermal displacement parameters are set to 0.3 Å^2 for Si-, Fe-atoms and 0.6 Å^2 for O-atoms

Pattern	a(Å)	b(Å)	c(Å)	Vol. Fraction (%)
(a)	10.456(8)	6.141(8)	4.806(8)	7(1)
(b)	10.440(6)	6.112(6)	4.826(6)	11(1)
(c)	10.464(7)	6.110(7)	4.825(7)	6(1)

	Fe (4a)			Fe (4c)			Si (4c)		
Pattern	x	y	z	x	y	z	x	y	z
(a)	0	0	0	0.2286	1/4	0.5174	0.4108	1/4	0.072
(b)	0	0	0	0.2286	1/4	0.5174	0.4108	1/4	0.072
(c)	0	0	0	0.2286	1/4	0.5174	0.4108	1/4	0.072

	O (4c)			O (4c)			O (8d)		
Pattern	x	y	z	x	y	z	x	y	z
(a)	0.3981	1/4	0.7168	0.0358	1/4	0.2955	0.3080	0.0462	0.1931
(b)	0.3981	1/4	0.7168	0.0358	1/4	0.2955	0.3080	0.0462	0.1931
(c)	0.3981	1/4	0.7168	0.0358	1/4	0.2955	0.3080	0.0462	0.1931

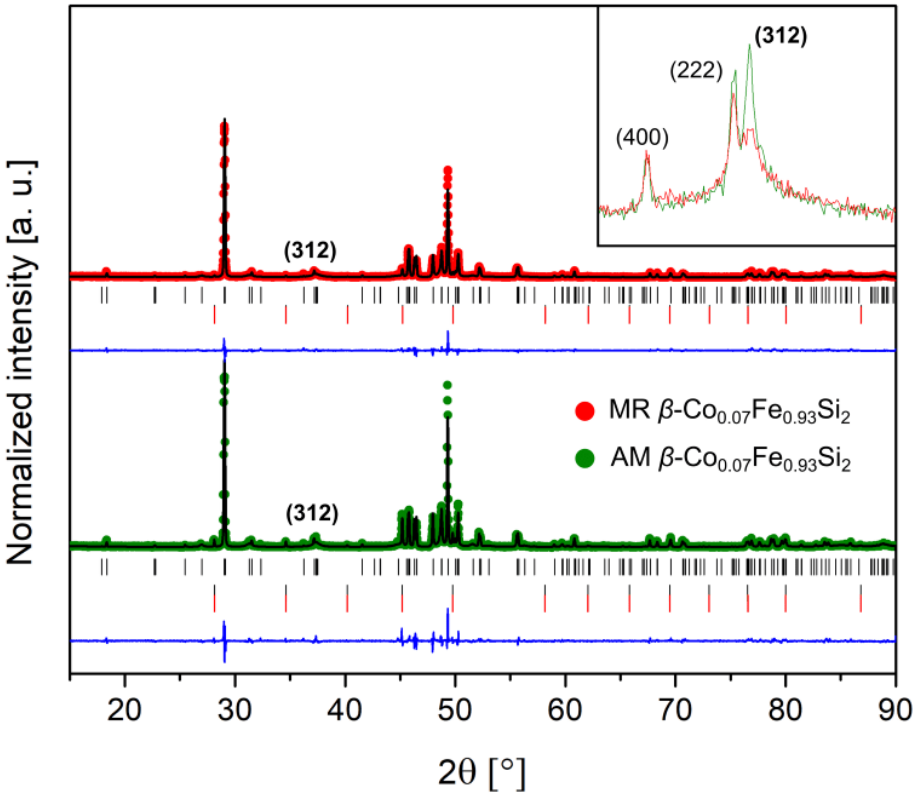

Figure SI 13: Rietveld refined powder XRD patters of the sintered MR β-$Co_{0.07}Fe_{0.93}Si_2$ (red) and AM β-$Co_{0.07}Fe_{0.93}Si_2$ (green). The experimental data are plotted in colored symbols, the calculated one with a black line and the difference with a blue line. The vertical ticks indicate the Bragg peak positions for β-$FeSi_2$ (black) and FeSi (red). The inset is a close up view of the (312) reflections showing the different peak broadening between both samples.

Table SI 23: Lattice parameters, atomic coordinates, isotropic displacement parameters and stacking fault probability (SF) extracted from the Rietveld refinements of sintered MR and AM β-$FeSi_2$ and MR and AM β-$Co_{0.07}Fe_{0.93}Si_2$ XRD patterns.

		MR-$FeSi_2$	AC-$FeSi_2$	MR-$Co_{0.07}Fe_{0.93}Si_2$	AC-$Co_{0.07}Fe_{0.93}Si_2$
	a (Å)	9.89104(6)	9.87518(4)	9.91176(8)	9.91200(4)
	b (Å)	7.81612(4)	7.79980(3)	7.81410(4)	7.81500(4)
	c (Å)	7.84209(3)	7.83727(2)	7.84084(5)	7.84060(3)
	x	0.126(1)	0.126(1)	0.122(1)	0.122(1)
Si ($16g$)	y	0.046(1)	0.045(1)	0.045(1)	0.044(1)
	z	0.272(1)	0.274(1)	0.274(1)	0.274(1)
	x	0.129(1)	0.128(1)	0.130(1)	0.130(1)
Si ($16g$)	y	0.273(1)	0.275(1)	0.274(1)	0.274(1)
	z	0.049(1)	0.050(1)	0.048(1)	0.048(1)
Fe1 ($8f$)	y	0.308(1)	0.309(1)	0.307(1)	0.308(1)
	z	0.313(1)	0.313(1)	0.311(1)	0.311(1)
Fe2 ($8g$)	x	0.216(1)	0.216(1)	0.217(1)	0.217(1)
	SF (%)	10.7(2)	3.7(1)	10.4(1)	3.2(1)
	B_{iso} Fe (Å^2)	0.3(1)	0.4(1)	0.6(1)	0.2(1)
	B_{iso} Si (Å^2)	0.1	0.1(1)	0.4(1)	0.1(1)

References

[1] P. Dusausoy, J. Protas, R.Wandji, B. Roques, *Acta Cryst. B* **1971**, *27*, 1209.

[2] L. Zwell, G. Speich, W. C. Leslie, *Metall. Trans.* **1973**, *4*, 1990–1992.

[3] J. Dismukes, L. Ekstrom, R. Paff, *J. Phys. Chem.* **1964**, *68*, 3021–3027.

[4] F. Weitzer, J. C. Schuster, *J. Solid State Chem.* **1987**, *70*, 178–184.

[5] B. A. . Wechsler, A. Navrotsky, *J. Solid State Chem.* **1984**, *55*, 165–180.

[6] J. G. Barlock, L. F. . Mondolfo, *Z. Metallkd.* **1975**, *66*, 605–611.

[7] T. Katsura, B. Iwasaki, S. Kimura, S. Akimoto, *J. Chem. Phys.* **1967**, *47*, 4559–4560.

[8] S. C. Parker, C. R. A. Catlow, A. N. Cormack, *Acta Crystallogr. B* **1984**, *40*, 200–208.

[9] C. Guéneau, C. Servant, *J. Appl. Crystallogr.* **1995**, *28*, 707–716.

Part VII

Discussion and perspectives

1 Reaction mechanisms and key parameters for magnesioreduction syntheses

A major effort has been undertaken during my thesis to understand and control the magnesioreduction syntheses. Many attempts were necessary to optimize the essential parameters to successful reactions. This could only be achieved thanks to the clamping system described in part II which greatly facilitates the realization of a large number of syntheses. The main challenge was to obtain products with high purity and controlled chemical composition. This has been achieved thanks to an important work realized especially on the precursors mixture preparation and optimization of the reaction conditions (temperature, dwell duration, Mg:MO_x ratio,...).

1.1 Magnesioreduction mechanisms

Magnesioreduction syntheses are composed of two steps: the reduction of the oxides and the interdiffusion of the native metals. Figure 66 represents the schematic reaction mechanism of the model reaction:

$$MO_x + M'O_y + (x+y)Mg \longrightarrow MM' + (x+y)MgO \tag{83}$$

In this example, the precursors mixture is composed of MO_x (red) and M'O_y (green) oxide powders intimately mixed together. The preform is obtained by pressing the mixture into pellets where the grains are maintained in contact to each other (fig. 66a). This helps to increase the reactivity between the precursors. In the first scenario (silicides), the heat treatment is realized above 973 K and the Mg vapor pressure strongly increases above 436 Pa in the crucible.[1] The Mg vapor penetrates inside the pellet through the open porosities and the surface of the grains directly in contact with Mg are reduced first (fig. 66b). The MgO by-product is deposited as a nanocrystalline layer at the surface of the grains. The reactivity of Mg toward the precursors is intensified during the process thanks to the large amount of heat released by the highly exothermic redox reaction. In the second scenario (skutterudites), the heat treatment is realized at temperature below 973 K and the Mg vapor pressure is much lower (*e.g.* 28.1 Pa at 810 K).[1] At any temperature, metal oxides are in thermodynamic equilibrium with O_2 according to the equations:

$$MO_x = M + (x/_2)O_2 \tag{84}$$

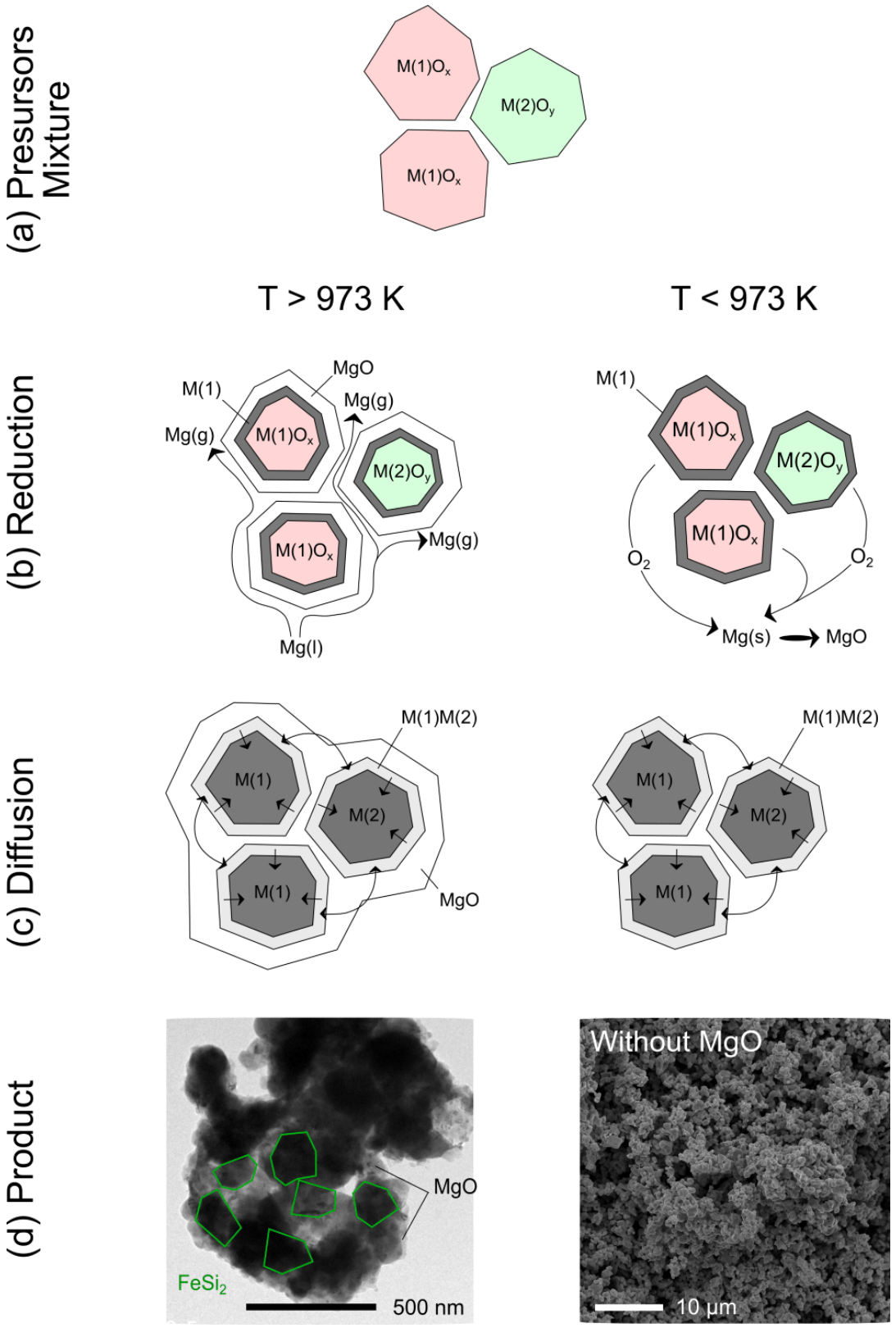

Figure 66: Schematic representation of the magnesioreduction mechanism for heat treatment above (left) and below 973 K (right).

$$\mathrm{M'O}_y = \mathrm{M'} + (\mathrm{y}/_2)\mathrm{O}_2 \tag{85}$$

For example, the O_2 partial pressure of Co_3O_4 and Sb_2O_4 at 810 K are about 1 10^{-14} and 2 10^{-13} Pa, respectively.[2] According to Le Chatelier principle, the consumption of the O_2 partial pressure in the crucible by Mg results in the oxides reduction. The slow oxidation of the Mg chunks from the surface to the core is clearly visible experimentally during the synthesis of $In_{0.25}Co_4Sb_{12}$. Logically, the reduction process is much slower for skutterudites (3 days) than for silicides (5 h) but the product do not contain any MgO by-product since it remains well-separated at the bottom of the crucible.

In both cases, the surface of the particles are reduced first. Thermodynamic equilibria resulting in the 'migration' of O^{2-} from the unreacted particles core to the reduced metallic surface must take place in order to achieve complete reduction of the oxides. The driving force of the reduction process is the formation of highly stable MgO. At one point, all the oxide precursors have been reduced in M and M' which react by solid-state diffusion to form MM' (fig. 66c). The diffusion process is usually slow and depends mostly on the diffusion rate of species in presence and the average diffusion path in the pellet. The MgO layer forming in the 1^{st} scenario can act as a diffusion barrier slowing down the reaction. The diffusion process may start even before the reduction is completely finished resulting in highly complex multiphases sample as evidenced experimentally by X-ray diffraction for $In_{0.25}Co_4Sb_{12}$ and $FeSi_2$. At the end of the reaction, the products synthesized above 1073 K consist in MM' particles embedded in a MgO matrix (TEM image in fig. 66d left) while at lower temperature they consist in well-separated grain (SEM image in fig. 66d right) without significant presence of MgO.

1.2 Precursors microstructure

For most syntheses realized during my thesis, the rate limiting step of the reactions is the solid state diffusion step of the native metals in the step (c) in fig. 66. The reaction kinetics is largely dependent on the precursors grain sizes. A strategy consists in preparing finely divided precursors mixtures (< 500 nm) which are more easily reduced while promoting faster formation of the product. This is attributed to the larger specific areas directly in contact with Mg and to the shorter average diffusion paths. On the contrary, precursors mixture made of large grains (typically > 1 μm) could not be reacted in a reasonable temperature and duration frame. This is especially true for elements with slow diffusion rate such as Si or Ge. However, highly reactive finely divided powders react more likely with Mg to form side-products. Faster reduction rate means more intense production of heat and thus higher Mg reactivity. In my case, Mg_2Si and Mg_3Sb_2 are the main side-products formed during the syntheses of silicides and skutterudites, respectively. Although these Mg-containing side-products are soluble in acids and can thus easily be washed

away, their formation is done at the expense of the complete reduction of the precursors. It results in products with compositions deviating from stoichiometry or contaminated with oxide phases as in Snedaker *et al.*'s work.[3] As pointed out by Bao *et al.*, the microstructure of the oxide precursors is mostly maintained upon reduction.[4] In the aim to produce thermoelectrics powder with grains as small as possible for the sintering of nanostructured materials, it might be interesting to start from precursors with small grain sizes.

The precursors morphology plays a significant role in the success of the reaction. It is primordial to find a compromise which enables fast reaction in appropriate conditions while avoiding subsequent uncontrollable side-reactions with Mg. For these reasons, many different preparation methods of precursors were tested. It includes manual milling in agate mortar, high-energy ball-milling, sol-gel and precipitation processes. The description of the typical product morphology obtained by these different methods are summarized in table 9.

Table 9: Summary of the typical microstructural characteristics of oxide precursors prepared by different methods.

	Manual milling	Ball-milling	Precipitation	Sol-gel
Grain-size	$>$ 500 nm	500 nm - 50 nm	$<$ 100 nm	$<$ 100 nm
Diffusion path	$\approx \mu$m	$\approx$ 100 nm	$\approx$ nm	$\approx$ nm
Scale-up perspective	no	yes	yes	no

To better illustrate the influence of the precursors morphology on the reaction output, fig. 67 shows secondary electron SEM and brightfield TEM images of HMS powders obtained for three different precursors preparation methods. The synthesis of silicides is a perfect example of reaction where the precursors preparation is of uttermost importance since Si has in the same time a low diffusion rate and a high reactivity toward Mg. In the case 1, coarse Si ($<$ 149 μ) and MnO ($<$ 74 μ) commercial powders were thoroughly ground by hand using an agate mortar. The precursors mixture is composed of Si and MnO with very heterogeneous grain sizes between 2 μm and 50 μm. Some of the grains are so large that Si can not properly react with Mn and the product is predominantly composed of MnSi and unreacted Si. The diffusion paths are so important that pure phase product could not be obtained even upon prolongated annealing at high temperature (7 days at 1223 K). This preparation method was rapidly given up for silicides.

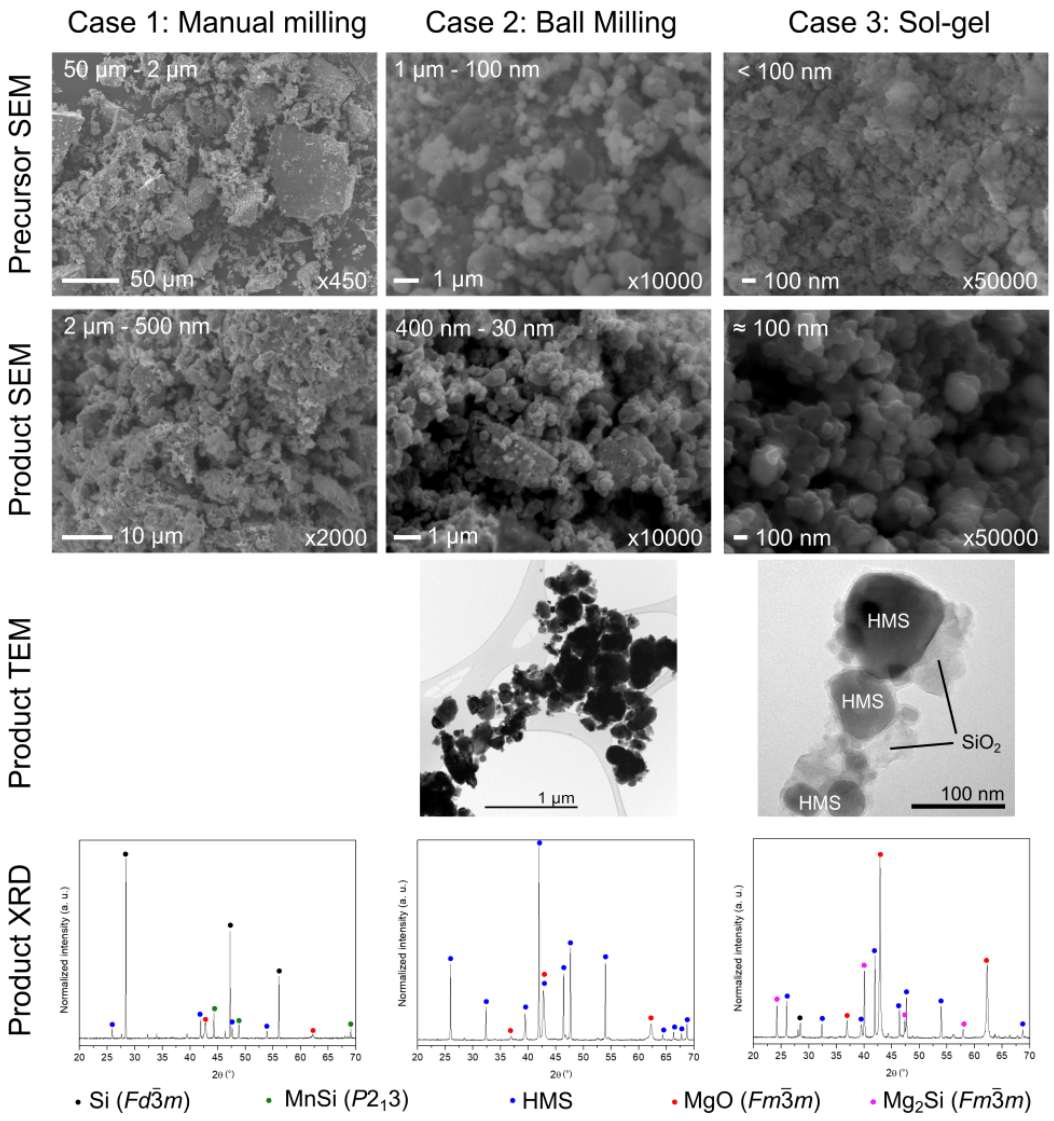

Figure 67: SEM secondary electron images, TEM brightfield images and XRD patterns of the HMS product synthesized from precursors prepared by manual milling (left), ball-milling (middle) and sol-gel method (right).

In the case 2, the precursors were prepared by reactive ball-milling and show intermediate grain sizes between 100 nm and 1 μm. This method gives the most satisfying results and was used for the synthesis of thermoelectric materials. As explained in the article, small amount of Mg_2Si is formed during the reaction but reacts rapidly with SiO_2 thanks to the short average diffusion paths. The product is free of SiO_2 as confirmed by careful TEM analyses and the reaction yield is higher than 95 %.

In the case 3, the precursor consists in a mixture of nano powder prepared by sol-gel synthesis. This preparation method is inspired from the works of Snedaker *et al.*[3] and of Sen *et al.*[5,6] for the synthesis of $Si_{0.8}Ge_{0.2}$ alloys and $FeSi_2$, respectively. The calcination of the gel results in a mixed amorphous oxide with average grain size below 30 nm and containing both Si- and Mn-atoms. Such precursor is very reactive

toward Mg and the preform often breaks in the crucible due to the violent reaction. As visible on the XRD pattern, the product contains a large quantity of Mg_2Si. The large background deviation at 22° and TEM observations reveal SiO_2 nanometric particles which could not be reduced by Mg due to the formation of Mg_2Si. In this case, the amount of side-products is so important that the reduction of SiO_2 by Mg_2Si could not be completed even after 4 days of annealing at 1173 K. This is in very good agreement with the result reported by Snedaker *et al.*[3] where Mg_2Si and SiO_2 are removed by HCl and HF leaching, respectively. While not mentioned in the article, the reaction yield is probably very low. Sen *et al.*[5,6] do not mention the formation of any side-products in their papers but similar results could not be reproduced despite many attempts. Interestingly, the HMS powder obtained in the case 3 has smaller average grain size than in the case 2. This seems to confirm the observations of Bao *et al.* that the grain size of the precursor determines the grain size of the product.[?] While such small average grain size is highly interesting for the preparation of nanostructured materials, the high reactivity of the precursor does not enable the production of pure silicides and was thus abandoned.

In the case of skutterudites, the commercial Co_3O_4 and Sb_2O_5 powders used for the reaction were much smaller, < 1 μm and < 500 nm, respectively. In addition, they are both more easily reduced than SiO_2 and they could thus be reacted at much lower temperature. In these conditions the reactivity of Mg is lower which strongly limits the formation of Mg_3Sb_2 side-product. A simple manual milling of the commercial powder in an agate mortar is sufficient in this case.

1.3 Precursors composition

If the synthesis of 'simple' binary compound can be quite complex, it becomes even more difficult when more than two elements are introduced in the reaction media. This was the case when $CoSb_3$, β-$FeSi_2$ and $MnSi_{1.74}$ were doped with a third element. In the case of skutterudites, the introduction of a third oxide (NiO, In_2O_3 or Fe_2O_3) directly in the precursors mixture did not lead to the full insertion of the dopant in the structure. XRD patterns (fig. 68) indicate the formation of side-products indexed as NiSb or $FeSb_2$. This is attributed to uneven distribution of the dopant atoms in the precursors mixture. Long annealings were not sufficient to form pure phase products.

The strategy imagined to overcome this difficulty consists in starting from properly doped precursors. On the contrary to powder mixtures, the dopant atoms in mixed-oxides are directly homogeneously distributed at the atomic scale and the average diffusion path is considerably reduced. This strategy was found to be essential for the synthesis of doped materials where good control of the composition is mandatory.

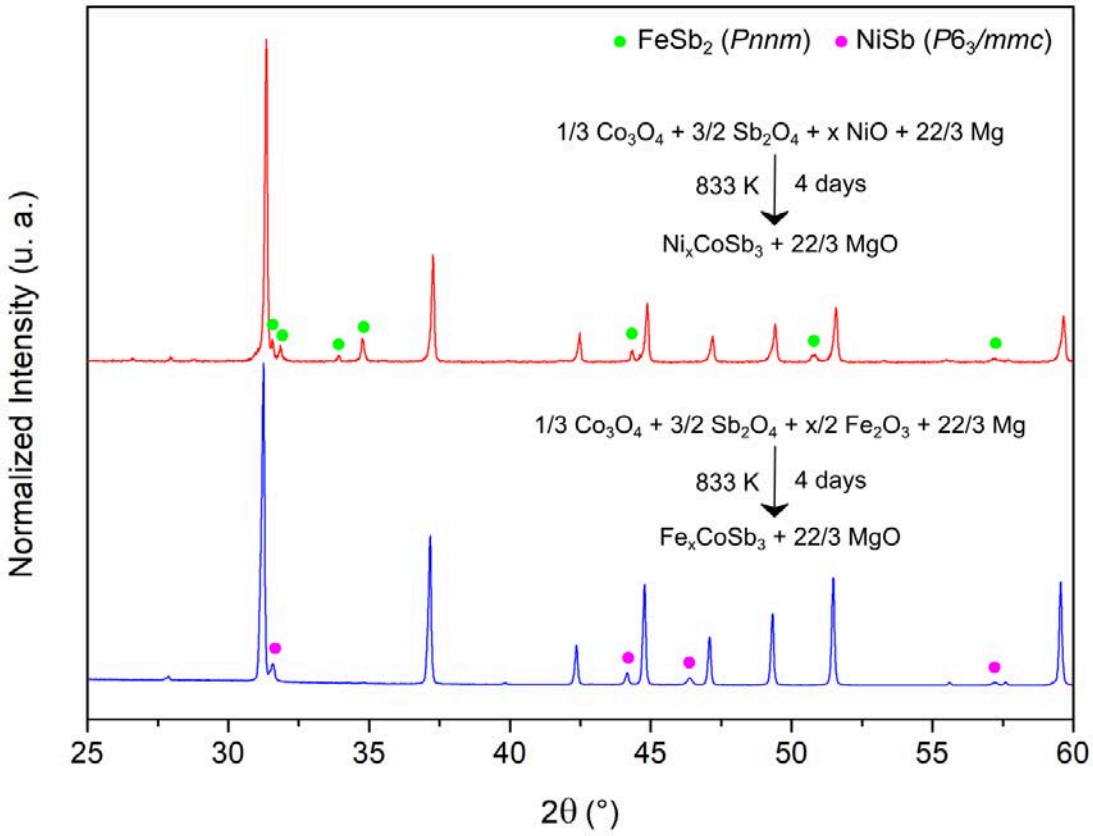

Figure 68: XRD patterns of Fe_xCoSb_3 (top) and Ni_xCoSb_3 (bottom) powders obtained by magnesioreduction synthesis realized by simply addition of Fe_2O_3 and NiO, respectively, to the precursors mixture.

However, it involves an additional preparation step. The precursors were prepared by dissolving the respective metal nitrates in distilled water. The water was then evaporated and the slurry calcined under air to form the oxides.

1.4 Pellet compaction

The degree of compaction of the precursors mixture in the pellet may influence the reaction output. Proper compaction (70 and 250 MPa) is expected to hold the grains in contact and promotes good solid-state diffusion while leaving enough open porosity to enable the penetration of Mg inside the pellets. If the pellet was shaped at higher pressure, only the surface of the pellet is reduced while the core remains predominantly composed of oxide precursors. On the opposite, reducing loose powder always resulted in uncompleted reaction with many impurities resulting from the poor diffusion of the elements. Additionally, recovery of the product after the reaction is much easier in the shape of a pellet.

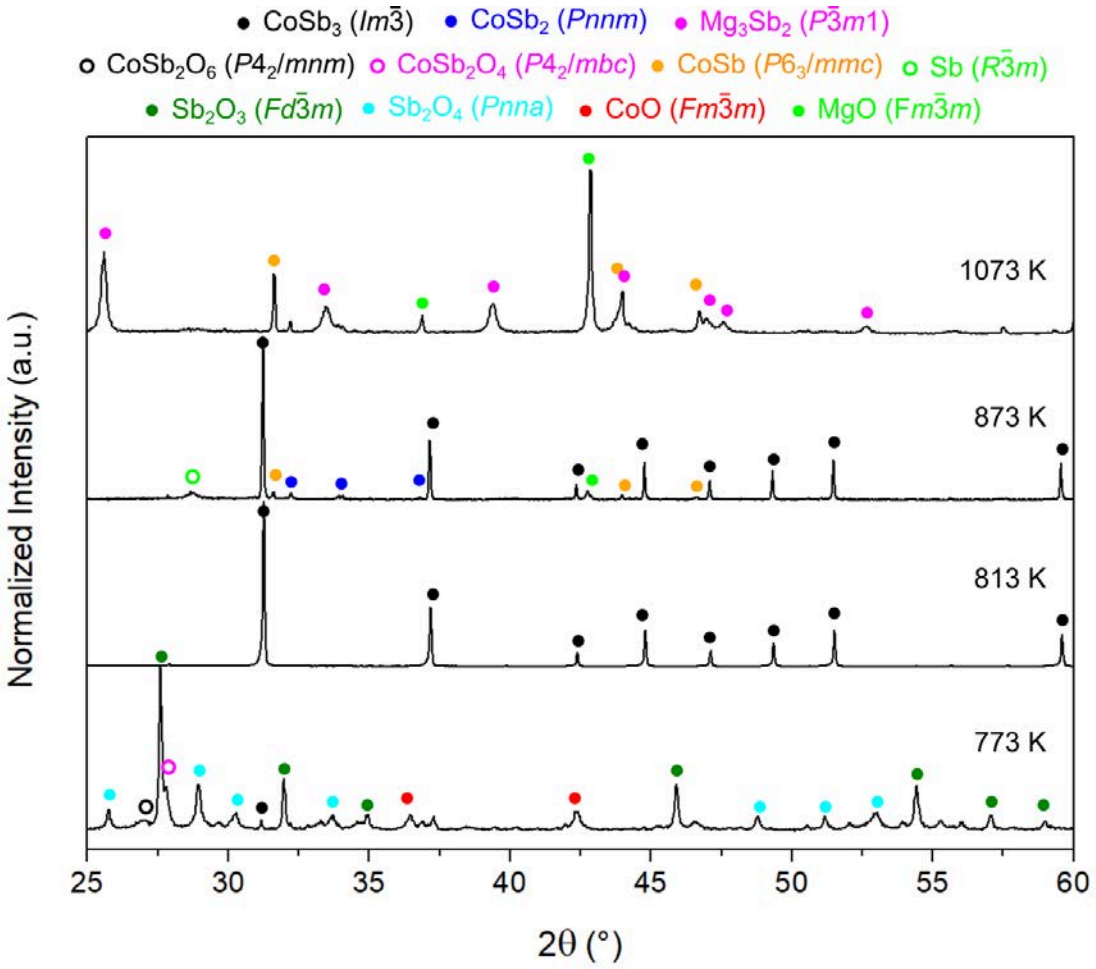

Figure 69: XRD patterns of $CoSb_3$ powders obtained by magnesioreduction synthesis realized at various temperatures for 4 days.

1.5 Reaction temperature

The temperature of reaction is the last important parameter that has been optimized to obtain pure products. The temperature at which the metal oxides in presence can be reduced is mostly dictated by the optimized conditions. On the one hand, according to the Le Chatelier principle, endothermic reactions are favored by temperature rising. A direct correlation can be drawn between the reduction temperature and the oxide enthalpy of formation. For example, during my thesis work, CoO could be slowly reduced in metallic Co at 813 K ($\Delta H°(298K) = 238.0$ kJ mol^{-1}) while BaO could only be reduced around 1173 K ($\Delta H°(298K) = 548.2$ kJ mol^{-1}).[7] On the other hand, the reaction temperature must be minimized in order to avoid grain growth as well as the melting or the vaporization of one of the species. Large chemical behavior difference can cause problems for the synthesis of some compounds.

For example, fig. 69 shows the XRD patterns of the products obtained for the syntheses of $CoSb_3$ at different temperatures. The reduction of Co_3O_4 and Sb_2O_4 is very slow at 773 K and only minor amount of $CoSb_3$ is formed after 4 days. By increasing the temperature to 813 K, both oxides have been reduced and pure phase

skutterudite is obtained after 4 days. This temperature was chosen for the synthesis. Only 60 K above this temperature, the vapor pressure of Sb increases and the loss of this element induced the presence of $CoSb_2$ and CoSb in the final product. Reaching 1073 K, the precursors start to be reduced by Mg vapor and MgO and Mg_3Sb_2 are mostly formed inside the pellets. Thus the magnesioreduction synthesis of $CoSb_3$ can only be performed in a small temperature range around 813 K. This temperature is too low to reduce BaO. For these reasons, high performance *p*-type $Ba_{0.20}Co_4Sb_{12}$ cannot be synthesized by magnesioreduction, at least within a single temperature dwell.

Heating rates between 60 and 100 K h^{-1} gave the best results and were therefore used for all the reactions. Mg excess in the order of 5 to 20 % are usually required to compensate the small losses during the reaction and the reduction of O_2 of the air inside the crucible.

2 Magnesioreduction reactions compared to other synthesis routes

The results obtained during this thesis work show that it is possible to produce pure intermetallics with controlled composition from metal oxides by magnesioreduction syntheses. The produced powders are characterized by well-crystallized grain sizes of about 300 nm - 1 μm for skutterudites and 30 - 400 nm for silicides. Reaction conditions from the literature to obtain powders with similar grain size by conventional syntheses are summarized in table 10.

Table 10: Reaction conditions reported for the syntheses of $CoSb_3$ and $MnSi_{1.74}$ by conventional melting/annealing/ball-milling process from the metals and realized under Ar atmosphere

	Melting	Annealing	Product	Milling	Product	Ref.
$CoSb_3$	1373 K, 24 h	1073 K, 4 days, intermediate grinding	> 10 μm polycrystalline ingot, 1% CoSb + Sb_2O_4	500 rpm, 4 h	≈ 200 nm	[8]
$MnSi_{1.74}$	1573 K, 10 h	1173 K, 24 h	ingot	18 h	≈ 40 nm + WC impurity	[9]

The traditional syntheses of $CoSb_3$ and $MnSi_{1.74}$ powders are highly time and energy consuming. In the case of $CoSb_3$, after the melting of the metals at 1373 K, 4 days of annealing at 1073 K are required to form the skutterudite phase from Sb and $CoSb_2$ by solid state diffusion. Then the ingots must be ground by high energy ball-milling for few hours to obtain nanocrystalline powders. In addition, samples prepared by

conventional synthesis are often polluted with oxides or CoSb and $CoSb_2$ due to the high vapor pressure of Sb at high temperatures. An arbitrary excess of this element is usually added to counterbalance this loss. The process is greatly simplified by magnesioreduction where a single step of 4 hours at only 813 K is needed to obtain pure phase powders. In addition, the product separation of the slag MgO does not require an additional leaching step in the case of $CoSb_3$. Controlled doping with Ni and insertion of In rattlers has been achieved starting from properly doped precursors. However, as already discussed above, many compositions such as all rare-earths and Ba-filled skutterudites could not be synthesized by the present magnesioreduction process. Complex skutterudites composed of multiple dopants and rattlers might also be difficult to synthesize considering the high probability to form side-products.

Although $MnSi_{1.74}$ is already formed to a great extent after the solidification from the melt, long annealings above 1100 K are required to dissipate the formation of metallic MnSi precipitates inside the grain which are detrimental to the thermoelectric properties.[10] As for $CoSb_3$, the ingot then needs to be ball-milled under Ar atmosphere to obtain nanopowders. In this case, the synthesis is improved as nanometric powders are obtained by magnesioreduction in less than 24 h including 3 steps: 4 h of precursors ball-milling, 19 h of heat treatment up to 1173 K and the acid leaching step to remove MgO by-product. Most importantly, the as-synthesized product do not contain any MnSi precipitates. The doping of HMS by magnesioreduction is however more difficult since only MnO can be doped which strongly limits the choice of doping elements. During my study, V_2O_5 was directly added to the mixture prior to ball milling but some amount of VSi_2 side-product forms during the relatively vigorous magnesioreduction reaction.

β-$FeSi_2$ is not commonly synthesized by similar conventional methods as $CoSb_3$ and $MnSi_{1.74}$ since the sintering has to be realized above its decomposition temperature. For this reason, a mixture of FeSi and α-$Fe_{1-\delta}Si_2$ obtained by melting or reactive ball-milling is directly sintered as it is and the β-phase is recovered by annealing the densified pellet at 1073 K for about 1 day.[11] Unfortunately, the sintering of the β-$FeSi_2$ nanopowder obtained by magnesioreduction could not be realized below the decomposition temperature despite the very small grain size of the particles. Both conventional and magnesioreduction synthesis must thus be processed *via* a relatively long annealing step. The advantage to directly obtain pure nanograined β-$FeSi_2$ is thus strongly reduced. The controlled doping with Co could however be easily realized from properly doped $Co_{0.14}Fe_{1.86}O_3$.

In standard conditions, Mg can only reduce oxides which are higher in the Ellingham's diagram. For these reasons, oxides of elements such as rare earths, except

CeO_2, are difficult to reduce. Increasing the amount of Mg might make the magnesioreduction possible but would also be highly reactive toward the precursors and thus form side-products. This strongly limits the applicability of magnesioreduction syntheses to materials composed of these elements which are having very interesting properties (thermoelectric, magneto-caloric, permanent magnet, superconductor...) and potential industrial applications. Finally, the acid leaching might not be used for some intermetallics reactive toward acids such as for example the thermoelectric clathrates $Ba_8Ga_{16}Sn_{30}$ or many Mg-based compounds or alloys.

3 Thermoelectric properties

The present magnesioreduction synthesis route combined with spark plasma sintering enabled the fabrication of densified materials with averages grain sizes of about 550 nm for HMS, 600 nm for skutterudites and lightly below 1 μm for β-$FeSi_2$. As shown is fig. 70, the lattice thermal conductivities of all the samples (symbols) have been reduced compared to the reference materials synthesized by conventional melting/annealing processes (line). This is attributed to the high density of grain interphases and related defects acting as phonon scattering centers. Indeed, most of the phonons disturbed by the microstructure are having similar or bigger characteristic phonons mean free paths than the average grain size. As a consequence, by reducing the average grain size we expect to scatter more efficiently a larger proportion of the phonons contributing to the heat transfer. However, we have seen that κ_L reduction is more efficient at room temperature than at 800 K for most materials (table 11). Increasing the temperature and therefore the lattice thermal vibration results in a global diminution of the phonons mean free paths.[12] As a consequence, the microstructure of the sample is expected to scatter less efficiently a larger proportion of the phonons at high temperature. It can explain why the thermal conductivity of most materials get closer to the bulk reference sample at 700 - 800 K. This corresponds also to the temperature where most of the investigated materials present their maximum figures-of-merit ZT_{max}.

The highest κ_L reductions are achieved for pristine $CoSb_3$ and β-$FeSi_2$ where the grain boundaries and intrinsic lattice defects are the major scattering centers. These are also the compositions having the largest thermal conductivities and the lowest ZT_{max}. Upon doping or insertion of rattlers, the microstructure reduces less efficiently κ_L. Indeed, insertion of dopants can be viewed as the creation of point defects that strongly scatter phonons. As for temperature changes, the averaged phonon mean free paths is expected to be reduced as the impurities concentration increases. As a consequence, the high-temperature thermal conductivities of the best materials such as In-filled or Ni-doped skutterudites could not be significantly improved by

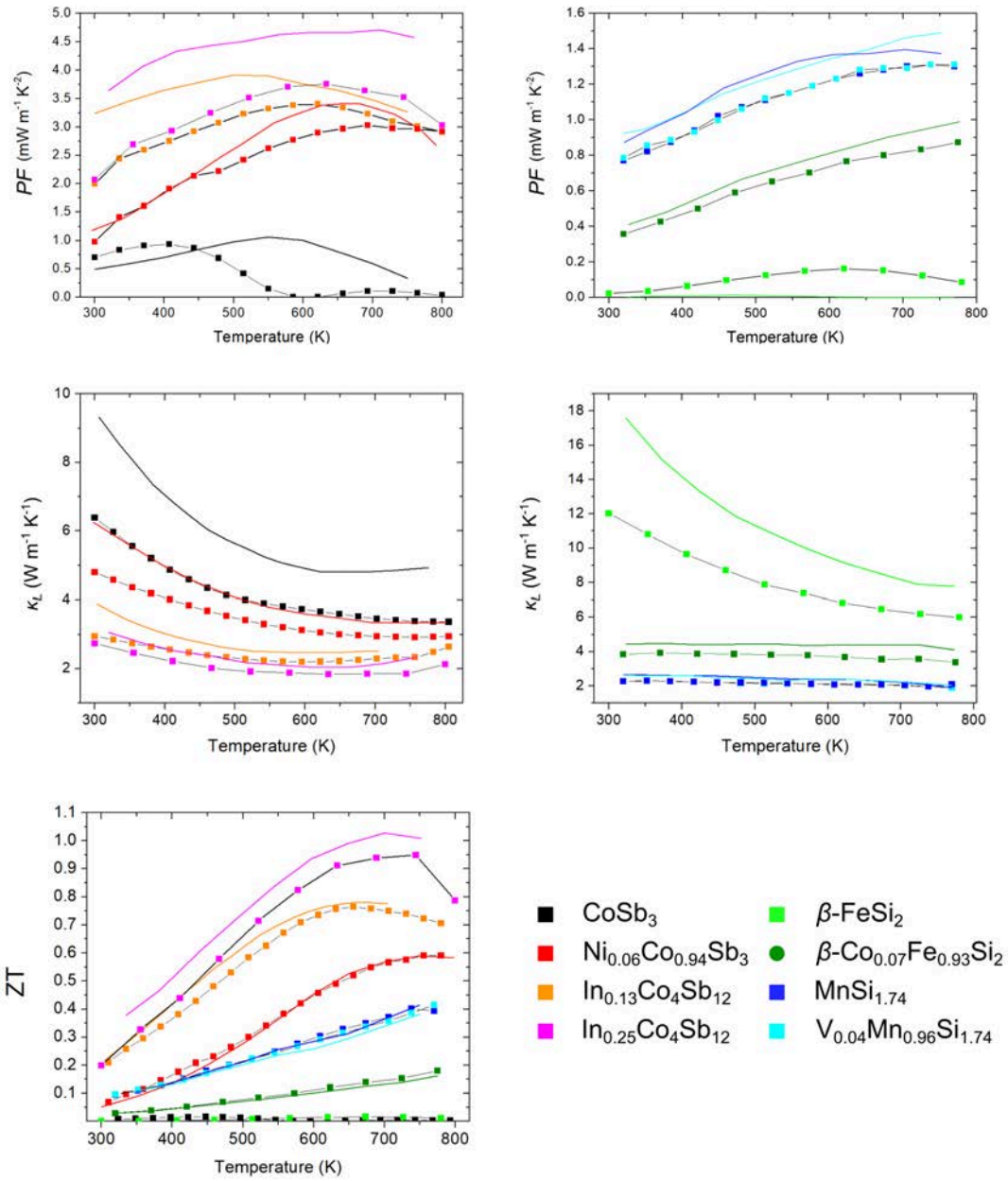

Figure 70: Thermal dependence of power factor (PF), lattice thermal conductivity (κ_L) and figure-of-merit ZT of several materials synthesized by magnesioreduction during my thesis are presented with symbols. Properties of similar materials synthesized by conventional fusion/solidification methods are drawn with lines for comparison.

the magnesioreduction process. On the contrary, the lattice thermal conductivity of β-$Co_{0.07}Fe_{0.93}Si_2$ has been reduced by about 15 % in the whole temperature range.

The electrical resistivity of the SPSed pellets is however systematically higher for all magnesiosynthesized materials. It results in lower PF for most materials (fig. 70 and table 11). This is attributed to non negligible scattering of the charge carriers at the grain boundaries or associated defects. The characteristic microstructure obtained by this synthesis route does not significantly uncouple the thermoelectric

Table 11: Comparison of the thermoelectric properties of the magnesioreduction and melting/annealing synthesized samples. Relative changes below 5 % are considered as non significative and are marked as =. Values marked with * were taken at 700 K.

	$\Delta\kappa_L$ (300 K)	$\Delta\kappa_L$ (800 K)	ΔPF_{max}	ΔZT_{max}	ZT_{max}
β-$FeSi_2$	-34 %	-23 %	+300 %	+3000 %	1.6 10^{-2}
β-$Co_{0.07}Fe_{0.93}Si_2$	-13 %	-18 %	-12 %	+12 %	0.18
$MnSi_{1.74}$	-15 %	=	-6 %	=	0.40
$V_{0.04}Mn_{0.96}Si_{1.74}$	-14 %	-7 %	-13 %	=	0.41
$CoSb_3$	-31 %	-32 %	-9 %	-84 %	1.6 10^{-2}
$Ni_{0.06}Co_{0.94}Sb_3$	-23 %	-12 %	-12 %	=	0.59
$In_{0.13}Co_4Sb_{12}$	-25 %	-9 % *	-13 %	=	0.76
$In_{0.25}Co_4Sb_{12}$	-13 %	-16 % *	-21 %	-6 %	0.95

properties. Indeed, the average grain sizes of 500 nm to 1 μm are larger than a large part of the phonons mean free path distribution for the materials considered here.[10,12] Further grain size reduction is thus expected to further reduce κ_L and significantly increase ZT. For example, in the case of filled skutterudites, significant uncoupling of the properties and improvement of the ZT by nanostructuration are usually achieved for grains with average size of 300 - 400 nm.[13] This is almost half of the size obtained by the present magnesioreduction process. As a result, the ZT values obtained for MR samples reach similar values as reference samples (fig. 70). Only the Co-doped $FeSi_2$ could be significantly improved on the whole temperature range thanks to the almost constant κ_L reduction.

Several methods were attempted to further reduce the average grain sizes of the products but all failed to produce single phase samples. Reducing the oxide precursors grain sizes results in the formation of Mg-containing side-products as already discussed in section 1.1. Some studies show that the use of a flux during the synthesis can efficiently prevent grain growth during the magnesioreduction synthesis.[5] In my case, it mainly blocked the diffusion of the species and resulted in multi-phases products. The grain sizes in the densified materials are systematically bigger than in the as-synthesized powders due to grain growth during the high temperature sintering step. Despite the optimization of the sintering conditions, any attempts to sinter $FeSi_2$ below the decomposition temperature (1255 K) always resulted in low density samples which would have presented exceedingly reduced electrical conductivity. Skutterudites were also sintered at lower temperature (below 723 K) and very high pressures (150-250 MPa) using WC dies and punches but the materials always broke inside the die during the procedure.

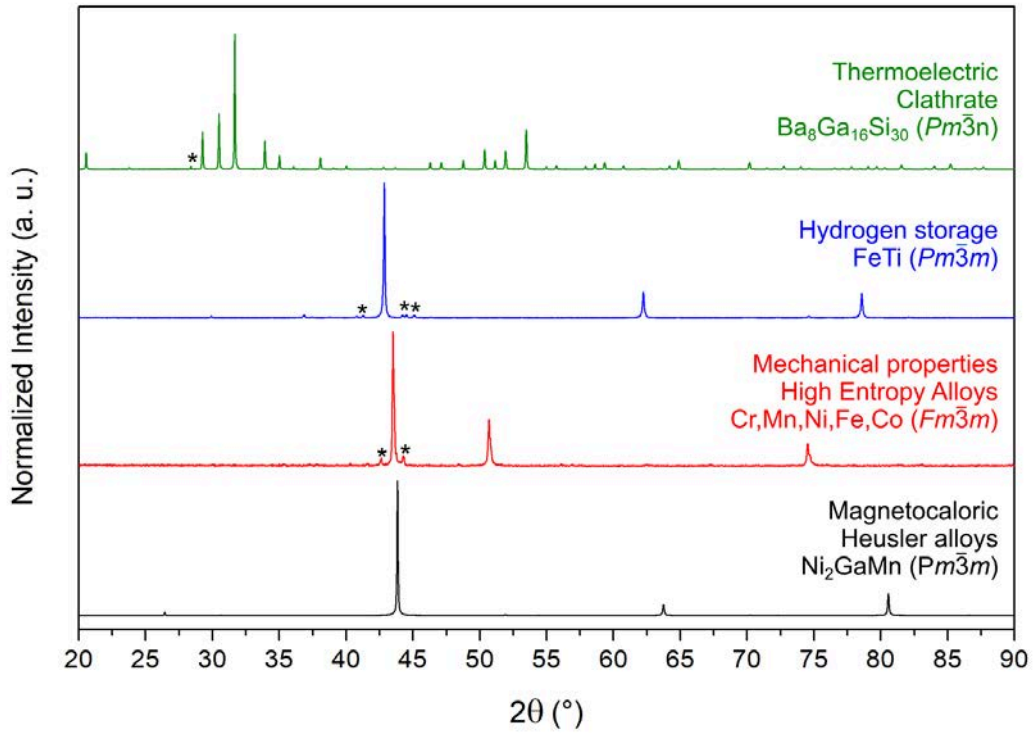

Figure 71: XRD patterns of various intermetallic materials synthesized by magnesioreduction. Impurities are shown with *.

4 Perspectives

The results obtained during my thesis work opened many interesting perspectives which will be presented in this section along with some preliminary results. The first of which is the up-scaling of the syntheses to show the feasibility of MRR to 'pre-industrial' scale. With the current crucible and clamping system, the quantity of product per batch is limited to about 1 g. Increasing the size of the crucible could have been possible only if larger diameter Inconel tubes could have been found on the market. Unfortunately, it was not possible to buy limited amount of Inconel tube at a reasonable price.

During my thesis it has been shown that magnesioreduction syntheses can be used to produce pure-phase samples with high yield. The synthesis of thermoelectric $Ba_8Ga_{16}X_{30}$ (X = Si, Ge, Sn) clathrates powders can be quite difficult due to the highly reducing Ba, low melting point of Ga and the slow diffusion rate of Si and Ge. Conventional syntheses reported in the literature often result in the formation of large single crystal (>100 μm) which needs to be crushed. The magnesioreduction synthesis of $Ba_8Ga_{16}Si_{30}$ has been attempted and relatively pure powder (fig. 71 and 72) of $Ba_8Ga_{16}Si_{30}$ has been obtained at 1073 K in about 48 h. After leaching of the MgO by-product, well-crystallized and homogeneous powder with grain sizes of about 100 - 300 nm is obtained. Doping and sintering conditions still have to be

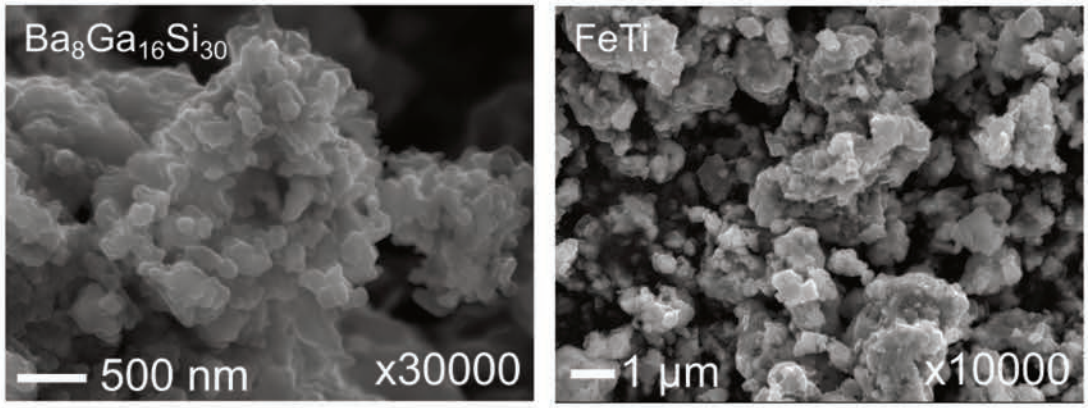

Figure 72: Secondary electrons SEM images of $Ba_8Ga_{16}Si_{30}$ and FeTi synthesized by magnesioreduction.

optimized.

Apart from thermoelectrics, many other materials can be beneficially synthesized by magnesioreduction reactions. For example, preliminary work on High Entropy Alloys (HEA) with composition CrMnNiFeCo has been realized. HEA have been increasingly studied in the past decades because of their excellent strength-to-weight ratios as well as corrosion and oxidation resistance at high temperatures compared to conventional refractory alloys.[14,15] The synthesis of HEA ingot by melting/annealing method is relatively easy. However, sintered materials are more desirable for many applications where higher mechanical properties or specific shape are required.[16] The milling of HEA ingots is very difficult since the materials tends to flatten into flakes which cannot be conveniently sintered afterwards. For this reason, the magnesioreduction synthesis of HEA from oxides might be a very interesting route to produce well-dispersed and crystallized powders more suitable for sintering. Typical XRD pattern is presented in fig. 71. The sample is relatively pure expect for some contamination by chromium carbide forming during the synthesis. The as-synthesized powder has grain sizes of about 100 - 300 nm. Further optimization of the reaction and sintering conditions are currently underway.

Powder morphology also has a key role in increasing the performances of hydrogen storage materials.[17] The diffusion of hydrogen *i.e.* the formation of hydride from H_2 is relatively slow in bulk intermetallics. An option to increase the absorption kinetics is to use finely divided powders with high specific surface. FeTi can reversibly form the $FeTiH_{1.9}$ hydride in relatively mild temperature/pressure conditions thanks to its moderate enthalpy of formation of 28.3 kJ mol^{-1}.[18] FeTi powders with average grain size around 500 nm have been recently synthesized by magnesioreduction of highly abundant TiO_2 and Fe_2O_3 (fig. 71 and 72). The properties of hydrogenation and dehydrogenation will be measured soon.

Finally, magnesioreduction have been applied to the field of magnetocaloric materials. The magnetocaloric effect (MCE) corresponds to the adiabatic temperature change observed in some materials when placed/removed from a magnetic field induced by the gain/loss of magnetic entropy ΔS_{mag}.[19] Giant MCE in the order of magnitude of $\Delta T = 15$ K can be observed in materials such as $La(Si,Fe)_{13}$,[20] $Gd_5Si_2Ge_2$[21] or Heusler alloys[22] where the magnetic transition is coupled to a structural transition. The Heusler alloy $Ni_{(2+x)}Mn_{(1-x)}Ga$ is very interesting since it shows a strong MCE close to room temperature which would make it suitable for refrigeration applications such as fridge or air-conditioning.[23] Moreover it is not composed of rare-earth elements which are subject to supply chain issues. The 1^{st} order transition temperature is closely related to the Ni and Mn stoichiometry. Good control of the composition is however difficult by conventional syntheses because of the low melting point of Ga and the high vapor pressure of Mn at elevated temperature. $Ni_{2.24}Mn_{0.76}Ga$ has been synthesized by magnesioreduction from the respective oxides (fig. 71). This composition was selected since the coupled magnetic/structural transition occurs just below room temperature which is the temperature range targeted for industrial refrigeration applications. Indeed the ΔS_{mag} plot determined from the isothermal magnetization measurement on our sample shows a broad peak near 273 K (fig. 73). Sintering, structural analyses by X-ray diffraction on temperature as well as specific heat measurements are being currently under investigation.

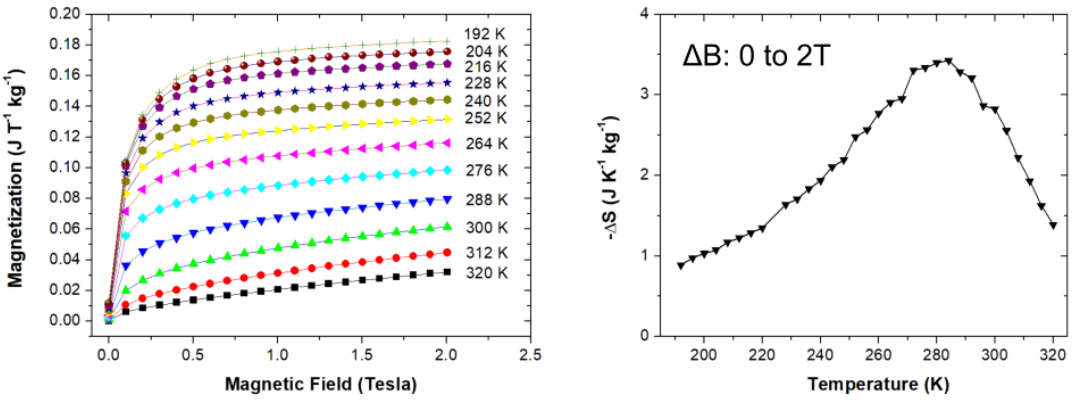

Figure 73: (left) Isothermal magnetization measurement of $Ni_{2.24}Mn_{0.76}Ga$ powder synthesized by magnesioreduction. (right) Thermal dependence of $-\Delta_{mag}$.

All these examples highlight the wide range of materials and properties that can be improved by the magnesioreduction process and open thus the doors of a wide and extensive research field.

References

[1] *CRC Handbook of Chemistry and Physics*.

[2] H. J. T. Ellingham, *J. Soc. Chem. Ind.* **1944**, *65*, 125.

[3] M. L. Snedaker, Y. Zhang, C. S. Birkel, H. Wang, T. Day, Y. Shi, X. Ji, S. Kraemer, C. E. Mills, A. Moosazadeh, M. Moskovits, G. J. Snyder, G. D. Stucky, *Chem. Mater.* **2013**, *25*, 4867–4873.

[4] Z. Bao, M. R. Weatherspoon, S. Shian, Y. Cai, P. D. Graham, S. M. Allan, G. Ahmad, M. B. Dickerson, B. C. Church, Z. Kang, H. W. Abernathy, C. J. Summers, M. Liu, K. H. Sandhage, *Nature* **2007**, *446*, 172–175.

[5] S. Sen, N. Gogurla, P. Banerji, P. K. Guha, P. Pramanik, *Mater. Sci. Eng. B* **2015**, *200*, 28–39.

[6] S. Sen, P. K. Guha, P. Banerji, P. Pramanik, *RSC Adv.* **2016**, *6*, 68238.

[7] O. Knacke, O. Kubaschewski, K. Hesselmann, *Thermo-chemical Properties of Inorganic Substances*.

[8] E. Alleno, L. Chen, Chubilleau, B. Lenoir, O. Rouleau, M. Trichet, B. Villeroy, *J. Electron. Mater.* **2010**, *39*, 1966.

[9] X. Chen, L. Shi, J. Zhou, J. B. Goodenough, *J. Alloys Compd.* **2015**, *641*, 30.

[10] K. Koumoto, T. Mori, *Springer, Series in Materials Science* **2013**, *182*.

[11] X. Qu, S. Lü, J. Hu, Q. Meng, *J. Alloys Compd.* **2011**, *509*, 10217–10221.

[12] R. Guo, X. Wang, B. Huang, *Sci. Rep.* **2010**, *5*, 7806.

[13] M. Benyahia, V. Ohorodniichuk, E. Leroy, A. Dauscher, B. Lenoir, E. Alleno, *J. Alloys Compd.* **2018**, *735*, 1096–1104.

[14] Y. Shi, B. Yang, P. K. Liaw, *Metals* **2017**, *7*, 43.

[15] D. B. Miracle, O. N. Senkov, *Acta Mater.* **2017**, *122*, 448–511.

[16] P. K. Samal, J. W. Newkirk, *ASM Handbook, Volume 7: Powder Metallurgy* **2015**.

[17] V. Bérubé, G. Radtke, M. Dresselhaus, G. Che, *Int. J. Energy Res.* **2007**, *31*, 637–663.

[18] J. J. Reilly, R. H. Wiswall, *Inorg. Chem.* **1974**, *13*, 218–222.

[19] E. Brüuck, *J. Phys. D: Appl. Phys.* **2005**, *38*, R381–R391.

[20] K. Fukamichi, A. Fujita, S. Fujieda, *J. Alloys Compd.* **2006**, *408*, 307–312.

[21] V. K. Pecharsky, K. A. Gschneidner, *Phys. Rev. Lett.* **1997**, *78*, 4494–4497.

[22] T. Krenke, E. Duman, M. Acet, E. F. Wassermann, X. Moya, L. Manosa, A. Planes, *Nature Materials* **2005**, *4*, 450–454.

[23] I. Dubenko, M. Khan, A. Kumar, P. Bhoj, R. Gautam, S. Stadler, N. Ali, *J. Magn. Magn. Mater* **2009**, *321*, 754–757.

Part VIII

Conclusion

This thesis is dedicated to the syntheses of thermoelectric intermetallics by magnesioreduction. These syntheses consist in the co-reduction of oxides by magnesium according to the reaction:

$$MO_x + M'O_y + (x+y)\,Mg \longrightarrow MM' + (x+y)\,MgO \tag{86}$$

This type of reaction is commonly used in the industry to extract metals (Ti, Zr, U, rare earths...) from ores but is rarely exploited for the syntheses of intermetallics. Only very few publications are reporting on the magnesioreduction synthesis of thermoelectric materials and, in the majority of the cases, the products are contaminated with large amounts of impurities and/or are obtained with low yields.

In the present work, magnesiothermic syntheses have been applied to two classes of materials: $CoSb_3$-based skutterudites and β-$FeSi_2$ and $MnSi_\gamma$ ($\gamma = 1.74$) silicides. A procedure was developed to obtain very pure products with yields higher than 95 %. In addition, the materials have been doped in a controlled way starting from properly doped precursors. The magnesioreduction process presents many advantages such as (i) the use of inexpensive and air stable metal oxide precursors, (ii) lower temperature and shorter reaction time thanks to the high reducing power of magnesium and (iii) direct production of well-crystallized powders with average grain sizes of about 200 nm for silicides and 500 nm for skutterudites. Careful analyses by X-ray diffraction reveal two types of reaction mechanisms. In the case of skutterudites, whose synthesis is carried out at the 'low' temperature of 810 K for 4 days, the O_2 vapor pressure of the oxides are oxidizing Mg resulting in the slow precursors reduction. In the case of the silicides, whose synthesis is carried out at the higher temperature of 1173 K, the oxide precursors are reduced by the high vapor pressure of liquid Mg in only 19 h. A direct consequence is that MgO by-product is present in the silicide samples and must therefore be washed away with diluted acid while it is absent in the skutterudite powders.

Densified mesostructured materials with average grain sizes ranging between 500 nm and 2 μm have been fabricated by spark plasma sintering. The structure and microstructure characteristics of the samples were studied by powder X-ray diffraction, EBSD and electron microscopies. The composite crystal structure of $MnSi_\gamma$ have been taken into account during the refinement of the XRD patterns by using a 3D+1 spacegroup approach with the help of the JANA software. The presence of (100)[011]/2 stacking faults in $FeSi_2$ has also been taken into account in the Rietveld refinement procedure and quantified using the FAULTS software. The high density of grain boundaries and the complex crystal structures of the materials result in the

presence of many defects which have been identified by TEM.

The mesostructuration of the obtained materials reduces the lattice thermal conductivities of about 15 - 20 % at room temperature compared to reference samples synthesized by conventional melting/annealing routes. However, except for β-$Co_{0.07}Fe_{0.93}Si_2$, the microstructure also results in higher electrical resistivities which prevents any significant improvements of the figure-of-merit ZT.

The promising results obtained and the knowledge gained on magnesioreduction syntheses during my thesis would hopefully help in applying this method to a wider range of materials.

UNIVERSITE MATIERE BRETAGNE MOLECULES LOIRE ET MATERIAUX

UNIVERSITÉ DE RENNES 1

Titre : Synthèse d'intermétalliques thermoélectriques par magnésiothermie : mécanismes, caractérisations multi-échelle et propriétés.

Mots clés : Magnésiothermie, Skutterudites, Siliciures, Thermoélectricité, Microstructure, Diffraction des rayons X.

Résumé : Une voie de synthèse alternative de matériaux intermétalliques thermoélectriques par magnésioréduction, a été mise au point et appliquée à deux types de matériaux: les skutterudites basées sur le composé $CoSb_3$ et les siliciures β-$FeSi_2$ et $MnSi_\gamma$ ($\gamma \approx 1.74$). Ces matériaux présentent un fort intérêt industriel mais ont des synthèses complexes par les méthodes conventionnelles et nécessitent un abaissement de leurs conductivités thermiques. Les résultats de ce travail montrent que ce type de synthèse permet, tout en diminuant les températures et durées de réaction, d'obtenir directement des poudres (i) de hautes puretés, (ii) de compositions chimiques contrôlées, notamment vis-à-vis de la concentration en dopants, et (iii) de tailles submicroniques adaptées à la fabrication par frittage SPS de matériaux massifs mésostructurés (grains entre 500 nm et 1 µm). Les caractéristiques structurales ont été étudiées par diffraction des rayons X sur poudre en prenant en compte des modèles avancés pour la structure composite (groupe d'espace 3D+1) de $MnSi_\gamma$ et les défauts d'empilement (100)[011]/2 de β-$FeSi_2$. La microstructure a été caractérisée par EBSD et MET afin de mettre en évidence les relations avec les propriétés thermoélectriques, notamment avec la réduction de la conductivité thermique de réseau. Le facteur de mérite thermoélectrique *ZT* n'est toutefois amélioré que dans le cas de β-$Co_{0,07}Fe_{0,93}Si_2$ car la résistivité électrique est aussi impactée par la mésostructure des matériaux. L'influence des conditions réactionnelles ainsi que les mécanismes de réaction ont été étudiés en détail afin de permettre l'application de cette méthode de synthèse à une large gamme de matériaux.

Title : Magnesiothermic synthesis of thermoelectric intermetallics: mechanisms, multi-scale characterizations and properties.

Keywords : Magnesiothermy, Skutterudites, Silicides, Thermoelectricity, Microstructure, X-ray diffraction.

Abstract : An alternative synthesis route for thermoelectric intermetallics by magnesioreduction was developed and applied to two classes of materials: $CoSb_3$-based skutterudites and the β-$FeSi_2$ and $MnSi_\gamma$ ($\gamma \approx 1.74$) silicides. These materials present a strong industrial potential but their syntheses by conventional methods are difficult and their lattice thermal conductivities must be reduced. The results of this work show that lower reaction temperatures and durations can be achieved by this route. In addition, it enables the direct synthesis of powders with (i) high purities, (ii) controlled chemical compositions and especially dopants concentration, and (iii) submicronic grain sizes which are suitable for the fabrication of mesostructured materials (grain size between 500 nm et 1 µm) by spark plasma sintering. The structural characteristics were studied by powder X-ray diffraction using advanced models taking into account the composite structure of $MnSi_\gamma$ (3D+1 space group) and the presence of (100)[011]/2 stacking faults in β-$FeSi_2$. The microstructure was characterized by EBSD and TEM in order to evidence relations with the thermoelectric properties and especially the reduction of the lattice thermal conductivities. However, the figure-of-merit *ZT* has only been improved in the case of β-$Co_{0.07}Fe_{0.93}Si_2$ because the electrical resistivities of the materials are also affected by the mesostructuration. The influence of the reaction parameters as well as the reaction mechanisms were studied in detail in order to apply the magnesioreduction syntheses to a wider range of materials.